The University Of Sheffield.

Strongly-coupled organic-based microcavities for polariton condensation and quantum batteries

Kirsty E. McGhee

A thesis submitted for the degree of Doctor of Philosophy
May 2022

Supervised by David G. Lidzey

Department of Physics and Astronomy
Faculty of Science
University of Sheffield

Dad

I know you would be proud of me.

Mum

For always being proud of me.

Acknowledgements

First of all, I would like to thank everyone who has provided joy in my life over the course of my PhD and the years leading up to it. There are far too many of you to list but you know who you are.

Particular thanks should go to:

Every member of EPMM over the last four years

For your invaluable help and the fabulously fun times I have had with you all.
(Also to the University Arms for facilitating far too much of said fun.)

Rahul & Kyriacos

I couldn't have done this PhD without you. You taught me everything I know.

David

For all your support and patience, your endless ideas, and the countless pints.

Catherine

For listening to all my stories, complaints and successes over the past few years.
I honestly couldn't have asked for a better housemate or friend.

Lewis

For everything.

Abstract

This thesis concerns the study of organic-based microcavities in both the strong and weak coupling regimes. The first three experimental chapters (Chapters 4-6) concern strongly-coupled microcavities for polariton condensation, whereas Chapter 7 studies a mix of weakly- and strongly-coupled cavities for use as quantum batteries.

A new cavity structure utilising a hybrid metal-dielectric mirror containing a boron dipyrromethene derivative was studied and found to give higher quality factors and Rabi splittings than the traditional double-distributed Bragg reflector (DBR) structure. It was then demonstrated that a hybrid-mirror cavity, whose bottom mirror consisted of only three layers, could support polariton condensation with only a slightly increased threshold compared to the double-DBR control.

A new dye, which has been used in weakly-coupled lasers, was investigated and shown to undergo polariton condensation despite a seemingly-broad absorption linewidth. Notably, polariton condensation was maintained for more than 37,000 pulses in air, showing remarkably enhanced photostability compared to previously studied small molecules.

A new technique for confining polariton condensates was studied in which two organic dyes were incorporated into a single microcavity such that one was strongly-coupled to the cavity mode and the other was weakly-coupled. The weakly-coupled dye was saturated optically to generate an ultrafast refractive index change, resulting in a blueshift of the polariton mode. This blueshift created an 'energy barrier' that could potentially be used to confine a polariton condensate that would be generated by pumping the strongly-coupled dye.

Microcavities containing a fluorescent dye at varying concentrations were used to demonstrate superabsorption in a prototype Dicke quantum battery. Here, each molecule was considered as a "battery" interacting with a common cavity mode. Fast spectroscopy was used to demonstrate superextensive charging power and energy storage density, giving the first evidence of superabsorption with a macroscopic number of molecules.

Publications

Jayaprakash, R., Whittaker, C. E., Georgiou, K., Game, O. S., **McGhee, K. E.**, Coles, D. M. & Lidzey, D. G. Two-Dimensional Organic-Exciton Polariton Lattice Fabricated Using Laser Patterning. *ACS Photonics* **7**, 2273-2281 (2020).

Putintsev, A., Zasedatelev, A., **McGhee, K. E.**, Cookson, T., Georgiou, K., Sannikov, D., Lidzey, D. G. & Lagoudakis, P. G. Nano-second exciton-polariton lasing in organic microcavities. *Applied Physics Letters* **117**, 123302 (2020).

Georgiou, K., **McGhee, K. E. (joint first author)**, Jayaprakash, R. & Lidzey, D. G. Observation of photon-mode decoupling in a strongly coupled multimode microcavity. *Journal of Chemical Physics* **154**, 124309 (2021).

McGhee, K. E., Putintsev, A., Jayaprakash, R., Georgiou, K., O'Kane, M. E., Kilbride, R. C., Cassella, E. J., Cavazzini, M., Sannikov, D. A., Lagoudakis, P. G. & Lidzey, D. G. Polariton condensation in an organic microcavity utilising a hybrid metal-DBR mirror. *Scientific Reports* **11**, 20879 (2021).

Quach, J. Q., **McGhee, K. E. (first experimental author)**, Ganzer, L., Rouse, D. M., Lovett, B. W., Gauger, E. M., Keeling, J., Cerullo, G., Lidzey, D. G., Virgili, T. Superabsorption in an organic microcavity: Toward a quantum battery. *Science Advances* **8**, eabk3160 (2022).

McGhee, K. E., Jayaprakash, R., Georgiou, K., Burg, S. L., Lidzey, D. G. Polariton condensation in a microcavity using a highly-stable molecular dye. *Journal of Materials Chemistry C* **10**, 4187 (2022).

Contents

1 Introduction

Everything that we see – and so much more that we don't – is governed by light and its interaction with matter. Indeed, life itself is only possible due to photosynthesis, in which light from the sun is harvested to create energy that is essential for all living species. Understanding the processes that occur when light and matter interact has been a focus of humankind for centuries and it is because of this fascination that we have been able to develop the life-changing technologies we now use on a daily basis.

In recent years, there has been a huge focus on nanoscale structures and electronics for communications, sensing, energy-harvesting, display technologies and more. Often it is necessary to confine light in such devices in order to exploit inter-atomic interactions and quantum mechanical effects that would not be evident otherwise. One simple method for confining light makes use of two-highly reflective mirrors whose separation is on the order of a micrometre or less. This facilitates the formation of a standing wave between the two mirrors whose wavelength can be varied simply by varying their separation. Such resonators are known as microcavities.

If a material with an electronic transition – for example an inorganic semiconductor or a fluorescent organic molecule – is placed inside a microcavity, and the transition is resonant with the confined electric field, the light (photons) and matter (excitons) will interact. If the strength of this interaction is relatively small, the system will operate in the weak coupling regime. In this regime, there is only a small perturbation in the energy levels and the system can be described by perturbation theory.

If, however, the interaction is sufficiently strong, a reversible exchange of energy will occur between the cavity photons and the intracavity material. This results in the formation of new quasiparticles known as polaritons for which perturbation theory is insufficient. These exciton-polaritons (or cavity polaritons) are a linear coherent superposition of the light and matter components and therefore possess properties of both. For example, polaritons have very small effective masses ($\sim 10^{-4}$-10^{-5} that of an electron [1]) and short lifetimes ($\sim$5-10 ps [2]), which they inherit from their photonic component, and a strong ability to interact with their environment, which they inherit from their excitonic component.

As both excitons and photons are bosonic in nature (i.e. they have integer spin), polaritons are also bosonic quasiparticles. Hence, at sufficiently high densities and low temperatures, they are able to undergo a non-equilibrium Bose-Einstein-like condensation. In this case, a macroscopic number of polaritons will occupy the lowest quantum state and will all possess the same energy, momentum and phase. If one of the mirrors is semi-transparent, the polaritons will be able to escape the cavity via their photonic component. The escaped photons will retain the properties of the polaritons and the emitted light will hence mimic laser emission. Polariton condensates can therefore be considered as lasers that do not require a population inversion: this means that in a sample that can support both non-linear processes, the polariton lasing threshold will be lower than the photon lasing threshold. In reality, however, polariton lasers cannot compete with the lowest threshold photon lasers [3].

The first demonstration of cavity-polaritons came 30 years ago in a GaAs-based cavity at cryogenic temperatures [4], followed a few years later by the observation of room temperature strong coupling in an organic-based cavity [5]. In the interceding decades, remarkable progress has been made with demonstrations of polariton condensation, superfluidity, transistors, LEDs, lattices and more. Notably, all of these have been shown at room temperature [6–13].

Microcavities can also be used for various other applications. For example, it is possible to enhance the output light intensity of organic LEDs (OLEDs) by inserting them into a microcavity. They have also been suggested as a potential architecture for quantum batteries [14]. These so-called Dicke quantum batteries take advantage of collective effects that occur when many molecules couple simultaneously to a single cavity mode. In this way they are able to exhibit superextensive charging and energy storage properties, which we have demonstrated experimentally for the first time (see Chapter 7).

1.1 Thesis outline

Chapter 2 gives an overview of the theory relevant to this thesis. Firstly, an introduction into organic semiconductors is given: this includes orbitals and bonding in organic molecules, their photophysics, and Frenkel excitons. Next, the basic physics of optical microcavities and their relevant properties are described, followed by a discussion on exciton-polaritons. Here, an overview of the weak and strong coupling regimes, photon lasing, and polariton condensation are provided, along with a historical review on proven and promising materials for polariton condensates. Finally, a brief introduction into quantum batteries is given.

Chapter 3 describes the methods used in this thesis. This covers fabrication techniques for thin films and microcavities, and optical characterisation techniques. Additional simple techniques are not described in this chapter, but can be found in the 'Methods' sections of the relevant papers.

The subsequent four chapters focus on experimental work. The first three contain studies on exciton-polaritons for polariton condensation, the first two of which (Chapters 4 and 5) have been published in *Scientific Reports* (2021) and *Journal of Materials Chemistry C* (2022), respectively. The third chapter (Chapter 6) is a conventional thesis chapter, which will be submitted for publication in the near future. The fourth experimental chapter (Chapter 7) concerns both weakly- and strongly-coupled organic-based microcavities and has been published in *Science Advances* (2022). The final section of each experimental chapter details the "Author contributions" in order to distinguish my work from that of my collaborators.

Chapter 4 describes studies on hybrid metal-DBR mirrors for polariton condensation. We show that hybrid mirrors, which were composed of a thick (200 nm) layer of silver and a few DBR pairs, have higher reflectivities and broader reflectivity bandwidths than a 10-pair DBR. We show that when used as the bottom mirror in strongly-coupled cavities containing BODIPY-Br, a boron dipyrromethene derivative, the hybrid-mirror cavities exhibit higher quality factors and larger Rabi splittings than a double-DBR control cavity. We then show that the simplest structure, whose bottom mirror consists only of 3 layers (silver, silicon dioxide and niobium pentoxide), is capable of supporting polariton condensation with only a slightly increased threshold compared to the control cavity. We observe that the condensate in the hybrid-mirror cavity does not fully collapse to $k = 0$ and we attribute this to poor adhesion between the silver and silicon dioxide layers, resulting in increased surface

roughness.

Chapter 5 focuses on a new dye in which polariton condensation had not previously been seen. Despite it appearing to have a very broad absorption linewidth, we demonstrate that, at sufficiently high concentrations, DPAVB – a styrylbenzene derivative that has previously been studied for use in weakly-coupled lasers and as a dopant for sky-blue LEDs – is able to enter the strong coupling regime. We then show that it exhibits polariton condensation at room temperature in air and can sustain this for more than 37,000 high-energy excitation pulses. This demonstrates remarkably high photostability compared to the BODIPY derivatives we have studied previously.

Chapter 6 is concerned with a new technique for the confinement of polariton condensates in organic-based microcavities. Double-DBR cavities were fabricated containing two organic dyes, one of which (BODIPY-Br) is strongly-coupled to the cavity mode and has previously been shown to undergo polariton condensation. The second dye, a modified polyfluorene derivative with statistical intrachain binaphthyl spacer groups (BN-PFO), is weakly-coupled to the cavity mode. Using transient reflectivity, we saturate the weakly-coupled dye to induce an effective decrease in the layer refractive index, resulting in a blueshift of the cavity mode and the lower polariton branch. We show that this blueshift happens on ultra-fast timescales (100s of fs) and its magnitude is dependent on the excitation fluence, with a maximum observed blueshift of 14 meV. Such a blueshift will act as an energy barrier in the cavity and therefore has potential applications in the confinement of polariton condensates.

Chapter 7 describes the first observation of superabsorption, which underpins the Dicke quantum battery effect, in a large number of molecules. Microcavities containing varying concentrations of the fluorescent dye lumogen-F orange were fabricated, where each cavity can be considered as a system containing a large number of "batteries" (molecules). We use transient reflectivity to measure the rise time and total energy stored in each cavity and demonstrate that those with higher dye concentrations charge faster and can store a greater quantity of energy per battery than those with lower concentrations, i.e. these quantities are superextensive. Along with this evidence for superabsorption, in which optical transitions working collectively through quantum coherence can absorb light more efficiently than if they acted alone, we show that the dissipation in the system is important to achieve long energy discharge times. This work provides the first proof-of-concept of a Dicke quantum battery, a battery that can charge faster and store more energy the larger it is.

Chapter 8 provides a summary of the work described in this thesis and discusses ideas for future work.

1.2 References

[1] Jiang, Z., Ren, A., Yan, Y., Yao, J. & Zhao, Y. S. Exciton-Polaritons and Their Bose–Einstein Condensates in Organic Semiconductor Microcavities. *Advanced Materials* **34**, 2106095 (2022).

[2] Keeling, J. & Berloff, N. Exciton-polariton condensation. *Contemporary Physics* **52**, 131–151 (2011).

[3] Sanvitto, D. & Kéna-Cohen, S. The road towards polaritonic devices. *Nature Materials* **15**, 1061–1073 (2016).

[4] Weisbuch, C., Nishioka, M., Ishikawa, A. & Arakawa, Y. Observation of the coupled exciton-photon mode splitting in a semiconductor quantum microcavity. *Physical Review Letters* **69**, 3314–3317 (1992).

[5] Lidzey, D. *et al.* Strong exciton–photon coupling in an organic semiconductor microcavity. *Nature* **395**, 53–55 (1998).

[6] Schneider, C. *et al.* An electrically pumped polariton laser. *Nature* **497**, 348–352 (2013).

[7] Daskalakis, K. S., Maier, S. A., Murray, R. & Kéna-Cohen, S. Nonlinear interactions in an organic polariton condensate. *Nature Materials* **13**, 271–278 (2014).

[8] Plumhof, J., Stöferle, T., Mai, L., Scherf, U. & Mahrt, R. Room-temperature Bose-Einstein condensation of cavity exciton-polaritons in a polymer. *Nature Materials* **13**, 247–252 (2014).

[9] Lerario, G. *et al.* Room-temperature superfluidity in a polariton condensate. *Nature Physics* **13**, 837–841 (2017).

[10] Zasedatelev, A. V. *et al.* A room-temperature organic polariton transistor. *Nature Photonics* **13**, 378–383 (2019).

[11] Jayaprakash, R. *et al.* A hybrid organic–inorganic polariton LED. *Light: Science and Applications* **8** (2019).

[12] Dusel, M. *et al.* Room temperature organic exciton–polariton condensate in a lattice. *Nature Communications* **11**, 1–7 (2020).

[13] Scafirimuto, F. *et al.* Tunable exciton–polariton condensation in a two-dimensional Lieb lattice at room temperature. *Communications Physics* **4**, 39 (2021).

[14] Ferraro, D., Campisi, M., Andolina, G. M., Pellegrini, V. & Polini, M. High-Power Collective Charging of a Solid-State Quantum Battery. *Physical Review Letters* **120**, 117702 (2018).

2 Theory of organic polariton microcavities

2.1 Organic semiconductors

Organic semiconductors are becoming increasingly popular due to their applications in solar cells, transistors, lasers and more [1–3]. Their light weight, low cost, flexibility and scalability are just some of the advantages that have encouraged researchers to move away from the traditional inorganic semiconductors such as silicon and gallium arsenide (GaAs). The recent growth of organic light-emitting diodes (OLEDs) in mobile phone, television and other screen technologies is just one example of the rapid commercialisation of organic semiconductors [4, 5].

Generally, organic materials are composed of carbon and hydrogen, with oxygen and nitrogen also commonly present. They exist as small molecules, polymers, oligomers, or in crystalline form. Contrary to inorganic semiconductors, organics are simple to fabricate and can be tailored through synthesis: by adding different functional groups to or altering other structural properties of small molecules, it is possible to change the emission and absorption properties, solubility, stability, and charge-carrier mobilities [6–8]. In this way, it is possible to synthesise soluble, stable compounds with absorption and emission properties which span the entire visible (as well as UV and IR) spectrum. The solubility of these compounds can then be exploited to fabricate cheap, large-scale films and devices through solution-processing techniques such as spray-coating, slot-die coating and blade-coating [9–11]. Additionally, they can also be deposited onto a wide range of surfaces, including flexible, stretchable and curved substrates [12]. This is in contrast to inorganic semiconductors which require very specific, high-quality substrates and careful deposition to avoid strain causing cracks in the films.

In recent years, there has been growing interest in organic semiconductor microcavity lasers due to their ease of fabrication, low cost, and potential for low-power/energy-efficient operation [13, 14]. There has been focus on weakly-coupled cavities, in which there is an irreversible exchange of energy between light and matter, and strongly-coupled cavities, in which the energy exchange is reversible [15]. Most notably, these microcavities utilise the 'customisability' of organic semiconductors to produce laser light at any desired wavelength. In addition to lasers, microcavities are also used in LEDs [16, 17], photovoltaics [1], and more recently as energy storage devices [18, 19].

2.1.1 Orbitals and bonding in organic molecules

In general, the electronic properties of solids can be divided into three categories. The first of these are insulators, in which the energy gap – known as the band gap – between the valence and conduction bands exceeds 4 eV. The second category are conductors – in this case there is no band gap and the electrons are free to move through the solid. Materials whose band gap lies between these two extremes are known as semiconductors. In this case, only a small amount of energy is needed to excite electrons from the valence band to the conduction band. This process can occur through

thermal, electrical or optical excitation. In inorganic semiconductors, which have until recent years been the material of choice in commercial electronics, the conduction and valence bands arise from the overlap of electronic orbitals in a periodic crystal structure. Organic semiconductors, however (although sometimes crystalline) are often amorphous and their band gap arises from their atomic bonding.

To understand bonds and the origin of band gaps in organic semiconductors, we must first discuss atomic orbitals. In atoms, each electron can be described by a unique set of four quantum numbers. This follows from the Pauli Exclusion Principle, which states that no two electrons can occupy the same quantum state simultaneously, i.e. no two electrons in a single atom can possess the same four quantum numbers. The principal quantum number, n, denotes the size of the electron shell and can take the integer values n = 1, 2, 3,... . This also determines the size of the atom, e.g. the larger the highest occupied shell, the bigger the atom. The angular momentum or azimuthal quantum number, l, denotes the shape of the orbital and can take the integer values l = 0, 1, 2,..., n-1, though it is perhaps more common to see l = s, p, d, f,... . According to the Aufbau principle, these subshells will be filled by electrons starting from the lowest energy and then filling by increasing energy. The magnetic quantum number, m_l, denotes the orbital orientation and can take the integer values m_l = -l, ..., -1, 0, 1,..., l. For the s orbital, l = 0 and so m_l = 0 is the only possible value. The s orbital therefore only has one orientation and is spherical in shape. The p orbitals, however, have l = 1 and are dumbbell-shaped. m_l can therefore take the value 1, 0 or -1 and so three orientations are possible. These are degenerate in energy and exist orthogonal to one another along the x, y and z axes. They are therefore denoted p_x, p_y and p_z. The d orbitals have l = 2 and therefore have 5 possible orientations. These orbitals are illustrated in Figure 2.1. The final quantum number is the spin quantum number, m_s, and this denotes the electron spin direction. This can be either 'spin up' or 'spin down' and takes the value $m_s = \pm 1/2$. Each orbital can therefore hold a maximum of two electrons [20]. The quantum numbers and their possible values are summarised in Table 2.1.

Quantum number	**Property**	**Possible values**
Principal (n)	Orbital size	0,1,2,...
Angular momentum (l)	Orbital shape	0,1,2,...,n-1 or s,p,d,f,...
Magnetic (m_l)	Orbital orientation	-l,...,-1,0,1,...,l
Spin (m_s)	Spin direction	$\pm 1/2$

Table 2.1. Summary of quantum numbers used to describe electrons in atoms and molecules.

We now consider an atom of carbon. Carbon has 6 electrons with an electronic configuration $1s^2 2s^2 2p^2$. This means that in each of the n = 1 and n = 2 shells there are two electrons with l = s = 0 and m_l = 0, with one electron having $m_s = +1/2$ and the other having $m_s = -1/2$. The n = 2 shell also has three p orbitals: two of these contain one electron each and the third is empty. This is illustrated in Figure 2.1(d).

Generally, atoms with incomplete outer shells will try to bond with other atoms to form more stable molecules. The noble gases have complete outer shells and hence do not readily form molecules. It can be seen from Figure 2.1(d) that carbon has four electron vacancies in the $2p$ orbitals. Therefore, it is said to be tetravalent and has four electrons available to participate in bonding.

When bonding, electrons in half-filled orbitals are shared between atoms to form complete outer

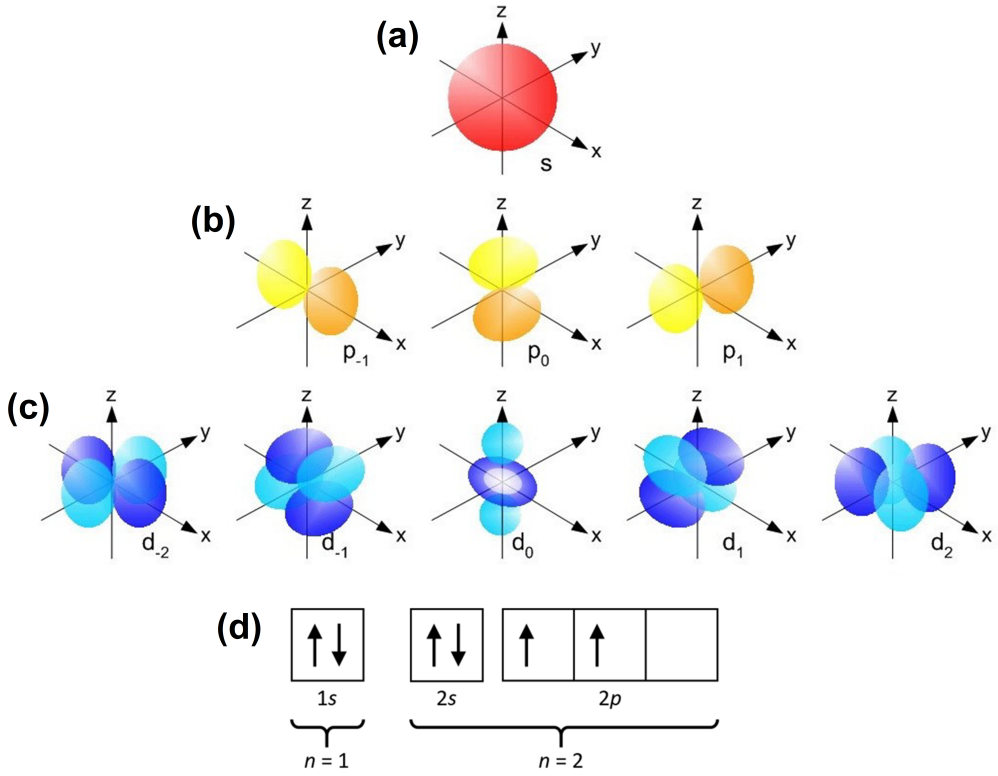

Figure 2.1. Atomic orbitals. Parts (a), (b) and (c) illustrate the shape and orientation of *s*, *p* and *d* orbitals, respectively. Part (d) depicts the electronic configuration of carbon, where each box represents an orbital and the arrows electrons. ((a)-(c) sourced from [21].)

shells. As we can see from the electronic configuration of carbon (Figure 2.1(d)), however, there are only three orbitals that are not full in each atom. In this case, the $2p$ and $2s$ orbitals (illustrated in Figure 2.2(a)) hybridise to form *sp* orbitals (illustrated in Figure 2.2(b)). The type of hybridisation can be termed *sp*, sp^2, or sp^3, with the superscript denoting the number of *p* orbitals involved. In all cases, we end up with four half-filled orbitals available for bonding and these are illustrated in Figure 2.2(c)-(e) [22].

When only single bonds are formed, sp^3 hybridisation occurs. In this case, a half-filled hybrid *sp* orbital of carbon will overlap with a half-filled orbital of another atom 'end-on', as is shown in Figure 2.3(b) for ethane (chemical structure shown in Figure 2.3(a)). These are strong covalent bonds known as σ bonds and, in ethane, the C-H and C-C bonds are all formed by this mechanism. If we instead consider ethene (chemical structure shown in Figure 2.3(c)), we see there is a double bond between the two carbon atoms. In this case, the orbitals undergo sp^2 hybridisation and each carbon atom forms three σ bonds (one C-C and two C-H) with their *sp* orbitals. The p_z orbitals also take part in the bonding; however, here, instead of overlapping 'end-on', they overlap 'side-on' as shown in Figure 2.3(d). This side-on bond is known as a π bond and these are much weaker than σ bonds. In the case of triple bonds, the carbon atom undergoes *sp* hybridisation. Similarly to in double bonding, the *sp* hybrid orbitals form σ bonds (one C-C and one C-H per carbon atom) and the p_y and p_z orbitals each form a π bond. This occurs in molecules such as ethyne, as shown in Figure 2.3(e) and (f) [22, 24].

Ethane, ethene and ethyne are some of the simplest organic molecules, with only one carbon-carbon bond. Larger molecules with more carbon atoms often have alternating single and multiple bonds

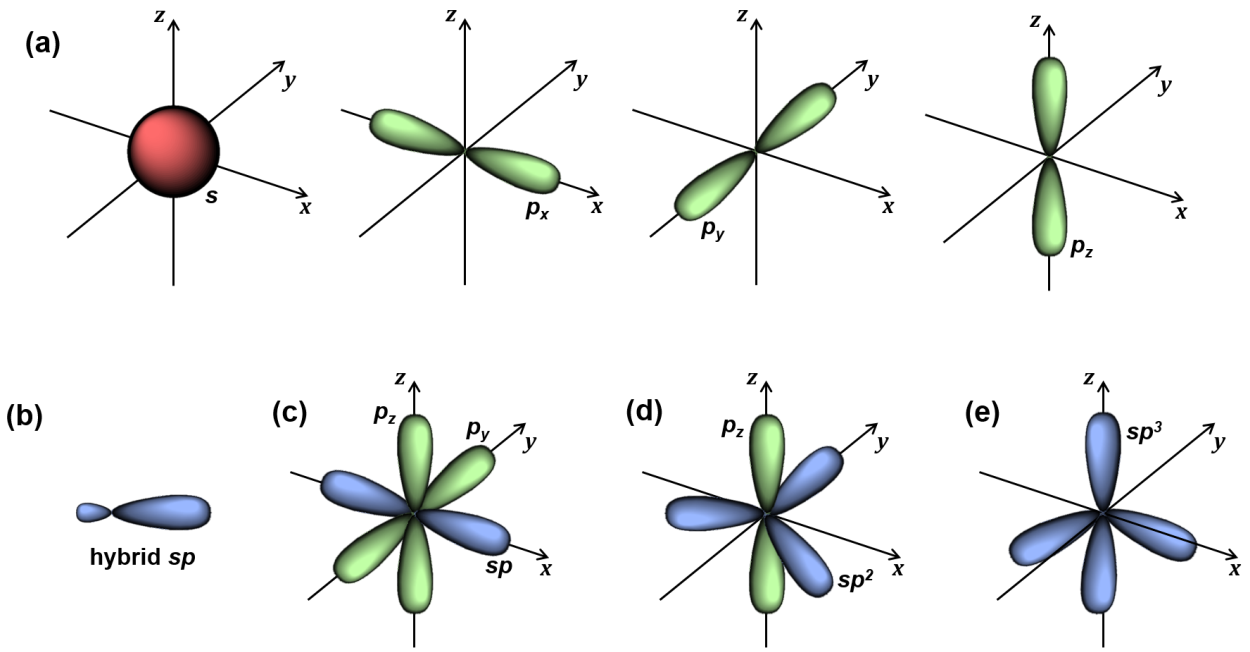

Figure 2.2. Hybridisation of $n = 2$ orbitals in the bonding of carbon. Part (a) shows the $2s$ orbital (red) and the three orthogonal $2p$ orbitals (green, p_x, p_y and p_z) before hybridisation. Part (b) shows the sp orbital after hybridisation (blue). Parts (c)-(e) show the n=2 orbitals after (c) sp, (d) sp^2, and (e) sp^3 hybridisation. In this case, the smaller lobe shown in part (c) is omitted for simplicity. The angles between the hybridised sp orbitals are (c) 180°, (d) 120° and (e) 109.5°. (Adapted from [23].)

between the carbon atoms and these are known as conjugated molecules. In this case, the π electrons are delocalised along the entire carbon-carbon chain in one large π orbital. Benzene, for example, is a cyclic conjugated molecule and its chemical structure is shown in Figure 2.4(a). We can see from this that benzene consists of six carbon atoms arranged in a hexagon, with each atom bonded to two other carbon atoms and one hydrogen atom. Three of these bonds are σ bonds formed by carbon's hybridised sp^2 orbitals, as shown in Figure 2.4(b). We are then left with six p_z orbitals (one from each carbon atom), as shown in part (c), which can form π bonds. However, instead of forming three π bonds as we might expect, the π electrons form a delocalised ring orbital that is more accurately depicted by the chemical structure shown in part (d). This ring lies above and below the plane of the hexagon, as shown in part (e), and the electrons are shared equally by all six carbon atoms. Due to this spreading of the electron wavefunctions, there is a reduction in confinement energy compared to σ bonds. If a molecule contains a sufficient number of π orbitals, the energy is lowered into the visible region of the electromagnetic spectrum. It is this kind of molecule that we are interested in for use in optoelectronics [24].

In solid form, organic molecules are held together by weak van der Waals' interactions. These interactions are much weaker than the covalent bonds that form the molecules from the constituent atoms; hence, organic molecular solids are relatively soft and have low boiling points. One interesting property that arises from the weak intermolecular interactions is that the electronic states are mostly unchanged and remain localised on the individual molecules. The electronic and optical properties of the solid are therefore almost identical to those of a single molecule [24].

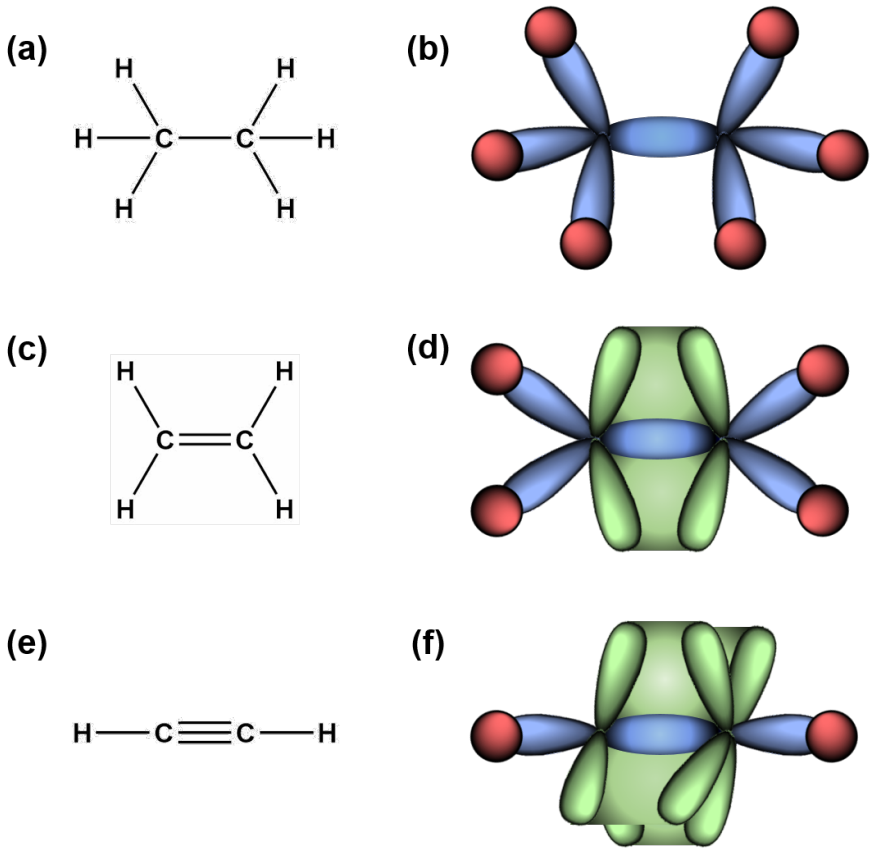

Figure 2.3. Illustration of carbon bonding. Parts (a), (c) and (e) show the chemical structure of ethane, ethene, and ethyne, respectively. Parts (b), (d) and (f) illustrate the orbitals involved in bonding in ethane, ethene and ethyne, respectively. The hybridised carbon orbitals are shown in blue, and the un-hybridised orbitals are shown in green. The red circles represent the $n = 1$ shell of the hydrogen atoms. ((b), (d), and (f) adapted from [23].)

2.1.2 Optical absorption and emission

When discussing organic molecules, there are three relevant regions of the electromagnetic spectrum: the ultraviolet-visible (UV-vis), which corresponds to electronic transitions, the infrared (IR), which corresponds to vibrational transitions, and the far-infrared (FIR), which corresponds to rotational transitions. These transitions involve the promotion (excitation) and demotion (relaxation) of electrons between energy levels and are accompanied by the absorption and emission of photons, respectively, whose energy corresponds to the energy of the transition.

2.1.2.1 Electronic transitions

Electronic transitions occur between different orbitals in organic molecules. The Aufbau principle, as discussed above, states that electrons must fill molecular orbitals in order from the lowest to the highest energy states. It therefore follows that there will exist an electron-containing orbital below which all orbitals are full and above which all orbitals are empty. This highest occupied energy level is known as the HOMO (highest occupied molecular orbital) and the orbital immediately above this in energy is known as the LUMO (lowest unoccupied molecular orbital). These are analogous to the valence and conduction band in inorganic semiconductors, respectively. The lowest possible transition is therefore between these two levels and is known as a $\pi \rightarrow \pi^*$ transition. This is because

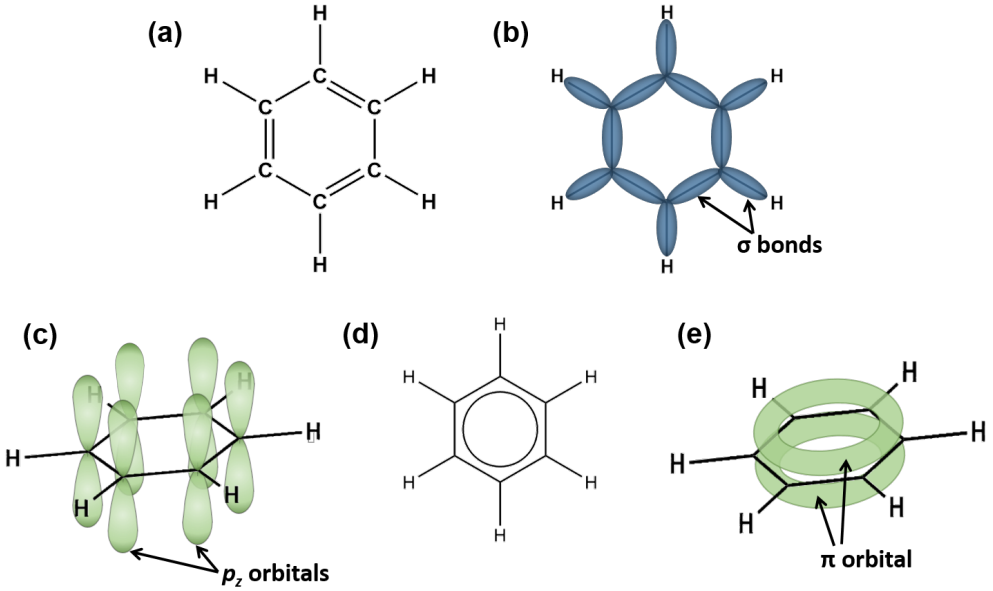

Figure 2.4. Structure of benzene. Part (a) shows the chemical structure with alternating single and double bonds between the carbon atoms. Parts (b) and (c) show illustrations of (b) the σ bonds formed by the hybrid *sp* orbitals (blue) and (c) the p_z orbitals (green) that are available for π bonding. Part (d) shows the more accurate chemical structure in which the double bonds have been replaced by a delocalised ring, and (e) illustrates the π ring orbital (green) that is formed.

both the HOMO and the LUMO are π orbitals, with the * denoting that the LUMO is an excited state. σ electrons are much more tightly bound and so much higher energies are required to excite electrons involved in σ bonds.

The energy of the absorbed photon, E, is equal to the energy difference between the two energy levels involved and is related to the wavelength, λ, through

$$E = \frac{hc}{\lambda}, \tag{2.1}$$

where h is Planck's constant and c is the speed of light in a vacuum. As the probability of absorption of a photon is dependent on the energy levels that exist within the molecule, it is therefore also dependent on the wavelength of the photon, and can be described by the molecule's absorption cross section, $\sigma(\lambda)$, which is usually expressed in cm^2. We can define the absorption coefficient, $\alpha(\lambda)$, as

$$\alpha(\lambda) = N\sigma(\lambda), \tag{2.2}$$

where N is the number of absorbing molecules per unit volume. $\alpha(\lambda)$ is therefore usually expressed in cm^{-1}. Now consider a material of thickness z upon which light of intensity (optical power per unit area) I_0 is incident, as is illustrated in Figure 2.5. The optical intensity lost by travelling a distance dz, dI, can be expressed using

$$dI = -IN\sigma(\lambda)dz = -I\alpha(\lambda)dz. \tag{2.3}$$

By integrating this expression, we obtain the Beer-Lambert law:

$$\frac{I_z}{I_0} = e^{-\alpha(\lambda)z}, \tag{2.4}$$

where I_z is the final intensity of the light after passing through the material. This describes the optical attenuation of an electromagnetic wave travelling through a material.

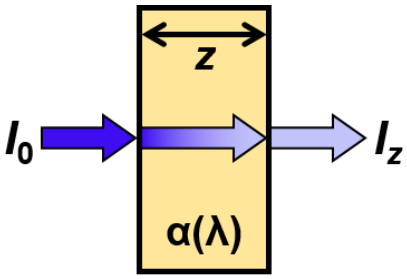

Figure 2.5. Attenuation of light travelling through a medium. After passing through a material with thickness z and absorption coefficient $\alpha(\lambda)$, light with initial intensity I_0 will have intensity $I_z = I_0 = e^{-\alpha(\lambda)z}$. This is the Beer-Lambert law.

Pauli's Exclusion Principle (as discussed above) states that no two electrons can have the same four quantum numbers. Thus, a full orbital contains two electrons and they must have opposite spin. The ground state of a molecule will therefore have a total spin S=0. This spin configuration is illustrated in Figure 2.6(a). When an electron is promoted to an excited state orbital, the electrons no longer need to have opposite spin and therefore the total spin of the system can either be S=0 or S=1. S=0 states, in which the excited electron retains its spin from the ground state, are known as singlets. This is because their multiplicity (the number of degenerate states) = $2S+1 = 1$. Here, the electron spins will be anti-parallel, as is illustrated in Figure 2.6(b). The ground state is also a singlet as S=0. For S=1 states, the excited electron's spin 'flips' and the two electrons have parallel spins, as is illustrated in Figure 2.6(c). This is possible due to spin-orbit coupling, which results in a non-zero probability of a singlet transitioning to a triplet state through intersystem crossing. In this case, the multiplicity = $2S+1 = 3$. These states are therefore known as triplets.

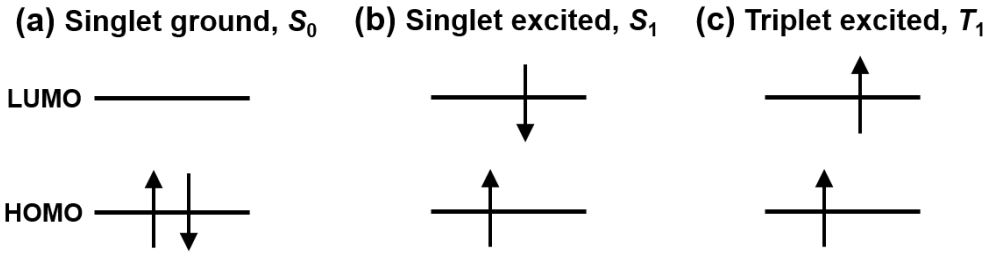

Figure 2.6. Illustration of electron spins in singlets and triplets. Part (a) shows the singlet ground state, S_0, in which both electrons are in the HOMO and their spins are anti-parallel. Part (b) shows the singlet excited state, S_1, in which there is one electron each in the HOMO and the LUMO and their spins are anti-parallel. Part (c) shows the triplet excited state, T_1, in which there is one electron each in the HOMO and the LUMO and their spins are parallel.

As photons have S=0 and spin must be conserved according to the spin selection rules, only transitions between states of the same spin are allowed. Hence, in organic molecules the absorption edge and emission peak tend to correspond to the transition between the ground state (which is a singlet), and the first excited singlet state. The light emitted in this type of transition is called fluorescence and occurs on a timescale of ∼ns [24]. Generally the ground state (the HOMO) is denoted by S_0 and the first excited state (the LUMO) by S_1. Hence, the transition involved in fluorescence is denoted by $S_1 \rightarrow S_0$.

As mentioned above, it is possible for an electron in S_1 to transition to the first triplet excited state, T_1, through intersystem crossing. This is more likely to occur if the vibrational energy levels (see next section) of S_1 and T_1 overlap so that no or very little energy is lost in the transition. Emission from T_1, although 'forbidden' (unfavourable), can occur but at a much slower rate than fluorescence. This process is called phosphorescence and generally happens on a ms scale, though it can take several seconds or even minutes [24].

When filling orbitals, electrons must first fill each orbital singly and all have the same spin before they start pairing up. This is known as Hund's rule of maximum multiplicity, which states that the configuration with the greatest multiplicity will have the lowest energy. Triplets tend to therefore have a slightly lower energy than the corresponding singlet state.

2.1.2.2 Vibrational transitions

Vibrational transitions occur between different vibrational levels in the same electronic orbital. These vibrational levels arise due to the bending or stretching of bonds within molecules. Each molecule has a unique set of allowed, quantised vibrational levels, which are determined by the atoms involved, their relative orientation, and the type of bond (e.g. single, double, triple). At room temperature, a molecule will generally exist in the vibrational ground state, which vibrates with a particular resonant frequency. However, upon the absorption of a photon in the near or mid IR, the molecule can be excited to a higher vibrational state. Due to the high sensitivity to the bond's surroundings, each molecule will have its own unique IR absorption spectrum, which can be used for identification purposes.

2.1.2.3 Rotational transitions

Rotational energy levels arise from the quantised angular momenta of molecules about their centre of mass: a transition to a higher rotational state corresponds to an increase in angular momentum, and a transition to a lower state corresponds to a decrease. This is accompanied by the absorption or emission of a far IR photon, respectively. Generally these transitions occur between rotational states of the same vibrational level, but they can also occur between vibrational levels. In this case, they are called rotational-vibrational or ro-vibrational transitions and the corresponding photon will lie in the mid IR region of the electromagnetic spectrum.

Electronic, vibrational and rotational transitions are summarised in the Jablonski diagram in Figure 2.7.

2.1.2.4 Stokes shift

The probability of transition depends on the overlap of the wavefunctions of the two energy levels: the greater the overlap, the higher the probability of transition. This is the Franck-Condon principle, which assumes there is no movement of a molecule's nuclei over the timescale of the transition [24]. When an electron undergoes an electronic transition through the absorption of a UV or visible photon, it is therefore often the case that it will also transition between vibrational states. These joint electronic-vibrational transitions are known as vibronic transitions.

If a photon of sufficient energy is absorbed, a transition to a higher excited state, S_n, where n is an integer greater than 1, is possible. However, according to Kasha's rule, the emission can only occur

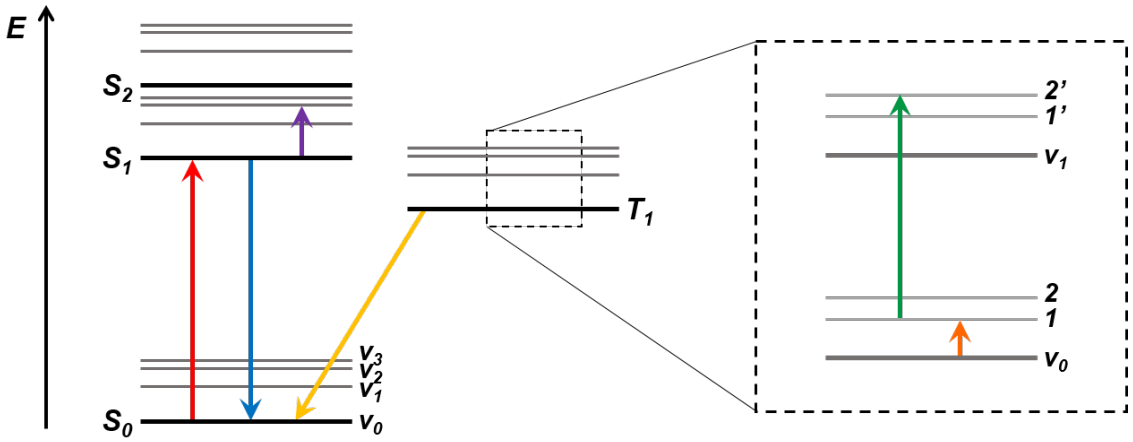

Figure 2.7. Jablonski diagram illustrating the different types of transition. S_0, S_1 and S_2 indicate the singlet ground state, first excited state and second excited state, respectively, and T_1 represents the first triplet excited state. v_0 represents the vibrational ground state and v_1, v_2 and v_3 represent vibrational excited states. The numbered levels in the dashed box represent the different rotational states. The coloured arrows illustrate absorption ($S_0 \rightarrow S_1$, red), fluorescence ($S_1 \rightarrow S_0$, blue), phosphorescence ($T_1 \rightarrow S_0$, gold), a vibrational transition (purple), a ro-vibrational transition (green) and a rotational transition (orange). The black arrow on the far left indicates the direction of increasing energy, E.

in appreciable yield from the lowest excited state of any given multiplicity, i.e. S_1 for a singlet and T_1 for a triplet. This is due to the probability of transitions between the different states and again relies on the Franck-Condon principle. This results in the emission spectra of organic molecules being dominated by the $S_1 \rightarrow S_0$ transition. Another way of expressing Kasha's rule, therefore, is that the emission wavelength is independent of the wavelength of the absorbed photon.

Electrons in higher excited and vibrational states therefore tend to relax non-radiatively to the ground vibrational state of S_1 through internal conversion and vibrational relaxation, respectively. The electron will then relax radiatively to a vibrational state of S_0. This is illustrated in the Jablonski diagram in Figure 2.8(a), where it can be seen that these processes result in the emitted photon being of lower energy and longer wavelength than the absorbed photon. This energy difference between absorption and emission peaks corresponding to the same electronic transition is known as Stokes shift. Example spectra are shown in Figure 2.8(b), where a 20 nm Stokes shift between the absorption and emission maxima can be seen.

2.1.3 Excitons in organic molecules

When an electron is promoted to an excited state, a vacancy is created in the ground state. This vacancy acts like a particle with positive charge equal in magnitude to that of the electron – this is termed a hole. The promotion of the electron, therefore, creates an electron-hole pair. Due to these opposite charges, the electron and hole are attracted to one another through Coulombic attraction and this can create a bound state known as an exciton with a lower energy than the sum of the two unbound particles [24]. Absorption can therefore be considered as the creation of an exciton. In the reverse process, when an electron and hole recombine, the exciton decays and a photon is emitted.

Inorganic materials (where the electron resides in the conduction band and the hole in the valence band) tend to have large dielectric constants, which screen the Coulombic attraction between the electron and hole. This results in weakly-bound excitons with large radii and small binding energies

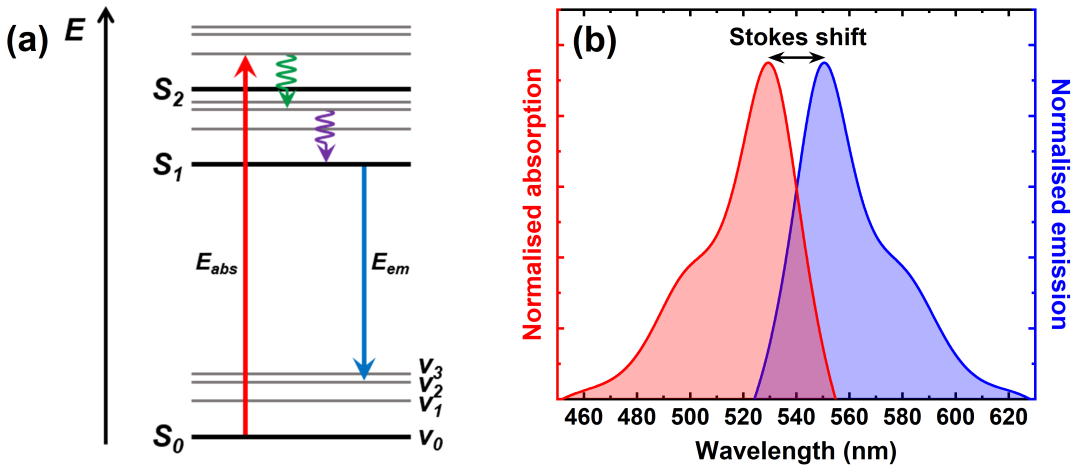

Figure 2.8. Stokes shift. Part (a) shows a Jablonksi diagram illustrating the processes responsible for Stokes shift. The red arrows represents the absorption of a photon with energy E_{abs} to an excited vibrational level in S_2. The electron then relaxes non-radiatively to the ground vibrational level of S_1 through internal conversion (green wavy arrow) and vibrational relaxation (purple wavy arrow). It then relaxes radiatively to an excited vibrational state of S_0, accompanied by the emission of a photon with energy E_{em}, where $E_{em}<E_{abs}$. Part (b) shows example absorption (red) and emission (blue) spectra for a molecule with a Stokes shift of 20 nm.

(∼10 meV) [25]. These Wannier-Mott excitons have radii much larger than the lattice spacing and are delocalised and free to move throughout the crystal. Hence, they are sometimes called 'free excitons'. Due to their small binding energies, they do not exist at room temperature and only form in appreciable numbers at cryogenic temperatures.

Organic materials on the other hand tend to have small dielectric constants and hence the Coulombic attraction between the electrons and holes is much larger. These so-called Frenkel excitons have small radii and large binding energies up to 1 eV [25], and are stable at room temperature. Unlike Wannier-Mott excitons, Frenkel excitons are localised and tend to be tightly-bound to specific atoms or molecules. They are therefore sometimes called 'tightly-bound excitons'. They can, however, move through a material by 'hopping' between sites.

The exciton energy is equal to the energy required to create the electron-hole pair (i.e. the band gap) minus the binding energy of the electron. The electron therefore resides in a state just below the LUMO and the hole in a state just above the HOMO. This energy gap is sometimes referred to as the optical band gap, with the energy required to create an unbound electron-hole pair known as the electrical band gap. The optical band gap manifests as a narrow peak in the absorption spectrum below the electrical band gap energy.

2.1.3.1 Photoluminescence

As with excited electrons, excitons can either be in a singlet or triplet state depending on the relative spin of the exciton and hole. When created by the absorption of a photon, the exciton will be in a singlet state due to the spin selection rules. When excited electrically, however, these rules do not apply and triplet states are also possible. In the singlet state, the electron and hole can recombine radiatively: if the exciton was created through electrical excitation, the emission is termed electroluminescence; if it was created through the absorption of a photon, it is termed photoluminescence.

The photoluminescence intensity, I, as a function of time, t, can be described by

$$I(t) = I_0 e^{-\kappa t} = I_0 e^{-t/\tau}, \tag{2.5}$$

where I_0 is the initial emission intensity, and κ and τ are the decay rate and time constant, respectively. κ can be expressed as the sum of the radiative, κ_r, and non-radiative, κ_{nr}, rates through

$$\kappa = \kappa_r + \kappa_{nr}. \tag{2.6}$$

Non-radiative processes that can occur in organic molecular systems include energy transfer to other molecules, trapping in defect states, internal conversion and intersystem crossing. The fraction of radiative decay transitions compared to total decay transitions in a material is known as the photoluminescence quantum yield (PLQY) or photoluminescence quantum efficiency (PLQE), Φ, and this is given by

$$\Phi = \frac{\kappa_r}{\kappa_r + \kappa_{nr}}. \tag{2.7}$$

Φ is a measure of how efficiently a material can re-emit absorbed light and can also be considered as the ratio of the number of photons emitted to those absorbed. It is often quoted as a percentage, with Φ=100% meaning every exciton decays radiatively. If Φ <100%, $\kappa_{nr} > 0$.

It is also possible for excitons to dissociate back into the constituent electrons and holes without recombining. This dissociation is often due to the presence of impurity sites, interfaces and charge transfer states [26].

2.2 Optical microcavities

Optical microcavities are commonly used to confine light, with the most common type of microcavity being the Fabry-Pérot resonator. This type of cavity consists of two highly-reflective parallel mirrors separated by a spacer layer with thickness such that the entire structure is on the order of a micrometre or less. Generally, at least one of the mirrors is semi-transparent to allow photons to enter and exit the cavity. These photons interfere constructively to form a standing wave perpendicular to the mirror surfaces with wavelength, $\lambda_\perp$, given by

$$\lambda_\perp = \frac{2 n_c d_c}{m}, \tag{2.8}$$

where n_c and d_c are the effective cavity refractive index and thickness respectively, and m is the cavity mode order which is an integer ($m \geq 1$). It can be seen from this that the cavity wavelength can be tuned by altering the thickness of the spacer layer. (It should be noted that, although in general, the cavity thickness and refractive index are defined by that of the spacer layer, any penetration of the confined electromagnetic field into the mirrors also need be considered – see Section 2.4.2.4.)

Instead of wavelength, we can consider light within a Fabry-Pérot microcavity in terms of its wavevector, k, where

$$k = \frac{2\pi}{\lambda}. \tag{2.9}$$

The total wavevector of the confined light can be divided into its perpendicular and parallel compo-

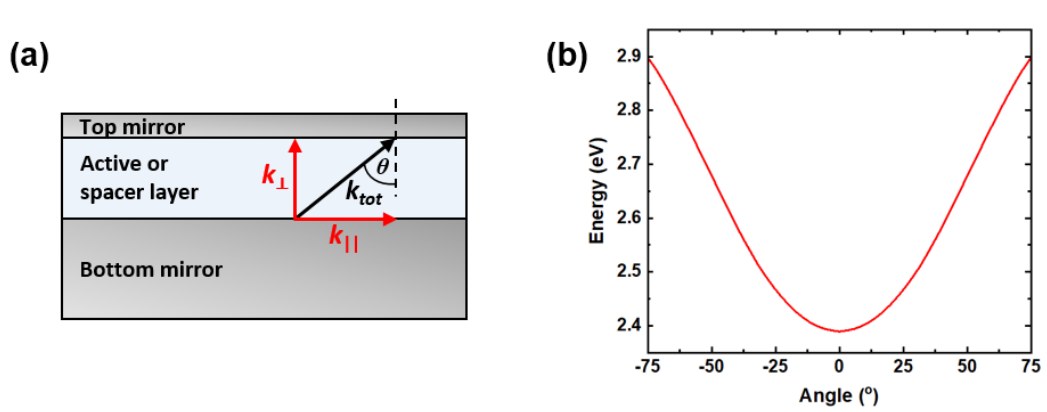

Figure 2.9. Fabry-Pérot microcavity. Part (a) shows a cavity schematic illustrating the total wavevector, k_{tot}, propagating at an angle θ to the cavity normal, showing how it is comprised of perpendicular, $k_\perp$, and parallel, $k_\parallel$, components. Part (b) shows a typical cavity dispersion. In this case the bottom mirror consists of 200 nm Ag and the top of 35 nm. The active or spacer layer is 120 nm, giving a cavity mode position of 537 nm at 0°.

nents, such that

$$k_{tot}^2 = k_\perp^2 + k_\parallel^2. \tag{2.10}$$

Here, $k_\perp = k_{tot} cos\theta$ is the component of the wavevector perpendicular to the cavity surface and $k_\parallel = k_{tot} sin\theta$ is the component parallel to it, with θ being the angle between k_{tot} and the cavity surface normal. This is illustrated in Figure 2.9(a). From Equations 2.8 and 2.9, it can be seen that

$$k_\perp = \frac{\pi m}{n_c d_c}. \tag{2.11}$$

From this we obtain

$$k_{tot} = \frac{\pi m}{n_c d_c \ cos\theta}, \tag{2.12}$$

$$k_\parallel = \frac{\pi m \ tan\theta}{n_c d_c}, \tag{2.13}$$

and

$$\lambda_c = \frac{2 n_c d_c \ cos\theta}{m}. \tag{2.14}$$

Here, λ_c is the angle-dependent wavelength of the cavity mode. The cavity mode energy, E_c, is then given by

$$E_c = \frac{hc}{\lambda_c} = \frac{hcm}{2 n_c d_c \ cos\theta} = \frac{E_0}{cos\theta}, \tag{2.15}$$

where h is Planck's constant, c is the speed of light, and $E_0 = {}^{hcm}/_{2 n_c d_c}$ is the cavity mode energy when viewed along the cavity normal. From this set of equations, it can be seen that the cavity mode wavelength decreases and the energy increases as you move to higher viewing angles.

Cavities are usually measured from outside the cavity and so we must consider the external viewing angle, θ_{ext}. We can do this using Snell's law: $n_1 sin\theta_1 = n_2 sin\theta_2$. Here, n_1 and θ_1 are the cavity refractive index, n_c, and the internal viewing angle with respect to the cavity normal, respectively, and n_2 and θ_2 are the refractive index outside the cavity and the external viewing angle with respect to the cavity normal, θ_{ext}, respectively. If we assume that the medium outside the cavity is air n_2=1

and substitute into Equation 2.15, we find

$$E_c = \frac{E_0}{\sqrt{1 - sin^2\theta_1}} = E_0 \left(1 - \frac{sin^2\theta_{ext}}{n_c^2}\right)^{-1/2}. \tag{2.16}$$

The cavity dispersion, as viewed from outside the cavity, looks similar to that shown in Figure 2.9(b), with the effective cavity length and refractive index determining the wavelength and the 'steepness' of the dispersion. It should be noted that the cavity mode is also polarisation-dependent, with the transverse electric (TE) and transverse magnetic (TM) modes exhibiting a different angle-dependence due to different penetration of the two polarisations into the cavity mirrors [27].

2.2.1 Cavity confinement

An important property of Fabry-Pérot microcavities is the finesse, F, which is given by

$$F = \frac{\pi(R_1R_2)^{1/4}}{1 - \sqrt{R_1R_2}} = \frac{\omega_m - \omega_{m-1}}{\Delta\omega}, \tag{2.17}$$

where R_1 and R_2 are the reflectivities of the two mirrors, ω_m and ω_{m-1} are the angular frequency of the m^{th} and $(m-1)^{th}$ modes, respectively, and $\Delta\omega$ is the full width at half-maximum (FWHM) of the modes. It can be seen from this that F, which is a measure of the confinement of light within the cavity, is dependent solely on the reflectivity of its mirrors. In reality, the confinement is lower due to scattering and absorption losses.

To calculate the lifetime of the cavity mode, consider a cavity of length d_c with refractive index n_c and mirrors with reflectivity R_1 and R_2. If we input N photons into the cavity, after one round trip, we will be left with R_1R_2N photons. If we assume that the mirrors have high reflectivity, i.e. $R_1 = R_2 = R \approx 1$, on average we will lose $\Delta N = (1-R)N$ photons in a time $t = {}^{n_cd_c}/_c$ (i.e. a half round-trip), where c is the speed of light. If we consider the rate of change of N, we get

$$\frac{dN}{dt} = -\frac{c(1-R)N}{n_cd_c}, \tag{2.18}$$

that has the solution $N = N_0e^{-t/\tau_c}$, where

$$\tau_c = -\frac{n_cd_c}{c(1-R)} \tag{2.19}$$

is the cavity photon lifetime. Additionally, for high reflectivity mirrors it is also true that

$$\tau_c \approx \frac{1}{\Delta\omega}. \tag{2.20}$$

It can be seen from this that the cavity photon lifetime and the linewidth depend on the reflectivity of the cavity mirrors, with higher reflectivity giving an increased lifetime and narrower linewidth [28].

Another, perhaps more commonly used, measure of the cavity confinement is the quality factor, also known as the Q-factor or simply Q. This gives the confinement of a specific cavity mode and is defined as

$$Q = \frac{\omega}{\Delta\omega} = \frac{\lambda}{\Delta\lambda}, \tag{2.21}$$

where λ and $\Delta\lambda$ are the wavelength and full width at half-maximum (FWHM) of the cavity mode, respectively. It is also a measure of the rate of energy loss from the cavity due to scattering, absorption and leakage, with $1/Q$ giving the fractional loss suffered during one round-trip of the cavity. A high Q-factor is therefore associated with a long photon lifetime and low energy loss.

2.2.2 Cavity mirrors

The reflectivity of a mirror – and indeed any material – can be described in terms of its complex refractive index, $\tilde{n}$, through

$$R = \frac{I_r}{I_i} = \left|\frac{\tilde{n}-1}{\tilde{n}+1}\right|^2, \tag{2.22}$$

where I_i and I_r are the intensity of the incident and reflected light, respectively, and

$$\tilde{n} = n + ik. \tag{2.23}$$

We then see that

$$R = \frac{(n-1)^2 + k^2}{(n-1)^2 + k^2}, \tag{2.24}$$

where k, the imaginary component of $\tilde{n}$, is known as the extinction coefficient and is related to a material's absorption (α, see Section 2.1.2) through

$$k = \frac{\alpha\lambda}{4\pi}. \tag{2.25}$$

It should be noted that both the real (n) and the imaginary (k) components of $\tilde{n}$ are wavelength-dependent [24, 29].

2.2.2.1 Metal mirrors

Metals such as gold (Au), silver (Ag) and aluminium (Al) are commonly used as microcavity mirrors due to their relatively high reflectivity across the visible spectrum. The main advantage of metals is that they are quick and simple to fabricate through thermal evaporation (see Section 3.1.2.1) and the magnitude of their reflectivity and transmission can be tailored by varying the layer thickness. In this way, a thick layer can be used as an opaque bottom mirror, and a thinner, semi-transparent top mirror can allow light to enter and exit the cavity. The main drawback of metal mirrors is their relatively high absorption, which results in low Q-factors typically <100. The reflectivity spectra for gold, silver and aluminium calculated using a transfer matrix reflectivity (TMR) model are shown in Figure 2.10.

2.2.2.2 Distributed Bragg reflectors

An alternative to metal mirrors are distributed Bragg reflectors (DBRs) which consist of a stack of alternating high- and low-refractive index dielectrics. Compared to metals, DBRs have higher reflectivity and lower absorption. Additionally, their reflectivity spectra can be very finely tailored for the specific application by altering the layer thicknesses, the number of layers in the stack, and the relative refractive indices of the materials.

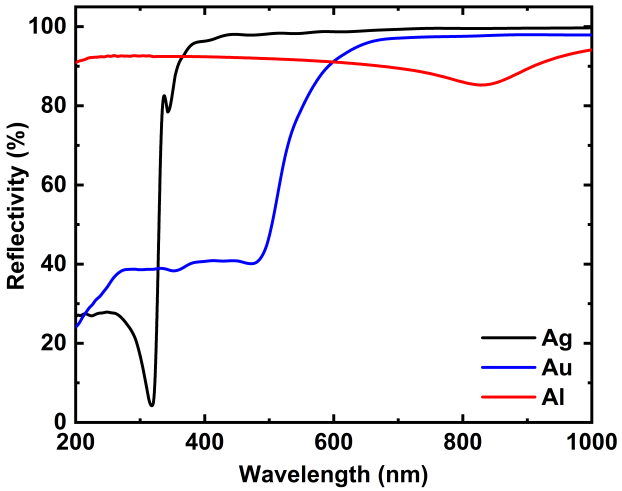

Figure 2.10. Reflectivity spectra of silver (Ag, black), gold (Au, blue) and aluminium (Al, red) in air. (Calculated using a transfer matrix reflectivity (TMR) model with n and k values obtained from [30, 31].)

Constructive interference of light reflected from the different interfaces in a DBR stack produces a spectrally-wide region of high reflectance called the stopband for which the reflectivity can exceed 99.9%. A simulated reflectivity spectrum of an 8-pair silicon dioxide/titanium dioxide (SiO_2/TiO_2) DBR centred at 550 nm is shown in Figure 2.11(a). Each layer is effectively a quarter-wave plate with thickness $d = \lambda_{DBR}/4n$, where λ_{DBR} is the central wavelength of the stopband, and n is the material refractive index. The spectral position of the stopband can therefore easily be controlled by adjusting the thickness of the layers. This is illustrated in Figure 2.11(b), which shows how the DBR reflectivity in part (a) is shifted to higher or lower wavelengths by altering d.

The peak reflectivity (the reflectivity at λ_{DBR} at normal incidence), R_{DBR}, is determined by the number of pairs (one high- and one low-refractive index layer), N, in the stack and is given by

$$R_{DBR} = \left(\frac{n_0 (n_{high})^{2N} - n_s (n_{low})^{2N}}{n_0 (n_{high})^{2N} + n_s (n_{low})^{2N}} \right)^2, \tag{2.26}$$

where n_0, n_s, n_{high}, and n_{low} are the refractive indices in front of the stack (e.g. air), behind the stack (e.g. the substrate or the active layer), and of the high- and low-refractive index dielectric materials, respectively [32]. It can be seen from this that increasing the number of pairs increases the mirror reflectivity, and this is shown in Figure 2.11(c), which indicates how the DBR reflectivity changes when the number of pairs is increased from 2 to 12. It should be noted, however, that large numbers of pairs are difficult to fabricate due to the risk of cracking, calibration errors and other deposition errors. Typically, Q-factors in double-DBR cavities are several hundred to >1000, though for inorganic semiconductor cavities, Q can exceed 10,000.

By increasing the refractive index contrast, $\Delta n = n_{high} - n_{low}$, it is also possible to increase the stopband width, $\Delta\lambda$, which is given by

$$\Delta\lambda = \frac{2\lambda_{DBR}(n_{high} - n_{low})}{\pi n_{eff}}, \tag{2.27}$$

where n_{eff} is the effective (mean) refractive index of the DBR stack [33]. This is shown in Figure 2.11(d), where the effect of increasing Δn from 0.3 to 1.5 can be seen. In Figure 2.11(a)-(c), Δn=0.85.

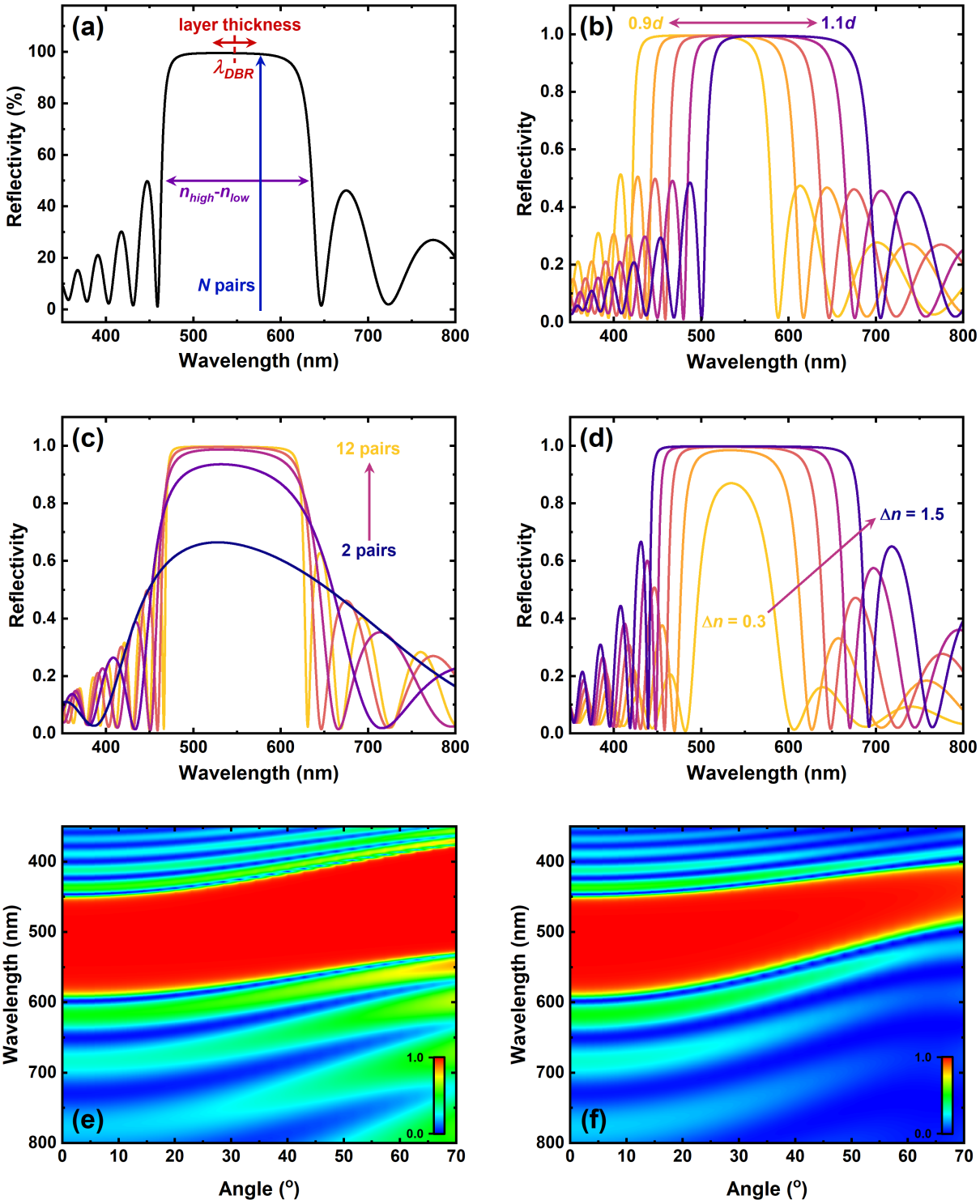

Figure 2.11. DBR reflectivity spectra. Part (a) shows the normal incidence reflectivity of an 8-pair SiO_2/TiO_2 DBR centred at 550 nm ($\Delta n = 0.85$), illustrating the effects of changing the thickness of the dielectric layers (red), the refractive index contrast ($\Delta n = n_{high} - n_{low}$, purple), and the number of pairs (N, blue). Parts (b), (c) and (d) show the effect of changing (b) the layer thicknesses by a factor of 0.9-1.1 compared to those needed for $\lambda_{DBR} = 550$ nm, (c) the number of pairs from 2 to 12, and (d) the refractive index contrast from 0.3-1.5. Parts (e) and (f) show the reflectivity angle dependence for the DBR shown in (a) for the TE and TM polarisations, respectively. All graphs were simulated using a TMR model.

As with the cavity mode in a Fabry-Pérot microcavity, DBR reflectivities also show angle dependence, with the stopband shifting to bluer wavelengths at higher angles (see Section 2.2). The TE

and TM modes also behave differently to one another. This is shown in Figures 2.11(e) and (f), respectively, where it can be seen that although the width of the stopband remains roughly constant for the TE polarisation, there is a significant narrowing at higher angles for the TM polarisation.

2.2.3 Transfer matrix reflectivity modelling

Transfer matrix reflectivity (TMR) modelling is an invaluable tool in the design and characterisation of multilayer optical structures such as DBR-DBR microcavities. Derived from Maxwell's equations and the Fresnel equations, the model takes into account the multiple internal reflections that occur at each interface and the consequent constructive and destructive interference effects. In the model, each layer is assigned a matrix that describes how electromagnetic waves propagate within it. This requires knowledge of the complex refractive index and thickness of the layer, and the incidence angle and polarisation of the light. Multiplying these matrices in the order they appear in the structure then allows the calculation of the reflected, absorbed and transmitted light as a function of angle and wavelength. The electric and magnetic field distributions can also be obtained. From this, any planar cavity structure can be simulated to determine how it will affect any light it interacts with. For a detailed derivation and explanation of TMR modelling, please see Hecht (2017) and Coles (2011) [29, 34].

2.3 Exciton-polaritons

If an absorbing material is placed inside an optical cavity, the dipole of the material can interact with the confined electric field if they are resonant with one another. This interaction will involve an exchange of energy between the light and matter with a coupling strength g that is dependent on the oscillator strength of the material. The type of coupling is determined by the value of g compared to the photon decay rate, $\kappa = {}^{1}/_{\tau_c}$ (see section 2.2.1 for a derivation of τ_c), and the exciton dephasing rate, γ.

2.3.1 Weak coupling

If $g \ll (\kappa, \gamma)$, the system will lie in the weak coupling regime. This is characterised by an irreversible exchange of energy between the light and matter, meaning that if the active material absorbs or emits light, the material and the electromagnetic field will dephase before they can interact again [15]. In this case, g does not exceed the system losses.

Because the interaction between light and matter in this type of system is small, it can be described using perturbation theory. Here, the photon density of states is altered by confining it within the cavity. If the electronic transition is resonant with the cavity mode, spontaneous emission will be enhanced according to the Purcell effect; if it is not, the rate will be reduced. Additionally (due to the directionality of the electric field), the orientation of the dipole is also important, with an enhancement of the spontaneous emission rate associated with dipole alignment to the field. This enhancement is described by the Purcell factor, F_P, which is given by

$$F_P = \frac{3}{4\pi^2}\left(\frac{\lambda_c}{n_{eff}}\right)^3 \frac{Q}{V_{eff}}, \tag{2.28}$$

where λ_c is the cavity mode wavelength, and n_{eff}, Q, and V_{eff} are the cavity effective refractive index, quality factor, and effective mode volume, respectively [32, 35]. This factor gives the ratio of the spontaneous emission rate within the cavity to that in free space, where the spontaneous emission rate is described by Fermi's golden rule:

$$\Gamma_{i\to f} = \frac{2\pi}{\hbar} |M_{i\to f}|^2 \rho_f(\omega). \tag{2.29}$$

Here, $\Gamma_{i\to f}$ is the transition probability between the initial state, i, and the final state, f, $M_{i\to f}$ is the matrix describing the transition and is dependent on the wavefunctions of the two states, and $\rho_f(\omega)$ is the final density of states as a function of angular frequency ($\omega = {}^{2\pi c}/_{\lambda}$) [24]. It is important to understand that the Purcell factor is the maximum enhancement of the rate possible and assumes the cavity mode and electronic transition are perfectly resonant, the dipole is aligned with the field, and there are no non-resonant transitions occurring simultaneously.

2.3.2 Strong coupling

In the case where $g \gg (\kappa, \gamma)$, the system will lie in the strong coupling regime. This is characterised by a reversible exchange of energy between light and matter at a frequency Ω known as the Rabi frequency. In this case, the excitons and photons form a new quasiparticle known as an exciton-polariton. Bosonic in nature, these exciton-polaritons (also known as cavity polaritons, or simply polaritons) are coherent superpositions of their two constituent components and are part light, part matter.

The condition for strong coupling is given by

$$g^2 > \sqrt{\frac{1}{2}(\gamma^2 + \kappa^2)}, \tag{2.30}$$

where the coupling strength g is related to the number of absorbers, N, and the effective cavity length, L_{eff}, through

$$g \propto \sqrt{\frac{N}{L_{eff}}}. \tag{2.31}$$

It is therefore obvious that in an organic-based cavity a high density of dye molecules is required for strong coupling. Looking back to Equations 2.20 and 2.21, and remembering that $\kappa = {}^{1}/_{\tau_c}$, we see that

$$\kappa = \frac{\omega}{Q}. \tag{2.32}$$

Therefore, high Q-factors are required for a small photon decay rate to achieve strong coupling. Calculating (or measuring) γ is more complicated as multiple effects must be taken into account. For example, when an exciton decays, a resonant photon could be emitted at an angle that does not coincide with the cavity mode, a non-resonant photon could be emitted, or the decay could be non-radiative [28]. These can all contribute to an increased value of γ. For a detailed derivation and discussion of Equation 2.30, please see Savona (1995,1999) [36, 37].

Due to the strength of the interaction between the exciton and photon mode in the strong coupling regime, perturbation theory is unable to sufficiently describe the system and we require a new model. For this, we can use a coupled oscillator model. If we consider the simplest case of a single electronic

transition coupled to a single cavity mode, the system can be described using the Hamiltonian in matrix form:

$$M = \begin{pmatrix} E_c(k) & g \\ g & E_x(k) \end{pmatrix}. \tag{2.33}$$

Here, $E_c(k)$ and $E_x(k)$ are the cavity mode and exciton energy as a function of wavevector, k, respectively. To determine the energy of the polariton branches, $E_p(k)$, we can diagonalise the Hamiltonian to calculate its eigenvalues through

$$\det(M - E_p(k)I) = \begin{pmatrix} E_c(k) - E_p(k) & g \\ g & E_x(k) - E_p(k) \end{pmatrix}, \tag{2.34}$$

where I is a 2x2 identity matrix. This gives

$$(E_c(k) - E_p(k))(E_x(k) - E_p(k)) - g^2 = 0. \tag{2.35}$$

Solving this we get

$$E_p(k) = \frac{E_c(k) + E_x(k)}{2} \pm \frac{1}{2}\sqrt{(E_c(k) - E_x(k))^2 + 4g^2}. \tag{2.36}$$

We can see from this that there are two solutions to the Hamiltonian and this gives us two angle-dependent polariton dispersions termed the lower (LPB) and (UPB) polariton branches. The UPB is at higher energies and is described by this equation when the second term is positive. When the second term is negative, the equation gives the energy of the LPB. It can be seen that at the angle at which the exciton and photon modes cross, i.e. $E_c = E_x$, the UPB-LPB separation will be equal to $2g$. This is known as the Rabi splitting energy (often simply referred to as the Rabi splitting) and is equal to $\hbar\Omega$. Here, the two branches undergo an avoided crossing or "anti-crossing", which is a hallmark of strong coupling. At this angle, the UPB and LPB will both be comprised of 50% photon and 50% exciton. Closer to $k = 0$, the LPB will have increased photonic character and the UPB will have increased excitonic character. Conversely, at higher angles, the LPB will be almost entirely excitonic and the UPB almost entirely photonic.

The energy difference between the exciton and cavity mode at $k = 0$, $\Delta = E_c - E_x$, is known as the cavity detuning. All the cavities considered in this thesis are negatively-detuned, i.e. $\Delta < 0$; however, it is also possible that $\Delta \geq 0$. Figures 2.12(a) and (b) show simulated polariton dispersions for a cavity with a small negative detuning (Δ = -91 meV) and a large negative detuning (Δ = -217 meV), respectively. In both of these figures, the anti-crossing can be seen clearly, demonstrating that the cavities lie in the strong coupling regime with a Rabi splitting energy of $\hbar\Omega = 170$ meV.

From these figures, it is easier to understand why the UPB is mostly photonic at high angles and excitonic at low angles, and vice versa for the LPB. However, this can be described quantitatively through

$$\begin{pmatrix} E_c(k) & g \\ g & E_x(k) \end{pmatrix} \begin{pmatrix} \alpha_i \\ \beta_i \end{pmatrix} = E_{p,i}(k) \begin{pmatrix} \alpha_i \\ \beta_i \end{pmatrix}, \tag{2.37}$$

where α_i and β_i are the angle-dependent photon and exciton mixing coefficient, respectively, and i=L,U corresponds to the LPB and UPB, respectively. The square of these mixing coefficients, $|\alpha_i|^2$ and $|\beta_i|^2$, are called the Hopfield coefficients and these give the photonic and excitonic fraction,

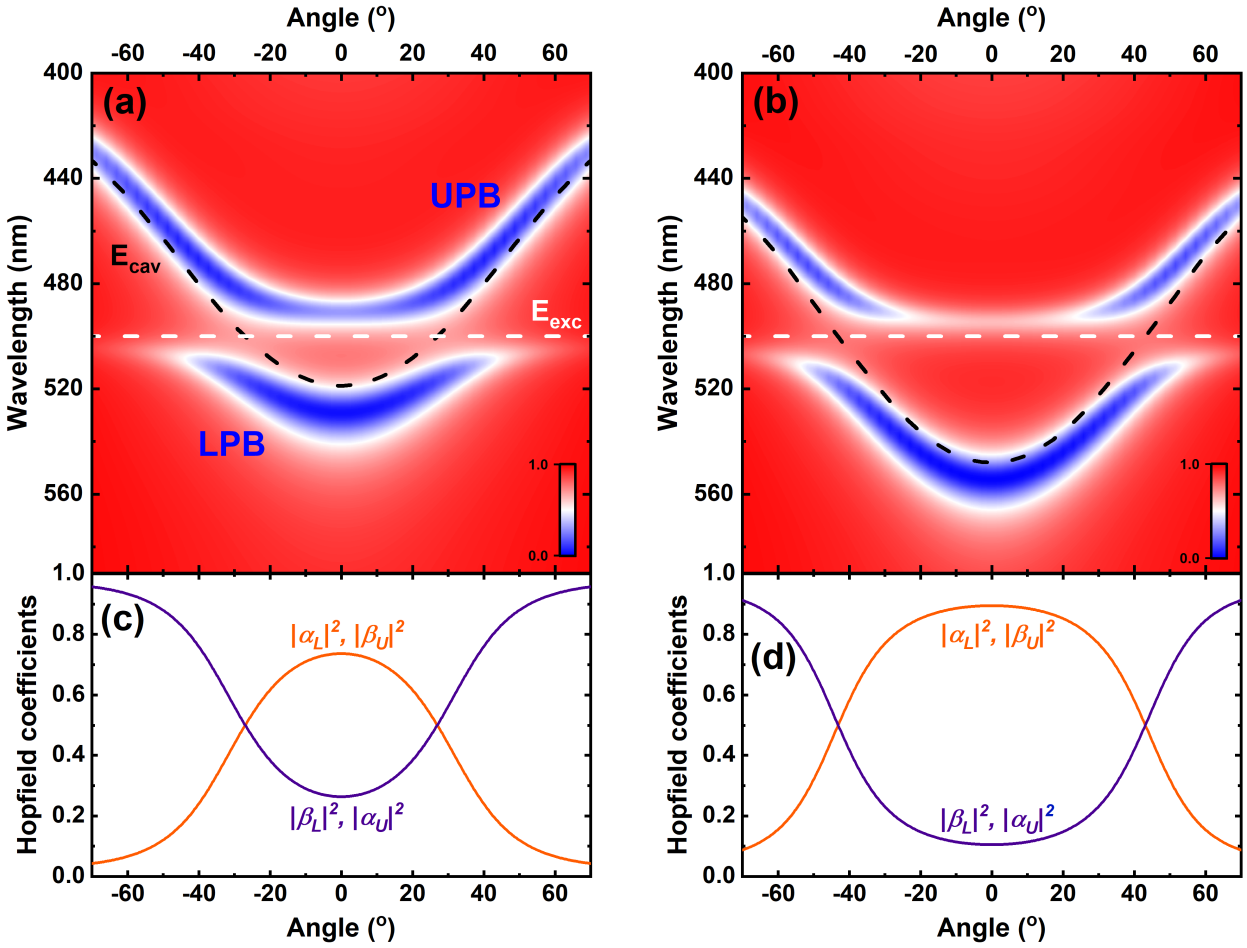

Figure 2.12. TMR model simulations for strongly-coupled Ag-Ag cavities. Parts (a) and (b) show cavity reflectivities for a small (Δ = -91 meV) and a large (Δ = -217 meV) negative detuning, respectively. The bare cavity (black) and exciton (white) dispersions are represented by the dashed lines. For both cavities, $\hbar\Omega$ = 170 meV. Parts (c) and (d) show the Hopfield coefficients for the cavities in (a) and (b), respectively, as a function of viewing angle. The orange line shows the photonic fraction of the LPB ($|\alpha_L|^2$) and the excitonic fraction of the UPB ($|\beta_U|^2$). The purple line shows the excitonic fraction of the LPB ($|\beta_L|^2$) and the photonic fraction of the UPB ($|\alpha_U|^2$). It can be seen in (a) and (c) that the anti-crossing for the cavity with the smaller negative detuning occurs at $\pm 27°$, whereas for the cavity with the larger negative detuning ((b) and (d)), it occurs at $\pm 43°$.

respectively, of the given polariton branch. For this reason, $|\alpha_i|^2 + |\beta_i|^2 = 1$. We therefore see

$$\alpha_i E_c(k) + \beta_i g = \alpha_i E_{p,i} \tag{2.38}$$

and

$$\alpha_i g + \beta_i E_x = \beta_i E_{p,i}. \tag{2.39}$$

Using $|\alpha_i|^2 + |\beta_i|^2 = 1$ and substituting in Equation 2.36 for the LPB (negative second term) to eliminate g, we get

$$|\alpha_L|^2 = \frac{E_x - E_{p,L}}{E_c + E_x - 2E_{p,L}} \tag{2.40}$$

and

$$|\beta_L|^2 = 1 - \frac{E_x - E_{p,L}}{E_c + E_x - 2E_{p,L}}. \tag{2.41}$$

It should be obvious that the coefficients are reversed for the UPB, i.e. $|\alpha_U|^2 = |\beta_L|^2$ and $|\beta_U|^2 = |\alpha_L|^2$. The Hopfield coefficients for the cavities shown in Figures 2.12(a) and (b) are shown in Figures 2.12(c) and (d), respectively. It can be seen from these figures that the LPB has the greatest photonic fraction at $k = 0$ and this decreases with increasing angle as the branch becomes more excitonic. The composition is 50:50 at the angle at which the exciton and photon modes are degenerate. Conversely, it can be seen that the UPB is most excitonic at $k = 0$, with the excitonic fraction decreasing and the photonic fraction increasing at higher angles.

The coupled oscillator model can also be extended to more than one transition or cavity mode. For example, if a material has vibronic transitions with sufficient oscillator strength, or the cavity contains more than one optically-active material, a single cavity mode can couple to multiple transitions. Similarly, multiple cavity modes can couple to a single transition. In this case, we can use the general matrix

$$M = \begin{pmatrix} E_1(k) & g_1 & \cdots & g_{n-1} \\ g_1 & E_2(k) & \ddots & 0 \\ \vdots & \ddots & \ddots & \vdots \\ g_{n-1} & 0 & \cdots & E_n(k) \end{pmatrix}, \tag{2.42}$$

where n is equal to the total number of transitions and cavity modes. In the case of a 3-level system (e.g. two transitions and one cavity mode or one transition and two cavity modes), there will be three distinct solutions to the Hamiltonian. This manifests in the dispersion as three polariton branches: a lower, middle (MPB), and upper. For a 4-level system, there will be four solutions, which gives a LPB, two MPBs, and an UPB. Examples of these dispersions are shown in Figure 2.13.

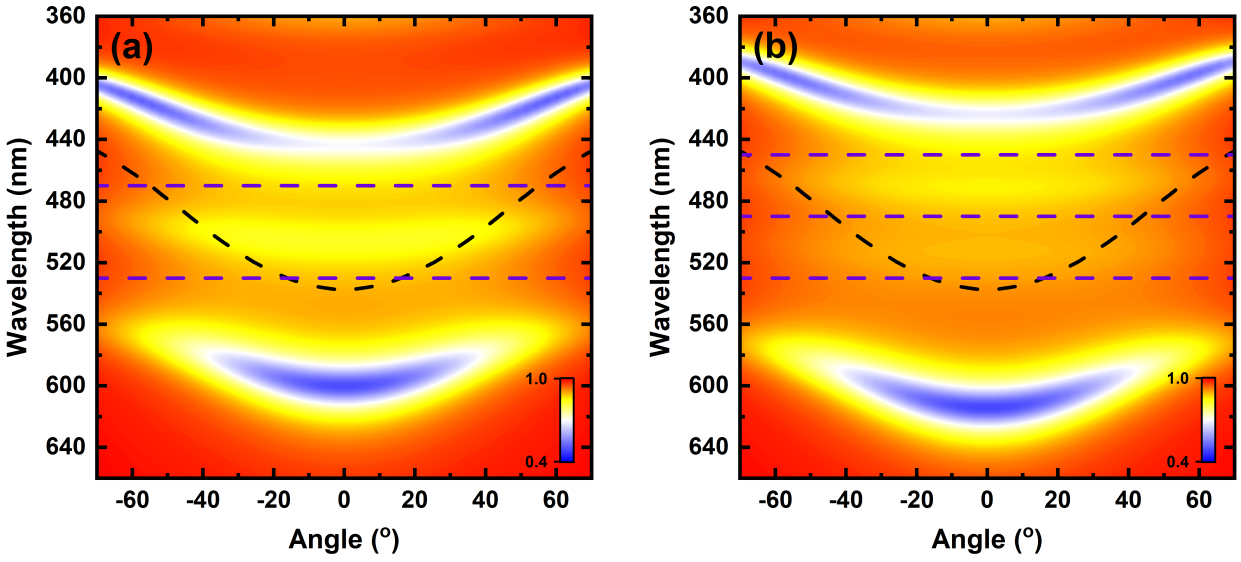

Figure 2.13. TMR model simulations for (a) a three-level system and (b) a four-level system. In part (a), the cavity mode (537 nm at $k = 0$, black dashed line) is strongly-coupled to two transitions of the cavity active layer at 470 nm and 530 nm (purple dashed lines). It can be seen that as well as the LPB and UPB, a middle polariton branch (MPB) is also evident between the two transitions. In part (b), the cavity mode (537 nm at $k = 0$, black dashed line) is strongly-coupled to three transitions of the cavity active layer at 450 nm, 490 nm and 530 nm (purple dashed lines). In this case there are two MPBs between the transitions, which can faintly be seen.

In addition to the coupled oscillator model, it has been shown that TMR modelling can be used

to predict and describe strong coupling in microcavities if a simple Lorentzian is used to describe the oscillator [38]. In organic systems, the n and k values can be measured experimentally using ellipsometry or calculated using the Lorentzian oscillator approximation (see Fox, 2010 [24]). In this way, polariton microcavities containing organic dyes can be well described using a series of Lorentzians fit to the extinction coefficient, k, which can be calculated using Equations 2.25 and 2.4. This requires knowledge only of the film absorbance spectrum and its thickness. TMR modelling is therefore effective for designing and characterising polariton microcavities. (See section 3.1.2 for further details on methods.)

2.3.3 Aside: other types of polariton

Although the experimental work in this thesis is concerned only with exciton-polaritons, it is interesting to note that there are other types of polaritons (light-matter quasiparticles) that have been identified.

One of these is the surface plasmon polariton (SPP). In metals, local charge fluctuations occur due to moving electrons and their mutually-repulsive effects. This results in oscillations known as plasmons [24]. Plasmons that occur at a metal-dielectric interface (e.g. metal-air) are known as surface plasmons and the intensity of the electromagnetic field they generate decays exponentially with increasing distance from the interface. They can either be localised – for example, if the metal is in the form of a nanoparticle – or delocalised – for example, at a planar metal-dielectric interface. In this latter case, the oscillations are termed SPPs and can be considered as the coupling of photons to collective excitations of conduction electrons [39]. Due to the confinement of the electromagnetic field near the interface, it is significantly enhanced, and SPPs are therefore extremely sensitive to their local environment. This allows confinement of light at sub-wavelength length scales (i.e. beyond the diffraction limit) and its manipulation at the nanoscale. Research is therefore ongoing to develop SPP nanodevices for sensing, communications, biophotonics and optical switching [40].

Similar to SPPs are plexcitons, which arise from the strong-coupling of plasmons to excitons. These have been shown to facilitate enhanced long-range energy transfer and spontaneous emission rates, giving them promising applications in high-efficiency LEDs, solar cells and as photocatalysts [41].

Another type of polariton is the phonon-polariton. Phonons are oscillations that arise due to the vibrations of atoms in lattices at a resonant frequency, usually in the infrared. If the momentum and frequency of an incoming photon matches that of the phonon, the two can strongly-couple to form phonon-polaritons with a characteristic anti-crossing. These polaritons allow the manipulation of infrared light beyond the diffraction limit, enhanced near-field heat transfer and thermal emission enhancement, giving them great potential in IR optoelectronic devices [42].

2.4 Polariton condensation

One of the main applications of exciton-polaritons is in low-threshold ‘lasers’. Unlike regular photon lasers, polariton lasers do not require a population inversion, which theoretically should allow for lower threshold devices. In fact, the laser-like emission from polaritonic systems results from a non-equilibrium Bose-Einstein-like condensate that is formed within the cavity. To understand how polariton lasers work, however, we must first consider photon lasers.

2.4.1 Photon lasing

Since their first experimental demonstration in 1958, lasers have become important in many aspects of life [43]. Applications include (but are not limited to) medicine, communications, construction, scientific research and metrology. The name 'laser' is an acronym standing for 'light amplification by stimulated emission of radiation', which refers to the process that underpins their operation. (Note that here we use the term 'photon lasers' to distinguish them from polariton lasers; however, they are generally referred to simply as lasers.)

In a photon laser, there are three important processes that occur simultaneously:

- Absorption
- Spontaneous emission
- Stimulated emission

We have already considered absorption (the promotion of a ground state electron to an excited state through the absorption of a photon) and spontaneous emission (the subsequent emission of a photon as the excited state electron relaxes back to its ground state) in Section 2.1.2. These are illustrated in Figure 2.14(a) and (b), where the electronic transition between a ground state E_1 and an excited state E_2 is shown. This is accompanied by the absorption and emission of a photon with energy $E_{ph} = E_2 - E_1$, respectively.

The rate of spontaneous emission can be described by

$$\frac{dN_2}{dt} = -A_{21}N_2, \tag{2.43}$$

where N_2 is the number of electrons in E_2 at time t and A_{21} is the Einstein A coefficient, which gives the probability per unit time that an electron will relax radiatively from E_2 to E_1. The solution to this equation is $N_2(t) = N_2(0)e^{-A_{21}t}$, from which it can be seen that A_{21} is related to the radiative lifetime τ through $A_{21} = 1/\tau$.

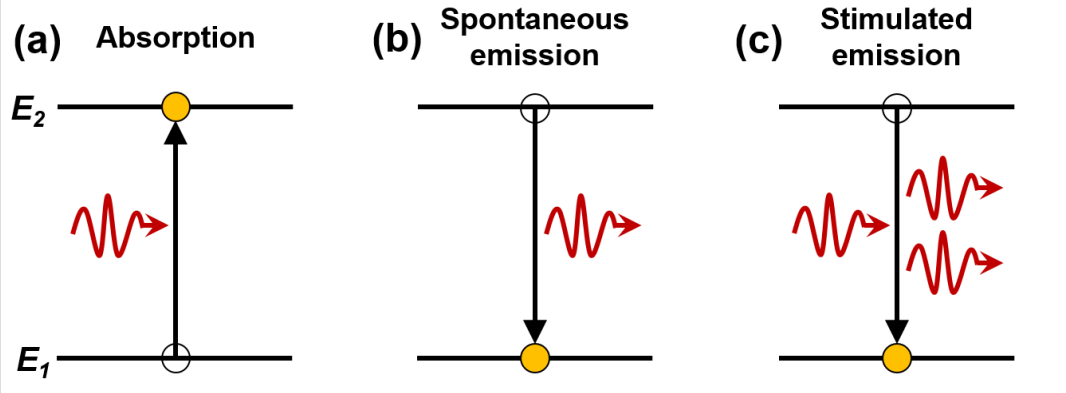

Figure 2.14. Illustrations of (a) absorption, (b) spontaneous emission, and (c) stimulated emission in a two-level system with energies E_1 and E_2. The energy of the photons involved in the transition is $E_{ph} = E_2 - E_1$.

The rate of absorption is given by a similar equation; however, as absorption is not a spontaneous process and requires the presence of a photon, an extra factor is required:

$$\frac{dN_1}{dt} = -B_{12}N_1\rho(\omega). \tag{2.44}$$

Here, N_1 is the number of electrons in the ground state at a time t and B_{12} is the Einstein B absorption coefficient that gives the probability per unit time that an electron will be promoted from E_1 to E_2 by the absorption of a photon. $\rho(\omega)$ is the spectral energy density of the electromagnetic field at the frequency of the transition, ω, where $E_{ph} = \hbar\omega$. This term indicates that only frequencies close to that of the electronic transition will be absorbed.

The third process, stimulated emission, occurs when a photon with energy E_{ph} is not absorbed, but instead induces an excited state electron to relax to the ground state, generating a second photon. This second photon will have the same energy and phase as the original photon. This process is sometimes referred to as "negative absorption" and this is reflected in its Einstein equation:

$$\frac{dN_2}{dt} = -B_{21}N_2\rho(\omega). \tag{2.45}$$

Here, B_{21} is the Einstein B coefficient for stimulated emission. This process underpins photon lasing and is illustrated in Figure 2.14(c).

We can work out the relationship between the three Einstein coefficients by considering a material enclosed in a box filled with N atoms with black walls at a temperature T. When the atoms reach thermal equilibrium with the walls of the box, assuming the atoms interact only with the black-body radiation and not each other, the rate of upward and downward transitions must be equal. From Equations 2.43, 2.44 and 2.45, we get

$$B_{12}N_1\rho(\omega) = B_{21}N_2\rho(\omega) + A_{21}N_2. \tag{2.46}$$

This will be valid for any two energy levels, regardless of the total number of levels partaking in transitions. Taking the Boltzmann factor, we see that

$$\frac{N_2}{N_1} = \frac{g_2}{g_1}e^{-\hbar\omega/k_BT}, \tag{2.47}$$

where g_1 and g_2 are the multiplicities of E_1 and E_2, respectively, and k_B is Boltzmann's constant. Additionally, Planck's law of black-body radiation shows us that

$$\rho(\omega) = \frac{\hbar\omega^3}{\pi^2c^2}\frac{1}{e^{\hbar\omega/k_BT-1}}. \tag{2.48}$$

If these equations (2.46-2.48) hold at all temperatures ($T \to \infty$), we can find that

$$g_1B_{12} = g_2B_{21} \tag{2.49}$$

and

$$A_{21} = \frac{\hbar\omega^3}{\pi^2c^2}B_{21}. \tag{2.50}$$

From this we can see that we only need to know one Einstein coefficient to calculate the other two. This could be done, for example, by measuring the radiative lifetime to obtain A_{21} and then calculating B_{12} and B_{21} from these equations. We also see that materials with a high probability of absorption will have a high probability of both spontaneous and stimulated emission. As we saw earlier, the spontaneous emission rate can be described by Fermi's golden rule (see section 2.3.1, Equation 2.3.1), where the matrix describing the transition depends on the wavefunctions of the

two states involved. It therefore follows that the Einstein coefficients are intrinsic properties of the atoms and Equations 2.49 and 2.50 hold for all cases, not just for black-body radiation at thermal equilibrium [28].

In order for lasing to occur, the rate of stimulated emission must exceed the rate of absorption so that the number of in-phase photons will increase as a beam propagates through an active material. Combining Equations 2.44, 2.43 and 2.49, we find

$$N_2 > \frac{g_2}{g_1} N_1. \tag{2.51}$$

This is known as population inversion and is necessary for laser operation. According to Equation 2.47, this is not possible in thermal equilibrium and the number of photons will decay as they propagate through the cavity. Therefore, to satisfy this condition, it is necessary to 'pump' the system using an external source of energy to promote electrons to higher levels. This can be done either optically or electrically.

The property of a material to increase the intensity of an optical beam propagating through it is known as gain, G, and can be described by

$$I(z) = I_0 e^{Gz}. \tag{2.52}$$

Here, $I(z)$ is the intensity after the beam has travelled a distance z through the gain medium and I_0 is the original beam intensity. From this it is obvious that if there is gain, the optical intensity will be maximised if the path through the gain medium is also maximised. This is done by inserting the gain medium inside a cavity with high reflectivity mirrors, R_1 and R_2, so that the beam traverses the gain medium many times. The threshold gain, G_{th}, for a cavity of length L and losses α, is then be given by

$$R_1 R_2 e^{2G_{th}L} e^{-2\alpha L} = 1. \tag{2.53}$$

This can be rearranged to give

$$G_{th} = \alpha - \frac{1}{2L} ln(R_1 R_2). \tag{2.54}$$

Below this threshold, gain is proportional to pump power, and the output light intensity increases linearly. In this regime, the emission is dominated by spontaneous emission. Once the threshold is reached, the gain is fixed at G_{th} and stimulated emission dominates. Above this pump power, the output light intensity increases dramatically and all the photons are coherent and monochromatic. The effect of pump power on output intensity and gain are shown in Figure 2.15.

Once the photonic lasing regime has been reached, a population inversion is still required. This requires large amounts of energy to reach and maintain. Therefore, systems which can produce 'laser' light without requiring a population inversion are highly desirable.

2.4.2 Polariton lasing

2.4.2.1 Bose-Einstein condensation

As discussed in Section 2.1.1, the Pauli Exclusion Principle forbids two electrons to occupy the same quantum state. This is in fact true for all fermionic particles, i.e. those with half-integer spin. However, this is not the case for bosons, which have integer spin, such as photons or helium-4 (^{4}He).

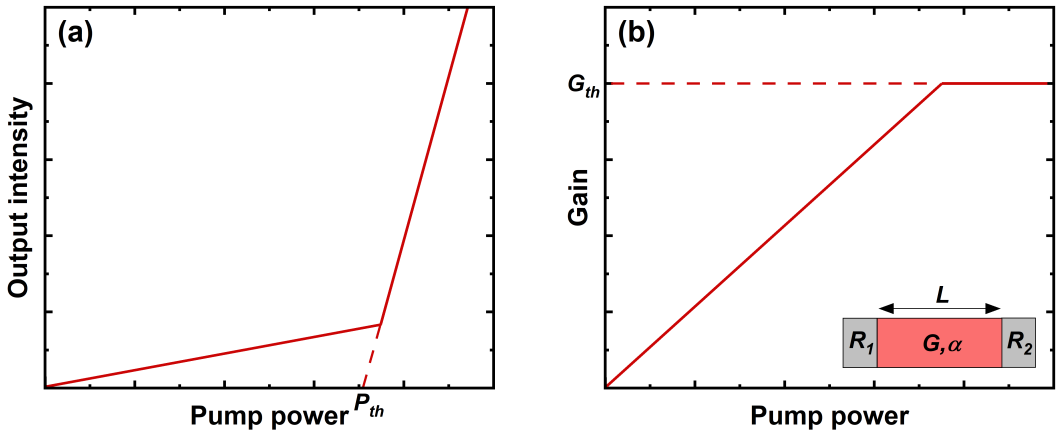

Figure 2.15. Effect of pump power on (a) output light intensity and (b) gain in a laser. The inset in (b) shows a schematic of the laser highlighting the relevant parameters: G - gain, α - losses, R_1 - mirror 1 reflectivity, R_2 - mirror 2 reflectivity, L - length of gain medium, P_{th} - pumping threshold, G_{th} - gain threshold.

These are instead governed by Bose-Einstein statistics and are able to simultaneously occupy the same quantum state. This was first hypothesised when Satyendra Nath Bose sent a paper to Albert Einstein in 1924 in which he derived Planck's law for black-body radiation by considering the photons as a gas of non-interacting identical particles [44]. Einstein developed on this idea and found that, below a critical temperature, a large proportion of atoms or molecules of a conserved, ideal gas of bosons were predicted to 'condense' into the lowest quantum state [45]. In this case, the particles are indistinguishable from one another and can be described by a single wavefunction. This phenomenon is known as Bose-Einstein condensation (BEC).

In order for BEC to occur, the wavefunctions of the individual bosons must overlap. This happens when the de Broglie wavelength, λ_{dB}, of the bosons becomes comparable to the inter-particle separation. λ_{dB} is a consequence of wave-particle duality in which a particle can behave as a wave with wavelength related to its momentum, p, through

$$\lambda_{dB} = \frac{h}{p} = \frac{h}{mv}. \tag{2.55}$$

Here, m and v are the particle's mass and velocity, respectively, and h is Planck's constant. In a gas of non-interacting particles, we can relate the kinetic energy of each particle to its thermal energy through

$$\frac{p^2}{2m} = \frac{1}{2m}\left(\frac{h}{\lambda_{dB}}\right)^2 = \frac{3}{2}k_B T. \tag{2.56}$$

Rearranging this we get

$$\lambda_{dB} = \sqrt{\frac{h^2}{3mk_B T}}. \tag{2.57}$$

The wavefunction of a particle will cover a distance approximately equal to its de Broglie wavelength. Therefore, the wavefunctions will begin to overlap when the particle's effective volume, λ_{dB}^3, is approximately equal to the inverse of the particle density of the gas, i.e. $\lambda_{dB}^3 \sim {}^{V}/_{N}$, where V is the volume of the gas and N is the total number of particles. We therefore find that the critical

temperature, T_c, below which condensation can occur is given by

$$T_c \sim \frac{h^2}{3mk_B}\left(\frac{N}{V}\right)^{\frac{2}{3}}. \tag{2.58}$$

Below this temperature, a large fraction of the particles will occupy the lowest possible quantum state and become indistinguishable [28]. This can be accompanied by many interesting effects, such as superfluidity and the emergence of quantised vortices.

2.4.2.2 Polariton condensation

It can be seen from Equation 2.58 that to increase the critical temperature, we must either decrease the mass of the particles or increase their density. Due to their photon component, polaritons are much lighter than atoms, with effective masses $\sim 10^{-4}$ to 10^{-5} that of an electron [46]. It is therefore possible to achieve condensation with polaritons at much higher temperatures than in atomic gases, which require cooling to near absolute zero. For example, in the first demonstration of BEC, performed in 1995 by Eric Cornell and Carl Wiemann, the rubidium atoms were held at a temperature of 170 nK [47].

It is also relatively simple to increase the density of polaritons in a system - this can be done either through optical pumping or electrical injection. Optical pumping can be applied resonantly, where the LPB is pumped by pulses of the same energy at a large angle, or non-resonantly using higher energy pulses that coincide with DBR stopband minima (see Sections 2.2.2.2 and 2.4.2.4). The two methods are illustrated in Figure 2.16. If the density of polaritons is raised sufficiently, they will condense into the $k = 0$ state and become indistinguishable. In this case, they will all possess the same energy, momentum and phase. Any photons that escape the cavity will retain these properties and therefore the emission will mimic laser light. As with photon lasers, there is a non-linear increase in emission intensity above threshold and a dramatic narrowing of the emission linewidth. This is accompanied by a blueshift, which is a fingerprint of polariton condensation and will be discussed further in Chapter 6. These laser-like characteristics are generated without a population inversion and this has been shown to reduce 'lasing' thresholds by two orders of magnitude [48]. In polaritonic systems, this often results in two thresholds: at lower excitation fluences, the system will move from the linear (spontaneous emission) regime into the polariton lasing (condensation) regime as the polariton condensation threshold is reached, and at higher fluences, the system will move into the photon lasing (stimulated emission) regime as the photon lasing threshold is reached.

Due to the similarities between the two types of non-linear emission, cavity-polariton condensates are often referred to as lasers (although technically they are not) and significant research has gone into achieving this kind of lasing at room temperature. It is important to note here, however, that as photons can escape the cavity through the mirror(s), polariton condensates are no longer in thermal equilibrium and are therefore not considered true BECs. It is possible to describe them using a generalised Gross-Pitaevski equation, into which loss, amplification, pumping and dissipative terms can be added to model such a non-equilibrium system [49]. Despite not being considered as true BECs, polariton condensates exhibit many of the same properties, such as long-range spatial coherence, vortices and superfluidity [50–53].

In order for a condensate to be formed, polaritons further along the LPB (at higher energies and

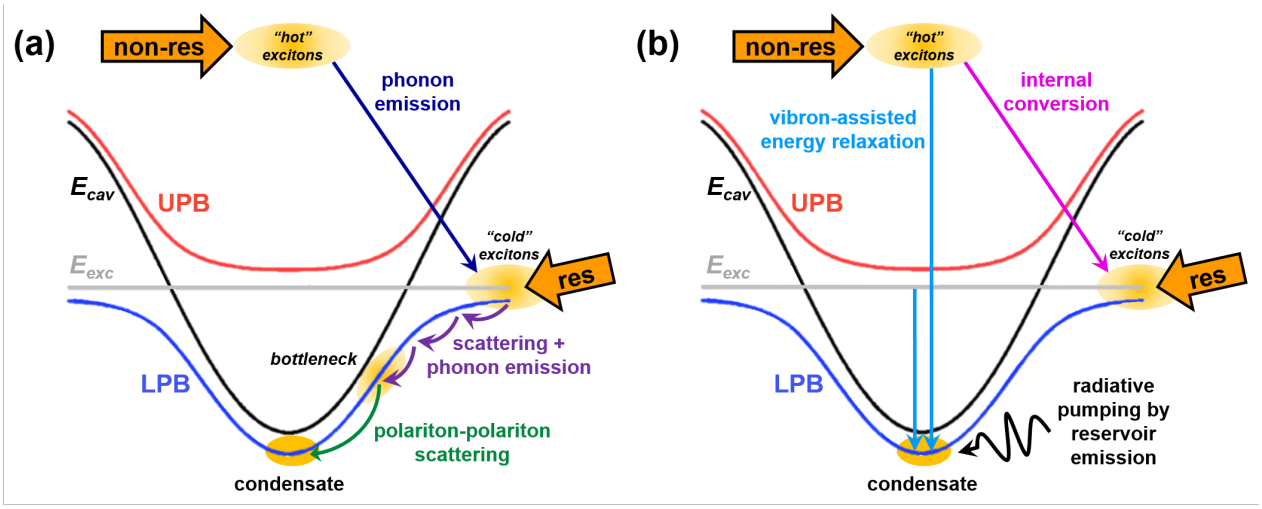

Figure 2.16. Mechanisms for populating a polariton condensate. Using optical pumping (large orange arrows), the LPB (blue line) can be populated resonantly using laser pulses that coincide with the LPB energy at a high angle (res), or non-resonantly at a much higher energy (non-res). Part (a) illustrates the relaxation mechanisms in inorganic-based systems. Following non-resonant pumping, "hot" excitons lose energy non-radiatively through the emission of phonons (navy arrow) to populate the exciton reservoir, creating "cold" excitons (E_{exc}, grey line). From here, polaritons can scatter from the crystal lattice, accompanied by the emission of phonons, to relax down the LPB (purple arrows). As the photon component of the polaritons becomes more significant lower down the branch, scattering by this mechanism becomes less efficient and a "bottleneck" is formed. Beyond this point polaritons need to cool through another mechanism; for example, polariton-polariton scattering (green arrow). Part (b) illustrates the relaxation mechanisms in organic-based systems. Non-resonant pumping can either be followed by internal conversion (pink arrow), in which the "hot" excitons relax to form "cold" excitons, or vibron-assisted energy relaxation (blue arrow), in which the bottom of the LPB is directly populated. Radiative pumping of the condensate by the organic emission is also possible, as well as vibron-assisted energy relaxation of "cold" excitons. The UPB (red line) and the cavity mode (E_{cav}, black line) are also shown.

angles) must migrate (scatter) down to the lowest energetic state. This is due to the fact that when polaritons are initially generated, they occupy all possible states. In inorganic systems, the required dissipation of energy is achieved through the emission of phonons due to scattering from the crystal lattice. As the polaritons relax down the branch and become more photon-like, their probability of scattering is reduced and their lifetimes shorten. They are therefore unable to fully relax to $k = 0$ using this mechanism and a "polariton bottleneck" is formed. At lower values of k, polariton-polariton scattering becomes the dominant cooling mechanism, resulting in one polariton ending up at $k = 0$ and the other at twice the bottleneck momentum [54]. These mechanisms are illustrated in Figure 2.16(a).

As discussed previously (see Section 2.1.3), inorganic materials mainly support Wannier-Mott excitons having binding energies of only a few meV and therefore only exist at low temperatures. It follows from this that polaritons and therefore polariton condensates only exist in inorganic systems at low temperatures. For example, the first demonstration of polariton condensation, which was in a GaAs-based cavity, required cooling to 19 K [50]. There are some exceptions to this such as gallium nitride (GaN) and zinc oxide (ZnO), which have exhibited room temperature polariton condensation [55–58]. However, these types of cavity are difficult to fabricate due to complicated deposition processes. Nevertheless, inorganic systems have a significant advantage over organic-based cavities in that their charge carrier mobilities are significantly higher, allowing for electrically-injected polariton lasers to be realised [59, 60].

One of the main advantages of organic materials is their ability to support Frenkel excitons, which have high binding energies (see Section 2.1.3), allowing for room temperature strong-coupling and condensation. The mechanism of relaxation to the bottom of the LPB is slightly different in organic-based cavities and is not entirely understood. However, it is believed that vibron-mediated energy relaxation of both "cold" (fully-thermalised) and "hot" (created at the pump energy) excitons, and radiative pumping by weakly-coupled states in the exciton reservoir are possible mechanisms [61–63]. These are illustrated in Figure 2.16(b).

Another advantage of organic-based cavities is that they are much simpler to fabricate than inorganic structures, with simple evaporation depositions and solution-processing the most common techniques employed. Additionally, the sheer quantity of optically-active organic materials allows for fine-tuning of emission wavelengths, allowing condensation at wavelengths traditionally not accessible using inorganic-based cavities. The downside, however, is that these materials tend to have low charge carrier mobilities, meaning electrically-injected organic polariton lasers have not yet been realised. Work is, however, ongoing to achieve this.

2.4.2.3 Proven and promising materials: a historical review

Despite polaritons being first hypothesised in 1950 [64] and experimentally demonstrated in bulk ZnO crystals in 1965 [65], the first experimental demonstration of exciton-polaritons in a cavity was not until 1992. This was in a GaAs-based system at temperatures up to 77 K [66]. In the following two decades, significant progress has been made in the field of inorganic-based polaritons, with the first demonstrations of optically-pumped polariton condensates and lasers at cryogenic temperatures in the mid-2000s [48, 50, 67]. This was quickly followed by room temperature operation, firstly with optical pumping and then with electrical injection [55, 56, 60]. This has included cavities based on GaAs, ZnO, GaN and CdTe.

The first evidence of exciton-polaritons in an organic-based system was by Lidzey *et al.* in 1998 using a porphyrin derivative [68]. Notably, this was the first demonstration of strong coupling at room temperature. It was not until the early 2010s, however, that polariton lasing and condensation in organic-based cavities were observed [69–71]. To this day, polariton condensation has been demonstrated using a number of different organic materials, including single crystals, polymers, molecular dyes, and fluorescent proteins [69–76]. However, as mentioned above, this has thus far only been achieved through optical pumping.

2.4.2.4 Metal vs dielectric cavities

We have already discussed some of the benefits of metal mirrors compared to DBRs and vice versa (see Section 2.2.2); however, there are additional properties of each type of mirror that must be taken into account when discussing polaritons and their condensates.

One advantage of metal mirrors is their small penetration depth, W. This is given by

$$W = \frac{1}{\alpha} = \frac{\lambda}{4\pi k}, \tag{2.59}$$

where α and k are the material absorption and extinction coefficient, respectively, and λ is the wavelength of the penetrating light [77]. Using this equation, the penetration depth of 550 nm

wavelength light into gold, silver and aluminium are found to be $W_{Au} = 18$ nm, $W_{Ag} = 12$ nm, and $W_{Al} = 7$ nm, respectively. In practice, this equation applies to very thick layers and W will vary for very thin films (<50 nm).

To maximise the Rabi splitting ($\hbar\Omega$) in a microcavity, the number of absorbers per unit length ($^{N}/_{L_{eff}}$) should be maximised (see Section 2.3.2 & Equation 2.31). In a metal-metal cavity,

$$L_{eff} \approx d_c, \tag{2.60}$$

and so the majority of the cavity length contains absorbers. Such cavities can therefore exhibit very large Rabi splittings (up to 1 eV [78, 79]).

We now consider the penetration depth into a DBR, W_{DBR}. This is given by

$$W_{DBR} = \frac{\lambda_{DBR}}{2} \frac{n_{low}}{(n_{high} + n_{low})(n_{high} - n_{low})}, \tag{2.61}$$

where λ_{DBR} is the central wavelength of the DBR, and n_{low} and n_{high} are the refractive indices of the low- and high-index material, respectively [80]. Generally, $W_{DBR} \sim$ 100-300 nm. Therefore, in a double-DBR cavity

$$L_{eff} = W_{bottomDBR} + d_c + W_{topDBR} >> d_c. \tag{2.62}$$

A large proportion of the effective cavity length will therefore not contain any absorbers and the Rabi splitting will be much-reduced compared to a metal-metal cavity containing an identical active layer. It is also important to note that the cavity mode will be redshifted in the double-DBR cavity and this must be taken into account during design.

The benefit of DBRs for polariton cavities, as with weakly-coupled systems, is their very high Q-factors. This is necessary for polariton condensation in order for a sufficient population of polaritons to build up before escaping the cavity via their photon component.

A summary of polariton cavities composed of metal mirrors and DBRs, including typical Rabi splitting and Q-factor values, is given in Table 2.2.

Property\Mirror type	**Silver**	**DBR**
Fabrication process	Thermal evaporation (simple)	PVD or CVD (complicated, prone to error)
# of layers per mirror	1	16-30+
Absorption*	2-18%	1%
Reflectivity*	80-98%	>99%
High-reflectivity region	Very broad	∼100 nm
Cavity Q-factor	10-65	100s-1000
Condensation possible?	No†	Yes
Penetration depth (nm)	5-40	100-300
Rabi splitting (meV)	100s-1 eV	∼100
References	[81–92]	[36, 57, 61, 70, 71, 93–95]

Table 2.2. Summary of the difference between silver and DBR mirrors. PVD: physical vapour deposition, CVD: chemical vapour deposition, *In the visible region, †With the exception of [76].

2.5 Quantum batteries

As the world moves away from traditional, highly-polluting energy sources, such as gas and oil, the storage of electrical energy is becoming ever more important. With the increasing usage of electric cars, electric heating and other electrically-powered devices, global battery demand has been increasing by 30% annually for almost a decade [96]. The storage of energy from renewable sources, such as wind or solar power, is particularly critical due to the high fluctuation and unreliability of their generation. For example (in the absence of fossil fuels), stored energy would be required during the night when no solar power is available or on windless days. The development of higher-capacity, faster-charging batteries is therefore imperative.

2.5.1 Classical batteries

Classical batteries – i.e. those currently employed in remote controls, electric cars, portable electronics, etc. – consist of one or more electrochemical cells, which store chemical energy and later convert it to electrical energy. Generally, each cell of a battery will consist of an anode, a cathode, an electrolyte and wiring. A basic schematic is shown in Figure 2.17. When a battery discharges (provides energy) the electrochemical reaction occurring is a reduction-oxidation or redox reaction. This can be considered as two simultaneously-occurring 'half-reactions': at one side of the cell, the electrolyte reacts with the anode to generate electrons in the anode (oxidation), and at the other side, it reacts with the cathode, causing the cathode to lose electrons to the electrolyte (reduction). Electrons generated at the anode then flow towards the cathode through a wire. This charge movement is balanced through the flow of positive ions from the anode to the cathode through the electrolyte, which can be either liquid or solid. If the device requiring energy is connected to the battery between the two electrodes, the flow of charge can be harnessed to power it.

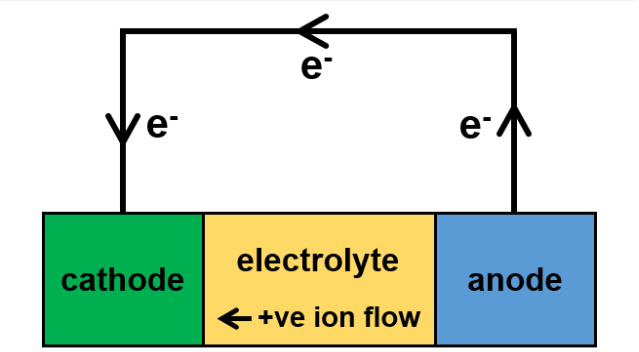

Figure 2.17. Schematic of a classical battery. At the anode (blue box), an oxidation reaction with the electrolyte (yellow box) generates electrons (e^-), which travel along a wire to the cathode (green box). Simultaneously, the cathode is able to gain electrons to balance those lost to the electrolyte in the reduction reaction. To balance the flow of charge, positive ions travel from the anode to the cathode through the electrolyte.

Batteries can be divided into two categories depending on whether they can be reused or not. Primary batteries cannot be recharged as the reactants are completely used up and the electrochemical process is therefore irreversible. This type of battery is generally used when long storage times are needed, such as in remote controls and smoke alarms. Secondary batteries are rechargeable and are used in devices such as smartphones and laptops. The chemical reaction in this type of battery can be reversed by applying external energy to re-generate the original reactants. The battery lifetime,

however, is finite and they can only be recharged so many times before needing to be replaced. Additionally, their finite energy capacity and their (relatively) long charging times are not ideal. Another problem with both primary and secondary batteries is the materials they are made of (e.g. lithium and zinc) require large amounts of energies to extract at high purity.

2.5.2 Quantum batteries

Traditionally, measurable quantities have been described as either intensive, where the quantity does not change with the size of the system – for example, density or concentration – or extensive, where the quantity increases proportionally with the system size – for example, mass or volume. However, a third possibility that relies on quantum effects is also possible: superextensivity. In this case, the quantity scales faster than the system size. It is this principle that underpins the processes of superradiance and superabsorption, the latter of which has applications in quantum batteries.

First proposed by Dicke in 1954 [97], superradiance occurs when N emitters – for example, fluorescent molecules – interact with a common light field and emit photons at a rate proportional to N^2 [98]. This emission enhancement is possible following coherent excitation of the emitters, whose interparticle distance should be much less than the wavelength of the light field. This coherence leads to a macroscopic dipole moment, allowing the emitters to interfere constructively to enhance the emission. This effect is in contrast to spontaneous emission (see Section 2.4.1), whose rate is suppressed with increasing N. To this day, superradiance has been demonstrated in a wide variety of systems, including gases, cavities, quantum dots, and Bose-Einstein condensates [98–103].

The opposite process to superradiance is superabsorption. Here, the dipole moments of N *absorbers* interfere constructively through quantum coherence to absorb light more efficiently. This leads to the states absorbing more light and at a quicker rate than if they acted alone [104]. This was only demonstrated experimentally for the first time very recently, where the absorption rate of a silicon carbide nanohole-array was found to scale as N^2 for $N \leq 16$ [105].

To scale this up to a macroscopic number of particles, we can consider a microcavity filled with a large number ($\sim 10^{10}$) of organic molecules, N. If we approximate each molecule as a two-level system interacting with a common light field (i.e. the cavity mode), we can apply the principles of superabsorption. In this way, we see that the molecules should store (absorb) more energy and at a faster rate than the same number of molecules not interacting with a common light field – for example, N molecules interacting with N separate cavity modes. These two systems are illustrated in Figure 2.18. Indeed, it was theoretically shown by Ferraro *et al.* that N entangled two-level systems interacting via a common cavity mode should exhibit a $\sqrt{N}$-fold increase in the maximum charging power [18]. This so-called Dicke quantum battery is in contrast to a classical battery, whose charging time increases with its size.

In this way, a quantum battery could be capable of super-fast charging times. Indeed, theoretically, a quantum battery consisting of a microcavity containing an infinite number of molecules would charge instantaneously and could store an infinite amount of energy. In practice, there would be limitations on this – for example, effects that occur at high molecular concentrations, such as aggregation and energy transfer, must be considered. However, it is expected that a practical quantum battery would still greatly outperform current batteries. Additionally, their fabrication would be far simpler and much less energy-intensive.

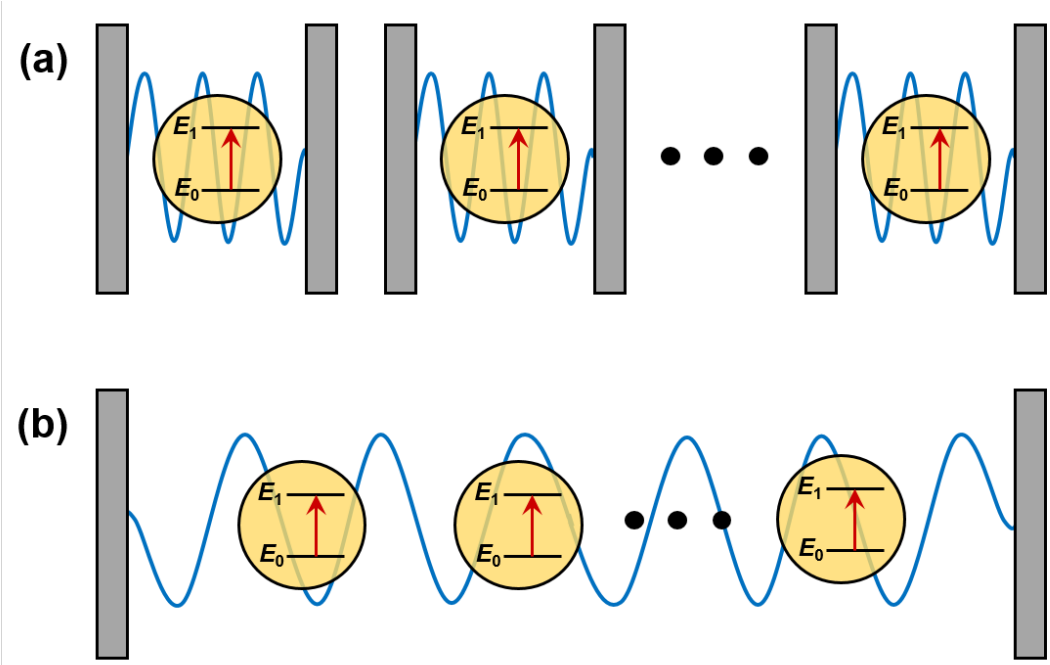

Figure 2.18. Microcavities containing N two-level states as batteries. Part (a) shows N cavities each containing a single state, which can be approximated as a two-level system, interacting with a single cavity mode (blue wavy line). Part (b) shows a Dicke quantum battery, which consists of a single cavity containing N states all interacting with the same cavity mode.

2.6 References

[1] Gao, J. *et al.* A Critical Review on Efficient Thick-Film Organic Solar Cells. *Solar RRL* **4**, 2000364 (2020).

[2] Tang, W. *et al.* Recent progress in printable organic field effect transistors. *Journal of Materials Chemistry C* **7**, 790–808 (2019).

[3] Kuehne, A. J. & Gather, M. C. Organic Lasers: Recent Developments on Materials, Device Geometries, and Fabrication Techniques. *Chemical Reviews* **116**, 12823–12864 (2016).

[4] Minaev, B., Baryshnikov, G. & Agren, H. Principles of phosphorescent organic light emitting devices. *Physical Chemistry Chemical Physics* **16**, 1719–1758 (2014).

[5] Bauri, J., Choudhary, R. B. & Mandal, G. Recent advances in efficient emissive materials-based OLED applications: a review. *Journal of Materials Science* (2021).

[6] Shaner, N. C. *et al.* Improved monomeric red, orange and yellow fluorescent proteins derived from Discosoma sp. red fluorescent protein. *Nature Biotechnology* **22**, 1567–1572 (2004).

[7] Umezawa, K., Matsui, A., Nakamura, Y., Citterio, D. & Suzuki, K. Bright, color-tunable fluorescent dyes in the Vis/NIR region: Establishment of new "tailor-made" multicolor fluorophores based on borondipyrromethene. *Chemistry - A European Journal* **15**, 1096–1106 (2009).

[8] Weil, T., Vosch, T., Hofkens, J., Peneva, K. & Müllen, K. The rylene colorant family-tailored nanoemitters for photonics research and applications. *Angewandte Chemie - International Edition* **49**, 9068–9093 (2010).

[9] Han, S. *et al.* Exploring the ultrasonic nozzle spray-coating technique for the fabrication of solution-processed organic electronics. *Organic Electronics* **49**, 212–217 (2017).

[10] Park, B., Bae, I. G., Kwon, O. E. & Jeon, H. G. Organic thin-film transistors fabricated using a slot-die-coating process and related sensing applications. *RSC Advances* **6**, 101613–101621 (2016).

[11] Chang, Y. H. *et al.* Polymer solar cell by blade coating. *Organic Electronics* **10**, 741–746 (2009).

[12] Rich, S. I., Jiang, Z., Fukuda, K. & Someya, T. Well-rounded devices: The fabrication of electronics on curved surfaces-a review. *Materials Horizons* **8**, 1926–1958 (2021).

[13] Dong, H., Zhang, C. & Zhao, Y. S. Controlling the Output of Organic Micro/Nanolasers. *Advanced Optical Materials* **7**, 1–12 (2019).

[14] Zhang, Q., Tao, W., Huang, J., Xia, R. & Cabanillas-Gonzalez, J. Toward Electrically Pumped Organic Lasers: A Review and Outlook on Material Developments and Resonator Architectures. *Advanced Photonics Research* **2**, 2000155 (2021).

[15] Bajoni, D. Polariton lasers. Hybrid light–matter lasers without inversion. *Journal of Physics D: Applied Physics* **45**, 313001 (2012).

[16] Park, C. H. *et al.* Enhanced light extraction efficiency and viewing angle characteristics of microcavity OLEDs by using a diffusion layer. *Scientific Reports* **11**, 3430 (2021).

[17] Saxena, K., Jain, V. & Mehta, D. S. A review on the light extraction techniques in organic electroluminescent devices. *Optical Materials* **32**, 221–233 (2009).

[18] Ferraro, D., Campisi, M., Andolina, G. M., Pellegrini, V. & Polini, M. High-Power Collective Charging of a Solid-State Quantum Battery. *Physical Review Letters* **120**, 117702 (2018).

[19] Quach, J. Q. *et al.* Superabsorption in an organic microcavity: Toward a quantum battery. *Science Advances* **8**, 3–10 (2022).

[20] Young, H. D. & Freedman, R. A. *University Physics with Modern Physics Technology Update* (Pearson Education, Harlow, Essex, 2014), 13th edn.

[21] Electronic Orbitals (2020).

[22] Patrick, G. L. *Organic chemistry.* BIOS instant notes (Garland Science, 2012), 2nd edn.

[23] McGhee, K. E. Spectroscopy for Organic Electronics (2022). URL `https://www.ossila.com/pages/organic-spectroscopy#`.

[24] Fox, M. *Optical Properties of Solids* (Oxford University Press, 2010), 2nd edn.

[25] Sanvitto, D. & Kéna-Cohen, S. The road towards polaritonic devices. *Nature Materials* **15**, 1061–1073 (2016).

[26] Geoghegan, M. & Hadziioannou, G. *Polymer Electronics* (Oxford University Press, 2013), first edn.

[27] Panzarini, G. *et al.* Cavity - Polariton dispersion and polarization splitting in single and coupled semiconductor microcavities. *Physics of the Solid State* **41**, 1223–1238 (1999).

[28] Fox, M. *Quantum Optics : An Introduction* (Oxford University Press, 2006).

[29] Hecht, E. *Optics* (Pearson Education, Inc., 2017), 5th edn.

[30] P. B. Johnson and R. W. Christy. Optical Constant of the Nobel Metals. *Physical Review B* **6**, 4370 (1972).

[31] McPeak, K. M. *et al.* Plasmonic Films Can Easily Be Better: Rules and Recipes. *ACS Photonics* **2**, 326–333 (2015).

[32] Kavokin, A., Baumberg, J. J., Malpuech, G. & Laussy, F. P. *Microcavities* (Oxford University Press, 2007), revised edn.

[33] Lagoudakis, K. *The Physics of Exciton-Polariton Condensates* (EPFL Press, 2013).

[34] Coles, D. Polaritons in Strongly-Coupled Organic Microcavities - Thesis. *University of Sheffield* (2011).

[35] Purcell, E. Spontaneous emission probabilities at radio frequencies. *Physical Review* **69**, 246–260 (1946).

[36] Savona, V., Andreani, L. C., Schwendimann, P. & Quattropani, A. Quantum well excitons in semiconductor microcavities: Unified treatment of weak and strong coupling regimes. *Solid State Communications* **93**, 733–739 (1995).

[37] Savona, V., Piermarocchi, C., Quattropani, A., Schwendimann, P. & Tassone, F. Optical properties of microcavity polaritons. *Phase Transitions* **68**, 169–279 (1999).

[38] Zhu, Y. *et al.* Vacuum Rabi splitting as a feature of linear-dispersion theory: Analysis and experimental observations. *Physical Review Letters* **64**, 2499–2502 (1990).

[39] Zayats, A. V., Smolyaninov, I. I. & Maradudin, A. A. Nano-optics of surface plasmon polaritons. *Physics Reports* **408**, 131–314 (2005).

[40] Zhang, J., Zhang, L. & Xu, W. Surface plasmon polaritons: physics and applications. *Journal of Physics D: Applied Physics* **45**, 113001 (2012).

[41] Manuel, A. P., Kirkey, A., Mahdi, N. & Shankar, K. Plexcitonics-fundamental principles and optoelectronic applications. *Journal of Materials Chemistry C* **7**, 1821–1853 (2019).

[42] Foteinopoulou, S., Devarapu, G. C. R., Subramania, G. S., Krishna, S. & Wasserman, D. Phonon-polaritonics: enabling powerful capabilities for infrared photonics. *Nanophotonics* **8**, 2129–2175 (2019).

[43] This Month in Physics History: December 1958: Invention of the Laser. *APS News* **12**, 2 (2003).

[44] Bose, S. Plancks Gesetz und Lichtquantenhypothese. *Zeitschrift für Physik* **26**, 178–181 (1924).

[45] Einstein, A. Quantentheorie des einatomigen idealen Gases. *Sitzungsberichte der Preussischen Akademie der Wissenschaften* 261–267 (1924).

[46] Jiang, Z., Ren, A., Yan, Y., Yao, J. & Zhao, Y. S. Exciton-Polaritons and Their Bose–Einstein Condensates in Organic Semiconductor Microcavities. *Advanced Materials* **34**, 2106095 (2022).

[47] Anderson, M. H., Ensher, J. R., Matthews, M. R., Wieman, C. E. & Cornell, E. A. Observation of Bose-Einstein Condensation in a Dilute Atomic Vapor. *Science* **269**, 198–201 (1995).

[48] Deng, H., Weihs, G., Snoke, D., Bloch, J. & Yamamoto, Y. Polariton lasing vs. photon lasing in a semiconductor microcavity. *Proceedings of the National Academy of Sciences* **100**, 15318–15323 (2003).

[49] Wouters, M. & Carusotto, I. Excitations in a nonequilibrium bose-einstein condensate of exciton polaritons. *Physical Review Letters* **99**, 1–4 (2007).

[50] Kasprzak, J. *et al.* Bose–Einstein condensation of exciton polaritons. *Nature* **443**, 409–414 (2006).

[51] Amo, A. *et al.* Superfluidity of polaritons in semiconductor microcavities. *Nature Physics* **5**, 805–810 (2009).

[52] Lagoudakis, K. *et al.* Quantized vortices in an exciton-polariton condensate. *Nature Physics* **4**, 706–710 (2008).

[53] Lerario, G. *et al.* Room-temperature superfluidity in a polariton condensate. *Nature Physics* **13**, 837–841 (2017).

[54] Byrnes, T., Kim, N. & Yamamoto, Y. Exciton-polariton condensates. *Nature Physics* **10**, 803–813 (2014).

[55] Christopoulos, S. *et al.* Room-Temperature Polariton Lasing in Semiconductor Microcavities. *Physical Review Letters* **98**, 126405 (2007).

[56] Christmann, G., Butté, R., Feltin, E., Carlin, J. F. & Grandjean, N. Room temperature polariton lasing in a GaNAlGaN multiple quantum well microcavity. *Applied Physics Letters* **93**, 1–4 (2008).

[57] Li, F. *et al.* From excitonic to photonic polariton condensate in a ZnO-based microcavity. *Physical Review Letters* **110**, 1–5 (2013).

[58] Li, F. *et al.* Fabrication and characterization of a room-temperature ZnO polariton laser. *Applied Physics Letters* **102** (2013).

[59] Bhattacharya, P., Xiao, B., Das, A., Bhowmick, S. & Heo, J. Solid state electrically injected exciton-polariton laser. *Physical Review Letters* **110**, 1–5 (2013).

[60] Schneider, C. *et al.* An electrically pumped polariton laser. *Nature* **497**, 348–352 (2013).

[61] Zasedatelev, A. V. *et al.* A room-temperature organic polariton transistor. *Nature Photonics* **13**, 378–383 (2019).

[62] Slootsky, M., Zhang, Y. & Forrest, S. R. Temperature dependence of polariton lasing in a crystalline anthracene microcavity. *Physical Review B - Condensed Matter and Materials Physics* **86**, 1–5 (2012).

[63] Grant, R. T. *et al.* Efficient Radiative Pumping of Polaritons in a Strongly Coupled Microcavity by a Fluorescent Molecular Dye. *Advanced Optical Materials* **4**, 1615–1623 (2016).

[64] Tolpygo, K. B. Physical Properties of a Rock Salt Lattice Made Up of Deformable Ions. *Zhurnal Eksperimental'noi i Teoreticheskoi Fiziki* **20**, 497–509 (1950).

[65] Hopfield, J. J. & Thomas, D. G. Polariton absorption lines. *Physical Review Letters* **15**, 22–25 (1965).

[66] Weisbuch, C., Nishioka, M., Ishikawa, A. & Arakawa, Y. Observation of the coupled exciton-photon mode splitting in a semiconductor quantum microcavity. *Physical Review Letters* **69**, 3314–3317 (1992).

[67] Kasprzak, J. *et al.* Second-order time correlations within a polariton Bose-Einstein condensate in a CdTe microcavity. *Physical Review Letters* **100**, 1–4 (2008).

[68] Lidzey, D. *et al.* Strong exciton–photon coupling in an organic semiconductor microcavity. *Nature* **395**, 53–55 (1998).

[69] Kéna-Cohen, S. & Forrest, S. R. Room-temperature polariton lasing in an organic single-crystal microcavity. *Nature Photonics* **4**, 371–375 (2010).

[70] Daskalakis, K. S., Maier, S. A., Murray, R. & Kéna-Cohen, S. Nonlinear interactions in an organic polariton condensate. *Nature Materials* **13**, 271–278 (2014).

[71] Plumhof, J., Stöferle, T., Mai, L., Scherf, U. & Mahrt, R. Room-temperature Bose-Einstein condensation of cavity exciton-polaritons in a polymer. *Nature Materials* **13**, 247–252 (2014).

[72] Dietrich, C. P. *et al.* An exciton-polariton laser based on biologically produced fluorescent protein. *Science Advances* **2**, 1–8 (2016).

[73] Cookson, T. *et al.* A Yellow Polariton Condensate in a Dye Filled Microcavity. *Advanced Optical Materials* **5**, 1700203 (2017).

[74] Sannikov, D. *et al.* Room Temperature Broadband Polariton Lasing from a Dye-Filled Microcavity. *Advanced Optical Materials* **7**, 1–5 (2019).

[75] Betzold, S. *et al.* Coherence and Interaction in Confined Room-Temperature Polariton Condensates with Frenkel Excitons. *ACS Photonics* **7**, 384–392 (2020).

[76] Ren, J. *et al.* Efficient Bosonic Condensation of Exciton Polaritons in an H-Aggregate Organic Single-Crystal Microcavity. *Nano Letters* **20**, 7550–7557 (2020).

[77] Hummel, R. E. *Electronic Properties of Materials* (Springer New York, 2013), 4th edn.

[78] Kéna-Cohen, S., Maier, S. A. & Bradley, D. D. Ultrastrongly coupled exciton-polaritons in metal-clad organic semiconductor microcavities. *Advanced Optical Materials* **1**, 827–833 (2013).

[79] Liu, B., Rai, P., Grezmak, J., Twieg, R. J. & Singer, K. D. Coupling of exciton-polaritons in low-Q coupled microcavities beyond the rotating wave approximation. *Physical Review B* **92**, 155301 (2015).

[80] Benisty, H., De Neve, H. & Weisbuch, C. Impact of planar microcavity effects on light extraction - Part II: Selected exact simulations and role of photon recycling. *IEEE Journal of Quantum Electronics* **34**, 1632–1643 (1998).

[81] Loebich, O. The optical properties of gold. *Gold Bulletin* **5**, 2–10 (1972).

[82] Hobson, P. A. *et al.* Strong exciton–photon coupling in a low-Q all-metal mirror microcavity. *Applied Physics Letters* **81**, 3519–3521 (2002).

[83] Ma, F. & Liu, X. Phase shift and penetration depth of metal mirrors in a microcavity structure. *Applied Optics* **46**, 6247–6250 (2007).

[84] Oda, M. *et al.* Strong exciton-photon coupling and its polarization dependence in a metal-mirror microcavity with oriented PIC J-aggregates. *physica status solidi c* **6**, 288–291 (2009).

[85] Obara, Y., Saitoh, K., Oda, M. & Tani, T. Room-Temperature Fluorescence Lifetime of Pseudoisocyanine (PIC) J Excitons with Various Aggregate Morphologies in Relation to Microcavity Polariton Formation. *International Journal of Molecular Sciences* **13**, 5851–5865 (2012).

[86] Coles, D. M., Grant, R. T., Lidzey, D. G., Clark, C. & Lagoudakis, P. G. Imaging the polariton relaxation bottleneck in strongly coupled organic semiconductor microcavities. *Physical Review B* **88**, 121303 (2013).

[87] Schwartz, T. *et al.* Polariton dynamics under strong light-molecule coupling. *ChemPhysChem* **14**, 125–131 (2013).

[88] Miyasaka, Y., Hashida, M., Nishii, T., Inoue, S. & Sakabe, S. Derivation of effective penetration depth of femtosecond laser pulses in metal from ablation rate dependence on laser fluence, incidence angle, and polarization. *Applied Physics Letters* **106** (2015).

[89] Mizuno, H. *et al.* Fabrication and characterization of silver mirror planar microcavity with dye J-aggregates. *Materials Letters* **168**, 210–213 (2016).

[90] Coles, D. M. *et al.* Strong Exciton-Photon Coupling in a Nanographene Filled Microcavity. *Nano Letters* **17**, 5521–5525 (2017).

[91] Georgiou, K. *et al.* Generation of Anti-Stokes Fluorescence in a Strongly Coupled Organic Semiconductor Microcavity. *ACS Photonics* **5**, 4343–4351 (2018).

[92] Sabatini, R. P. *et al.* Molecularly isolated perylene diimides enable both strong exciton-photon coupling and high photoluminescence quantum yield. *Journal of Materials Chemistry C* **7**, 2954–2960 (2019).

[93] Ramezani, M. *et al.* Plasmon-exciton-polariton lasing. *Optica* **4**, 31 (2017).

[94] Ramezani, M., Le-Van, Q., Halpin, A. & Gómez Rivas, J. Nonlinear Emission of Molecular Ensembles Strongly Coupled to Plasmonic Lattices with Structural Imperfections. *Physical Review Letters* **121**, 243904 (2018).

[95] Hakala, T. K. *et al.* Bose-Einstein condensation in a plasmonic lattice. *Nature Physics* **14**, 739–744 (2018).

[96] Alliance, G. B. A Vision for a Sustainable Battery Value Chain in 2030. Tech. Rep. September, World Economic Forum (2019).

[97] Dicke, R. H. Coherence in spontaneous radiation processes. *Physical Review* **93**, 99–110 (1954).

[98] Angerer, A. *et al.* Superradiant emission from colour centres in diamond. *Nature Physics* **14**, 1168–1172 (2018).

[99] Skribanowitz, N., Herman, I. P., MacGillivray, J. C. & Feld, M. S. Observation of dicke superradiance in optically pumped HF gas. *Physical Review Letters* **30**, 309–312 (1973).

[100] Inouye, S. *et al.* Superradiant Rayleigh scattering from a Bose-Einstein condensate. *Science* **285**, 571–574 (1999).

[101] Mlynek, J. A., Abdumalikov, A. A., Eichler, C. & Wallraff, A. Observation of Dicke superradiance for two artificial atoms in a cavity with high decay rate. *Nature Communications* **5**, 1–6 (2014).

[102] Tighineanu, P. *et al.* Single-Photon Superradiance from a Quantum Dot. *Physical Review Letters* **116**, 1–6 (2016).

[103] Kim, J., Yang, D., Oh, S.-h. & An, K. Coherent single-atom superradiance. *Science* **359**, 662–666 (2018).

[104] Higgins, K. D. *et al.* Superabsorption of light via quantum engineering. *Nature Communications* **5**, 1–7 (2014).

[105] Yang, D. *et al.* Realization of superabsorption by time reversal of superradiance. *Nature Photonics* **15**, 272–276 (2021).

3 Experimental methods

This chapter covers the experimental techniques used in the following four chapters of this thesis. It contains all the fabrication and characterisation methods used in the preparation and characterisation of the organic thin films and microcavities used in this research.

3.1 Fabrication techniques

3.1.1 Thin film fabrication

A key property of organic small molecules is that they are solution-processable, allowing cheap, easy and large-scale fabrication. One solution-processing technique for fabricating thin films is spin-coating. By dissolving the organic molecule in a solvent, the solution can then be deposited onto a substrate rotating at several thousand rotations per minute (rpm). This distributes the solution evenly across the surface of the substrate and the solvent evaporates, leaving a thin film of the organic molecule(s). It is important to note, however, that a large proportion of the solution is ejected from the surface of the substrate prior to evaporation, meaning it is wasted.

The thickness, d, of the film is related to the spin speed, ω, through

$$d \propto \frac{1}{\sqrt{\omega}}. \tag{3.1}$$

Solution viscosity, density and evaporation rate also play a role but sources disagree on the exact contribution [1, 2]. The easiest method, therefore, to produce films with a specific thickness is to first spin a control film onto a blank substrate and measure the thickness. This was done by scratching the film down to the substrate and using a Bruker DektakXT stylus profilometer to measure the depth of the scratches. This value can then be used with Equation 3.1 to calibrate the spin speed for the desired film thickness.

In almost all cases in this thesis, the organic molecule was dissolved into a solution of polystyrene (PS) and solvent. In this way, the dye molecules in the spin-coated film are dispersed (more or less evenly) within a layer of the PS after the solvent evaporates. This allows the concentration of dye in the film to be controlled and reduces molecular aggregation. Aggregation can be problematic as it tends to reduce the photoluminescence quantum yield (PLQY) of the film (see Section 2.1.3.1). This is because aggregation increases intermolecular interactions, which results in an increase in non-radiative pathways. The polystyrene matrix also helps to planarise the film surface ($<$ 1 nm RMS roughness), which is important for producing high quality (Q) factor cavities, and offers additional scope in controlling film thickness.

For all dyes discussed here, toluene was the first choice of solvent as it gives highly uniform films with good surface coverage. The dye was added to a ∼25-35 mg/mL solution of PS/toluene at the desired concentration. Alternatively, solvents such as dichloromethane (DCM) and tetrahydrofuran

(THF) were used. All films were spin-coated dynamically (the spin-coater was allowed to reach the desired spin speed before deposition) using 100 μL of solution.

3.1.2 Microcavity fabrication

The design and fabrication of every microcavity followed the same process. The first step was to spin a thin film of the dye/PS blend with the desired concentration. UV-vis absorption measurements were taken with a Horiba Fluoromax 4 Fluorometer with a Xe lamp, and the thickness measured as in Section 3.1.1. Equations 2.25 and 2.4 were then used to calculate the wavelength-dependent extinction coefficient of the film. A multiple-peak Lorentzian was then fit to the extinction coefficient (in eV) such that the peak wavelength, linewidth and amplitude could be extracted. These values were input into a transfer matrix reflectivity (TMR) model and adjusted such that the TMR model reproduced the original absorbance of the film. Mirrors could then be added to the TMR model and the thickness of the film adjusted to shift the cavity mode to the desired spectral region.

The TMR model allowed a determination of whether the oscillator strength was sufficient to achieve strong coupling. If not, a higher concentration film was made and the process repeated. If the TMR model predicted the cavity would lie in the strong coupling regime, the layer thicknesses were then adjusted to give the desired detuning. They were then fabricated as described in the previous and following sections. In all cases, the bottom mirror (the one deposited onto the substrate) had a higher reflectivity and lower transmission than the top. The active layer (dye/PS blend) was then spin coated on top of this and then the top mirror deposited on top.

3.1.2.1 Silver mirror fabrication

All silver (Ag) mirrors were fabricated using an Angstrom Engineering thermal evaporator. Under vacuum, a current was passed through a resistive boat containing Ag pellets, heating them until they evaporated. The samples or substrates to be coated were suspended face down in a mask, which can be patterned or not depending on the application, and was suspended above the boat. For all microcavities, the mask was unpatterned. The evaporated Ag travelled upwards, coating the samples, with a quartz crystal microbalance (QCM) allowing the thickness of the deposited material to be monitored. A tooling factor could be used to calibrate the QCM thickness value, d_{QCM}, by measuring the thickness of a control film, d_{meas} (see Section 3.1.1), and calculating the new tooling factor, T_{new} according to

$$T_{new} = T_{old} \times \frac{d_{meas}}{d_{QCM}}. \tag{3.2}$$

Here, T_{old} is the tooling factor used to deposit the control film. This calibration ensured that the thickness measured by the system and the actual thickness were the same. All Ag mirrors fabricated had a thickness of 200 nm and 35 nm for bottom and top mirrors, respectively.

3.1.2.2 Distributed Bragg reflector fabrication

DBRs were either home-grown using an Angstrom Engineering electron beam (e-beam) or commissioned from Helia Photonics Ltd, where a mix of ion-assisted e-beam depositions and thermal evaporations were used. Silicon dioxide (SiO_2, n∼1.5) was used as the low refractive index material,

and niobium pentoxide (Nb_2O_5, n∼2.2) or titanium dioxide (TiO_2, n∼2.5) as the high-refractive index material. Top DBRs had 8 or 9 pairs and bottom 10 or 12 pairs.

An e-beam (as the names suggests) uses a beam of electrons to evaporate materials for high-quality, high-precision depositions. It is advantageous over thermal and chemical processes as it can reach much higher temperatures, allowing higher deposition rates and the evaporation of higher boiling point materials. The electrons are generated under a high vacuum by passing an electric current through a tungsten filament, causing it to heat up and emit electrons. A high voltage accelerates the electrons towards the deposition material and a magnetic field is used to focus the beam. Upon impact, the electrons transfer their energy to the material, which evaporates and coats the substrates, which are suspended above. A QCM was employed to monitor growth rates as for the thermal evaporator discussed in the previous section.

In the case of the home-grown DBRs, the system was calibrated by depositing 100 nm of each dielectric material onto individual silicon wafers. The refractive indices and thicknesses were then measured using a J.A. Woolam M-2000 ellipsometer at an angle of incidence of 75°. This allowed the desired thickness of each layer and the crystal tooling factors (Equation 3.2) to be calculated in order to produce DBRs as close to the design wavelength as possible. The DBRs were then fabricated by depositing each material in turn, with the high-refractive material (Nb_2O_5 or TiO_2) closest to the cavity active layer, resulting in as high a refractive index contrast as possible. Most of the organic materials used had refractive indices around 1.5-1.8 and in the case of low dye:PS ratios, the refractive index was dominated by that of PS (n∼1.59).

The Helia DBRs used an ion-assisted e-beam for the Nb_2O_5 (Helia did not use TiO_2) and the SiO_2 was thermally evaporated. In this process, an ion gun is fired at the substrates during the e-beam deposition in order to transfer kinetic energy to the Nb_2O_5 molecules. This produced films of higher density and more even coverage. In the case of the top mirror, the ion gun was turned off for the first 20 nm of the first layer to avoid damaging the organic.

3.2 Optical characterisation techniques

3.2.1 Angle-dependent photoluminescence and reflectivity

The easiest way to confirm strong coupling in a microcavity is to measure the angle-dependent reflectivity to see whether two distinctive polariton branches can be seen. To do this, a motorised goniometer setup was employed to automatically measure the reflectivity and PL at different angles. A schematic of the setup is shown in Figure 3.1. A DH-2000-BAL Ocean Optics deuterium-halogen white light was coupled through an optic fibre to the excitation arm of the goniometer and two lenses were employed to collimate the beam and then focus it onto the sample. The sample was positioned so that its surface lay at the centre of the goniometer and the focus of both arms. The collection arm had another two lenses to collimate and focus the beam onto an optic fibre coupled to an Andor Shamrock SR-303i-A CCD spectrometer. It was also possible to insert a polariser to collect only the transverse magnetic (TM) or transverse electric (TE) polarisations. A continuous wave (CW) diode laser was focused onto the sample from above for PL measurements – this was to ensure the laser light was not reflected into the collection fibre.

This setup was also used to take single-angle PL and photostability measurements on thin films.

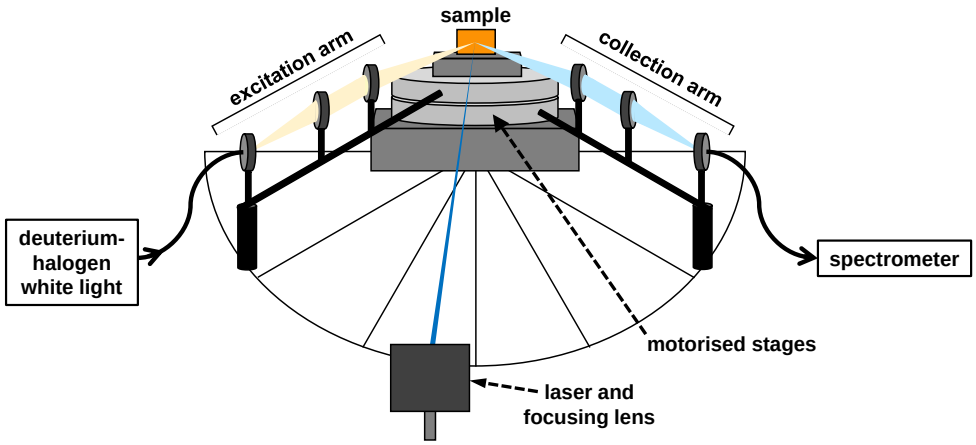

Figure 3.1. Motorised goniometer setup used to measure angle-dependent PL and reflectivity. A deuterium-halogen light was coupled to the excitation arm by an optic fibre. Two lenses collimated and focused the beam onto the sample. The collection arm consisted of two further lenses, which collimated and focused the reflected light onto a fibre leading to an Andor Shamrock SR-303i-A CCD spectrometer. A CW laser was focused onto the sample for PL measurements (including single-angle PL and photostability) and the emitted light was collected by the collection arm. The excitation arm was not used for PL measurements.

For photostability measurements, the sample was illuminated continuously over periods of time from several minutes to an hour, with spectra taken regularly to track the sample emission over time.

3.2.2 k-space imaging

k-space (also known as Fourier) imaging was used to accurately measure cavity linewidths and map the PL emission from cavities. More detail on these measurements can be found in the methods section of the publication presented in Chapter 4. The setup was also used in Chapter 5 to generate polariton condensation and this technique is described in the methods there.

A schematic of the setup is shown in Figure 3.2. Part (a) shows the full setup, different portions of which are used for different measurement techniques. Part (b) shows a close-up of the section most relevant for Fourier imaging. In this section, PL from the sample was collected by the objective and focused on its back focal plane. This corresponds to the Fourier plane. Light focused on this plane at a specific position will correspond to light emitted from the sample at a specific angle, regardless of where on the same the PL is emitted from. This technique can therefore be used to study the angular dispersion of cavity modes and polariton branches in microcavities. The light focused on the Fourier plane was then collimated by a 250 mm focal length lens and focused onto the CCD of the spectrometer by a 125 mm focal length lens. This resulted in a magnification of 0.5, i.e. a demagnification. The size of the image at the Fourier plane was 12 mm; therefore, the image on the CCD had a size of 6 mm.

3.2.3 Transient absorption and reflectivity

Transient absorption and reflectivity measurements were used to measure time-resolved changes in samples when pumped by high energy laser pulses. These measurements were carried out at the Istituto di Fotonica e Nanotecnologia–CNR at Politecnico di Milano in collaboration with Dr. Lucia Ganzer, Dr. Michele Guizzardi, Dr. Tersilla Virgili and Prof. Guilio Cerullo.

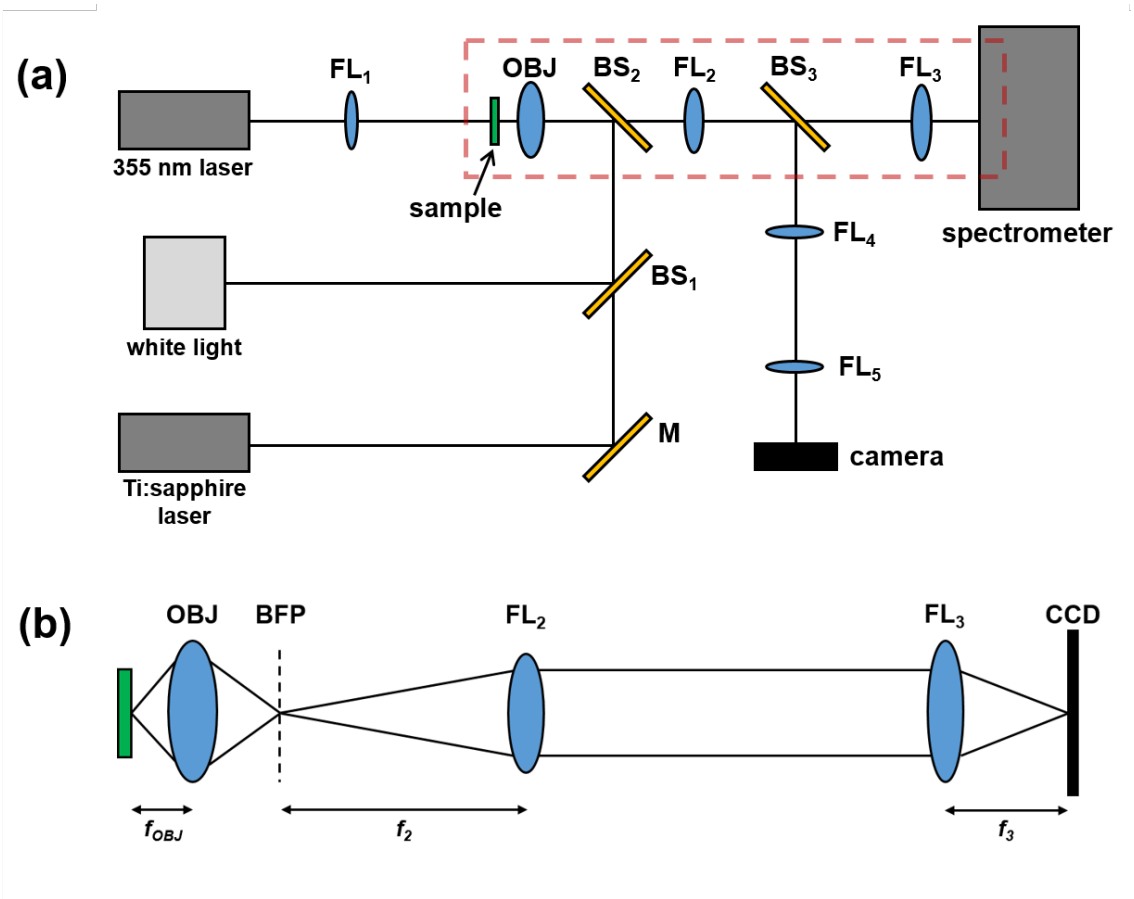

Figure 3.2. *k*-space setup setup used for measuring cavity linewidths, mapping their photoluminescence, and exploring polariton condensation. Part (a) shows a schematic of the entire setup. There are three possible light sources for the setup: a Teem Photonics pulsed Q-switched 355 nm Nd:YAG laser (PNV-M02510-1 x 0), a DH-2000-BAL Ocean Optics deuterium-halogen white light, and a Coherent pulsed, frequency-doubled Ti:sapphire (MIRA 900) at 445 nm. For linewidth measurements, the Ti:sapphire was reflected from a mirror (M) through beamsplitter 1 (BS_1), reflected from BS_2, and focused onto the sample using an Edmund Optics 20 x HR infinity corrected objective (OBJ, numerical aperture = 0.6). PL from the sample was collected by OBJ, transmitted by BS_2, collimated by focusing lens 2 (FL_2), transmitted by BS_3, and focused onto the spectrometer CCD by FL_3. For condensation measurements, the 355 nm was focused onto the sample by FL_1 and the PL from the sample was again collected by OBJ and focused into the spectrometer. A filter was placed between the sample and OBJ to protect OBJ from the laser. The white light was used to align and focus the system: the beam was focused onto the sample by OBJ, and the reflected light was directed towards and focused onto the CCD of a ThorLabs camera. For PL mapping measurements, a ThorLabs 445 nm diode laser was placed in the Ti:sapphire arm before BS_1. Part (b) shows a close-up of the part of the setup enclosed by the dashed red box in part (a). PL from the sample was collected by OBJ and was focused on its back focal plane (BFP), i.e. the Fourier plane. The plane is imaged onto the CCD of the spectrometer using FL_2 and FL_3. The beamsplitters have been removed for clarity.

In the measurements described in this thesis, a regeneratively amplified Ti:sapphire laser (fundamental wavelength = 800 nm, pulse width = 100 fs, repetition rate = 2 kHz) was split into two paths to give a pump and a probe beam. The setup is illustrated schematically in Figure 3.3, with (a) showing the transmission configuration used to measure films (transient absorption), and (b) showing the reflection configuration used to measure cavities (transient reflectivity). Note that lenses and mirrors are not included in the schematics for clarity.

In both configurations, the fundamental 800 nm beam was split into a pump (reflected portion) and a probe (transmitted portion) beam. The probe beam was focused onto a sapphire crystal to

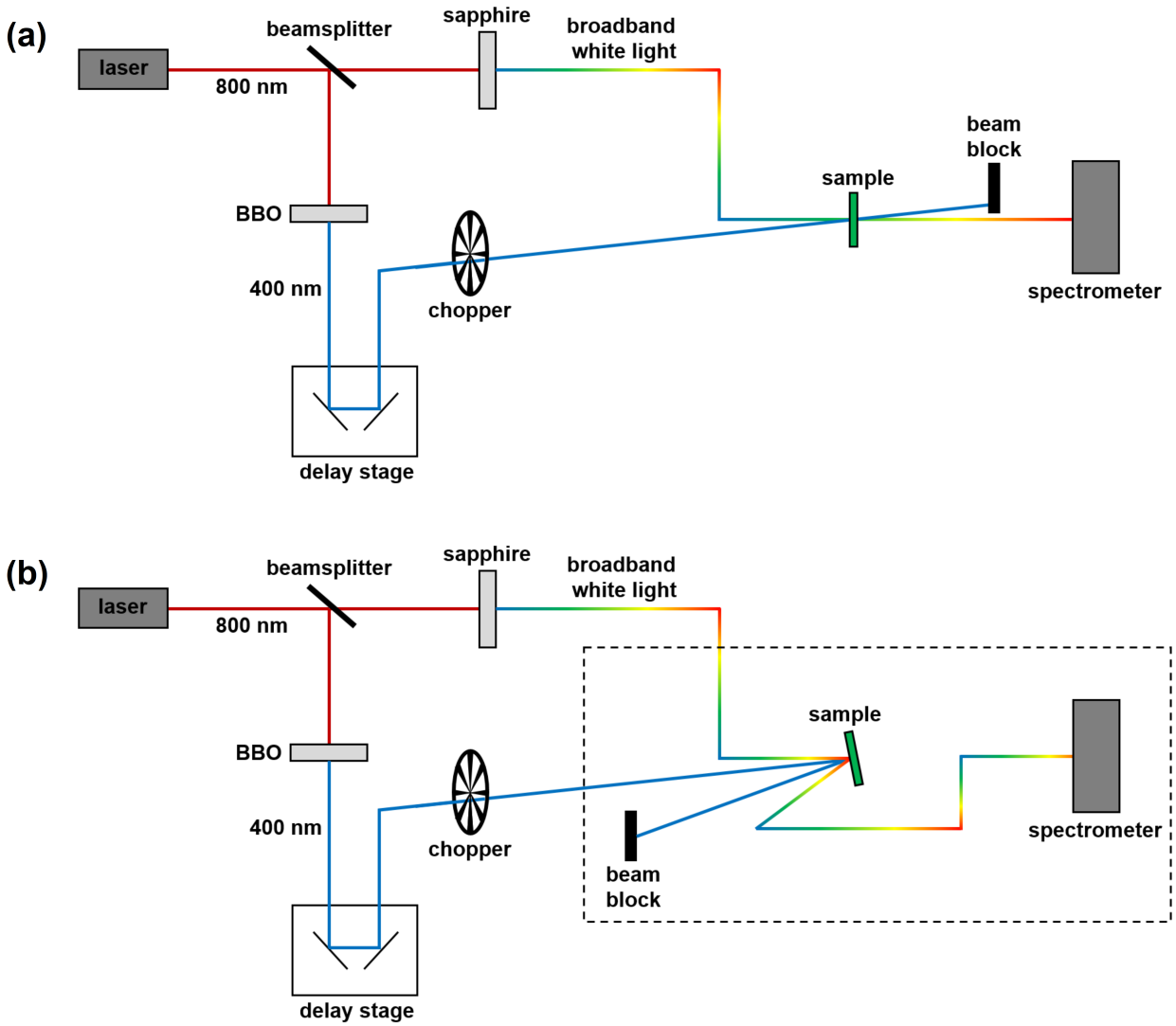

Figure 3.3. Pump probe setup. Parts (a) and (b) show a schematic of the transient absorption and transient reflectivity setups, respectively. In both configurations, the fundamental 800 nm beam is split into a pump (reflected portion) and a probe (transmitted portion) beam. The probe beam is focused onto a sapphire crystal to generate a broadband white light and directed onto the sample. In (a), the transmitted probe is collected by the spectrometer. In (b), the reflected probe is directed into the spectrometer. In both configurations (after it has been reflected by the beam splitter) the pump beam is focused onto a BBO crystal to produce a 400 nm beam. It then passes through a motorised delay stage and a mechanical chopper before being focused onto the sample surface. The transmitted or reflected beam is then blocked by a beam block. The dashed box in (b) indicates the portion of the setup that differs from (a). Outside of this region, the setups are identical.

generate a broadband white light and focused onto the sample. In the transmission configuration, the transmitted probe was collected by the spectrometer, and in the reflectivity configuration, the reflected probe was directed into the spectrometer. After the pump beam was reflected by the beamsplitter, it was focused onto a barium borate (BaB_2O_4, BBO) crystal, where it underwent second harmonic generation to produce a 400 nm beam. This wavelength was used to pump the samples. The pump beam then passed through a motorised delay stage to produce a controllable delay between pump and probe pulses, and then through a mechanical chopper to cut the repetition rate of the pump beam to 1 kHz. This was to allow pump-probe and probe-only measurements. The pump was then focused onto the same position on the sample as the probe. This was done such that the

pump spot was larger than the probe spot to ensure that the probe was only probing areas that had been affected by the pump. The transmitted or reflected pump was then directed onto a beam block to avoid it entering the spectrometer.

In the transmission configuration, the output signal is given in terms of the fractional change in the *transmission*, $^{\Delta T}/_{T}$, of the probe as a function of the pump-probe delay time, t, with and without the pump:

$$\frac{\Delta T}{T} = \frac{T_{ON}(t) - T_{OFF}(t)}{T_{OFF}(t)}. \tag{3.3}$$

Here, $T_{ON}(t)$ and $T_{OFF}(t)$ give the transmitted probe signal with and without the pump, respectively, and a positive delay time denotes that the pump pulse arrived at the sample before the probe pulse.

Some of the possible processes that are likely to occur in a fluorescent thin film during transient absorption measurements are ground state bleaching (GSB), stimulated emission (SE), and excited state absorption (ESA). These are illustrated in Figure 3.4, where in every case the probe$_{\mathrm{ON}}$ signal is for a positive pump-probe delay. Part (a) shows an example probe spectrum when there is no sample in the setup. Part (b) shows the effect of the pump on the probe due to GSB and the resulting $^{\Delta T}/_{T}$ signal. It can be seen that without the pump, there is a dip in the probe signal due to ground state absorption. When the pump arrives before the probe, less of the probe is absorbed as a large number of excited states have already been created. This process is called ground state bleaching and gives a positive $^{\Delta T}/_{T}$ signal. Part (c) shows the effect of the pump on the probe due to SE and the resulting $^{\Delta T}/_{T}$ signal. In this case, the sample shows minimal signal change when the sample is inserted as the power from the probe is very small and emission is minimal. When the pump is present, however, there is enough power to generate noticeable stimulated emission as the dye molecules relax back down to the ground state. This also gives a positive $^{\Delta T}/_{T}$ signal. Part (d) shows the effect of the pump on the probe due to ESA and the resulting $^{\Delta T}/_{T}$ signal. In this case, the there is no change in the probe when the sample is inserted. When the pump is present, there is a reduction in the probe signal: this is because the pump has excited electrons to the first excited state (S_1) and the sample can now absorb probe photons to excite the electrons to higher excited states (S_n, n>1). This process is called excited state absorption and results in a negative $^{\Delta T}/_{T}$ signal.

When using the reflectivity configuration, the output signal is given in terms of the fractional change in the *reflectivity*, $^{\Delta R}/_{R}$, of the probe as a function of the pump-probe delay time, t, with and without the pump:

$$\frac{\Delta R}{R} = \frac{R_{ON}(t) - R_{OFF}(t)}{R_{OFF}(t)}. \tag{3.4}$$

Here, $R_{ON}(t)$ and $R_{OFF}(t)$ give the reflected probe signal with and without the pump, respectively, and a positive delay time denotes that the pump arrives at the sample before the probe.

When cavities were investigated in this configuration, the effect of the pump on the LPB or cavity mode (depending on whether the cavity was strongly- or weakly-coupled) was studied. One such effect was a blueshift. This is illustrated in Figure 3.5, where part (a) again shows the probe without the sample present. Part (b) shows the effect of the pump on the probe due to a blueshift in the cavity mode and the resulting $^{\Delta R}/_{R}$ signal. It can be seen that without the pump, there is a dip in the probe signal corresponding to the cavity mode or LPB. When the pump is present, the cavity mode is blueshifted and this produces a derivative shape in the $^{\Delta R}/_{R}$. More details on the cause of this blueshift can be found in Section 6.1.

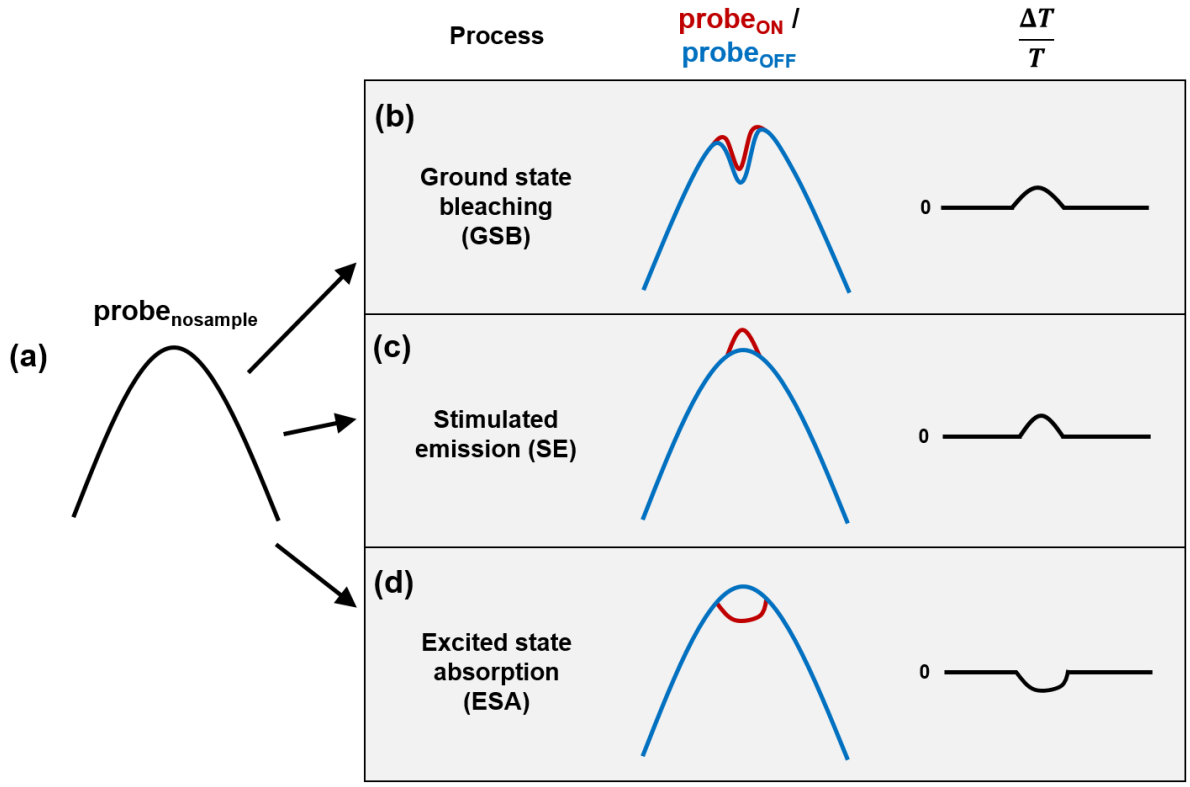

Figure 3.4. Example $^{\Delta T}/_{T}$ signals in films for different processes. Part (a) shows the probe with no sample present. Part (b) shows the effect on the probe signal with (probe$_{\mathrm{ON}}$, red) and without (probe$_{\mathrm{OFF}}$, blue) the pump due to ground state bleaching (GSB) and the resulting $^{\Delta T}/_{T}$ signal. Parts (c) and (d) show the effect on the signals due to stimulated emission (SE) and excited state absorption (ESA), respectively. It can be seen that the resulting $^{\Delta T}/_{T}$ signal is positive for GSB and SE, and negative for ESA.

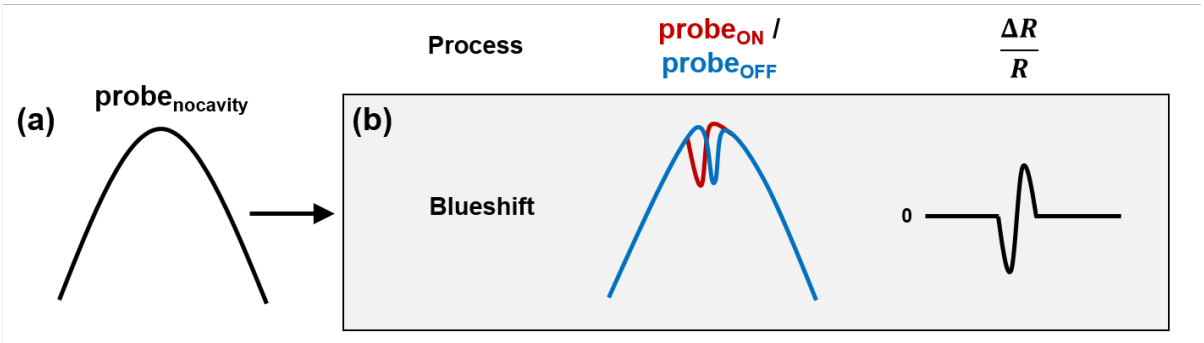

Figure 3.5. Example $^{\Delta R}/_{R}$ in a cavity corresponding to a blueshift. Part (a) shows the probe without the cavity present. Part (b) shows the effect on the probe signal with (probe$_{\mathrm{ON}}$, red) and without (probe$_{\mathrm{OFF}}$, blue) the pump, showing a blueshift of the cavity mode or LPB. It can be seen that this blueshift produces a derivative shape in the $^{\Delta R}/_{R}$ signal.

3.3 References

[1] Dietrich Meyerhofer. Characteristics of resist films produced by spinning. *Journal of Applied Physics*, 49(7):3993–3997, 1978.

[2] David B. Hall, Patrick Underhill, and John M. Torkelson. Spin coating of thin and ultrathin polymer films. *Polymer Engineering and Science*, 38(12):2039–2045, 1998.

4 Polariton condensation in an organic microcavity utilising a hybrid metal-DBR mirror

4.1 Motivation for project

At the time of starting this project, polariton condensation had been seen in many organic systems; however, this had only been demonstrated in cavities that utilised two DBR mirrors. The fabrication of such high-quality mirrors requires complicated, many-step deposition processes and is prone to error. Silver mirrors, on the other hand, are easy to thermally evaporate and do not require fine control over the thickness. They also have a very small penetration depth, giving enhanced Rabi splittings in polariton microcavities. However, the absorption losses associated with metal mirrors are generally too large to facilitate sufficient quality factors for condensation.

Here, I investigated a "hybrid" mirror that contained silver and a few DBR pairs in the hopes of harnessing the best properties of both. I found that hybrid mirrors possessed enhanced reflectivity and a broader reflectivity bandwidth than a 10-pair DBR, even with only a few DBR pairs in the hybrid mirror. I then fabricated cavities which replaced a bottom 10-pair DBR with a hybrid mirror and found these cavities had increased quality factors and larger Rabi splittings. Most notably, we demonstrated that a hybrid cavity in which the bottom mirror consisted only of 200 nm of silver, 60 nm of silicon dioxide, and 90 nm of niobium pentoxide was able to support polariton condensation at only a slightly increased threshed compared to a double-DBR cavity. This is a highly notable result, greatly simplifiying the fabrication of organic polariton microcavities for the generation of polariton condensates.

4.2 Publication

This section contains the publication as it appears online in *Scientific Reports*:

McGhee, K. E. *et al.* Polariton condensation in an organic microcavity utilising a hybrid metal-DBR mirror. *Scientific Reports* **11**, 20879 (2021).

The Supplementary Information for this publication can be found in Appendix A.

www.nature.com/scientificreports

scientific reports

Check for updates

OPEN

Polariton condensation in an organic microcavity utilising a hybrid metal-DBR mirror

Kirsty E. McGhee[1], Anton Putintsev[2], Rahul Jayaprakash[1], Kyriacos Georgiou[1,3], Mary E. O'Kane[1], Rachel C. Kilbride[1], Elena J. Cassella[1], Marco Cavazzini[4], Denis A. Sannikov[2], Pavlos G. Lagoudakis[2,5] & David G. Lidzey[1]✉

We have developed a simplified approach to fabricate high-reflectivity mirrors suitable for applications in a strongly-coupled organic-semiconductor microcavity. Such mirrors are based on a small number of quarter-wave dielectric pairs deposited on top of a thick silver film that combine high reflectivity and broad reflectivity bandwidth. Using this approach, we construct a microcavity containing the molecular dye BODIPY-Br in which the bottom cavity mirror is composed of a silver layer coated by a SiO_2 and a Nb_2O_5 film, and show that this cavity undergoes polariton condensation at a similar threshold to that of a control cavity whose bottom mirror consists of ten quarter-wave dielectric pairs. We observe, however, that the roughness of the hybrid mirror—caused by limited adhesion between the silver and the dielectric pair—apparently prevents complete collapse of the population to the ground polariton state above the condensation threshold.

A cavity-polariton is a quasiparticle formed by coupling an exciton to a confined photon mode within an optical cavity. Cavity-polaritons are bosons and have an effective mass of ~ 10^{-11} that of an atom[1] and therefore undergo Bose–Einstein condensation (BEC) at temperatures much higher than those observed with atomic gases[2]. In this process, polaritons condense into a single state once their density reaches a certain critical threshold, with all polaritons within the condensate having the same energy, momentum, and phase. Photons emitted by the condensate share these properties and as such possess the same characteristics as a laser[3]. This type of emission has been termed polariton lasing[4–7], with these devices being of emerging interest as novel low-threshold lasers and light-sources.

In recent years, increasing attention has been shown to the exploration of polariton condensation effects in organic semiconductor microcavities[1,8–12]. Here, Frenkel excitons have a binding energy that is much greater than k_BT at room temperature[13] and thus organic exciton–polariton microcavities are able to undergo room temperature condensation[1,8,9], a property that opens new routes to practical applications. A range of different organic semiconductors have been shown to undergo polariton condensation, including single crystals[8,14], conjugated polymers[1,15,16], and small-molecules, either in a crystalline form[9,17] or dispersed in a transparent polymer-matrix[18–20].

Many microcavities are based on two distributed Bragg reflectors (DBRs) placed either side of the active layer. Such DBRs generally consist of a stack of alternating high- and low- refractive index quarter-wave layers, producing mirrors that possess both high reflectivity (> 99%) and low optical absorption. In a Fabry-Pérot microcavity, the reflectivity of the cavity mirrors directly controls the degree of optical confinement and the cavity mode linewidth. Optical confinement can be defined by the cavity quality-factor (Q-factor) that is expressed using $Q = \lambda/\Delta\lambda$, where λ is the cavity mode wavelength and $\Delta\lambda$ is its spectral full-width at half maximum (FWHM) [21].

Many organic semiconductors have been shown to enter the strong coupling regime using microcavities with relatively low-reflectivity mirrors. Despite the fact that photon mode linewidths in low Q-factor cavities are relatively large (10–100 meV), the high oscillator strength of organic semiconductors results in large Rabi splitting energies (the energy splitting between the upper and lower polariton branches at resonance), $\hbar\Omega_{Rabi}$, of 100 s meV to ~ 1 eV [22–25]. Many of the highest Rabi splittings using organic semiconductors have been observed

[1]Department of Physics and Astronomy, University of Sheffield, Hicks Building, Hounsfield Road, Sheffield S3 7RH, UK. [2]Centre of Photonics and Quantum Materials, Skolkovo Institute of Science and Technology, Moscow, Russian Federation 121205. [3]Department of Physics, University of Cyprus, P.O. Box 20537, 1678 Nicosia, Cyprus. [4]Consiglio Nazionale delle Ricerche, Istituto di Scienze e Tecnologie Chimiche "Giulio Natta", Via C. Golgi 19, 20133 Milano, Italy. [5]Department of Physics and Astronomy, University of Southampton, University Road, Southampton SO17 1BJ, UK. ✉email: d.g.lidzey@sheffield.ac.uk

in structures based on two metallic reflectors (at least one of which is semi-transparent) with Q-factors of 10–65 [22,26–29]. Here, the small optical penetration depth of metals such as silver (Ag) results in a high degree of optical confinement, which reduces the effective cavity length (L_{eff}). As the Rabi splitting is inversely proportional to L_{eff}, 'all metal' cavities are generally characterised by increased Rabi splittings, and—as they are simple to fabricate via thermal evaporation—have effectively become the structure of choice in which to explore polaritonic properties that do not rely on non-linear effects[10,26,27].

To achieve polariton condensation, however, relatively extended polariton lifetimes are required. Most exciton–polariton microcavities that have been reported to undergo condensation are based on two DBR mirrors and typically have Q-factors of several hundred to > 1000 [19,30,31]. (It is worth noting here that Ren et al. recently demonstrated polariton condensation in a single crystal all-metal cavity[14]; however, it is difficult to fabricate such single crystals into microcavities with sufficiently high uniformity to support polariton condensation.) The reflectivity of a DBR is a strong function of the number of dielectric pairs[21], and thus such mirrors often comprise in excess of 30 individual layers[1,18,32,33]. Fabricating such structures is time-consuming, costly, and prone to error.

In this study, we address this issue and explore a new type of 'hybrid' dielectric mirror that is composed of a thick layer of a metal (Ag) onto which we deposit one or more dielectric mirror pairs. Here, the function of the silver mirror is to provide a high, broadband optical reflectivity that is then enhanced by a low number of DBR pairs, with such structures being significantly easier to fabricate. We characterise the properties of these hybrid mirrors and show that a structure composed of 4 DBR pairs backed by a silver film have a comparable reflectivity to that of a conventional 10-pair DBR. We explore the properties of strongly-coupled cavities made using a hybrid mirror, an organic semiconductor dye, and a conventional DBR, and show that cavities incorporating a 1-pair hybrid mirror have a Rabi splitting energy that is around 14% larger than a 9-pair/10-pair DBR–DBR control. We also demonstrate enhanced confinement, with structures based on a 10-pair hybrid mirror having a Q-factor that is 24% larger than the DBR control. We then explore the non-linear properties of a cavity utilising a 1-pair hybrid mirror and show that it can undergo polariton-condensation. However, we find in contrast to the DBR control cavity, emission from the hybrid cavity does not fully coincide with the bottom of the lower polariton branch. Using atomic force microscopy (AFM) and scanning electron microscopy (SEM), we show that this effect most likely results from disorder at the interface between the Ag mirror and the DBR.

Results

Hybrid distributed Bragg reflectors (DBRs). We have fabricated hybrid metal-DBR mirrors by thermally evaporating a 200 nm Ag film onto a quartz-coated glass substrate, followed by the deposition of various numbers (between 1 and 10) of SiO_2/Nb_2O_5 quarter-wave pairs (refractive index ~ 1.46 and ~ 2.20, respectively) by electron beam evaporation. The structure of such a hybrid mirror is shown schematically in Fig. 1a. Figure 1b shows the normal incidence white light reflectivity of a 1-pair hybrid, 5-pair hybrid and 10-pair (conventional) DBR mirror, with a 200 nm Ag mirror used as a reference. Figure 1c plots the reflectivity determined using a transfer matrix reflectivity (TMR) model for the same three mirrors and also that of silver. Here, our structures are based on a relatively thick silver film (200 nm) to maximise its optical reflectivity. Our TMR model (see Figure S1 in the "Supplementary Information") indicates that the reflectivity of a silver film does not increase once its thickness exceeds 200 nm. The cavity structures that we use (see "Optical properties of microcavities fabricated using hybrid-DBR mirrors" below) are designed to extract light through a conventional 'top' DBR, and thus our approach allows us to use relatively thick silver films having high reflectivity and low optical transmission on the bottom mirror.

We can see from Fig. 1c that the hybrid mirrors have a comparable reflectivity to a conventional DBR, together with a significantly broader stopband (high-reflectivity region) resulting from the use of a silver mirror. Indeed, our TMR simulations indicate that the hybrid mirrors (except for the 1-pair hybrid) have a reflectivity that is > 99.5% over a bandwidth of 130–140 nm (corresponding to ~ 530 meV). This high-reflectivity band is wider than the stop-band of the control DBR, which is limited to around 90 nm (~ 350 meV). This widened stop-band is potentially useful, as the large oscillator strength of organic semiconductors can result in large Rabi splittings (100's of meV) that are often greater than the width of the stopband of a conventional DBR. Figure 1d plots the TMR model reflectivity of each mirror explored (Ag, hybrid, DBR) at 550 nm. It can be seen from this that, at this wavelength, hybrid mirrors with five or more pairs have increased reflectivity compared to a 10-pair DBR.

Optical properties of microcavities fabricated using hybrid-DBR mirrors. We have used the hybrid mirrors outlined in Fig. 1 to fabricate a series of strongly-coupled microcavities containing the molecular dye bromine-substituted boron-dipyrromethene (BODIPY-Br). This dye combines high oscillator strength and relatively high photoluminescence quantum yield, and has previously been shown to undergo polariton-condensation[18,34]. Additionally, its photoluminescence (PL) emission lies in a spectral region not easily accessible with traditional inorganic semiconductors (green/yellow), making it desirable for laser applications.

To process BODIPY-Br it was first dispersed into a polystyrene (PS) matrix at 10% by mass in toluene. Here, the function of polystyrene is to prevent molecular aggregation, a process that results in the quenching of BODIPY-Br luminescence. To create thin films, the BODIPY-Br/PS blend was deposited by spin-coating. Figure 2a shows the normalised absorption and PL spectra of a BODIPY-Br/PS film on a quartz substrate, with the molecular structure of BODIPY-Br shown in the inset. It can be seen that the absorption and PL peak around 530 nm and 547 nm, respectively.

Microcavities were fabricated by spin-coating a BODIPY-Br/PS solution onto the hybrid-DBR mirrors. This was followed by the deposition of a 9-pair DBR (via e-beam evaporation) on top of the active layer to create the full structure as shown in Fig. 2b. In all cases, the thickness of the BODIPY-Br/PS layer was chosen to give a

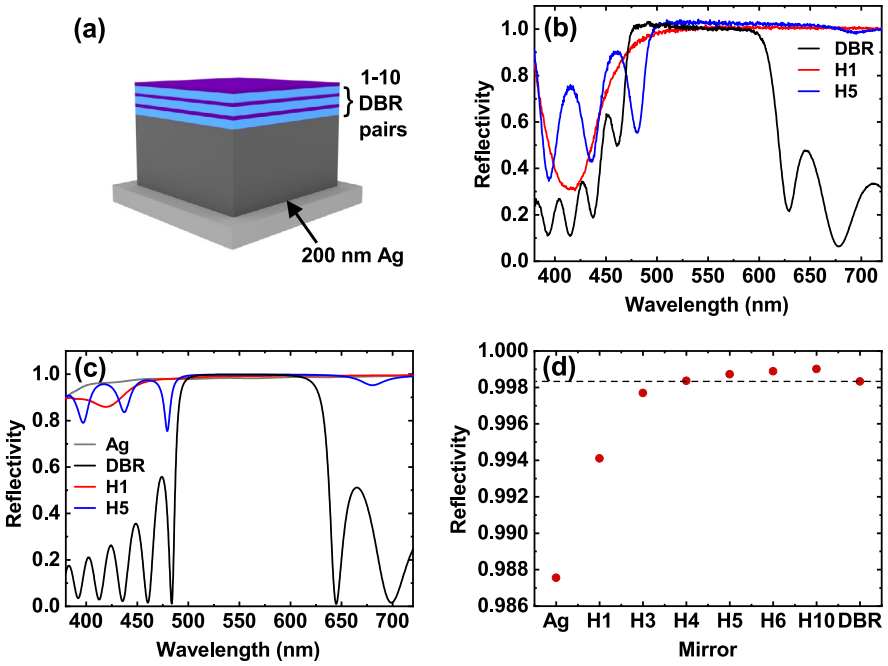

Figure 1. Hybrid metal-DBR mirrors. (**a**) Schematic of hybrid mirror. (**b**) Shows the experimentally measured reflectivity of the 1-pair hybrid (red), 5-pair hybrid (blue) and 10-pair DBR (black) mirrors, with transfer matrix reflectivity data for the same mirrors plus Ag (grey) shown in (**c**). (**d**) Plots the calculated reflectivity of each mirror at 550 nm. The horizontal dashed black line corresponds to the reflectivity of a 10-pair DBR. In (**b**–**d**), legend and x-axis labels 'HX' correspond to the hybrid mirrors, where *X* is the number of DBR pairs on top of the Ag, and 'Ag' and 'DBR' correspond to an Ag film and the 10-pair DBR, respectively.

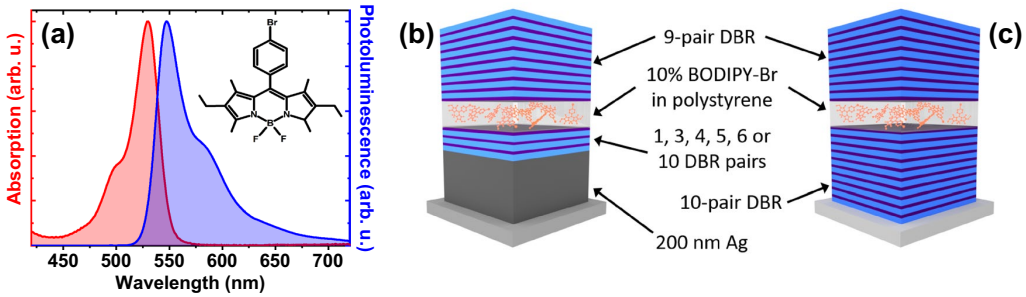

Figure 2. (**a**) Normalised absorption (red) and photoluminescence (blue) spectra of BODIPY-Br at 10% by mass in polystyrene. The molecular structure is shown in the inset. Schematic of (**b**) the hybrid Ag-DBR microcavity and (**c**) a conventional DBR–DBR microcavity.

cavity mode positioned around 547 nm. As a control, we also fabricated a DBR–DBR cavity with a 10-pair bottom DBR, an active BODIPY-Br/PS layer, and a 9-pair top DBR. The structure of this cavity is shown in Fig. 2c.

To characterise the cavities, we first performed angle-dependent white light reflectivity measurements to confirm they operated within the strong coupling regime. Here, measurements were performed using a goniometer setup in which a lens system positioned on a rotating optical rail was used to focus unpolarised white light onto the cavity surface. A series of lenses on a second rotating optical rail were used to collect the light and deliver it to a spectrometer (see Ref.[35] for more details). The angle-dependent reflectivity of a 4-pair hybrid cavity is shown in Fig. 3a. Here we observe two dispersive dips in the reflectivity spectra that undergo anticrossing around the energy of the BODIPY-Br exciton (530 nm). These two features are identified as the lower (LPB) and upper

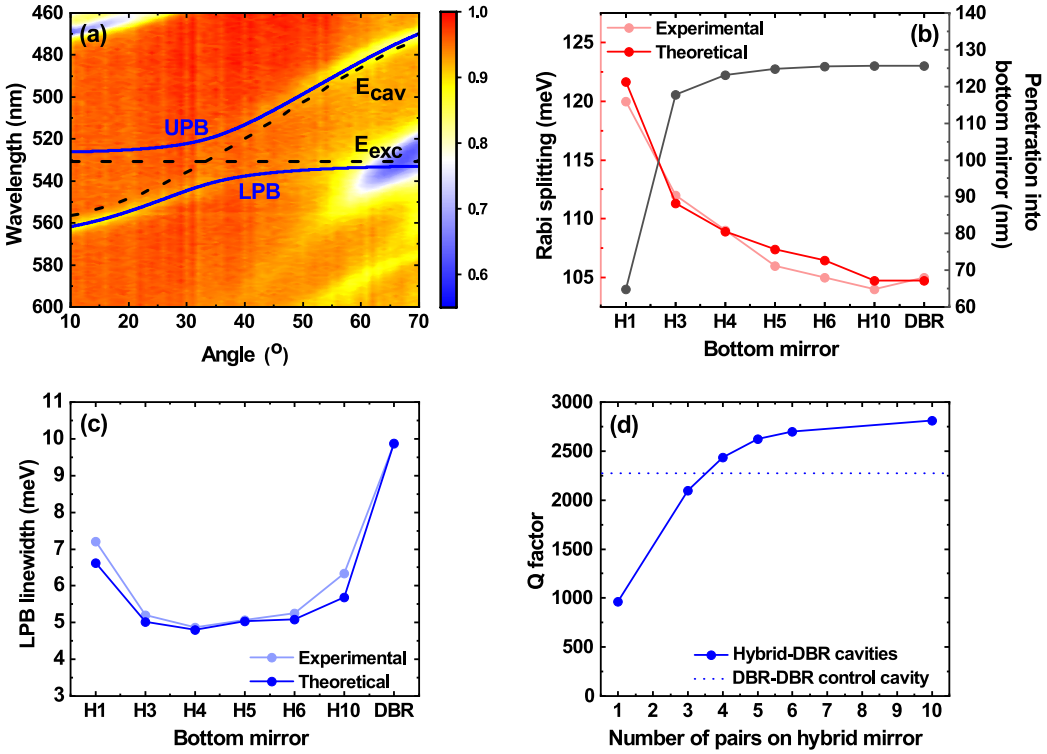

Figure 3. The effect of the number of hybrid mirror pairs on microcavity optical properties. (**a**) Plots the angle-dependent reflectivity measurement of a 4-pair hybrid mirror cavity. Fits of upper (UPB) and lower (LPB) polariton branches (blue solid lines) are made using a standard two-level oscillator model. The dispersion of the cavity photon mode (E_{cav}) and the exciton energy (E_{exc}) are also shown (black dashed lines). (**b**) Shows the Rabi splitting for the hybrid mirror cavities and the DBR control, where good agreement can be seen between experimental (light red, two-level oscillator) and theoretical (dark red, TMR) values. The modelled penetration of the electromagnetic field into the bottom mirror (grey) is also shown here. (**c**) Shows the linewidth of the LPB for the hybrid mirror and DBR cavities, comparing experimental (light blue) and theoretical (dark blue, from TMR) values. In both (**b**) and (**c**), the x-axis labels 'H*X*' correspond to the hybrid mirrors, where *X* is the number of DBR pairs on top of the Ag, and 'DBR' corresponds to the 10-pair DBR. In (**d**), we plot the modelled *Q*-factor for hybrid mirror cavities with cavity mode at 547 nm. The modelled *Q*-factor of the DBR control cavity is indicated by a horizontal blue dotted line.

polariton (UPB) branches, and we have used a two-level oscillator model to fit their dispersions (the solid lines in Fig. 3a). It can be seen that the description of the measured data is excellent.

We have used our model to extract the Rabi splitting energy for each of the different cavities and this is shown in Fig. 3b together with experimentally measured data. We note that the Rabi splitting energy is primarily dependent on the number of absorbers per unit length in a cavity as discussed Sect. 2 of the "Supplementary Information". However, here we attribute changes in the Rabi splitting to variations in the effective cavity length (L_{eff}). As can be seen, we observe an increase in Rabi splitting energy as the number of DBR pairs on the bottom hybrid mirror is reduced, with the cavity incorporating a 1-pair hybrid DBR having a Rabi splitting energy that is around 14% larger than the DBR–DBR control. Evidently, as the number of DBR pairs in the hybrid mirror is reduced, L_{eff} is reduced which results in an effective "concentration" of the electromagnetic field into the active cavity region and an increase in the Rabi splitting. In Figure S3 of the "Supplementary Information", we show electric field simulations of the cavity mode for the 1-pair and 5-pair hybrid cavities and the DBR control cavity, showing the penetration of the field into the different mirrors and the refractive index variation in each structure. This confirms the increased effective cavity length of structures incorporating an increased number of DBR pairs and we have calculated this (see Figure S2 of the "Supplementary Information") using Ref.[36]. However, for simplicity, in Fig. 3b we show the penetration depth of the electromagnetic field into the bottom mirror only.

To explore the effect of the hybrid mirror on cavity *Q*-factor, we focused imaged a 445 nm pulsed laser beam into a 4 μm diameter spot on the cavity surface to generate PL emission. A *k*-space imaging setup was then used to collect the luminescence and image it into a CCD spectrometer, allowing the FWHM emission linewidth of the LPB at normal incidence to be determined. Figure 3c plots the normal incidence LPB linewidth measured from the various structures. It can be seen that there is an apparent reduction in LPB linewidth as the number of mirror pairs is increased, with this trend reversing for structures having more than 5 DBR pairs. However,

this 'reversal' effect largely results from the fact that there was a small variation in the cavity mode wavelength caused by unintended variations in the thickness of the cavity active layer caused by the spin-coating process. This modifies the relative exciton–photon fraction of the LPB, with the photon fraction increasing (and linewidth reducing) as the negative detuning (energetic separation between the photon mode and the exciton) increases. We can account for this effect in our model by using the known n and k data for the BODIPY-Br/PS film. This was input into a TMR model to describe the dispersion of the LPB and UPB for each cavity. From this, we were able to calculate the physical thickness of the organic film, the position of the cavity mode at normal incidence, and the LPB linewidth. This data is also plotted in Fig. 3c, where we again find a good agreement between model and experimental results.

Using our model, we are then able to calculate expected cavity Q-factor as a function of the number of DBR mirror pairs. Here, we 'turn-off' the exciton oscillator strength and calculate the LPB linewidth and cavity Q-factor assuming in all cases the cavity mode is located at 547 nm. The results of our model are shown in Fig. 3d. Here, we find the cavity Q-factor increases as the number of DBR pairs in the hybrid mirror is increased, and for 4 or more pairs, exceeds that of the DBR–DBR control. Furthermore, our model suggests that a cavity utilising a hybrid mirror consisting of 10 DBR pairs on top of an Ag film is expected to have a Q-factor that is 24% larger than an equivalent 'conventional' cavity whose bottom mirror does not contain Ag, (i.e. simply composed of a 10-pair DBR).

As expected, we find that the measured and modelled polariton linewidths shown in Fig. 3c are strongly dependent on mixing between the exciton and photon. For example, for the 1-pair hybrid cavity, we determine (by modelling and experiment) an LPB linewidth of around 7 meV at normal incidence. However, the Q-factor of the same cavity is ~ 1000, suggesting an uncoupled photon-linewidth of around 2.2 meV. This substantial broadening of the LPB linewidth occurs even though the excitonic fraction of this state is relatively small (being 13% exciton and 87% photon). As we discuss below, this broadened polariton linewidth masks a small amount of site-to-site variation of the cavity photon energy that occurs as a result of structural disorder within the cavity that only becomes apparent when polaritons undergo condensation and lasing.

Polariton condensation in hybrid-DBR microcavities. We have explored our structures for evidence of polariton condensation. Here, it was decided to explore such effects in cavities that had the largest difference in their structural properties. Condensation effects were therefore studied in a 1-pair hybrid cavity and compared to a DBR–DBR control. In these experiments, the hybrid cavity utilised an 8-pair top DBR mirror. The DBR–DBR control structure was based on 10 and 8 DBR pairs, with the 10-pair mirror being fabricated by Helia Photonics Ltd. In both cases, the cavities had a very similar exciton–photon detuning, with the LPB being positioned at 567 and 569 nm in the hybrid and DBR cavities, respectively.

To generate polariton condensation, the microcavities were pumped non-resonantly at normal-incidence using a single-shot imaging technique in reflection configuration, with emission detected using k-space imaging. Here, the laser pulses (width of 150 fs, repetition frequency of 15 Hz) were focused onto the cavity surface into a spot with a FWHM diameter of 30 μm. For both cavities, the excitation laser wavelength was tuned to the first Bragg minimum at the edge of the stopband (467 nm for the hybrid cavity and 462 nm in the DBR–DBR control) to maximise the transmission of light into the cavity. In the data presented below, the PL intensity for the power dependence graphs was obtained by integrating single-shot real-space images of the cavity emission. The blueshift and FWHM data were extracted from the single-shot k-space dispersion images profiles filtered over ± 0.075 cm^{-1} range around $k = 0$.

Figure 4a plots the normalised PL emission from the hybrid mirror cavity recorded below the condensation threshold, together with a TMR model fit to the LPB dispersion. Here it can be seen that emission is initially distributed across a large angular range. We find that as the pump fluence is increased above the condensation threshold, there is a non-linear increase in PL intensity (see Fig. 4c), accompanied by an energy blueshift (Fig. 4d) and a decrease in the linewidth (Fig. 4e). Such blueshifts of the LPB have previously been explained on the basis of a partial saturation of the BODIPY optical transition[12]. Figure 4b shows the normalised PL emission above threshold, with the fit to the LPB below threshold also shown, allowing the extent of the energy blueshift to be clearly seen. Specifically, we determine a condensation threshold (determined from the measured absorbed fluence) of 295 μJ/cm^2 which is accompanied by a blueshift of 7 meV and a reduction in LPB FWHM linewidth from 11 meV to ~ 2.8 meV.

The equivalent condensation dataset to Fig. 4 for the DBR–DBR control is shown in Fig. 5. From part (c), we determine a condensation threshold of 180 μJ/cm^2, which is accompanied by a blueshift of approximately 3 meV (part d) and a reduction in emission linewidth from 5 meV to ~ 1.6 meV (part e). Interestingly, it is clear that the blueshift observed in the hybrid mirror cavity (7 meV) is more than twice that in the DBR cavity (3 meV). In Figure S4 in the "Supplementary Information", we use a TMR model to show that a larger blueshift is expected in the hybrid mirror cavity for a given reduction in molecular oscillator strength, an effect that we attribute to its enhanced Rabi splitting[37].

If we compare the distribution of emission in k-space for both cavities above threshold (Figs. 4b and 5b), it is evident that in the DBR–DBR control, the emission is strongly concentrated around the bottom of the LPB. In contrast, we do not evidence a full collapse to $k = 0$ in the hybrid mirror cavity; rather, the emission appears to be distributed over a wider range of k-vectors and energies and is apparently finely structured. We investigate the cause of this effect in "Investigating cavity homogeneity" below. For completeness, we also plot real-space images of the emission from both types of cavity below and above condensation threshold in Figure S5. Below threshold, the emission from both cavities is unstructured and has a size approximating the laser excitation spot (20–30 μm (FWHM)). Above threshold, the condensate in both types of cavity has a complex structure and

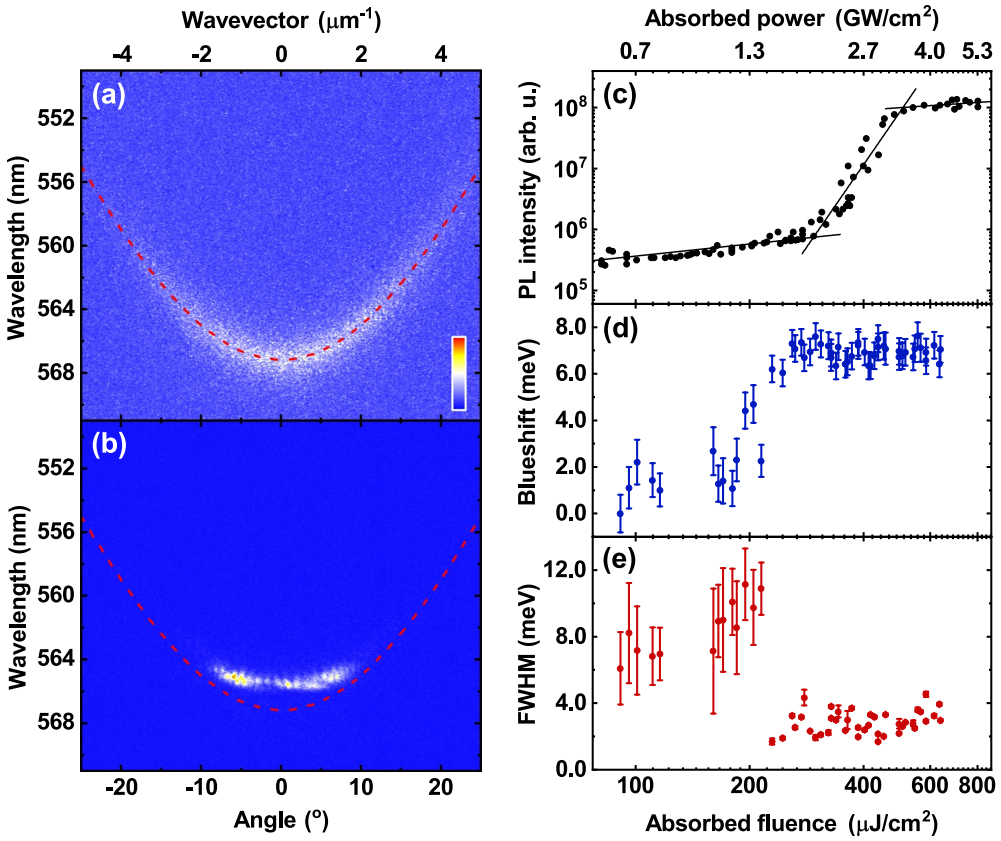

Figure 4. 1-pair hybrid mirror cavity condensation results. Normalised dispersions taken (**a**) below threshold and (**b**) above threshold. In both cases the red dashed line is a fit to the LPB in the linear regime. (**c**–**e**) Show the dependence of (**c**) PL intensity, (**d**) blueshift, and (**e**) full-width at half-maximum (FWHM) of the LPB on the absorbed pump fluence. From straight line fits to the power-dependent PL intensity in (**c**) (black solid lines), we determine a condensation threshold for this cavity of 295 μJ/cm^2. Here we see a non-linear increase in PL intensity, a spectral blueshift, and a decrease in the FWHM of the LPB. The error bars in (**d**) and (**e**) were calculated from the error on a Gaussian fit to the LPB at each fluence.

consists of one or more separate domains having a size of between ~ 5 and 20 μm. This effect has been previously observed and has been ascribed to interactions between the polariton condensate and the exciton reservoir[38,39].

Investigating cavity homogeneity. To explore the origin of the structure in the LPB dispersion above threshold, we used a spatial mapping technique to measure the PL emission from the LPB as a function of position for both the 1-pair hybrid cavity and the DBR–DBR control. Here, the sample was mounted on a motorised (x, y) stage that was incorporated into the k-space imaging setup, with sub-threshold emission mapped over an area of (26×26) μm^2 in step-sizes of 1 μm using a laser focused to a diameter of around 4 μm. From the PL spectra recorded, the peak emission energy at $k = 0$ at each position was then determined across the cavity surface. We also calculated the range of peak emission energies across the cavity and their standard deviation (SD). To gauge the significance of our results, we also attempted to characterise the spectral resolution of the mapping system. Here, light from a Ne/Ar lamp was directed into the spectrometer with its entrance slit set to 20 μm, and it was found that the emission line at 585 nm had an apparent linewidth (FWHM) of 0.68 meV (see Figure S6). Note, however, this measurement should only be viewed as an approximation of the true system resolution, as the k-space mapping setup required the entrance slit of the spectrometer to be fully-open in order to characterise the emission dispersion.

We first explored the emission from the DBR–DBR control cavity. A typical (25×25) μm^2 image is shown in Fig. 6a, with a second PL map shown in Figure S6 in the "Supplementary Information". From Fig. 6a it can be seen that there is a gradual transition in LPB energy across the image, indicating that there is a slight 'wedge' in the cavity optical path-length. This effect possibly results from a gradual variation in the thickness of the BODIPY-Br active layer. From an analysis of the two images collected, it was determined that the peak energy of the LPB is distributed over an energy range of around 1.3 meV with a standard deviation of 0.29 meV. For completeness, Figure S6 also plots example spectra collected at two points, approximately corresponding to the extremes of LPB energy. Here, each peak has a linewidth of 4 meV, with the peaks differing in the peak emission energy by ~ 1 meV, with this difference being greater than the spectral resolution of our spectrometer.

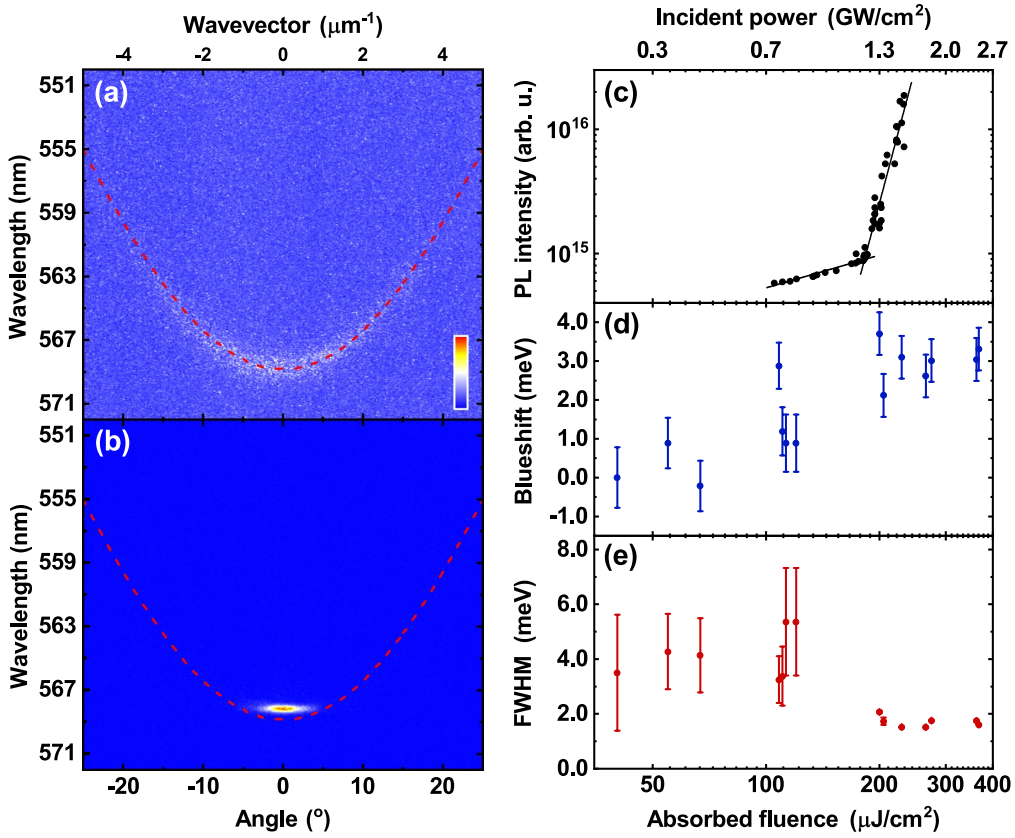

Figure 5. DBR–DBR control cavity condensation results. Normalised dispersions taken (**a**) below threshold and (**b**) above threshold. In both cases the red dashed line is a fit to the LPB in the linear regime. (**c**–**e**) Show the dependence of (**c**) PL intensity, (**d**) blueshift, and (**e**) full-width at half-maximum (FWHM) of the LPB on the absorbed pump fluence. From straight line fits to the power-dependent PL intensity in (**c**) (black solid lines), we determine a condensation threshold for this cavity of 180 μJ/cm^2. Here we see a non-linear increase in PL intensity, a spectral blueshift, and a decrease in the FWHM of the LPB. The error bars in (**d**) and (**e**) were calculated from the error on a Gaussian fit to the LPB at each fluence.

Using the same technique, we attempted to characterise the 1-pair hybrid cavity. Here, the cavity that was used had a slightly lower *Q*-factor than the cavity discussed in "Optical properties of microcavities fabricated using hybrid-DBR mirrors" as a result of a reduced number (8) of DBR pairs in the top mirror. In this case, due to the relatively broad LPB linewidth (10 meV at $k = 0$) we were unable to resolve statistically significant differences in LPB energy across the cavity surface.

Therefore, to further characterise cavity homogeneity, cross-sectional SEM images were recorded, with AFM and profilometry maps also made to explore the structure of the different cavity mirrors. Figure 6b,c show SEM images of the 4-pair hybrid and 10-pair DBR mirrors, respectively. Significantly, we find evidence for voids between the Ag and SiO_2 layer in the hybrid mirror structure having a lateral length-scale of a few 100 nm, with resultant disorder apparently propagating into the DBR layers. In contrast, no such voids are evident in the DBR–DBR control, with the individual mirror layers having a high degree of uniformity. We speculate that such voids in the hybrid mirror cavity are highly likely to result in local fluctuations in effective cavity length. We have also used AFM to image the various layers that constitute the hybrid mirror and the DBR control and have used this to extract the root mean square roughness (see Table 1 and images in Figure S7). Here, we find that both the Ag and SiO_2 layers are individually very smooth; however, we detect enhanced roughness from both an Ag/SiO_2 bilayer and the 1-pair hybrid mirror. Such layers are in fact rougher than the 10-pair DBR fabricated by Helia Photonics Ltd. We suspect the enhanced roughness of the 1-pair hybrid mirror results from poor adhesion between the Ag and SiO_2 layers and results in the voids observed in Fig. 6b. These results are further supported by surface profilometry measurements, which we discuss in Sect. 6 of the "Supplementary Information".

Discussion

We have observed polariton condensation in a hybrid mirror cavity and in the DBR–DBR control at an absorbed fluence threshold of 295 μJ/cm^2 and 180 μJ/cm^2, respectively. It appears that the ratio of condensation thresholds scales inversely with cavity *Q*-factor, with the DBR–DBR cavity undergoing condensation at a threshold that is 1.6 times lower than that of the hybrid mirror cavity and possessing a cavity *Q*-factor that is 1.7 times

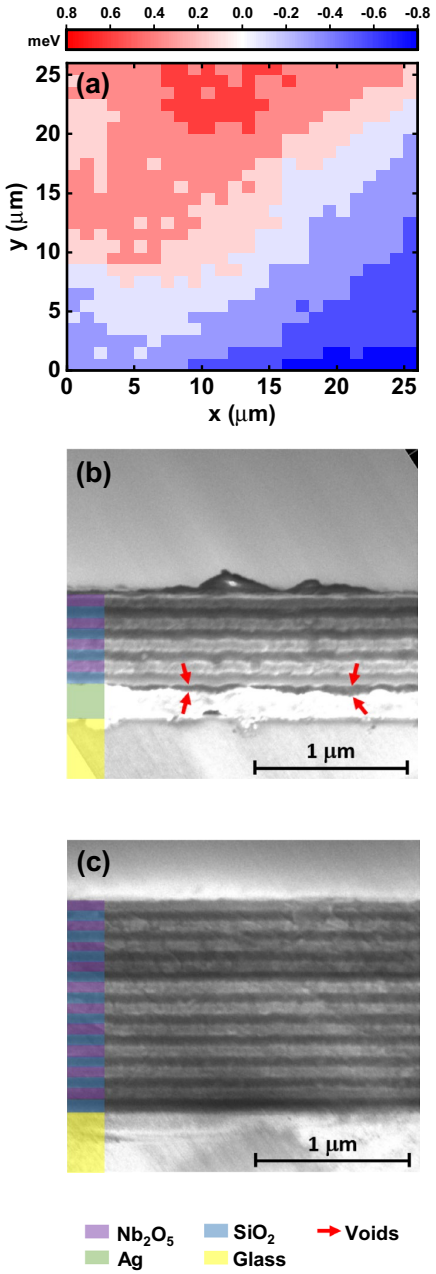

Figure 6. (**a**) Shows a sub-threshold polariton emission map of the variation in LPB emission energy from the DBR–DBR cavity from which condensation was observed. The colour scale corresponds to the variation of the LPB energy (in units of meV) around its average emission energy. (**b**,**c**) Show SEM images of the 4-pair hybrid and 10-pair DBR mirrors respectively. In (**b**), voids can be seen between the Ag and first SiO_2 layer.

greater (1190 and 710, respectively). We note that the condensation threshold of 180 μJ/cm^2 in the DBR–DBR control observed here is slightly lower than that observed in previous studies on a similar microcavity containing BODIPY-Br which was determined as 530 μJ/cm^2[18]. We suspect such differences may result from the shorter pump-laser pulse-lengths used here (150 fs compared to 2 ps pulses used in previous experiments), with reductions in lasing threshold being previously observed in weakly-coupled organic microcavities excited using shorter pump-pulses[40].

We now discuss polariton relaxation processes in the two types of cavities explored. It is clear that the mapping experiments described in "Investigating cavity homogeneity" evidence a slowly changing energy landscape in the DBR–DBR cavity, with the lateral size of the polariton condensate being either similar to, or smaller than

Structure	Ag	SiO_2	Ag + SiO_2	1-pair hybrid	10-pair DBR
RMS roughness (nm)	1.27	1.08	2.53	3.60	2.70
Schematic	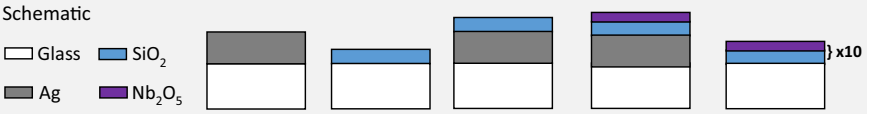				

Table 1. Root mean square (RMS) roughness of the different structures investigated, with a schematic of the structure shown beneath. These values were obtained by averaging multiple AFM maps.

the length-scales over which the cavity path-length fluctuates. Specifically, we find that the energy of the LPB changes by around 0.6 meV over distances of around 10–20 μm (the typical condensate size). This level of disorder is smaller than the linewidth of the condensate emission (1.6 meV at $k = 0$), and thus the 'energetically flat' landscape of this cavity allows complete relaxation to the ground polariton state.

In the hybrid mirror cavity, however, we find that condensate emission does not undergo complete collapse to $k = 0$, but is finely structured and distributed over a wider range of k-vectors. In these cavities, SEM images evidence spatial disorder at the interface between the DBR and the silver mirror having a lateral length-scale of a few 100 nm, with this disorder propagating through the DBR. At present, the relatively large linewidth (10 meV) of the LPB below the condensation threshold (which is mainly broadened by exciton–photon mixing) effectively masks energetic disorder within the cavity. Once the condensation threshold is reached, however, the narrowed condensate emission linewidth now allows energetic disorder within the cavity to be evidenced through the fine-structure that emerges in the emission dispersion curve (see Fig. 4b). This structure indicates that the 'fragmented' condensates that are formed exist in a relatively disordered landscape resulting from local variations in the cavity path-length, with the condensate linewidth (2.8 meV at $k = 0$) being almost a factor of two greater than that observed in the DBR–DBR control cavity. We note that similar structure in k-space emission has previously been observed in GaN and MeLPPP microcavities and has also been attributed to thickness variations in the active layers[41,42].

We suspect that the increased structural disorder in the hybrid mirror cavity results from poor adhesion between the Ag and SiO_2 layers, which results in a series of voids at this interface. We have made preliminary attempts to reduce this issue; for example, we have determined that the surface roughness of an Ag/SiO_2 bilayer is not dependent on the deposition rate of SiO_2 (see Sect. 5 of the "Supplementary Information"). It is possible that other techniques could be used to improve the quality of the interface between these layers—for example, using adhesion promoters or thermal annealing during deposition to encourage the SiO_2 to better adhere to the Ag film. Conversely, it may be possible to construct 'upside-down' hybrid mirror cavities, with the Ag layer deposited onto the final top surface of the cavity. This approach might result in an improved interface between the SiO_2 and Ag layers; however, such cavities would likely require optical measurements to be made through the bottom glass substrate. While this would not be an issue for linear optical spectroscopy, such a geometry is not well suited to transient measurements due to multiple internal reflections within the thick glass substrate.

Summary

We have developed a strategy to realise high-reflectivity 'hybrid' mirrors based on a silver film coated with a series of quarter-wave DBR pairs. This approach allows very high-reflectivity mirrors to be realised that are considerably simpler to fabricate than a regular dielectric mirror. Such mirrors are also anticipated to have enhanced thermal conductivity compared to a regular DBR and thus may dissipate heat more effectively when they are pumped with high energy lasers. We use such mirrors to fabricate a series of strongly-coupled organic semiconductor microcavities and show that by using a silver film coated with 4, 5 or 6 DBR mirror pairs, we create a structure having both a higher Q-factor and a larger Rabi splitting than could be realised using a conventional cavity based on two regular 9- and 10-pair dielectric mirrors. We use this approach to fabricate a strongly-coupled cavity in which the bottom hybrid mirror consists of a layer of silver coated by a single DBR pair, and show that this structure is able to demonstrate polariton condensation with a slightly increased threshold compared to a conventional DBR–DBR control cavity. Interestingly, however, we evidence a partial break-up of the k-space emission above threshold in the hybrid mirror cavity that we conclude occurs from spatial disorder at the interface between the single DBR pair and the silver film which propagates through the structure. In contrast, very little disorder is evidenced in the DBR–DBR based cavity, a result confirmed by mapping the LPB emission energy across the cavity surface. Despite such disorder effects, we believe that the approach demonstrated here allows a simplified route to construct high-performance mirrors for organic polariton lasers.

Methods

Sample preparation. BODIPY-Br was dissolved at 10% by mass in a solution of 35 mg/mL PS (Sigma-Aldrich, molecular weight ~ 192,000) in toluene and spin-coated onto a quartz-coated glass substrate. A Bruker DektakXT profilometer was used to measure the thickness of the films. To fabricate the hybrid mirrors, a silver film was first evaporated onto a quartz-coated glass substrate using an Ångstrom Engineering thermal evaporator. The DBR mirror pairs were fabricated using an Ångstrom Engineering electron beam to evaporate alternating λ/4 layers of SiO_2 and Nb_2O_5. The hybrid cavities had 1, 3, 4, 5, 6 or 10 pairs on top of a 200 nm thick Ag

layer. The 10-pair bottom DBR in the DBR–DBR cavity used in the condensation measurements was fabricated by Helia Photonics Ltd.

Transfer matrix reflectivity modelling. To model the Rabi splittings and linewidths, a multiple-peak Voigt profile was fit to the BODIPY-Br extinction coefficient (calculated from the UV–Vis absorption data) to describe the exciton. The Voigt function was chosen as it was found that using a simple Lorentz function was not sufficient to properly model the Rabi splittings and LPB linewidths of the cavities. The background refractive index of the BODIPY-Br/PS film was assumed to be similar to that of the polystyrene. The refractive indices for polystyrene and Ag were obtained from Refs.[43,44], respectively through the Refractiveindex.info database.

Basic optical characterisation. UV–Vis absorption measurements on BODIPY-Br films were carried out using a Horiba Fluoromax 4 fluorometer using a xenon lamp. Angle-dependent reflectivity measurements used a motorised goniometer to scan from 10° to 70° in 1° increments. An Ocean Optics Deuterium-Tungsten lamp (DH-2000-BAL) and an Andor Shamrock SR-303i-A CCD spectrometer were coupled by an optic fibre to the excitation and collection arms of the goniometer, respectively. In order to collect data on the LPB linewidths, *k*-space images were taken by focusing a pulsed, frequency-doubled Ti:sapphire (Coherent MIRA 900) laser at 445 nm onto the cavity at normal incidence using an Edmund Optics 20×HR infinity corrected objective (numerical aperture = 0.6). A beamsplitter and lens were used to direct and focus the reflected light onto the CCD of the same Andor Shamrock spectrometer. This same setup was used for the PL mapping measurements with a 445 nm continuous wave ThorLabs diode laser used to excite the cavities. For these measurements, the sample was positioned on an (*x*, *y*) motorised stage which was used to move the sample in a raster pattern.

Condensation measurements. A Ti:Sapphire laser (Coherent LibraHE) with ~ 150 fs pulses was tuned to the first Bragg minimum of each cavity (467 and 462 nm for the hybrid and DBR cavities, respectively) using an OPerA Solo optical parametric amplifier. This pump beam was focused onto the sample by a Mitutoyo Plan Apo 20× microscope objective (numerical aperture = 0.42) to produce a pump spot of FWHM diameter ~ 30 μm. The emission from the cavities was collected in reflection configuration by the same objective. To block the residual reflected light from the excitation beam a Semrock long-pass filter BLP01-473R-25 was placed in the collection path. The filtered photoluminescence was then coupled into a 750 mm focal length spectrometer (Princeton Instruments SP2750) equipped with an electron-multiplying CCD camera (Princeton Instruments ProEM-HS 1024×1024). A 300 grooves mm^{-1} grating and a 20 μm entrance slit were used to achieve a spectral resolution of 150 pm.

AFM, SEM and profilometry measurements. AFM measurements were performed in tapping mode in air using a Dimension 3100 (Veeco) scanning probe microscope equipped with a nanoscope 3A feedback controller. The AFM tips were silicon Scout 350 RAI (NuNano) probes with a spring constant of 42 N/m and resonance frequency of 350 kHz. Data was levelled by mean plane subtraction using Gwyddion 2.55 software and roughness values were extracted using the Gwyddion statistical quantities tool. Scans were in most cases (10×10) μm^2, but some were (2×2) μm^2 or (1×1) μm^2. The size of the scan did not seem to have an effect on the RMS roughness values determined. SEM images were taken using an FEI NovaNano SEM operating at a beam energy of 1.5 kV at a working distance of 4–5 mm, with an in-lens detector used to collect backscattered electrons. Samples for cross-sectional imaging were first scribed using a diamond stylus and then snapped. For the profilometry measurements, the same Bruker DektakXT profilometer as described above was used to make (100×100) μm^2 surface maps.

Received: 15 July 2021; Accepted: 30 September 2021
Published online: 22 October 2021

References

1. Plumhof, J. D., Stöferle, T., Mai, L., Scherf, U. & Mahrt, R. F. Room-temperature Bose–Einstein condensation of cavity exciton–polaritons in a polymer. *Nat. Mater.* **13**, 247–252 (2014).
2. Snoke, D. & Littlewood, P. Polariton condensates. *Phys. Today* **63**, 42–47 (2010).
3. Keeling, J. & Berloff, N. G. Exciton–polaritons condensation. *Contemp. Phys.* **52**, 131–151 (2011).
4. Byrnes, T., Kim, N. Y. & Yamamoto, Y. Exciton–polaritons condensates. *Nat. Phys.* **10**, 803–813 (2014).
5. Deng, H., Weihs, G., Snoke, D., Bloch, J. & Yamamoto, Y. Polariton lasing vs. photon lasing in a semiconductor microcavity. *Proc. Natl. Acad. Sci.* **100**, 15318–15323 (2003).
6. Kasprzak, J. *et al.* Bose–Einstein condensation of exciton polaritons. *Nature* **443**, 409–414 (2006).
7. Wertz, E. *et al.* Spontaneous formation of a polariton condensate in a planar GaAs microcavity. *Appl. Phys. Lett.* **95**, 051108 (2009)
8. Kéna-Cohen, S. & Forrest, S. R. Room-temperature polariton lasing in an organic single-crystal microcavity. *Nat. Photon.* **4**, 371–375 (2010).
9. Daskalakis, K. S., Maier, S. A., Murray, R. & Kéna-Cohen, S. Nonlinear interactions in an organic polariton condensate. *Nat. Mater.* **13**, 271–278 (2014).
10. Georgiou, K. *et al.* Generation of anti-stokes fluorescence in a strongly coupled organic semiconductor microcavity. *ACS Photon.* **5**, 4343–4351 (2018).
11. Zasedatelev, A. V. *et al.* A room-temperature organic polariton transistor. *Nat. Photon.* **13**, 378–383 (2019).
12. Yagafarov, T. *et al.* Mechanisms of blueshifts in organic polariton condensates. *Commun. Phys.* **3**, 1–10 (2020).
13. Sanvitto, D. & Kéna-Cohen, S. The road towards polaritonic devices. *Nat. Mater.* **15**, 1061–1073 (2016).

14. Ren, J. *et al.* Efficient Bosonic Condensation of Exciton Polaritons in an H-Aggregate Organic Single-Crystal Microcavity. *Nano Lett.* **20**, 7550–7557 (2020).
15. Wei, M. *et al.* Low-threshold polariton lasing in a highly disordered conjugated polymer. *Optica* **6**, 1124 (2019).
16. Scafirimuto, F., Urbonas, D., Scherf, U., Mahrt, R. F. & Stöferle, T. Room-temperature exciton–polariton condensation in a tunable zero-dimensional microcavity. *ACS Photon.* **5**, 85-89 (2018).
17. Lerario, G. *et al.* Room-temperature superfluidity in a polariton condensate. *Nat. Phys.* **13**, 837–841 (2017).
18. Cookson, T. *et al.* A yellow polariton condensate in a dye filled microcavity. *Adv. Opt. Mater.* **5**, 1700203 (2017).
19. Sannikov, D. *et al.* Room temperature broadband polariton lasing from a dye-filled microcavity. *Adv. Opt. Mater.* **7**, 1–5 (2019).
20. Sabatini, R. P. *et al.* Organic polariton lasing with molecularly isolated perylene diimides. *Appl. Phys. Lett.* **117**, 041103 (2020).
21. Kavokin, A., Baumberg, J. J., Malpuech, G. & Laussy, F. P. *Microcavities. Contemporary Physics* (Oxford University Press, 2007).
22. Hobson, P. A. *et al.* Strong exciton–photon coupling in a low-Q all-metal mirror microcavity. *Appl. Phys. Lett.* **81**, 3519–3521 (2002).
23. Schwartz, T. *et al.* Polariton dynamics under strong light-molecule coupling. *ChemPhysChem* **14**, 125–131 (2013).
24. Kéna-Cohen, S., Maier, S. A. & Bradley, D. D. C. Ultrastrongly coupled exciton–polaritons in metal-clad organic semiconductor microcavities. *Adv. Opt. Mater.* **1**, 827–833 (2013).
25. Liu, B., Rai, P., Grezmak, J., Twieg, R. J. & Singer, K. D. Coupling of exciton–polaritons in low-Q coupled microcavities beyond the rotating wave approximation. *Phys. Rev. B Condens. Matter Mater. Phys.* **92**, 155301 (2015).
26. Obara, Y., Saitoh, K., Oda, M. & Tani, T. Room-temperature fluorescence lifetime of pseudoisocyanine (PIC) J excitons with various aggregate morphologies in relation to microcavity polariton formation. *Int. J. Mol. Sci.* **13**, 5851–5865 (2012).
27. Coles, D. M., Grant, R. T., Lidzey, D. G., Clark, C. & Lagoudakis, P. G. Imaging the polariton relaxation bottleneck in strongly coupled organic semiconductor microcavities. *Phys. Rev. B Condens. Matter Mater. Phys.* **88**, 121303 (2013).
28. Sabatini, R. P. *et al.* Molecularly isolated perylene diimides enable both strong exciton–photon coupling and high photoluminescence quantum yield. *J. Mater. Chem. C* **7**, 2954–2960 (2019).
29. Coles, D. M. *et al.* Strong exciton–photon coupling in a nanographene filled microcavity. *Nano Lett.* **17**, 5521–5525 (2017).
30. Connolly, L. G. *et al.* Strong coupling in high-finesse organic semiconductor microcavities. *Appl. Phys. Lett.* **83**, 5377–5379 (2003).
31. Virgili, T. *et al.* Ultrafast polariton relaxation dynamics in an organic semiconductor microcavity. *Phys. Rev. B Condens. Matter Mater. Phys.* **83**, 245309 (2011).
32. Kulakovskii, V. D. *et al.* Bose–Einstein condensation of exciton polaritons in high-Q planar microcavities with GaAs quantum wells. *JETP Lett.* **92**, 595–599 (2010).
33. Tsotsis, P. *et al.* Lasing threshold doubling at the crossover from strong to weak coupling regime in GaAs microcavity. *New J. Phys.* **14**, 023060 (2012).
34. Putintsev, A. *et al.* Nano-second exciton–polaritons lasing in organic microcavities. *Appl. Phys. Lett.* **117**, 123302 (2020).
35. Jayaprakash, R. *et al.* Two-dimensional organic-exciton polariton lattice fabricated using laser patterning. *ACS Photon.* **7**, 2273–2281 (2020).
36. Wang, S. C. *et al.* Optically pumped GaN-based vertical cavity surface emitting lasers: Technology and characteristics. *Japan. J. Appl. Phys. Part 1 Regul. Pap. Short Notes Rev. Pap.* **46**, 5397–5407 (2007).
37. Betzold, S. *et al.* Coherence and interaction in confined room-temperature polariton condensates with frenkel excitons. *ACS Photon.* **7**, 384–392 (2020).
38. Daskalakis, K. S., Maier, S. A. & Kéna-Cohen, S. Spatial coherence and stability in a disordered organic polariton condensate. *Phys. Rev. Lett.* **115**, 1–5 (2015).
39. Bobrovska, N., Matuszewski, M., Daskalakis, K. S., Maier, S. A. & Kéna-Cohen, S. Dynamical instability of a nonequilibrium exciton–polaritons condensate. *ACS Photon.* **5**, 111–118 (2018).
40. Akselrod, G. M. *et al.* Reduced lasing threshold from organic dye microcavities. *Phys. Rev. B* **90**, 035209 (2014).
41. Jayaprakash, R. *et al.* Ultra-low threshold polariton lasing at room temperature in a GaN membrane microcavity with a zero-dimensional trap. *Sci. Rep.* **7**, 1–9 (2017).
42. Scafirimuto, F. *et al.* Tunable exciton–polariton condensation in a two-dimensional Lieb lattice at room temperature. *Commun. Phys.* **4**, 39 (2021).
43. Sultanova, N. G., Kasarova, S. N. & Nikolov, I. D. Characterization of optical properties of optical polymers. *Opt. Quantum Electron.* **45**, 221–232 (2013).
44. P. B. Johnson & R. W. Christy. Optical constant of the nobel metals. *Phys. Rev. B* **6**, 4370 (1972).

Acknowledgements
We thank the U.K. EPSRC for funding this research via the 'Hybrid Polaritonics' Programme Grant (EP/M025330/1). K.E.M. thanks the EPSRC for a DTA PhD scholarship.

Author contributions
K.E.M. fabricated all microcavities and performed the linear spectroscopy and mapping experiments and TMR modelling. A.P. performed the polariton condensation measurements. R.J. built the PL mapping setup and conceived the idea for the hybrid mirror. R.J. and K.G. helped perform linear spectroscopy measurements and TMR modelling. M.E.O. performed scanning electron microscopy measurements, R.C.K. and K.E.M. performed AFM measurements and E.J.C. recorded the surface profilometry maps. M.C. synthesised the BODIPY-Br. D.S. assisted through the development of the condensation experiment setup. P.G.L and D.G.L co-supervised the research. All authors contributed to the preparation of the manuscript. The data used in this publication can be obtained by request from D.G.L.

Competing interests
The authors declare no competing interests.

Additional information
Supplementary Information The online version contains supplementary material available at https://doi.org/10.1038/s41598-021-00203-y.

Correspondence and requests for materials should be addressed to D.G.L.

Reprints and permissions information is available at www.nature.com/reprints.

4.3 Author contributions

K.E.M. fabricated all microcavities and performed the linear spectroscopy and mapping experiments and TMR modelling. A.P. performed the polariton condensation measurements. R.J. built the PL mapping setup and conceived the idea for the hybrid mirror. R.J. and K.G. helped perform linear spectroscopy measurements and TMR modelling. M.E.O. performed scanning electron microscopy measurements, R.C.K. and K.E.M. performed AFM measurements and E.J.C. recorded the surface profilometry maps. M.C. synthesised the BODIPY-Br. D.S. assisted through the development of the condensation experiment setup. P.G.L. and D.G.L. co-supervised the research. All authors contributed to the preparation of the manuscript. The data used in this publication can be obtained by request from D.G.L.

5 Polariton condensation in a microcavity using a highly-stable molecular dye

5.1 Motivation for project

Before I started on this project, polariton condensation had only been seen in a handful of organic molecules. One strategy for such cavities is to disperse the dyes in a transparent polymer matrix, as has been done with BODIPY derivatives. This method of fabrication has advantages over pure dye films in that it is easy to control the concentration - which allows easy tuning of the exciton-photon coupling strength and the photoluminescence quantum yield - and there is more control over thickness. However, the BODIPY derivatives have notoriously low photostability when it comes to non-linear behaviour and require complicated single-shot techniques and vacuums if polariton condensation is to be observed.

Here, I investigated a laser dye known as DPAVB that has a seemingly broad absorption linewidth. Despite this, I demonstrated that at high concentration in a double-DBR cavity it is able to exhibit strong coupling and polariton condensation. Notably, it was able to remain in the condensation regime for more than 37,000 pulses when excited by sub-ns pulses in air. This demonstrates remarkable photostability compared to the BODIPY derivatives and therefore is a very promising material for studies that rely on a certain degree of stability, such as interacting polariton condensates, polariton lattices and other non-linear polaritonic devices.

5.2 Publication

This section contains the publication as it appears online in *Journal of Materials Chemistry C*:

McGhee, *et al.* Polariton condensation in a microcavity using a highly-stable molecular dye. *Journal of Materials Chemistry C* **10**, 4187 (2022).

The Supplementary Information for this publication can be found in Appendix B.

Journal of Materials Chemistry C

ROYAL SOCIETY OF CHEMISTRY

PAPER

Cite this: J. Mater. Chem. C, 2022, 10, 4187

Polariton condensation in a microcavity using a highly-stable molecular dye†

Kirsty E. McGhee, [a] Rahul Jayaprakash, [a] Kyriacos Georgiou, [ab] Stephanie L. Burg [a] and David G. Lidzey *[a]

Received 17th November 2021, Accepted 20th February 2022

DOI: 10.1039/d1tc05554b

rsc.li/materials-c

We have fabricated dielectric microcavities containing the molecular dye 1,4-bis[2-[4-[*N*,*N*-di(*p*-tolyl) amino]phenyl]vinyl]benzene (DPAVB) dispersed in a transparent polymer matrix. We show that despite the relatively broad absorption linewidth of the DPAVB, the cavities enter the strong coupling regime. We use <330 ps pulses at 355 nm from a Nd:YAG laser to generate amplified spontaneous emission from control films and polariton condensation from the strongly-coupled microcavity in air and at room temperature. Here, polariton condensation is observed at an excitation threshold of 215 μJ cm^{-2}. Significantly, we show that the DPAVB dye has a very high degree of photostability, with polariton condensation still observed from the cavity after 37 000 excitation pulses, showing promise for its use in practical polaritonic devices.

1. Introduction

Organic exciton-polaritons are of great interest due to their ability to undergo room temperature polariton lasing.[1] Exciton-polaritons arise from the strong coupling between Frenkel excitons (bound electron–hole pairs) and a confined photon mode within an optical cavity. Such quasiparticles are a mixture of light and matter, and for convenience are referred to as cavity-polaritons or simply polaritons. Unlike polaritons in most inorganic based microcavities (which mainly exist at cryogenic temperatures due to their low exciton binding energies), organic polaritons exist at room temperature due to the high binding energy of Frenkel excitons (100's of meV). Such a high degree of thermal stability makes organic polaritons of significant interest for practical room temperature applications.[2]

Polaritons can be described using Bose-Einstein statistics and – at high occupation density – can undergo condensation. Such polariton condensates are usually formed at the bottom of the lower polariton branch, which acts as an energetic trap in momentum space. This results from a stimulated scattering process by which uncoupled excitons located in a reservoir populate the ground polariton state. The condensates formed can have macroscopic dimensions (10's of microns diameter) and have long-range spatial and temporal coherence (100's of ps).[3,4] Such condensates are non-equilibrium in nature as they undergo spontaneous emission as their photonic component escapes the cavity.[1,5] The emitted photons have the same energy and phase, with such emission considered a form of lasing (often referred to as polariton lasing).[5,6] Significantly, this lasing process does not require the formation of a population inversion and thus it can occur at a lower excitation threshold than conventional photon lasing. Polariton condensates are of interest as new types of high-efficiency light sources and as 'polariton simulators'; here, complex problems can be mapped onto the pseudo-spins of a lattice of interacting condensates, with the ground state of the lattice corresponding to the solution of the Hamiltonian of interest.[7–9]

A number of different molecular materials have been shown to undergo polariton condensation in suitably-designed structures. These include the conjugated polymers MeLPPP[10] and PFO;[4] the molecular dyes BODIPY-Br,[11] BODIPY-G1,[12] and TDAF;[13] the fluorescent proteins eGFP[14] and m-Cherry;[15] and PDI-O microcrystals.[16] For a recent review on polariton condensation in organic microcavities, see ref. 17. For practical applications, it is desirable that such molecules have a high degree of photostability. The BODIPY family of molecular dyes that we have previously studied have relatively low stability, a feature that required a single-pulse imaging technique for lasing studies.[11,12,18]

In this paper, we demonstrate polariton condensation in a cavity containing an organic laser dye with a much higher degree of photostability. We confirm this enhanced stability by performing measurements in both the linear and non-linear regimes and demonstrate that the cavity can exhibit non-linear emission over more than 37 000 excitation pulses. We believe that such a material will be of interest for studies that wish to explore the interactions between organic exciton-polariton condensates.

[a] Department of Physics and Astronomy, University of Sheffield, Hicks Building, Hounsfield Road, Sheffield, S3 7RH, UK. E-mail: d.g.lidzey@sheffield.ac.uk
[b] Department of Physics, University of Cyprus, P.O. Box 20537, Nicosia 1678, Cyprus

† Electronic supplementary information (ESI) available. See DOI: 10.1039/d1tc05554b

2. Results and discussion

We have used the fluorescent dye 1,4-bis[2-[4-[*N*,*N*-di(*p*-tolyl)amino]phenyl]vinyl]benzene (DPAVB) as the active material in our microcavities. The molecular structure of DPAVB is shown in Fig. 1(a). This styrylbenzene derivative has been investigated as a laser dye,[19,20] as a dopant for other laser dyes,[21] and as a dopant for sky-blue organic light emitting diodes (OLEDs).[22–24] It has a high optical gain (19.8 cm^{-1} for a 2% DPAVB/polystyrene film[25]) and a low lasing threshold of 2.3 μJ cm^{-2} in a distributed feedback structure.[19] Such low thresholds have been previously attributed to the symmetrical structure of the dye, which results in reduced intermolecular interactions.[20] Used as a dopant, DPAVB (at 4% weight) has also been shown to reduce the threshold of distributed feedback lasers based on the conjugated polymer BN-PFO from 3 μJ cm^{-2} to 0.75 μJ cm^{-2} using an ultraviolet diode laser with a pulse width of 50 ns.[21,26] However, it was also found that a build-up of long-lived triplet states on the DPAVB molecules resulted in a large increase in the lasing threshold when longer excitation pulses were used. This effect was not observed in undoped BN-PFO structures, which are able to undergo quasi-CW lasing.[27]

2.1 Characterisation of DPAVB films

To investigate the properties of DPAVB, we explored it when doped at a range of concentrations into a polystyrene (PS) matrix. Here, we focus our discussion on DPAVB/PS films where the DPAVB is present at high concentration (50% by mass). This is because to achieve strong coupling, it is necessary that the Rabi splitting energy, Ω, is greater than the absorption linewidth according to

$$\frac{\Omega}{2} > \sqrt{\frac{\gamma_c^2 + \gamma_x^2}{2}}, \quad (1)$$

where γ_c and γ_x are the cavity and exciton half-width at half maximum, respectively.[28] Additionally, the Rabi splitting in a planar microcavity is proportional to the number of absorbers, *N*, per unit length according to

$$\Omega \propto \sqrt{\frac{N}{L}}, \quad (2)$$

where *L* is the effective cavity length.[29] For this reason, high molecular number densities are required to reach the strong coupling regime when using materials with very broad absorption linewidths.

To prepare DPAVB/PS films, the materials were first dissolved in dichloromethane. This solution was then spin-coated onto a glass substrate to form a thin film, with the DPAVB molecules dispersed in the PS. Here, the role of the PS is to spatially separate the individual DPAVB molecules in order to supress aggregation and crystallisation. The PS also provides additional control over the thickness of the films (by varying its concentration in the solvent), allowing the fabrication of films several hundred nm thick. In this way, they can support waveguide modes for amplified spontaneous emission (ASE) and optical modes within a microcavity.

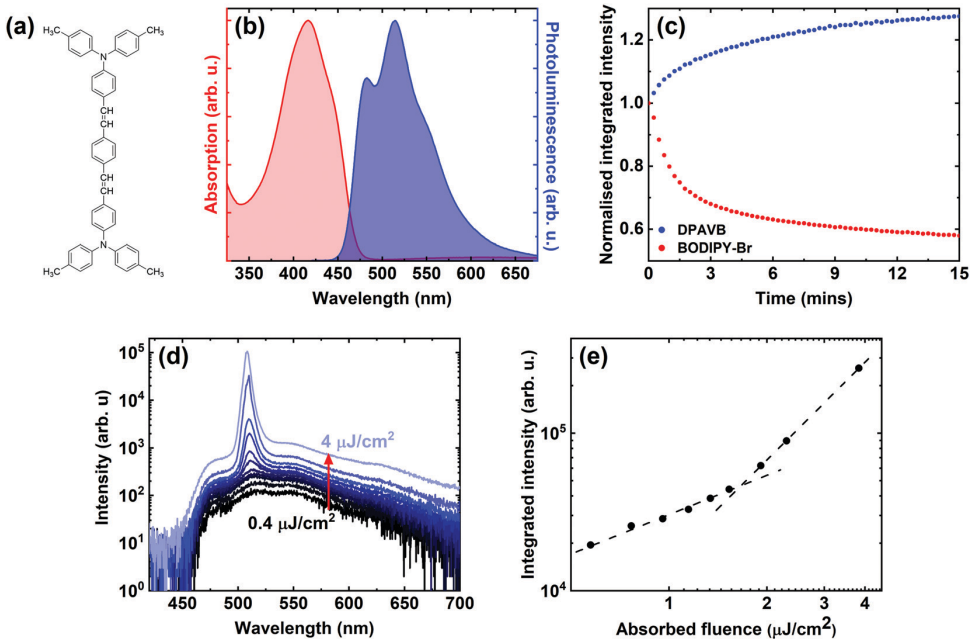

Fig. 1 Studies on 50% DPAVB/PS film. Part (a) shows the molecular structure of DPAVB, with part (b) showing the normalised absorption (red) and photoluminescence (blue) of a DPAVB/PS thin film. Part (c) shows the relative photoluminescence intensity over 15 minutes of a DPAVB (blue) and BODIPY-Br film (red), with both films absorbing an optical power of 34 μW at 405 nm. Part (d) shows the amplified spontaneous emission spectra (ASE) from DPAVB recorded at a range of pump powers. Part (e) shows the integrated emission intensity *versus* absorbed fluence. Here, we determine an ASE threshold of 1.7 μJ cm^{-2}.

The normalised absorption and photoluminescence of a DPAVB/PS film are shown in Fig. 1(b) where the DPAVB has a relative mass fraction of 50%. It can be seen that the absorption of the DPAVB peaks around 420 nm (2.95 eV) and has a total linewidth of 140 nm (0.5 eV). The DPAVB emission is characterised by a number of poorly-resolved peaks at 479 nm, 512 nm and 551 nm that we associate with the 0–0, 0–1 and 0–2 transitions (see peak fit in ESI† Fig. S1). We have found that the 50% DPAVB/PS films explored have a photoluminescence quantum yield between 5 and 10% dependent on measurement protocols.

We have explored the relative photostability of DPAVB. This measurement was benchmarked against a thin film of BODIPY-Br (10% by mass in PS). This molecule was chosen as it has been widely explored in both strong coupling and polariton lasing experiments.[8,11,30–32] In our measurements, 200 nm thick films of DPAVB/PS and BODIPY-Br/PS coated by a thin film of PVA were exposed to light from a 405 nm continuous wavelength diode laser in air, with the laser flux adjusted such that both films absorbed an optical power of 34 μW. Experiments were carried out over 15 minutes with the PL emission recorded every 15 seconds. This experiment was designed to explore the relative photostability of the two dyes when exposed in a linear excitation regime. The relative emission intensity of the two films are shown in Fig. 1(c). Here it can be seen that at the end of the 15 minutes, the emission from the DPAVB film has actually increased by nearly 30%, with the emission from the BODIPY-Br dropping by more than 40% over the same time period. The exact origin of the increase in the emission intensity from DPAVB is not understood; however, it is consistent with a relative decrease in the number of non-radiative decay channels open to exciton decay. This rise in intensity extends for around half an hour, at which point the emission intensity saturates, with no changes observed in spectral emission shape (see Fig. S2 of the ESI†). We suspect therefore that this effect results from an inactivation of molecules that have some type of structural defect associated with non-radiative emission. Indeed, our measurements indicate that this 'inactivation' of non-radiative defects appears to be essentially non-recoverable. Significantly, this result suggests that DPAVB is a highly-photostable material and should be of interest for polariton lasing applications.

To characterise the non-linear emission properties of DPAVB, we have measured its amplified spontaneous emission (ASE). Here, we focused a 355 nm pulsed (<330 ps) laser with a cylindrical lens into a stripe that was positioned close to the edge of a 200 nm thick DPAVB/PS film. Here, the stripe essentially acts as a waveguide, with the resultant emission from the edge of the sample collected by an optical fibre coupled to a spectrometer. Measurements were made as a function of laser fluence as shown in Fig. 1(d). Here it can be seen that a peak emerges at 508 nm having a linewidth of 4.4 nm (21 meV), indicating the action of ASE. This peak coincides with the 0–1 peak observed in the PL emission, indicating the action of a 4-level laser. Fig. 1(e) plots the integrated intensity under each spectrum on a log–log scale as a function of absorbed laser fluence, where the fluence is defined as the energy per pulse divided by the excitation area. Here, two straight-line fits have been used to identify the ASE threshold, which in this film is around 1.7 μJ cm^{-2}.

2.2 DPAVB cavity design, fabrication and linear characterisation

DPAVB cavities were designed using a transfer matrix reflectivity (TMR) model. The refractive index (n) and extinction coefficient (k) of DPAVB were first determined using spectroscopic ellipsometry. Here, a pure solution of DPAVB in dichloromethane was spin-coated onto a silicon wafer. Literature values (from ref. 33) for the optical properties of the silicon and its native oxide were used as included in the Woollam analysis software, which resulted in an excellent fit to the substrates based on a 1.8 nm thick layer of native oxide. Ellipsometry data for the DPAVB films was then fit with a transparent b-spline wavelength expansion to obtain the n and k values (see Fig. S1 in the ESI†). These values were used with known n and k values for PS (from ref. 34) to calculate the values for the 50% DPAVB/PS film. Three Lorentzian functions were fit to the DPAVB/PS k data and these were used in the TMR model to describe three transitions (see Fig. S1, ESI†).

To explore strong coupling using DPAVB, initial experiments focused on lower-finesse cavities that were designed to allow the observation of an anti-crossing between the polariton branches. Additionally, the exciton-photon detuning was chosen to ensure that resonance occurred at relatively low angles ($\sim 35^\circ$). Microcavities were fabricated by depositing a distributed Bragg reflector (DBR) made of alternating $\lambda/4$ thick layers of SiO_2 and TiO_2 onto a quartz-coated glass substrate using electron-beam evaporation. DPAVB/PS solutions at different relative DPAVB concentrations (10%, 20%, 30%, 40% and 50% by mass) were spin-coated onto the DBRs to form 265 nm thick films. A second DBR was then deposited on top of this using the electron beam.

To characterise the cavities, we performed angle-dependent white light reflectivity measurements. Fig. 2(a) shows reflectivity data for a cavity containing 50% DPAVB/PS with both DBRs consisting of 6 SiO_2/TiO_2 pairs. The data for the lower concentration cavities is shown in Fig. S3 in the ESI.† Here, we find that no Rabi splitting is evident in the cavity containing 10% DPAVB. As the DPAVB concentration is increased, a splitting begins to appear and the cavities enter the strong coupling regime around 30–40%. It can be seen that the cavity containing 50% DPAVB (see Fig. 2(a)) shows a distinct splitting between the lower (LPB) and upper (UPB) polariton branches. To quantify this, we have used a coupled oscillator model to determine the magnitude of the Rabi splitting. We again use three Lorentzians centred at 447 nm, 420 nm and 393 nm, which we henceforth label as T1, T2 and T3 (see the fit to the imaginary part of the refractive index determined from ellipsometry in Fig. S1, ESI†). The coupling of these transitions to the cavity mode is described using the following Hamiltonian

$$M(k) = \begin{bmatrix} E_c(k) - i\gamma_c & g_1 & g_2 & g_3 \\ g_1 & E_{T1}(k) - i\gamma_{T1} & 0 & 0 \\ g_2 & 0 & E_{T2}(k) - i\gamma_{T2} & 0 \\ g_3 & 0 & 0 & E_{T3}(k) - i\gamma_{T3} \end{bmatrix}. \quad (3)$$

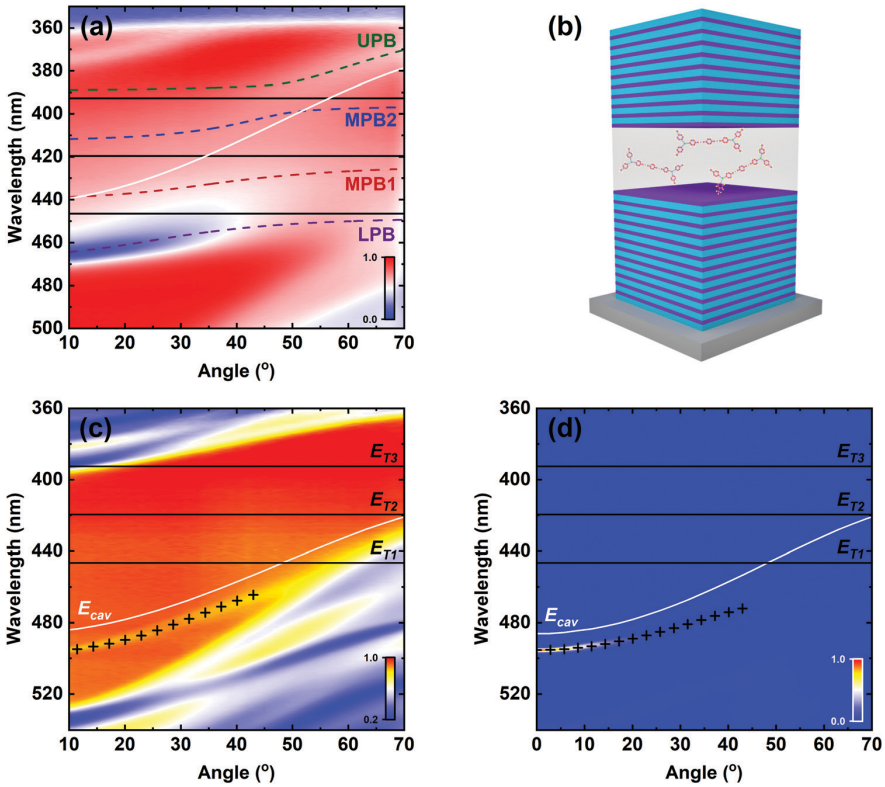

Fig. 2 Cavity design and linear characterisation. Part (a) shows the angle-dependent white light reflectivity data for a cavity constructed from two 6-pair DBRs and containing 50% DPAVB by mass in PS. The data is overlaid with fits from a coupled oscillator model, where the LPB (purple), MPB1 (red), MPB2 (blue) and UPB (green) are indicated by the dashed lines. From this we obtain Rabi splittings of Ω_1 = 168 meV, Ω_2 = 260 meV and Ω_3 = 227 meV between the cavity mode and the transitions at 447 nm, 420 nm and 393 nm, respectively. Part (b) illustrates the structure of cavities again containing 50% DPAVB by mass in PS, but instead with 10- and 12-pair DBR mirrors. Parts (c and d) show the angle-dependent white light reflectivity and photoluminescence, respectively, of one of these microcavities. We superimpose on the diagram the dispersion of the LPB as simulated using a TMR model (black crosses), with excellent agreement observed between data and theory. For completeness, in (a, c and d) we also include the dispersions of the cavity mode (E_{cav}, white solid lines) and the peak positions of the Lorentzians used to describe the transitions (E_{Tn}, where n = 1–3, solid black lines).

Here E_c and E_{Tn} are the energies of the cavity mode and the three DPAVB transitions (n = 1–3), respectively. The model also includes γ_c and γ_{Tn} which are the linewidth (half-width at half maximum) of the cavity mode and each of the DPAVB transitions, respectively, with g_1, g_2 and g_3 being the coupling strength of each of the molecular transitions to the cavity mode and $g = \frac{\Omega}{2}$.

This model is then fit to the LPB and UPB dispersions as shown in Fig. 2(a). To do this, we used the relative height of each of the transitions from our Lorentzian fits and scaled their coupling strength according to these ratios. We find that the model describes the data very well, and we determine Rabi splittings of Ω_1 = 168 meV, Ω_2 = 260 meV and Ω_3 = 227 meV. Here, two middle polariton branches (MPB1 and MPB2) are predicted; however, these are not resolvable in the experimental data due to strong absorption by the DPAVB molecules at these wavelengths. Applying eqn (1) to the three transitions, we find that the Rabi splittings for T1 and T2 exceed the condition required for strong coupling. When we apply the same analysis to T3, we find that it does not meet the condition and is therefore weakly-coupled. The parameters used in these calculations are shown in Table S1 in the ESI.†

As the Q-factor of these cavities was relatively low ($\sim$400 according to TMR modelling), they were less suitable for condensation measurements and higher Q-factor structures were fabricated. Here, a 12-pair DBR was used for the bottom mirror with a 10-pair top DBR. To ensure the cavities operated in the strong coupling regime, 50% DPAVB/PS was used. Preliminary measurements (data not shown) indicated that to achieve polariton condensation, it was necessary to position the LPB around 495–500 nm (see discussion on scattering mechanisms in Section 2.3). A schematic of the microcavities constructed is shown in Fig. 2(b).

The angle-dependent white light reflectivity and PL emission from one of these higher Q-factor cavities are shown in Fig. 2(c and d), respectively. To generate PL, the cavity was excited non-resonantly using a CW laser at 405 nm, with a 450 nm long-pass filter used in the collection arm. In both PL and reflectivity measurements, we detect a dispersive branch located around normal incidence at 496 nm, which

(using results from a TMR model) we identify as the lower polariton branch. We note that the UPB is not visible in these cavities and indeed it is also not visible in our TMR model. We believe this is caused by a combination of large negative cavity detuning and the high reflectivity of the DBRs. We note that studies on strong coupling in inorganic microcavities based on GaN and ZnO similarly do not report the observation of an UPB[35–37] where it is masked by absorption from exciton continuum states. Other studies on organic polariton condensation in strongly-coupled microcavities also indicate that the upper polariton branch can be difficult to detect.[4,13,38] Nevertheless, despite the absence of an UPB, we have used a combination of TMR modelling together with a coupled oscillator model (fit shown together with discussion in Fig. S4 of the ESI†) to estimate Rabi splittings between the photon and the different excitonic transitions in this cavity of Ω_1 = 168 meV, Ω_2 = 260 meV and Ω_3 = 227 meV.

2.3 Polariton condensation

To generate polariton condensation, the 10-/12-pair DBR microcavity was pumped non-resonantly at normal incidence in a transmission configuration, with emission detected using a *k*-space imaging technique. The cavity was excited through the quartz substrate by a pulsed Nd:YAG laser at 355 nm focused into a 30 μm diameter spot. The pulse width and repetition frequency were <330 ps and 100 Hz, respectively. The microcavity emission was then collected through the top 10-pair DBR using a 10 mm objective (NA = 0.6) and focused into a CCD spectrometer with a spectral resolution of 0.39 meV (0.09 nm).

Fig. 3(a) shows a plot of the power-dependent PL intensity determined over a solid angle of ±1.56° around the bottom of the lower polariton branch (k = 0) for the cavity shown in Fig. 2(c and d). Fig. 3(b and c) show the blueshift of the LPB and its linewidth at full-width half maximum (FWHM), respectively, as a function of excitation power. Here, the blueshift and FWHM data were extracted from Lorentzian fits to the emission spectra recorded at k = 0. From this data, we identify a condensation threshold fluence (P_{th}) of 215 μJ cm^{-2}. This threshold is accompanied by a reduction in the emission linewidth from 1.5 meV to ~0.2 meV. We note that the condensation threshold is significantly higher than the ASE threshold (~130 times), which we attribute to the different excitation geometries, resonator structure and nature of the emitting state in the two measurements. The methods used to calculate the two thresholds are outlined in Section 3 of the ESI.† In Fig. 3(d and e), we show the normalised PL dispersion recorded at P = 0.5 P_{th} and P = 1.5 P_{th}, respectively. In (e), the collapse of all emission to the bottom of the LPB is clearly evident.

We now discuss the origin of the emission blueshift in more detail. This spectral blueshift occurs around threshold and then continues to increase (albeit at a slower rate) as the pump power is further increased, with the total blueshift observed

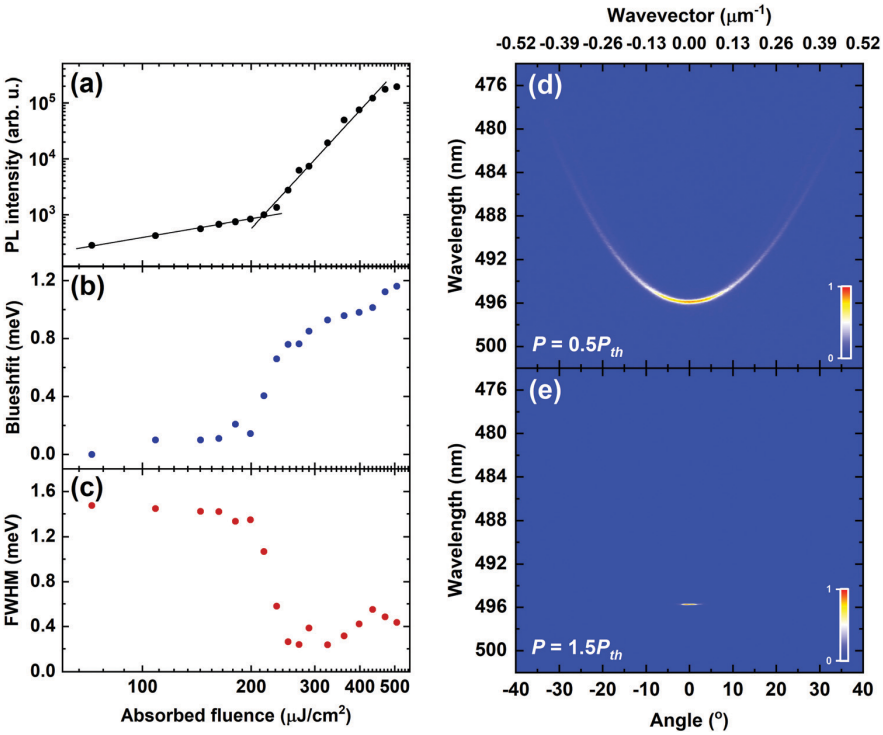

Fig. 3 Condensation data. Parts (a–c) plot the fluence dependence of (a) integrated PL intensity, (b) blueshift, and (c) full-width at half maximum (FWHM). By using two straight-line fits to the data shown in part (a) below and above threshold, we determine a threshold of 215 μJ cm^{-2}. Parts (d and e) show the *k*-space emission dispersion of the cavity at (d) P = 0.5 P_{th} and (e) P = 1.5 P_{th}.

being around 1.2 meV. We suspect that this is mostly attributable to a reversible photobleaching of the DPAVB molecular ground-state as the excitation is increased, resulting in a change in the effective refractive index of the active layer and a reduction in the Rabi splitting.[39] Indeed, we show (by recording cavity emission below, above and then below the condensation threshold) that a fully reversible blueshift of as much as 1.6 meV can occur following excitation at 1.7 P_{th} (see Fig. S5(a), ESI†). We believe, however, that some part of the maximum blueshift observed in Fig. 3(b) results from a degree of irreversible photodegradation of the sample caused by extended exposure to the excitation laser (see Fig. S5(b) and Section 4 of the ESI†). Indeed, photodegradation most likely explains the slow blueshift observed at the highest pump powers, with our findings highlighting the need to consider the effect of even limited amounts of photodegradation when interpreting spectral blueshifts.

The non-linear properties of our microcavity are consistent with previous reports on polariton condensation. Indeed, we note that the condensation threshold is similar to that observed in microcavities containing BODIPY-Br and BODIPY-G1 (also suspended in PS matrices)[11,12] and also the polymer MeLPPP.[10] Similarly, the reduction in linewidth ($\sim$7 times) is consistent with that observed in BODIPY containing cavities.

The condensate formed is created by a stimulated scattering mechanism that is determined by the occupation of the final state.[40] It has previously been shown that polariton condensates can be populated through vibron-mediated energy relaxation, with this process being efficient when the energy separation between a "hot-exciton" and the bottom of the LPB is equal to the energy of a molecular vibrational mode.[41,42] We have considered this mechanism as the origin of the stimulated scattering process in these cavities. To do this, we have performed Raman spectroscopy on a DPAVB solution, the results of which are shown in Fig. S6 of the ESI.† This identifies a strong Raman-active peak at 1593 cm^{-1}, corresponding to an energy shift of 198 meV. Interestingly, this energy corresponds to the difference in energy between the edge of the DPAVB absorption (around 460 nm) and the condensate energy, indicating that a fully-thermalised DPAVB exciton in the reservoir could scatter into the LPB following the emission of a vibrational quantum. Indeed, we note that polariton condensation was only observed in cavities whose LPB was positioned around 496 nm at k = 0. We do not, however, rule out a radiative pumping mechanism in which photon emission from weakly-coupled excitons in the DPAVB reservoir "pumps" the photon component of the lower branch polaritons. We have previously shown that this mechanism dominates the population of the LPB at low pumping densities in strongly-coupled microcavities containing BODIPY-Br.[30] Indeed, this process is expected to be highly efficient in the cavities studied here as states at the bottom of the LPB are highly photon-like ($\sim$90%) due to the relatively large cavity detuning used. We believe, therefore, that further studies are required to determine the relative importance of these two mechanisms in the observed stimulated scattering processes.

Finally, we have explored the stability of the condensate emission from our cavities. Here, the laser excitation power was adjusted to $P = 2\ P_{th}$ and PL spectra were recorded by integrating the cavity emission over 0.5 seconds. The excitation laser had a repetition frequency of 100 Hz, and thus each spectrum was generated using 50 pulses. The experiment was performed 755 times sequentially, with the cavity being exposed to a total of 37 750 pulses.

In Fig. 4(a), we plot the normalised integrated PL intensity against pulse number. From the data plotted in Fig. 3(a), we determine that the integrated PL intensity at $P = 2\ P_{th}$ is $\sim$150 times that at $P = P_{th}$, and thus we expect the cavity to remain in the non-linear emission regime until the emission intensity drops to a factor of $\sim$0.007 of its initial normalised value. It can be clearly seen in Fig. 4(a) that although there is a fast initial decay in the cavity emission (occurring over the first $\sim$4000 pulses), it then stabilises and remains at an intensity of $\sim$50% of its initial value for the remaining duration of the experiment. This indicates a very promising level of condensate emission stability and is consistent with the high degree of stability evidenced in the linear emission measurements presented in Fig. 1(c). In Fig. 4(b), we plot the first and last spectra recorded,

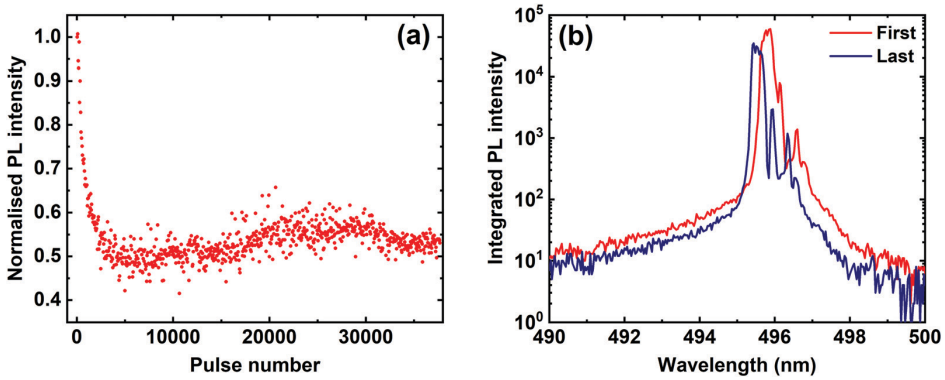

Fig. 4 Above threshold photostability data. Part (a) shows the integrated intensity *versus* number of pulses for the DPAVB/PS cavity at $P = 2\ P_{th}$. Part (b) shows the first (red) and last (blue) spectra recorded, indicating that the microcavity remained in the non-linear emission regime over more than 37 000 pulses.

where it can be seen that the emission is very similar in both, indicating that the cavity is still in a non-linear regime at the end of the measurement.

3. Conclusions

We have fabricated polariton microcavities containing a green-emitting molecular dye (DPAVB) dispersed into a polystyrene (PS) matrix despite the fact that the DPAVB has a relatively broad absorption linewidth. Using angular-dependent white light reflectivity measurements, we demonstrate that cavities constructed from two low reflectivity (6-pair) DBRs that contain 50% DPAVB in PS by mass operate within the strong coupling regime, with the observation of a lower (LPB) and an upper (UPB) polariton branch. At lower DPAVB concentrations, no clear splitting is observed and we conclude that such structures were weakly-coupled. Higher *Q*-factor microcavities were then constructed from higher reflectivity DBR mirrors (10 and 12 pairs) containing 50% DPAVB/PS by mass that had a larger exciton-photon detuning. Here, an LPB was observed in reflectivity and non-resonant photoluminescence measurements; however, the UPB was not evident due to the high reflectivity of the DBRs and the large angle at which the exciton-photon crossing occurs. Nevertheless, we are certain these cavities operate in the strong coupling regime and we have explored non-linear emission from them, demonstrating that they undergo polariton condensation at a threshold of 215 μJ cm^{-2} following excitation using sub-ns (<330 ps) pulses. This process is accompanied by a spectral blueshift of the LPB by 1.2 meV, which likely occurs from a combination of reversible ground-state bleaching together with a limited degree of irreversible photodegradation, and a linewidth reduction of the LPB around k = 0 from 1.5 meV to 0.2 meV. We have explored the photostability of control DPAVB/PS thin films, and find an unexpected slow, photo-brightening effect that we ascribe to a gradual reduction in the relative density of non-radiative channels. We have also studied polariton condensate emission at double the threshold fluence and have shown that it displays remarkable photostability, with the cavity remaining in the non-linear regime for more than 37 000 pulses. This result is especially promising as all measurements were performed in air. We expect that this material will be of interest in experiments looking to explore condensate-condensate interactions and condensation in polariton lattices.[7,9]

Methods

Film fabrication. DPAVB (B2080, Tokyo Chemical Industry) was dissolved at various concentrations by mass in a solution of 20 mg mL^{-1} polystyrene (Sigma-Aldrich, molecular weight ~192 000) in dichloromethane. Thin films were made by spin coating the solution onto quartz-coated glass substrates, with a Bruker DektakXT profilometer then used to measure film thickness.

Cavity design and fabrication. Cavities were designed using a transfer matrix reflectivity (TMR) model. The refractive index (n_{DPAVB}) and extinction coefficient (k_{DPAVB}) of DPAVB films on silicon were measured using spectroscopic ellipsometry (1.24–3.35 eV, Woollam M-2000) at an angle of incidence of 75°. Data for three films of pure DPAVB were fit using a multi-sample analysis in CompleteEASE 6.59. Initially the data sets were fit using an empirical Cauchy dispersion relation for wavelengths greater than 550 nm, which allowed the thickness each film to be determined.[43] The Cauchy fit was then converted to a transparent b-spline using a resolution of 0.1 eV to determine the n and k values across all the measured wavelengths assuming all the films had the same optical properties. The values of the refractive index and extinction coefficient of the 50% DPAVB/PS (n_{film} and k_{film}) were then calculated using known values for polystyrene (PS)[34] using the following expression: $n_{film} = fn_{DPAVB} + (1-f)n_{PS}$ and $k_{film} = f \cdot n_{DPAVB} + (1-f) \cdot k_{PS}$, where f = 0.33. We note that the absorption coefficient (α) that we determine using the relation $\alpha = \frac{4\pi k}{\lambda}$ closely matches the absorption spectrum shown in Fig. 1(b). These values along with the n and k values of the SiO_2 and TiO_2 layers (determined using ellipsometry) were used in the TMR model. DBRs were fabricated using an Ångstrom Engineering electron beam to deposit λ/4-thick alternating layers of SiO_2 and TiO_2. The bottom and top mirrors consisted various numbers of DBR pairs and were centred around 460 nm. The bottom mirror was deposited onto a piece of quartz-coated glass. This was followed by the deposition of a film of DPAVB/PS by spin-coating, followed by the top DBR.

Linear optical characterisation. UV-vis absorption measurements were recorded using a Horiba Fluoromax 4 fluorometer equipped with a xenon lamp. Angle-dependent white light reflectivity measurements used an Ocean Optics Deuterium–Tungsten 378 lamp (DH-2000-BAL) fibre-coupled to the excitation arm of a motorised goniometer setup. The reflected light was collected by an optical fibre on a collection arm, which was connected to an Andor Shamrock SR-303i-A triple-grating CCD spectrometer. For PL measurements, a 405 nm Thorlabs diode laser was focused onto the sample *via* a third arm that was out-of-plane with respect to the excitation and collection arms. This setup was also used for linear PL and photostability measurements on DPAVB/PS films. In the latter measurement, the sample was irradiated for a total of 15 minutes, with a spectrum recorded every 15 seconds. Raman measurements were carried out using a 785 nm Innovative Photonic Solutions laser module (IO785MM0350MF). A dual-core optical fibre transmitted the laser light to the solution, which was held in a glass cuvette, and the scattered light was transmitted along the second core of the fibre to an Ocean Optics QE *Pro*-Raman spectrometer. Measurements were carried out using the Ocean-View software on a 10 mg mL^{-1} DPAVB/dichloromethane solution and on a pure dichloromethane solution, allowing the solvent peaks to be subtracted from the DPAVB spectra.

Non-linear optical characterisation. ASE measurements were carried out using a Teem Photonics pulsed Q-switched 355 nm Nd:YAG laser (PNV-M02510-1 × 0) producing ~330 ps pulses at 100 Hz. A cylindrical lens was used to focus the excitation beam onto a strip (dimensions = 330 μm × 4100 μm) on the 200 nm thick DPAVB/PS film. The emission from the film was collected

from the edge of the sample *via* an optical fibre positioned perpendicular to the excitation path. The fibre then directed the light into an Andor Shamrock SR-303i-A CCD spectrometer (300 grooves mm^{-1}, 100 μm entrance slit). Condensation measurements were carried out using the same laser and spectrometer. Here, the pump beam was focused onto the cavity using a 200 mm focal length lens and the transmitted light was passed through a UQG Optics UV blocking filter and collected by an Edmund Optics 20x HR infinity 382 corrected objective (numerical aperture = 0.6, focal length = 10 mm). A 125 mm focal length lens was used to focus the signal into the spectrometer equipped with an 1800 grooves mm^{-1} grating through a 50 μm entrance slit. The same setup was also used to measure the photostability of the cavity above threshold. Here, pump power was set to $P = 2\ P_{th}$ and *k*-space images recorded every 2 seconds. All measurements were carried out in air at room temperature.

Conflicts of interest

There are no conflicts to declare.

Acknowledgements

We thank the UK EPSRC for funding this research *via* the Programme Grant 'Hybrid Polaritonics' (EP/M025330/1). K. E. M. also thanks the EPSRC for the award of a Doctoral Training Account PhD studentship.

References

1 J. Keeling and S. Kéna-Cohen, Bose–Einstein Condensation of Exciton-Polaritons in Organic Microcavities, *Annu. Rev. Phys. Chem.*, 2020, **71**, 435–459.
2 D. Sanvitto and S. Kéna-Cohen, The road towards polaritonic devices, *Nat. Mater.*, 2016, **15**, 1061–1073.
3 K. S. Daskalakis, S. A. Maier and S. Kéna-Cohen, Spatial Coherence and Stability in a Disordered Organic Polariton Condensate, *Phys. Rev. Lett.*, 2015, **115**, 035301.
4 M. Wei, *et al.*, Low-threshold polariton lasing in a highly disordered conjugated polymer, *Optica*, 2019, **6**, 1124.
5 T. Byrnes, N. Y. Kim and Y. Yamamoto, Exciton-polariton condensates, *Nat. Phys.*, 2014, **10**, 803–813.
6 D. Bajoni, Polariton lasers. Hybrid light–matter lasers without inversion, *J. Phys. D: Appl. Phys.*, 2012, **45**, 313001.
7 M. Dusel, *et al.*, Room temperature organic exciton–polariton condensate in a lattice, *Nat. Commun.*, 2020, **11**, 1–7.
8 R. Jayaprakash, *et al.*, Two-Dimensional Organic-Exciton Polariton Lattice Fabricated Using Laser Patterning, *ACS Photonics*, 2020, **7**, 2273–2281.
9 F. Scafirimuto, *et al.*, Tunable exciton–polariton condensation in a two-dimensional Lieb lattice at room temperature, *Commun. Phys.*, 2021, **4**, 39.
10 J. D. Plumhof, T. Stöferle, L. Mai, U. Scherf and R. F. Mahrt, Room-temperature Bose-Einstein condensation of cavity exciton-polaritons in a polymer, *Nat. Mater.*, 2014, **13**, 247–252.
11 T. Cookson, *et al.*, A Yellow Polariton Condensate in a Dye Filled Microcavity, *Adv. Opt. Mater.*, 2017, **5**, 1700203.
12 D. Sannikov, *et al.*, Room Temperature Broadband Polariton Lasing from a Dye-Filled Microcavity, *Adv. Opt. Mater.*, 2019, **7**, 1–5.
13 K. S. Daskalakis, S. A. Maier, R. Murray and S. Kéna-Cohen, Nonlinear interactions in an organic polariton condensate, *Nat. Mater.*, 2014, **13**, 271–278.
14 C. P. Dietrich, *et al.*, An exciton-polariton laser based on biologically produced fluorescent protein, *Sci. Adv.*, 2016, **2**, 1–8.
15 S. Betzold, *et al.*, Coherence and Interaction in Confined Room-Temperature Polariton Condensates with Frenkel Excitons, *ACS Photonics*, 2020, **7**, 384–392.
16 J. Tang, *et al.*, Room temperature exciton–polariton Bose–Einstein condensation in organic single-crystal microribbon cavities, *Nat. Commun.*, 2021, **12**, 1–8.
17 Z. Jiang, A. Ren, Y. Yan, J. Yao and Y. S. Zhao, Exciton-Polaritons and Their Bose–Einstein Condensates in Organic Semiconductor Microcavities, *Adv. Mater.*, 2022, **34**, 2106095.
18 K. E. McGhee, *et al.*, Polariton condensation in an organic microcavity utilising a hybrid metal-DBR mirror, *Sci. Rep.*, 2021, **11**, 20879.
19 K. P. Kretsch, *et al.*, Distributed feedback laser action from polymeric waveguides doped with oligo phenylene vinylene model compounds, *Appl. Phys. Lett.*, 2000, **76**, 2149–2151.
20 M. Ichikawa, *et al.*, Gain-narrowing characteristics of fluorescent organic molecules with symmetrical or asymmetrical structures in a neat thin-film optical waveguide, *J. Photochem. Photobiol., A*, 2003, **158**, 219–221.
21 T. Riedl, *et al.*, Tunable organic thin-film laser pumped by an inorganic violet diode laser, *Appl. Phys. Lett.*, 2006, **88**, 2–4.
22 M. T. Lee, H. H. Chen, C. H. Liao, C. H. Tsai and C. H. Chen, Stable styrylamine-doped blue organic electroluminescent device based on 2-methyl-9, 10-d/(2-naphthyl)anthracene, *Appl. Phys. Lett.*, 2004, **85**, 3301–3303.
23 C.-H. Liao, M.-T. Lee, C.-H. Tsai and C. H. Chen, Highly efficient blue organic light-emitting devices incorporating a composite hole transport layer, *Appl. Phys. Lett.*, 2005, **86**, 203507.
24 X. R. Wang, J. S. Chen, H. You, D. G. Ma and R. G. Sun, Efficiency and color coordinate improvement using codopants in blue organic light-emitting diode, *Jpn. J. Appl. Phys., Part 1*, 2005, **44**, 8480–8483.
25 K. P. Kretsch, *et al.*, Amplified spontaneous emission and optical gain spectra from stilbenoid and phenylene vinylene derivative model compounds, *J. Appl. Phys.*, 1999, **86**, 6155–6159.
26 T. Rabe, *et al.*, Threshold reduction in polymer lasers based on poly(9,9-dioctylfluorene) with statistical binaphthyl units, *Adv. Funct. Mater.*, 2005, **15**, 1188–1192.
27 M. Lehnhardt, T. Riedl, U. Scherf, T. Rabe and W. Kowalsky, Spectrally separated optical gain and triplet absorption: Towards continuous wave lasing in organic thin film lasers, *Org. Electron.*, 2011, **12**, 1346–1351.

28 V. Savona, L. C. Andreani, P. Schwendimann and A. Quattropani, Quantum well excitons in semiconductor microcavities: Unified treatment of weak and strong coupling regimes, *Solid State Commun.*, 1995, **93**, 733–739.

29 D. Ballarini and S. De Liberato, Polaritonics: From microcavities to sub-wavelength confinement, *Nanophotonics*, 2019, **8**, 641–654.

30 R. T. Grant, *et al.*, Efficient Radiative Pumping of Polaritons in a Strongly Coupled Microcavity by a Fluorescent Molecular Dye, *Adv. Opt. Mater.*, 2016, **4**, 1615–1623.

31 K. Georgiou, *et al.*, Generation of Anti-Stokes Fluorescence in a Strongly Coupled Organic Semiconductor Microcavity, *ACS Photonics*, 2018, **5**, 4343–4351.

32 A. Putintsev, *et al.*, Nano-second exciton-polariton lasing in organic microcavities, *Appl. Phys. Lett.*, 2020, **117**, 123302.

33 C. M. Herzinger, B. Johs, W. A. McGahan, J. A. Woollam and W. Paulson, Ellipsometric determination of optical constants for silicon and thermally grown silicon dioxide via a multi-sample, multi-wavelength, multi-angle investigation, *J. Appl. Phys.*, 1998, **83**, 3323–3336.

34 N. Sultanova, S. Kasarova and I. Nikolov, Dispersion properties of optical polymers, *Acta Phys. Pol., A*, 2009, **116**, 585–587.

35 S. Christopoulos, *et al.*, Room-Temperature Polariton Lasing in Semiconductor Microcavities, *Phys. Rev. Lett.*, 2007, **98**, 126405.

36 L. Orosz, *et al.*, LO-phonon-assisted polariton lasing in a ZnO-based microcavity, *Phys. Rev. B: Condens. Matter Mater. Phys.*, 2012, **85**, 1–5.

37 R. Jayaprakash, *et al.*, Ultra-low threshold polariton lasing at room temperature in a GaN membrane microcavity with a zero-dimensional trap, *Sci. Rep.*, 2017, **7**, 1–9.

38 M. Wei, *et al.*, Room Temperature Polariton Lasing in Ladder-Type Oligo(p-Phenylene)s with Different π-Conjugation Lengths, *Adv. Photonics Res.*, 2021, **2**, 2000044.

39 T. Yagafarov, *et al.*, Mechanisms of blueshifts in organic polariton condensates, *Commun. Phys.*, 2020, **3**, 1–10.

40 J. Kasprzak, *et al.*, Bose–Einstein condensation of exciton polaritons, *Nature*, 2006, **443**, 409–414.

41 C. Gadermaier, *et al.*, Dynamics of higher photoexcited states in m-LPPP probed with sub-20 fs time resolution, *Chem. Phys. Lett.*, 2004, **384**, 251–255.

42 A. V. Zasedatelev, *et al.*, A room-temperature organic polariton transistor, *Nat. Photonics*, 2019, **13**, 378–383.

43 H. Fujiwara, *Spectroscopic Ellipsometry: Principles and Applications*, John Wiley & Sons Ltd, 2007.

5.3 Author contributions

K.E.M. and K.G. carried out preliminary measurements on the films and designed the cavities. K.E.M. fabricated the cavities and carried out preliminary optical characterisation measurements on them. R.J. built the condensation setup. K.E.M. and R.J. carried out the condensation and non-linear stability measurements and performed transfer matrix reflectivity modelling. K.E.M., R.J. and S.L.B. carried out the ellipsometry measurements and analysis. D.G.L. supervised the project. All authors contributed to preparation of the manuscript.

6 Controlling the blueshift in organic polariton microcavities

This chapter focuses on controlling the blueshift in organic polariton microcavities with the aim of creating structures that trap polariton condensates. Multilayer cavities were fabricated that contained BODIPY-Br, to which the cavity mode strongly-couples, and BN-PFO, a modified polyfluorene derivative containing statistical intrachain binaphthyl spacer groups. The BN-PFO was selectively optically saturated to induce a refractive index change. This resulted in an effective change in the cavity length, a shift of the cavity mode, and hence a shift of the lower polariton branch. This shift is confirmed through transient reflectivity measurements, where a large blueshift is evidenced that is dependent on the excitation fluence.

6.1 Introduction

In recent years, there has been a significant focus on the trapping of polariton condensates through the confinement of their excitonic or photonic component. Such traps alter the energy and density of the polaritons, allowing control over their transport, interactions and scattering mechanisms. As well as providing a basis for fundamental studies, this effect has potential applications in nonlinear photonic integrated circuits and polariton logic devices [1–4]. Due to the low effective mass of polaritons (10^{-5}–10^{-4} times that of an electron [5]) and their large propagation distances, such electronics are likely to be extremely fast and efficient [6]. The use of multiple traps in lattice designs has also been studied extensively due to their potential ability to simulate complex many-body phenomena [7–9].

A range of physical techniques can be used to confine the photonic component of a polariton; for example, using micropillars fabricated through lithography and etching [10–12], or in Gaussian defects fabricated through laser patterning [13]. The excitonic component can also be trapped, either physically through mechanical strain [5, 14, 15] or optically using structured laser beams [16, 17]. The advantage of these latter techniques is that the traps can be moved and adjusted dynamically, allowing a further degree of control of polariton condensate dynamics.

In inorganic systems, optically-induced traps rely on the strong Coulombic repulsion between polaritons and the exciton reservoir, this repulsion being the cause of the blueshift in such systems. In organic-based cavities, however, the blueshift arises from two mechanisms that occur when the oscillator strength of the organic is saturated [18]. The first mechanism is due to a reduction of the Rabi splitting: the splitting energy is proportional to the square-root of the oscillator strength [19], therefore saturating the organic will result in a reduced Rabi splitting causing the LPB to blueshift. This effect is illustrated in Figure 6.1(a). The second mechanism is an effective change in refractive index: at energies above the optical transition, there is an effective increase in refractive index, and below, there is an effective decrease in refractive index. This will result in a blueshift of the LPB

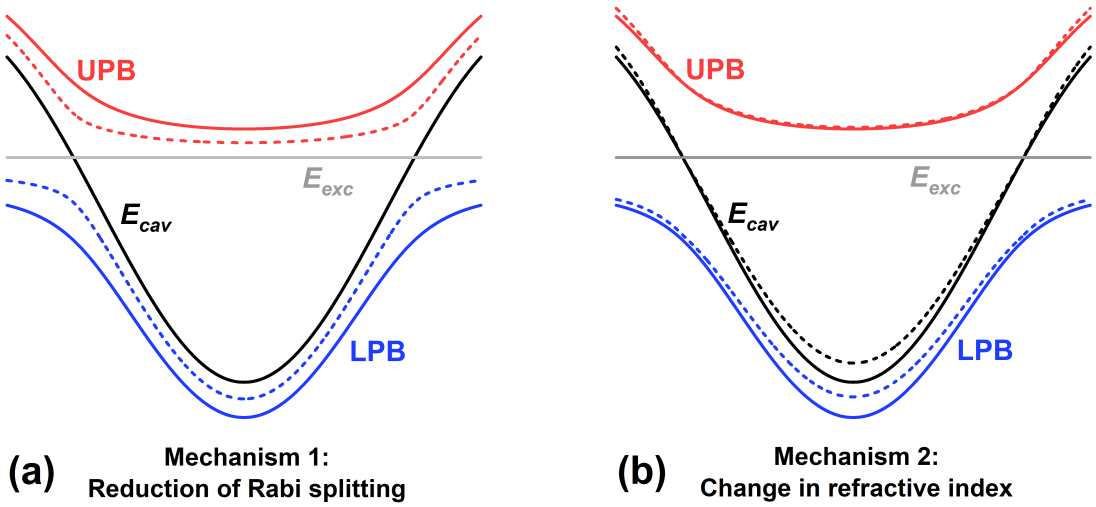

Figure 6.1. Effect on polariton branches when the organic oscillator strength is saturated. In both (a) and (b), the solid lines show the energy dispersion in a polariton system with a Rabi splitting of 100 meV between the UPB (red solid) and LPB (blue solid). The cavity mode (black solid) and exciton (grey solid) energies are also shown. Part (a) shows the effect on the UPB (red dashed) and LPB (blue dashed) when the Rabi splitting is reduced to 70 meV. It can be seen that this results in a blueshift of the LPB. Part (b) shows the effect of changing the refractive index on the cavity mode (black dashed), the UPB (red dashed) the LPB (blue dashed). In this case, the refractive index has been increased by 10% above the exciton resonance and decreased by 10% below it. It can be seen that this also results in a blueshift of the LPB.

and this is illustrated in Figure 6.1(b). This effect should be dependent on the degree of saturation of the oscillator strength. Using such effects, it should be possible to control the energy of the lower polariton branch in organic semiconductor microcavities. Notably, this is expected to be a dynamic effect, where high-energy laser pulses could be used to turn a blueshift "on" and "off" at will.

We first consider the use of an excitation beam with a ring profile, such as is illustrated in Figure 6.2(a). If a cavity is negatively-detuned, the LPB will be at longer wavelengths (lower energies) than the optical transition of the strongly-coupled dye and will experience a decrease in effective refractive index and therefore a blueshift. This will create a region of higher potential energy surrounding a spot that is unperturbed in the centre of the excitation ring (white circle in (a)). This will form a polariton trap, as is illustrated in Figure 6.2(b), with the blueshifted region acting as an energy barrier that would confine a polariton condensate. Similarly, a series of ring excitations could be generated – for example, using a spatial light modulator to create a patterned excitation. This would form a lattice of polariton condensates as is illustrated in 6.2(c).

However, we note that simply saturating the oscillator strength will reduce the Rabi splitting. This is undesirable as it could push cavities from the strong to the weak coupling regime. To avoid this, we have fabricated multilayer cavities containing BODIPY-Br, which is strongly-coupled to the cavity mode, together with a second dye that absorbs at shorter wavelengths and is weakly-coupled. In our experiments, these two dyes are spatially separated by a layer of polyvinyl alcohol (PVA) to avoid energy transfer. By saturating the "bluer" dye, we show it is possible to induce a large blueshift of the LPB without reducing the Rabi splitting. We have modelled such cavities using BN-PFO as the 'blue' absorbing species. This material consists of repeat units of the copolymer 2,7-9,9-dioctylfluorene, containing 9.8% of statistical intrachain 6,6'-(2,2'-octyloxy-1,1'-binaphthalene) binaphthyl spacer groups (see Figure 6.3(a)). Our transfer matrix reflectivity (TMR) simulations suggested that a 50%

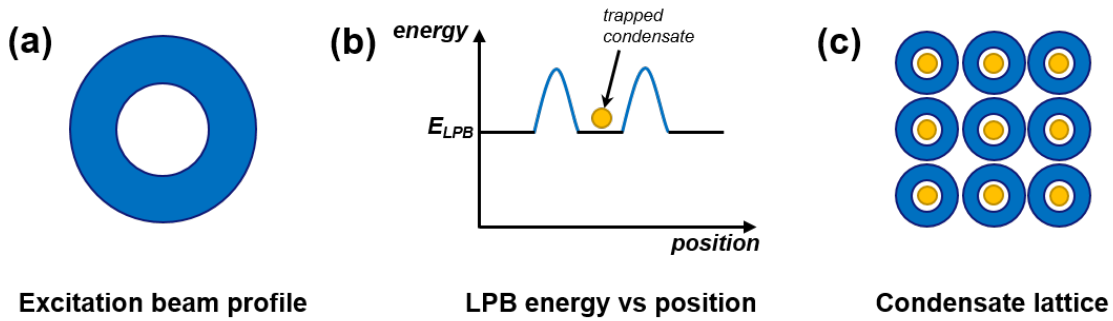

Figure 6.2. Illustration of a dynamic polariton condensate lattice. Part (a) illustrates the ring-shaped excitation profile that would be used. Part (b) illustrates the energy barrier that would be formed by blueshifting this ring-shape around a polariton condensate, trapping it within. Part (c) illustrates (in real space) a lattice of these trapped condensates.

saturation of the BN-PFO oscillator strength would result in a large blueshift of the LPB of 12 meV. We have fabricated such cavities and performed transient reflectivity measurements, confirming a maximum blueshift of around 14 meV. We find that this energy shift occurs on very short timescales, reaching a maximum value after 600 fs and decaying halfway back to the original LPB position in 380 fs. This method therefore has potential in confining polariton condensates in arrays, with a fast switching time to modify the confinement potentials anticipated. As we discuss, this process should allow the controlled interaction between neighbouring condensates, with more applications in polariton logic anticipated.

6.2 Investigating films

BN-PFO has previously been investigated as a material for organic solid state lasers and has been shown to exhibit quasi-continuous-wave lasing at low thresholds. Indeed, in a second order distributed feedback structure, BN-PFO can exhibit photon lasing with a threshold of 2.5 μJ/cm^2 with excitation repetition rates of up to 5 MHz [20, 21]. It has a large absorption coefficient that peaks around 400 nm (the exact wavelength depends on the percentage of binaphthyl units). It is also relatively photostable, making it an ideal material for lasing experiments. The structure of BN-PFO is shown in Figure 6.3(a), where m and n give the relative number of PFO and BN units, respectively, and $^{n}/_{(n+m)} = 9.8\%$.

BN-PFO was dissolved in toluene at a concentration of 30 mg/mL and spin-coated to form thin films. The absorption spectrum was then used with TMR modelling to design a multilayer cavity having an LPB at 570 nm at k=0. The multilayer film explored consisted of 285 nm of BODIPY-Br/polystyrene (PS), 60 nm of PVA and 170 nm of BN-PFO (see Figure 6.3(b)). The BODIPY-Br and PVA layers were spin-coated from solutions of 10% BODIPY-Br in 35 mg/mL PS in toluene and 15 mg/mL PVA in deionised water, respectively. The absorbance of the multilayer film is shown in Figure 6.3(c), alongside that of pure BN-PFO and BODIPY-Br/PS. It can be seen that the multilayer absorption is a superposition of the two component dye films as expected. It can also be seen that as the BN-PFO absorption is spectrally broad, it will likely be weakly-coupled in a cavity.

The photoluminescence spectra of the films were measured using a 405 nm CW laser diode as the excitation source, and these are shown in part (c). It can be seen that there is significant PL from the

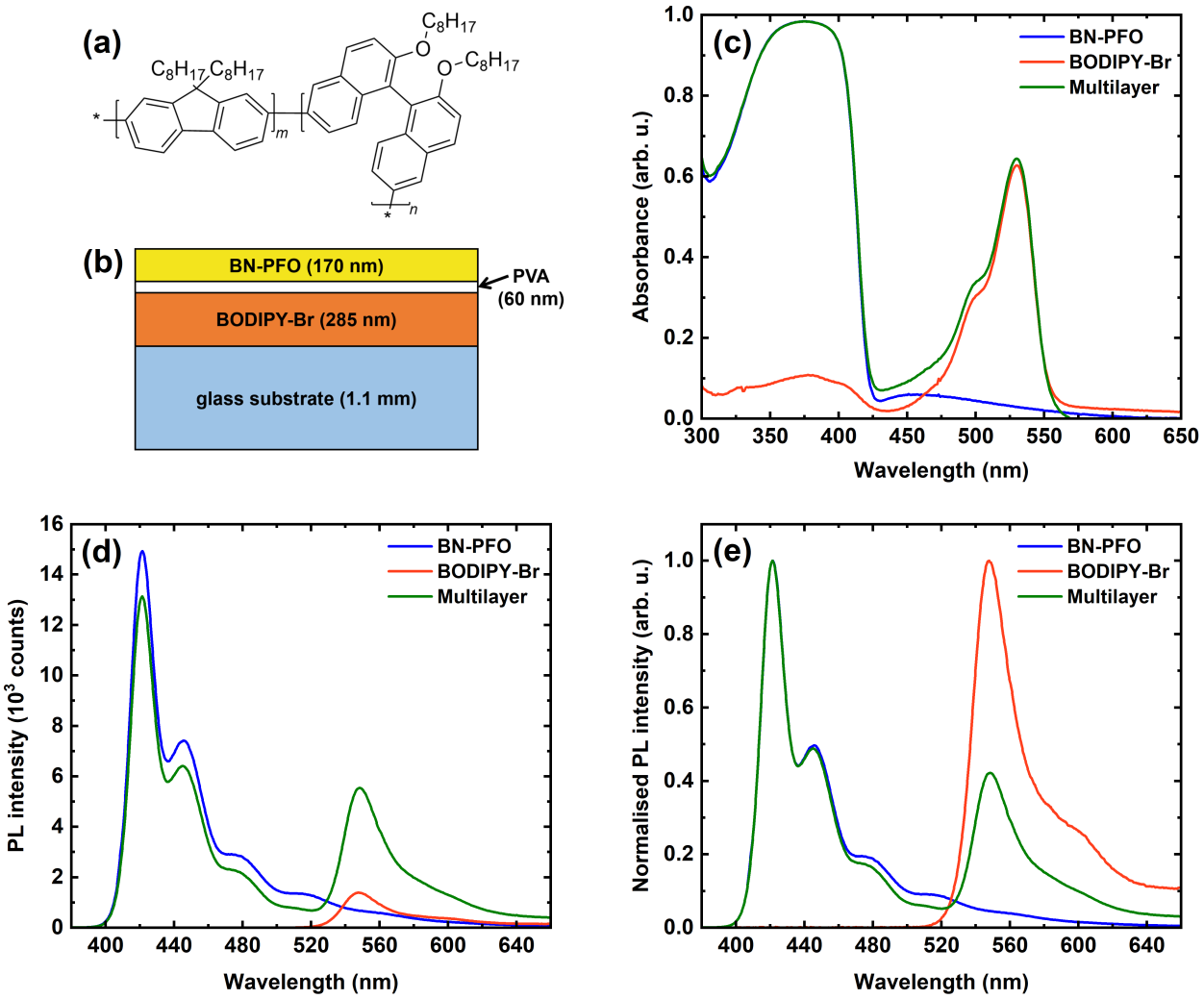

Figure 6.3. Preliminary characterisation of the BN-PFO and BODIPY-Br/PVA/BN-PFO films. Part (a) shows the molecular structure of BN-PFO. In the BN-PFO used here, $^{n}/_{(n+m)}$=9.8%, where m and n represent the relative number of polyfluorene (PFO) and binaphthyl (BN) units, respectively. Part (b) shows the structure of the multilayer film, which is composed of 285 nm of 10% BODIPY-Br/PS, 60 nm of PVA, and 170 nm of BN-PFO. Part (c) shows the absorbance spectra for a 170 nm BN-PFO film (blue), a 285 nm BODIPY-Br film (orange), and a multilayer film (green). Parts (d) and (e) show the raw and normalised photoluminescence spectra, respectively, for the same films. Scatter from the laser was removed from the data post-processing.

BODIPY in the multilayer film. Indeed, the PL intensity from the BODIPY exceeds that from the pure BODIPY film. This is likely due to the PL of the BN-PFO being reabsorbed by the BODIPY layer and then re-emitted. This is confirmed by the reduced intensity of the BN-PFO PL from the multilayer film compared to the pure BN-PFO film. These results further suggest that there is no quenching of the BODIPY PL by the BN-PFO and that the PL from the BN-PFO may actually aid condensation in a cavity. Part (e) shows the normalised PL spectra for the films. It can be seen that the BN-PFO emission spectrum is made up of a main peak at 421 nm, corresponding to the 0-0 transition, and shoulders at 446 nm and 470 nm, corresponding to the 0-1 and 0-2 transitions, respectively. In the BODIPY-Br emission spectrum, the 0-0 and 0-1 transitions can be seen at 548 nm and 592 nm, respectively. In the data shown here, the samples were excited through the glass substrate. Exciting from the opposite side resulted in reduced emission from all samples due

to degradation arising from photo-oxidation, but there was little difference in the shape of the PL spectra.

6.3 Designing and fabricating multilayer cavities

A double-DBR cavity containing the multilayer was then designed using the TMR model. The structure of the cavity is shown in Figure 6.4(a). Here, the DBRs are centred at 560 nm, with the bottom DBR consisting of 10-pairs of SiO_2/Nb_2O_5 and the top consisting of 8-pairs of SiO_2/TiO_2. The TMR model indicated that the BODIPY-Br would strongly-couple to the cavity mode with a Rabi splitting of 103 meV, while the BN-PFO would remain weakly-coupled. The modelled angle-dependent reflectivity is shown in part (b), where the splitting between the UPB and LPB is evident in both the colour map and the cross-section at 41° (shown in the right-hand panel). If the BN-PFO oscillator strength was saturated (reduced) by 50%, this resulted in a predicted blueshift of the LPB of 3.1 nm (12.0 meV), as can be seen in part (c). The effects of this saturation on the refractive index (n) and extinction coefficient (k) of the BN-PFO are shown in Figure 8.1 in Appendix C (Section 3). We have previously found $\lambda/2$ BODIPY-Br cavities composed of similar DBRs supported polariton condensation with a blueshift of up to 5 meV [22, 23]. The TMR model therefore suggests that the blueshift generated upon saturation of the BN-PFO should exceed the blueshift of the condensate and act as an effective confinement barrier (see Figure 6.2).

The cavity was fabricated according to the design outlined above. The 10-pair SiO_2/Nb_2O_5 bottom DBR was fabricated by Helia Photonics Ltd., with the 8-pair SiO_2/TiO_2 top DBR fabricated using an Angstrom electron beam deposition system as described in Chapter 3 (Section 3.1.2.2). An angle-dependent white light reflectivity measurement of the cavity was taken and this is shown in Figure 6.4(d). The experimental data is overlaid with the TMR model from part (b) (black crosses in (d)). It can be seen that it describes the data well and there is a Rabi splitting of 103 meV between the upper and lower polariton branches as predicted by the model.

6.4 Pump probe measurements

In order to investigate blueshift effects in these cavities upon saturation of the BN-PFO, pump probe measurements were carried out on the cavity and the control films. The control films had high transmission and minimal reflectivity, so were measured in a transmission configuration. In the cavity, however, the transmitted signal was not sufficient to observe the cavity mode, and so such structures were measured in a reflection configuration. For this reason, all measurements on films are discussed in terms of the fractional change in the transmitted probe signal, $\Delta T/T$, while the measurements on cavities are discussed in terms of the fractional change in the reflected probe signal, $\Delta R/R$.

Both configurations used a regeneratively amplified Ti:sapphire laser that generated 100 fs pulses at 800 nm with a repetition rate of 2 kHz. A broadband probe beam was generated by focusing the fundamental (800 nm) onto a sapphire crystal, with an example spectrum shown in Figure 8.2 of Appendix C. A 400 nm pump beam was generated by focusing the fundamental beam onto a BBO crystal, which was then directed through a delay line and a mechanical chopper that reduced the repetition rate to 1 kHz. This was to allow both pump-probe and probe-only measurements. More details regarding the experimental methods used can be found in Chapter 3 in Section 3.2.3.

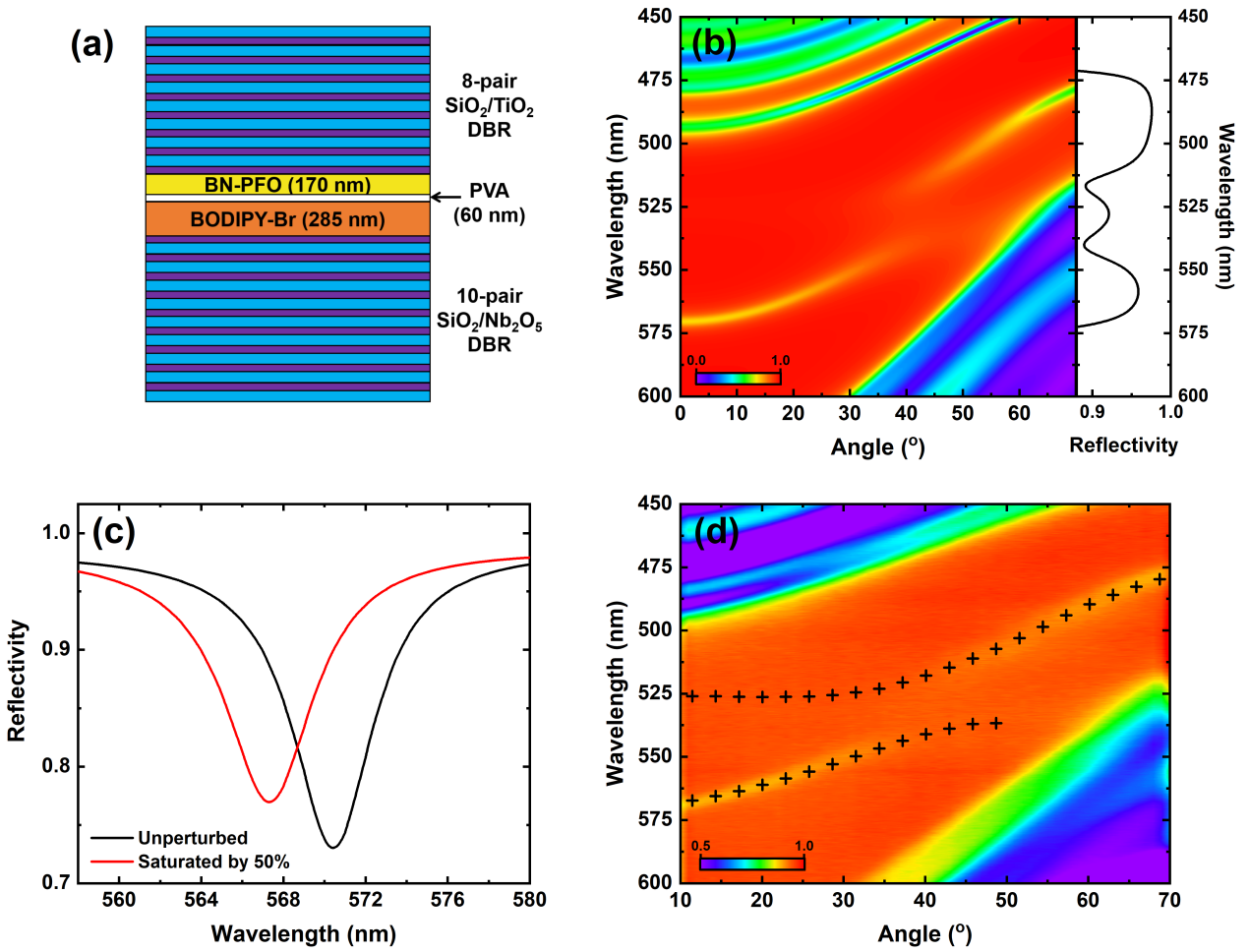

Figure 6.4. BN-PFO multilayer cavities. Part (a) shows a schematic of the cavity. Part (b) shows the TMR simulation of the cavity reflectivity, with the right-hand panel showing a cross-section at 41°. Part (c) shows the LPB reflectivity at 0° when the BN-PFO oscillator strength is unperturbed (black) and when it has been saturated by 50% (red), clearly showing a blueshift of 3.1 nm (12.0 meV). Part (d) shows the experimental reflectivity data for the cavity overlaid with the TMR model (black crosses). It can be seen that there is good agreement between theory and data.

6.4.1 Transient absorption on control films

Before investigating the cavities, we have explored the control films to determine their response to pumping at 400 nm. The films investigated were a 170 nm BN-PFO film, a 285 nm BODIPY-Br film, and a BODIPY-Br(285 nm)/PVA(60 nm)/BN-PFO(170 nm) multilayer. All three structures were pumped at a high fluence of 35 μJ/cm^2 and the probe spectrum was recorded for delays between -0.5 ps and 290 ps. Here, a negative delay means the probe arrived before the pump, and a positive delay means the probe arrived after the pump. The spectral $^{\Delta T}/_{T}$ data is shown for all three films at a delay of 0.48 ps in Figure 6.5(a). This delay corresponds to the maximum or near maximum $^{\Delta T}/_{T}$ signal for all films. It can be seen that the BN-PFO $^{\Delta T}/_{T}$ signal is positive until about 510 nm, with peaks observed at 445 nm and 467 nm. From Figure 6.3(c) and (d), it can be seen that these peaks coincide with the peak in the BN-PFO PL emission at 446 nm and the shoulder around 470 nm. Above 510 nm, there is an increasing negative signal, which is due to excited state photo-induced absorption – this has previously been attributed to singlet excitons [24, 25]. There is a small positive peak in the BODIPY $^{\Delta T}/_{T}$ spectrum at 540 nm that is likely a combined signal from ground state

absorption and PL emission, which peak at 530 nm and 548 nm, respectively. The small signal from the BODIPY suggests that it absorbs some of the pump pulse energy; however, its relative size compared to the BN-PFO $^{\Delta T}/_{T}$ signal suggests that the majority of the excitation beam absorbed in the multilayer film is by BN-PFO. This is also expected to be the case in the cavity.

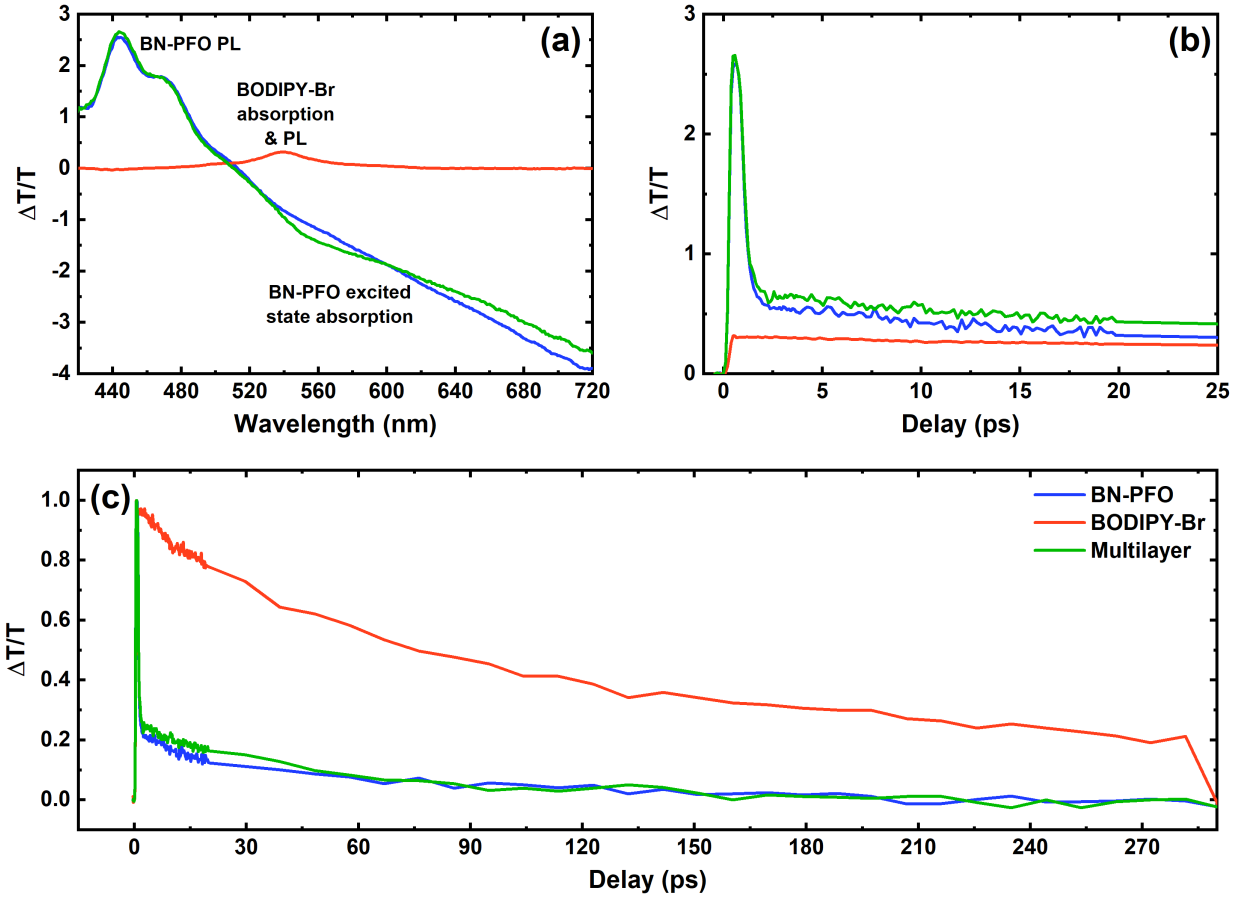

Figure 6.5. Transient absorption measurements on BN-PFO and BODIPY films. Part (a) shows the fractional change in the transmission spectra, $^{\Delta T}/_{T}$, for the BN-PFO (blue), BODIPY-Br (orange), and multilayer (green) films at a fluence of 35 μJ/cm^2 and a delay time of 0.48 ps between the pump and probe pulses. At this delay, the peaks in the $^{\Delta T}/_{T}$ spectra (445 nm in the BN-PFO and multilayer films and 540 nm in the BODIPY-Br film) were at a maximum or very near maximum. Part (b) shows the time dynamics of the $^{\Delta T}/_{T}$ signal up to a delay time of 25 ps at the peak wavelength for each film. For BN-PFO and the multilayer film, this corresponds to the peak of the PL emission at ∼445 nm, and for the BODIPY-Br film, this corresponds to a combination of the absorption (main peak at 530 nm) and the PL (main peak at 548 nm) at 540 nm. Part (c) shows the normalised dynamics for the same features up to a delay time of 290 ps.

The time dynamics of the peaks at 445 nm for the BN-PFO and multilayer films and at 540 nm for the BODIPY-Br film are shown in Figure 6.5(b) up to a delay time of 25 ps. For all films, the $^{\Delta T}/_{T}$ signal rises to a maximum at a delay time of approximately 0.48 ps, after which it decays. In the BN-PFO and multilayer films, there is a fast initial decay, which is likely due to exciton-exciton annihilation [24, 25]. Figure 6.5(c) shows the normalised dynamics of the same peaks for the three films up to a delay time of 290 ps.

Figure 6.6 shows fluence-dependent TA data for the BN-PFO film. Part (a) shows the spectral $^{\Delta T}/_{T}$ data for different fluences at 0.48 ps. The origin of the spectral features here are the same as in Figure 6.5(a), with a large positive signal between 420 nm and ∼500 nm corresponding to the BN-PFO photoluminescence and a large negative signal at longer wavelengths likely corresponding

to excited state absorption. Part (b) shows the dynamics of the peak around 445 nm up to a delay of 25 ps. Part (c) shows the normalised dynamics of the same peak up to the maximum delay time of 290 ps, with the inset showing a close-up of the first 15 ps.

The equivalent data for the multilayer film is shown in Figure 8.3 in Appendix C. It should be noted that there are slight differences between the spectra and dynamics of BN-PFO and the multilayer – this is likely due to the effects of limited absorption by the BODIPY-Br and multiple reflections at the different interfaces in the multilayer film. However, it is clear that the general trends are the same.

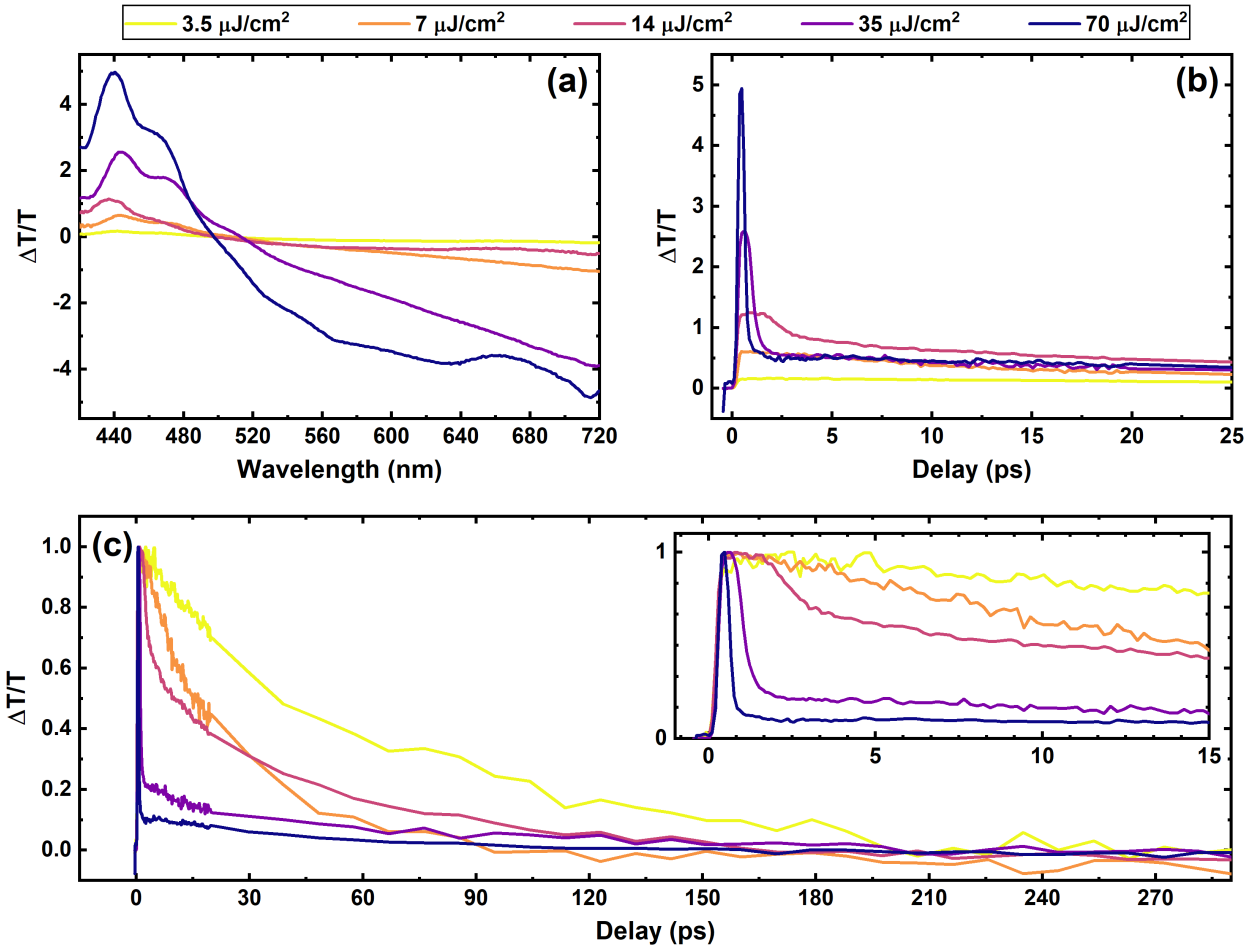

Figure 6.6. Fluence dependent transient absorption measurements on the BN-PFO film. Part (a) shows the fractional change in the transmission spectrum at a range of fluences. Part (b) shows the time dynamics of the $^{\Delta T}/_{T}$ signal up to a delay time of 25 ps at the peak of the PL emission (445 nm). Part (c) shows the normalised dynamics for the same spectra up to a delay time of 290 ps, with a close-up of the first 15 ps shown in the inset.

From these figures, it can been seen that at low fluences (3.5 and 7 μJ/cm^2), there is a slow decay of $^{\Delta T}/_{T}$ after the initial maximum, which is attributed to monomolecular decay (monoexponential) of the singlet excitons [24, 25]. At 14 μJ/cm^2, a faster initial decay becomes evident, and at greater fluences, the initial decay becomes very fast due to exciton-exciton annihilation. Looking at Figures 6.6(c) and 8.3(c), it can be seen that the $^{\Delta T}/_{T}$ signal becomes negative at long delay times. This is likely due to the presence of a higher order excited state with a longer lifetime than the BN-PFO photoluminescence. At short times, the $^{\Delta T}/_{T}$ signal below 500 nm is dominated by the positive contribution from the PL; however, due to the relatively fast decay of this emission, the $^{\Delta T}/_{T}$ signal

quickly falls to zero. At longer times, the negative contribution from the excited state photo-induced absorption dominates and the $\Delta T/T$ signal becomes negative. It therefore is not possible to extract quantitative lifetimes from this data. Previous studies on BN-PFO and PFO have found the lifetime of the BN-PFO PL to be around 230-460 ps at low fluences, where the decay is monoexponential [24–28]. At higher fluences, the decay is biexponential due to the effects of exciton-exciton annihilation.

6.4.2 Transient reflectivity on cavities

The multilayer cavity was then investigated to determine whether a blueshift of the LPB could be generated when pumping at 400 nm. This measurement was carried out at probe angles of 10°, 20° and 30° to the cavity normal. The data taken at 10° is presented here, with the equivalent data taken at 20° and 30° shown in Appendix C.

Figure 6.7 shows the spectral transient reflectivity data with the probe incident at an angle of 10° at a range of fluences. Part (a) shows the maximum $\Delta R/R$ signal for each fluence as a function of wavelength over the range 550-585 nm, i.e. the region that covers the LPB at 568 nm. At each fluence, a derivative line shape can be seen that is negative at shorter wavelengths (∼565 nm, labelled in the figure as "shifted LPB") and positive at longer wavelengths (∼568 nm, labelled in the figure as "original LPB"). This type of feature is characteristic of a blueshift of the lower polariton branch. Part (b) shows the probe signal at different pump fluences along with the probe signal recorded with no pump present. It can be seen that when there is no pump, the probe has a negative dip at 568 nm that corresponds to the original LPB. When the pump is present, this dip blueshifts as the BN-PFO is saturated and the effective cavity refractive index changes. At 568 nm, the probe signal is therefore increased when the pump is present compared to when it is not. This results in a positive peak in the $\Delta R/R$ signal at this wavelength in part (a) (original LPB). At the new LPB position, the probe is reduced due to the decreased reflectivity due to the mode and this results in a negative peak in the $\Delta R/R$ signal in part (a) at around 565-566 nm (shifted LPB). (See Section 3.2.3 for a further discussion on the origin of the derivative shape.) The fact that both the positive and negative peaks in the $\Delta R/R$ signal in part (a) increase in magnitude and move to bluer wavelengths as the fluence is increased implies the blueshift is larger at larger fluences. This is confirmed in part (b), where we can see the increasing magnitude of blueshift with increasing fluence. This is accompanied by a significant broadening of the LPB linewidth. It is important to note here that the probe data shown in part (b) ($R_{ON}(t)$) has been calculated from the $\Delta R/R$ signal at each fluence and the probe signal at negative delay ($R_{OFF}(t)$) using Equation 3.4. This is because the software did not save the probe signal at each delay time and instead recorded only a single probe spectrum (at a negative delay) at the start of each measurement.

To quantify the magnitude of the blueshift and linewidth, it was necessary to apply a Lorenztian fit to the probe data presented in part (b). A baseline subtraction was applied to all signals before fitting. The probe signals for the data taken at 10° after the baseline subtraction are shown in part (c), where the blueshift and broadening are again obvious. Lorentzian fits were then made to each spectrum to extract the peak position and the linewidth. The blueshift was calculated by subtracting the position of the "pump on" signal from the position of the "pump off" signal for each measurement. The calculated blueshifts and linewidths (where the linewidth is the FWHM of the Lorentzian fit) are plotted against excitation fluence in part (d). Note that the scales of the two y-axes have been

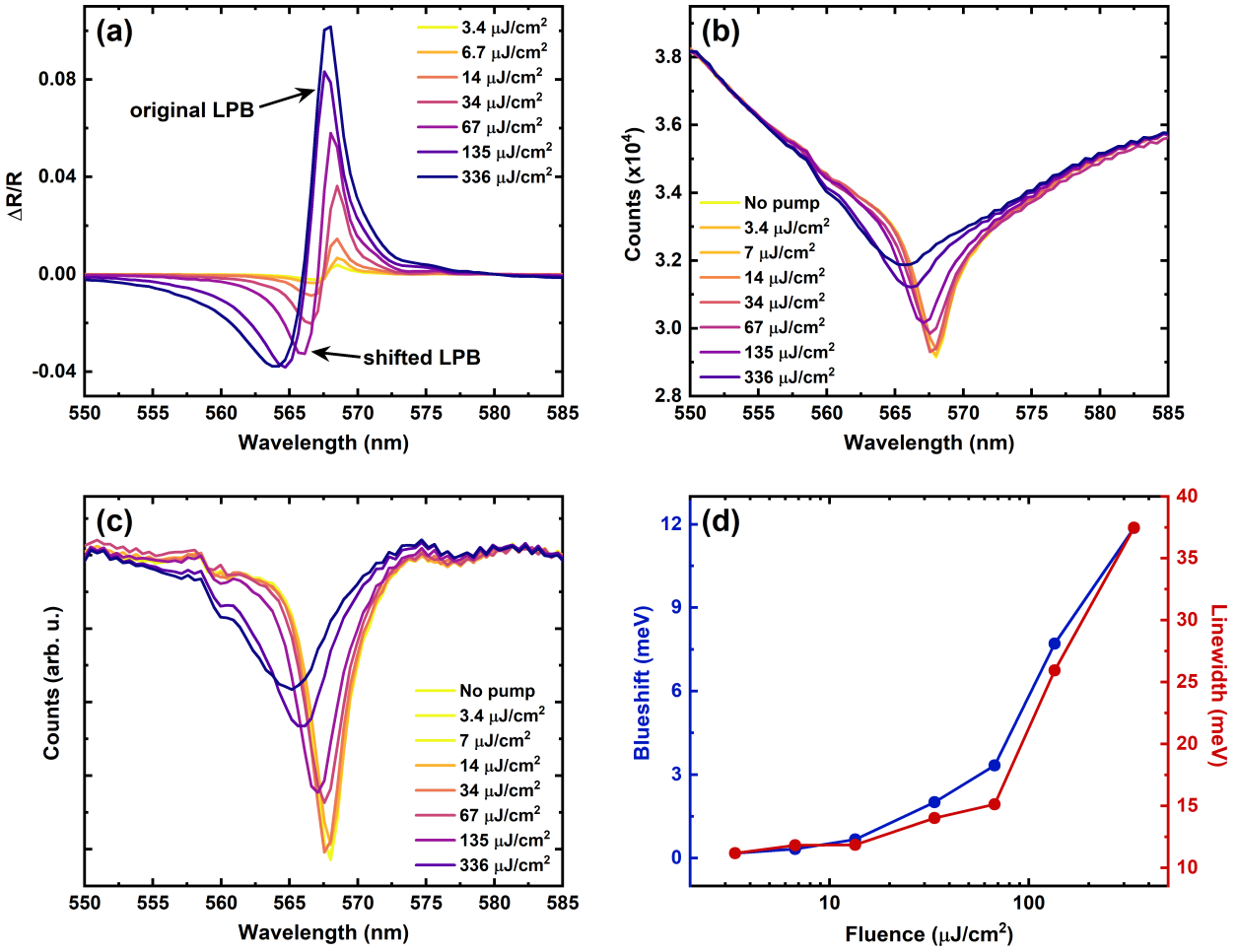

Figure 6.7. Transient reflectivity measurements on BODIPY-Br/BN-PFO cavity at an angle of 10° to the cavity normal. Part (a) shows the fractional change in the cavity reflectivity, $^{\Delta R}/_{R}$, at different fluences. The derivative shape is characteristic of a blueshift of the mode – in this case, the LPB. Part (b) shows the reflected probe at different fluences, showing that there is indeed a blueshift of the LPB as the fluence is increased. Part (c) shows the same data after a baseline subtraction. Part (d) shows the blueshift (blue) and linewidth (red) (in meV) as a function of fluence with a double y-axis, with the scales chosen in such a way that the first and last data points overlap. From this it can be seen that they follow a similar trend with increasing fluence. There is a maximum blueshift of 3.1 nm or 11.9 meV at a fluence of 336 μJ/cm^2. The blueshift and linewidth were extracted from a Lorentzian fit to the LPB in part (c).

adjusted so that the data overlap for the minimum and maximum fluences. From this it can be seen that they follow a similar trend. Notably, there is indeed a large blueshift of 11.9 meV (3.1 nm) at a fluence of 336 μJ/cm^2. Above this fluence, there was a noticeable reduction of the $^{\Delta R}/_{R}$ signal due to photo-degradation of the BN-PFO. This blueshift coincides with that predicted by the TMR model at a saturation of the BN-PFO oscillator strength of 50%.

Although we observe a significant broadening of the LPB linewidth from 11 meV to 37 meV (∼3.4 times), we do not expect that this should be a problem when creating polariton traps. As indicated in Figure 6.2(b), the polariton trap is generated by exciting the area *surrounding* the condensate to produce a high-energy ring (barrier). The condensate should therefore be unaffected by any broadening.

The equivalent data to that shown in Figure 6.7 for 20° and 30° is shown in Figures 8.4 and 8.5 in Appendix C, respectively. At 20°, we have observed a maximum blueshift of 14.1 meV (3.5 nm) and

a linewidth broadening of ∼2.1 times from 17 meV to 35 meV. At an angle of 30°, these are found to be 9.0 meV (2.2 nm) and ∼1.8 times from 19 meV to 33 meV, respectively.

The blueshift and linewidth as a function of fluence are shown in Figure 6.8(a) and (b), respectively, for the different angles. Looking at part (a), it can be seen that the blueshift for all angles seems to follow a similar trend with fluence, but with different magnitudes. The data seems to suggest that the blueshift is smallest at an angle of 30° and largest at 20°, with the 10° placed in between. We suspect, however, that the blueshift is influenced by the thicknesses of the different layers, and this is confirmed in TMR simulations. Indeed, the simulations do not seem to show a clear trend in blueshift with angle, even when the same thicknesses are used. Our model indicates that for some multilayer film thickness combinations, the largest blueshift occurs at 10°, but for other combinations it is predicted 20° or 30° will result in a larger blueshift.

Looking at Figure 6.8(b), a similar trend for the linewidths can be seen. At low fluences, the LPB linewidths in measurements performed at 10° are the narrowest, with them becoming broader at 20° and broadest at 30°, as would be expected due to the increasing excitonic fraction at higher angles. At greater fluences, the linewidths seem to converge to approximately the same value due to the increasing excitonic fraction as the cavity mode blueshifts.

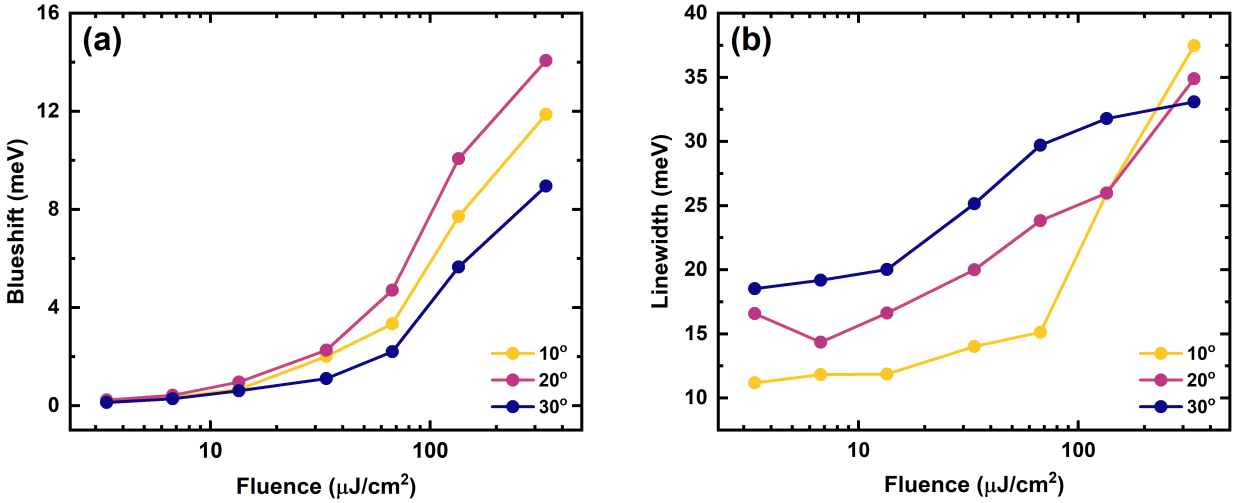

Figure 6.8. Comparison of fluence dependence for different probe angles. Part (a) and (b) show the blueshift and linewidth, respectively, as a function of fluence at 10° (gold), 20° (pink), and 30° (purple).

The increase in linewidth that is observed is likely due to an excited state absorption by the BN-PFO that is not taken into account by the TMR model. Indeed, from Figures 6.5(a) and 6.6(a), it can be seen that the excited state absorption around the spectral region of the LPB and cavity mode is significant. This will clearly act as a loss mechanism in the cavity, resulting in a decreased Q-factor and an increased LPB linewidth. We have tried to simulate this by including a broad Lorentzian absorption peaking at 720 nm (linewidth = 600 meV) into the TMR model when the BN-PFO oscillator strength is partially reduced (simulating the effect of the pump beam). Encouragingly, we find that this reproduces the observed broadening of the LPB along with the blueshift. This is shown in Figure 6.9, where we plot the cavity reflectivity when the BN-PFO is unperturbed (and no additional excited state absorption is included), along with the cavity reflectivity when the BN-PFO oscillator strength has been reduced by 17% and the excited state absorption included. Here, we are able to recreate the 12 meV blueshift and 3.4 times broadening of the linewidth that

we see in the cavity transient reflectivity data taken at 10°. Note, however, that we only obtain a qualitative agreement between the data and the model - although the spectral shape of the excited state absorption used in the model was obtained from the $\Delta T/T$ spectra (see Figure 6.6(a)), it was necessary to multiply its magnitude by ∼1.8 times in order to fully recreate the observed increase in LPB linewidth. The origin of this discrepancy is not entirely clear - we suspect that there may be other loss mechanisms that operate in the cavity that are not fully apparent in the $\Delta T/T$ spectrum. More work is clearly needed to obtain a full quantitative explanation of our results.

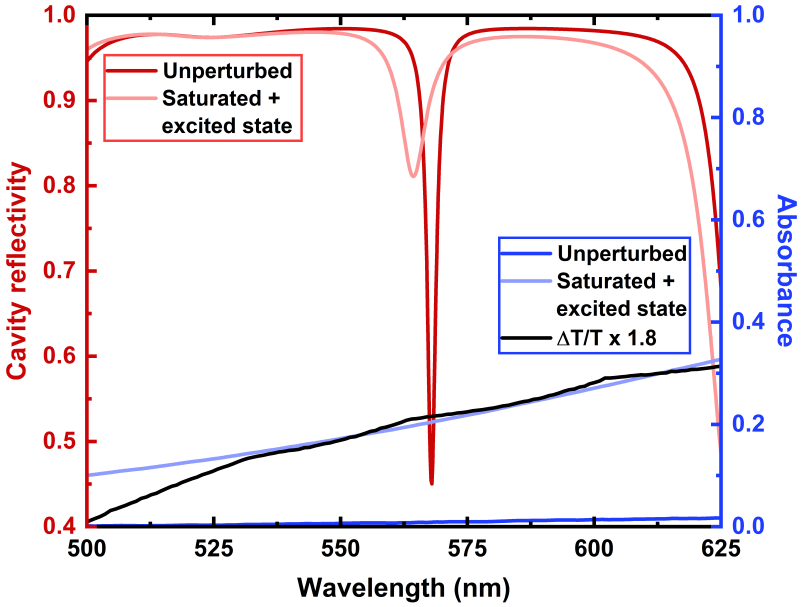

Figure 6.9. Effect of excited state absorption on LPB linewidth. The cavity reflectivity (dark red, left-hand y-axis) and BN-PFO absorption (dark blue, right-hand y-axis) are shown when the BN-PFO is unperturbed, i.e. the oscillator strength is 100% of its measured value. The BN-PFO is then saturated by 17%, i.e. 83% oscillator strength, and the excited state absorption is turned on. The input Lorentzian for the excited state absorption (light blue) was modelled on the shape of the BN-PFO film $\Delta T/T$ spectrum and was centred at 720 nm with a linewidth of 0.6 eV. The BN-PFO $\Delta T/T$ signal scaled by 1.8 times (black) is also plotted, showing a reasonable match. It can be seen from the resulting cavity reflectivity (pale red) that the LPB is blueshifted by 12 meV and is ∼3.4 times broader.

Finally we consider the dynamics of the blueshift to determine the lifetime of the LPB energy shift. To do this, the probe with the pump on was again reconstructed from the $\Delta R/R$ signal and the probe without the pump. The same baseline subtraction was applied as in Figure 6.7(c) and Lorentzian fits were applied to the LPB to extract the central wavelength and therefore the blueshift at different time delays. Data is shown at a range of fluences in Figure 6.10. Parts (a), (b) and (c) show the blueshift as a function of delay at a fluence of 34 μJ/cm^2, 135 μJ/cm^2, and 336 μJ/cm^2, respectively. In each case, a biexponential fit has been applied to extract the lifetimes τ_1 and τ_2, and these values are given in Table 6.1. It can be seen from this that there is a sharp decrease in τ_1 with increasing fluence. The data for τ_2 is less conclusive, but it can be seen that it is significantly shorter at 336 μJ/cm^2 than at lower fluences. This reduction in lifetime is clearly evident in Figure 6.10(d), where the normalised blueshift as a function of delay is shown for each fluence.

Although the LPB does not fully return to its original position over the delay time range studied (which was limited by the setup), it can be seen that the blueshift reduces by more than 50% in less than 1 ps at high fluences. This is highly promising as it potentially allows fast switching of the

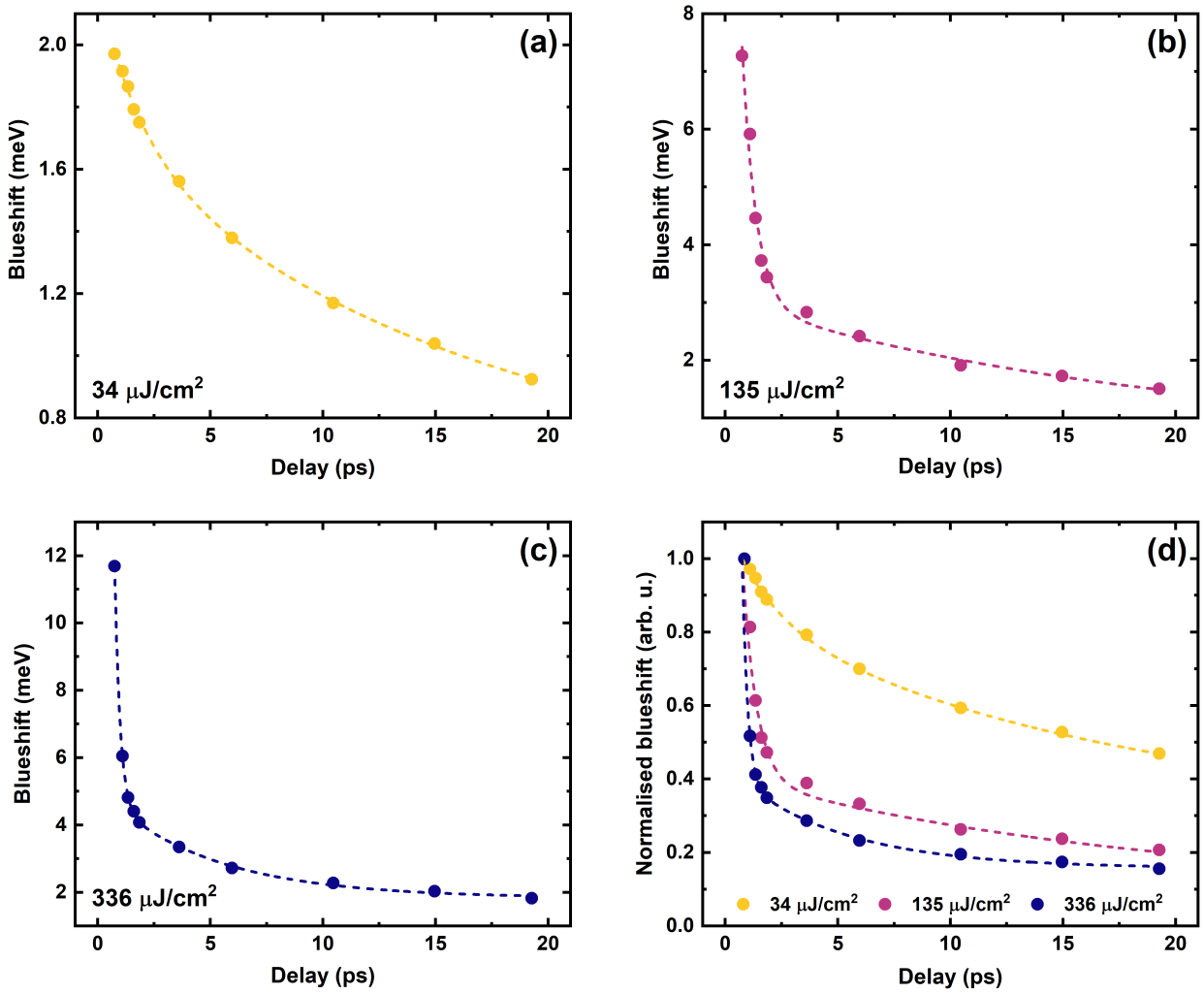

Figure 6.10. Comparison of blueshift dynamics at different fluences. Parts (a), (b) and (c) show the blueshift as a function of delay at a fluence of 34 μJ/cm^2 (gold), 135 μJ/cm^2 (pink), and 336 μJ/cm^2 (purple), respectively. The dashed lines in each panel represent a biexponential fit to the data. Part (d) shows the normalised blueshift dynamics from parts (a)-(c).

Fluence (μJ/cm^2)	τ_1 **(ps)**	τ_2 **(ps)**
34	1.90	16.7
135	0.62	18.8
336	0.24	4.9

Table 6.1. Lifetimes of blueshift at different fluences according to a biexponential fit.

cavity energy and therefore of turning 'on' and 'off' the confinement of the condensate. Indeed, we find that the 'turn on' of the maximum blueshift is also fast and is reached in 600 fs after a pump pulse of 336 μJ/cm^2.

The dynamics of the positive and negative peaks in Figure 6.7(a) were also explored, and these are shown in Figure 8.6 in Appendix C. Although quantitative fits to the data were not possible, it is again evident that the $^{\Delta R}/_{R}$ signal decays quicker at higher fluences as expected.

6.5 Conclusion

We have fabricated multilayer organic polariton cavities that show a controllable blueshift of as much as 14 meV. The magnitude of the blueshift is directly dependent on the excitation fluence and therefore can be tailored as required. The lifetime is also dependent on the excitation fluence and reaches the maximum value of 12 meV in 600 fs when pumped with a fluence of 336 μJ/cm^2 and measured at an angle of 10° to the cavity normal. The decay of the blueshift is also very fast, with the blueshift reaching 50% of its maximum value in 380 fs and $1/e$ of its maximum value in 890 fs. This fast switching of the LPB energy in organic polariton cavities has direct applications as a method to confine polariton condensates and dynamically modulate polariton landscapes, e.g. creating polariton waveguides and routers [16, 17].

6.6 Contributions & acknowledgments

David G. Lidzey[1] and Pavlos G. Lagoudakis[2,3] conceived the project. Kirsty E. McGhee characterised the organic dyes and thin films, and designed, fabricated and characterised the cavities with the assistance of Rahul Jayaprakash[1] and under the supervision of D.G.L.. K.E.M. and Michele Guizzardi[4] performed and analysed the transient absorption and reflectivity measurements under the supervision of Tersilla Virgili[4] and Giulio Cerullo[4].

I would like to thank the Rank Prize for funding my research trip to Politecnico di Milano via their Return to Research grant.

[1]Department of Physics and Astronomy, University of Sheffield, Hicks Building, Hounsfield Road, Sheffield S3 7RH, UK. [2]Department of Physics and Astronomy, University of Southampton, University Road, Southampton SO17 1BJ, UK. [3]Centre of Photonics and Quantum Materials, Skolkovo Institute of Science and Technology, Moscow, Russian Federation 121205. [4]Istituto di Fotonica e Nanotecnologia–CNR, IFN–Dipartimento di Fisica, Politecnico di Milano, Piazza Leonardo da Vinci 32, 20133 Milano, Italy.

6.7 References

[1] Liew, T. C., Kavokin, A. V. & Shelykh, I. A. Optical circuits based on polariton neurons in semiconductor microcavities. *Physical Review Letters* **101**, 1–4 (2008). 0803.0891.

[2] Liew, T. C. *et al.* Exciton-polariton integrated circuits. *Physical Review B - Condensed Matter and Materials Physics* **82**, 1–4 (2010).

[3] Liew, T. C., Shelykh, I. A. & Malpuech, G. Polaritonic devices. *Physica E: Low-Dimensional Systems and Nanostructures* **43**, 1543–1568 (2011).

[4] Sturm, C. *et al.* All-optical phase modulation in a cavity-polariton Mach-Zehnder interferometer. *Nature Communications* **5**, 1–7 (2014).

[5] Kuznetsov, A. S., Biermann, K. & Santos, P. V. Dynamic acousto-optical control of confined polariton condensates: From single traps to coupled lattices. *Physical Review Research* **1**, 1–14 (2019).

[6] Schneider, C. *et al.* Exciton-polariton trapping and potential landscape engineering. *Reports on Progress in Physics* **80** (2017). 1510.07540.

[7] Amo, A. & Bloch, J. Exciton-polaritons in lattices: A non-linear photonic simulator. *Comptes Rendus Physique* **17**, 934–945 (2016).

[8] Dusel, M. *et al.* Room temperature organic exciton–polariton condensate in a lattice. *Nature Communications* **11**, 1–7 (2020).

[9] Scafirimuto, F. *et al.* Tunable exciton–polariton condensation in a two-dimensional Lieb lattice at room temperature. *Communications Physics* **4**, 39 (2021).

[10] Obert, M. *et al.* Nonlinear emission in II-VI pillar microcavities: Strong versus weak coupling. *Applied Physics Letters* **84**, 1435–1437 (2004).

[11] Adawi, A. M. *et al.* Spontaneous emission control in micropillar cavities containing a fluorescent molecular dye. *Advanced Materials* **18**, 742–747 (2006).

[12] Bajoni, D. *et al.* Polariton laser using single micropillar GaAs-GaAlAs semiconductor cavities. *Physical Review Letters* **100**, 1–4 (2008).

[13] Jayaprakash, R. *et al.* Two-Dimensional Organic-Exciton Polariton Lattice Fabricated Using Laser Patterning. *ACS Photonics* **7**, 2273–2281 (2020).

[14] Balili, R., Hartwell, V., Snoke, D., Pfeiffer, L. & West, K. Bose-Einstein Condensation of Microcavity Polaritons in a Trap. *Science* **316**, 1007–1010 (2007).

[15] Balili, R., Nelsen, B., Snoke, D. W., Pfeiffer, L. & West, K. Role of the stress trap in the polariton quasiequilibrium condensation in GaAs microcavities. *Physical Review B - Condensed Matter and Materials Physics* **79**, 1–6 (2009).

[16] Tosi, G. *et al.* Sculpting oscillators with light within a nonlinear quantum fluid. *Nature Physics* **8**, 190–194 (2012).

[17] Cristofolini, P. *et al.* Optical Superfluid Phase Transitions and Trapping of Polariton Condensates. *Physical Review Letters* **110**, 186403 (2013).

[18] Yagafarov, T. *et al.* Mechanisms of blueshifts in organic polariton condensates. *Communications Physics* **3**, 1–10 (2020).

[19] Kadoya, Y. *et al.* Oscillator strength dependence of cavity-polariton mode splitting in semiconductor microcavities. *Applied Physics Letters* **281**, 281 (1995).

[20] Rabe, T. *et al.* Threshold reduction in polymer lasers based on poly(9,9-dioctylfluorene) with statistical binaphthyl units. *Advanced Functional Materials* **15**, 1188–1192 (2005).

[21] Lehnhardt, M., Riedl, T., Scherf, U., Rabe, T. & Kowalsky, W. Spectrally separated optical gain and triplet absorption: Towards continuous wave lasing in organic thin film lasers. *Organic Electronics* **12**, 1346–1351 (2011).

[22] Cookson, T. *et al.* A Yellow Polariton Condensate in a Dye Filled Microcavity. *Advanced Optical Materials* **5**, 1700203 (2017).

[23] McGhee, K. E. *et al.* Polariton condensation in an organic microcavity utilising a hybrid metal-DBR mirror. *Scientific Reports* **11**, 20879 (2021).

[24] Cerullo, G. *et al.* Ultrafast Förster transfer dynamics in tetraphenylporphyrin doped poly(9,9-dioctylfluorene). *Chemical Physics Letters* **335**, 27–33 (2001).

[25] Marciniak, H. *et al.* Photoexcitation dynamics in polyfluorene-based thin films: Energy transfer and amplified spontaneous emission. *Physical Review B* **85**, 214204 (2012).

[26] Xia, R., Heliotis, G., Hou, Y. & Bradley, D. D. Fluorene-based conjugated polymer optical gain media. *Organic Electronics* **4**, 165–177 (2003).

[27] Bansal, A. K., Ruseckas, A., Shaw, P. E. & Samuel, I. D. W. Fluorescence Quenchers in Mixed Phase Polyfluorene Films. *The Journal of Physical Chemistry C* **114**, 17864–17867 (2010).

[28] Tamai, Y., Ohkita, H., Benten, H. & Ito, S. Singlet Fission in Poly(9,9'-di-*n*-octylfluorene) Films. *Journal of Physical Chemistry C* **117**, 10277 (2013).

7 Superabsorption in an organic microcavity: Toward a quantum battery

7.1 Motivation for project

With the world's increasing reliance on technology and its miniaturisation, high-capacity, fast-charging, and compact batteries are going to be crucial in the coming years. The idea of quantum batteries – batteries that charge faster and can store more energy the more you have – is therefore a highly exciting one.

In this work, we have demonstrated superabsorption, the physical process that underpins the quantum battery effect, in a large number of molecules for the first time. Classically, each molecule is able to exist in one of two electronic states: the ground state and the first excited state. Each molecule can therefore be considered as a battery, where the excited state corresponds to the charged state and the ground state to the uncharged state. Quantum mechanically, however, the molecule exists in a superposition of these two states, with a probability of being in either state – this is analogous to a qubit in a quantum computer that can simultaneously be both 0 and 1. In superabsorption, the electronic transitions of the molecules can interfere constructively in a process known as quantum coherence. This allows the molecules to absorb light more efficiently than if they were uncoupled.

By inserting our molecules – the organic dye lumogen-F orange – into a microcavity, we are able to couple them – our batteries – through shared interaction with the cavity mode. By blending the dye at different concentrations in polystyrene, we are able to control the molecule density and therefore the number of batteries. Using pump-probe spectroscopy, we then studied the evolution of the cavity mode as a way of investigating the charging properties of the system. Here, the pump power per battery was kept constant, such that it increased with dye concentration. In this way, the pump-probe signal amplitude and rise time could be used to study battery energy density, charging time and charging power. We found that as the number of batteries (dye molecules) in the system increased, so too did the energy density (energy per battery) and the charging time. In other words, one microcavity containing N molecules charges faster and can store more energy than N individual microcavities each containing a single molecule. These results were confirmed theoretically, where we have also shown that the dissipation in the system is important to achieve long energy discharge times.

We have therefore demonstrated the concept of superabsorption in a large system for the first time and have fabricated a prototype quantum battery that exhibits superextensive energy storage and charging. Although a long way from a practical and commercialisable device, this work is an important proof-of-concept that will spark a new field of research focused on making such technology viable.

7.2 Media coverage

Due to the considerable and far-reaching implications of this work, it has received appreciable coverage in the media. Articles on this research have been published in nearly 20 media outlets, including online science magazines, such as the Institute of Physics' *Physics World* [1], AAAS's *EurekAlert!* [2], IEEE's *Spectrum* [3], and *New Atlas* [4], as well as in more mainstream news outlets, such as *The Independent* [5] and Australian TV news service 7*NEWS* [6]. Perhaps unexpectedly, it has also been picked up by motorcycle news site *Ride Apart* [7] and by construction and farm vehicle news site *Industrial Vehicle Technology International* [8].

It just goes to show that if you put the word 'quantum' in front of anything, people will go wild for it.

7.3 Publication

This section contains the publication as it appears online in *Science Advances*:

Quach, J. Q., McGhee, K. E., *et al.* Superabsorption in an organic microcavity: Toward a quantum battery. *Science Advances* **8**, eabk3160 (2022).

The Supplementary Materials for this publication can be found in Appendix D.

SCIENCE ADVANCES | RESEARCH ARTICLE

PHYSICS

Superabsorption in an organic microcavity: Toward a quantum battery

James Q. Quach[1]*, Kirsty E. McGhee[2], Lucia Ganzer[3], Dominic M. Rouse[4], Brendon W. Lovett[4], Erik M. Gauger[5], Jonathan Keeling[4], Giulio Cerullo[3], David G. Lidzey[2], Tersilla Virgili[3]*

The rate at which matter emits or absorbs light can be modified by its environment, as markedly exemplified by the widely studied phenomenon of superradiance. The reverse process, superabsorption, is harder to demonstrate because of the challenges of probing ultrafast processes and has only been seen for small numbers of atoms. Its central idea—superextensive scaling of absorption, meaning larger systems absorb faster—is also the key idea underpinning quantum batteries. Here, we implement experimentally a paradigmatic model of a quantum battery, constructed of a microcavity enclosing a molecular dye. Ultrafast optical spectroscopy allows us to observe charging dynamics at femtosecond resolution to demonstrate superextensive charging rates and storage capacity, in agreement with our theoretical modeling. We find that decoherence plays an important role in stabilizing energy storage. Our work opens future opportunities for harnessing collective effects in light-matter coupling for nanoscale energy capture, storage, and transport technologies.

INTRODUCTION

The properties of physical systems can typically be categorized as intensive (i.e., they are independent of the system size, such as density) or extensive (i.e., they grow in proportion to system size, such as mass). However, in some cases, cooperative effects can lead to superextensive scaling. A well-studied example of this is superradiant emission (*1*). In its original form, this describes emission from an ensemble of N emitters into free space. Constructive interference in the emission process means that the time for emission scales as $1/N$, so that peak emission power is superextensive, scaling as N^2. This behavior has been demonstrated on a number of platforms [low-pressure gases (*2*, *3*), quantum wells (*4*, *5*) and dots (*6*), J aggregates (*7*), Bose-Einstein condensates (*8*), trapped atoms (*9*), and nitrogen-vacancy centers (*10*)]. A less-studied example is superabsorption (*11*), describing the N-dependent enhancement of absorption of radiation by an ensemble of N two-level systems (TLSs). Only very recently has this been demonstrated for a small number of atoms (*12*). In principle, superabsorption could have important implications for energy storage and capture technologies, particularly if realized in platforms compatible with energy harvesting, such as organic photovoltaic devices. However, there are challenges in engineering the precise environment in which such behavior can occur and in monitoring the ultrashort charging time scales. Here, we show how these can be overcome, by combining organic microcavity fabrication with ultrafast pump-probe spectroscopy.

Superextensive scaling of energy absorption is also a key property of quantum batteries (QBs). These represent a new class of energy storage devices that operate on distinctly quantum mechanical principles. In particular, they are driven either by quantum entanglement, which reduces the number of traversed states in the Hilbert space compared to (classical) separable states alone (*13*–*21*), or by cooperative behavior that increases the effective quantum coupling between battery and source (*22*–*24*). These effects mean that QBs exhibit a charging time that is inversely related to the battery capacity. This leads to the intriguing idea that the charging power of QBs is superextensive, that is, it increases faster than the size of the battery. For a QB consisting of a collection of N identical quantum systems, a superextensive charging rate density (charging rate per subsystem) that scales as N or $\sqrt{N}$ in the thermodynamic limit (*20*) has been predicted.

Here, we experimentally realize a paradigmatic model proposed as a Dicke QB (*24*), which displays superextensive scaling of energy absorption, using an organic semiconductor as an ensemble of TLSs coupled to a confined optical mode in a microcavity. We also demonstrate how dissipation plays a crucial role; in a closed system, the coherent effects that lead to fast charging can also lead to subsequent fast discharging. Hence, stabilization of stored energy remains an open question: Proposed stabilization methods include continuous measurements (*25*), dark states (*21*), and novel energy trapping mechanisms (*26*, *27*). In our open noisy system, dephasing causes transitions between the optically active bright mode and inactive dark modes. This suppresses emission into the cavity mode, so that we have fast absorption of energy but slow decay, allowing retention of the stored energy until it can be used.

RESULTS

Device structure

The structures fabricated consist of a thin (active) layer of a low-mass molecular semiconductor dispersed into a polymer matrix that is deposited by spin coating and positioned between two dielectric mirrors, forming a microcavity as illustrated schematically in Fig. 1A (see Materials and Methods for fabrication details). Organic semiconductors are particularly promising for many applications as the high oscillator strength and binding energy of molecular excitons mean that light can be absorbed efficiently, and excitons can exist at

[1]Institute for Photonics and Advanced Sensing and School of Chemistry and Physics, The University of Adelaide, South Australia 5005, Australia. [2]Department of Physics and Astronomy, University of Sheffield, Hicks Building, Hounsfield Road, Sheffield S3 7RH, UK. [3]Istituto di Fotonica e Nanotecnologia–CNR, IFN–Dipartimento di Fisica, Politecnico di Milano, Piazza Leonardo da Vinci 32, 20133 Milano, Italy. [4]SUPA, School of Physics and Astronomy, University of St Andrews, St Andrews KY16 9SS, UK. [5]SUPA, Institute of Photonics and Quantum Sciences, Heriot-Watt University, Edinburgh EH14 4AS, UK.
*Corresponding author. Email: quach.james@gmail.com (J.Q.Q.); tersilla.virgili@polimi.it (T.V.)

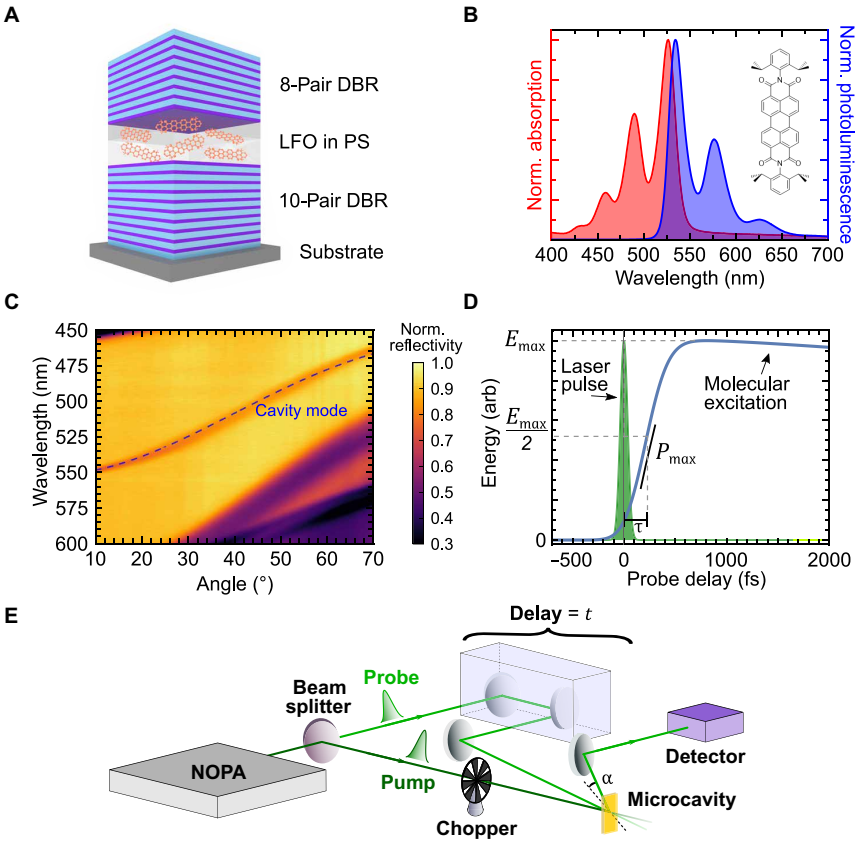

Fig. 1. Schematics of the LFO microcavity and experimental setup. (**A**) Microcavity consisting of Lumogen-F orange (LFO) dispersed in a polystyrene (PS) matrix between distributed Bragg reflectors (DBRs). (**B**) Normalized absorption (red) and photoluminescence (blue) spectra for 1% concentration LFO film, with the molecular structure shown in the inset. We operate near peak absorption/photoluminescence. (**C**) Angle-dependent reflectivity of the 1% cavity, with a fit for the cavity mode shown by the blue dashed line. (**D**) A laser pump pulse excites the LFO molecules. The energetics of the molecules are then measured with probe pulses delayed by time *t*, from which we can ascertain the peak energy density (E_{max}), rise time (τ), and peak charging power (P_{max}). (**E**) Experimental setup for ultrafast transient reflectivity measurements. The output of a noncollinear optical parametric amplifier (NOPA) is split to generate pump (dark green) and probe (light green) pulses. A mechanical chopper is used to modulate the pump pulse to produce alternating pump-probe and probe-only pulses.

room temperature (*28*). The organic semiconductor used in this study was the dye Lumogen-F orange (LFO), whose chemical structure is shown in Fig. 1B. The normalized absorption and photoluminescence spectra for LFO dispersed at 1% concentration by mass in a polystyrene (PS) matrix are shown in Fig. 1B. By diluting the LFO, we reduce intermolecular interactions that lead to emission quenching, producing a high photoluminescence quantum yield of around 60% at low concentration (see fig. S1). The absorption peak at 526 nm and the emission peak at 534 nm correspond to the 0-0 transition, i.e., an electronic transition from and to the lowest vibrational state. Operating around the 0-0 transition, the LFO molecules can reasonably be considered as a TLS. We prepared samples with 0.5, 1, 5, and 10% concentrations, as these are representative of the optimal operating regimes; further increases in concentration lead to quenching, and signals from lower concentrations are indiscernible from noise. The absorption and photoluminescence spectra for the 0.5, 5, and 10% concentrations are given in fig. S2.

The optical microcavities fabricated support cavity modes whose energy is determined by the optical thickness of the LFO layer and the penetration of the optical field into the cavity mirrors (*29*). The confined photon field drives coherent interactions with the molecules, which underpin the collective effects that drive superabsorption. The LFO concentration dictates the operating coupling regime, with the 0.5 and 1% LFO cavities operating in the weak coupling regime, the 5% in the intermediate coupling regime, and the 10% in the strong coupling regime (see fig. S2 and discussion in Materials and Methods).

Experimental setup

Charging and energy storage dynamics were measured using ultrafast transient-absorption spectroscopy (*30*), allowing femtosecond charging times to be measured. In this technique, we excite the microcavity with a pump pulse and then measure the evolution of stored energy (i.e., corresponding to the number of excited molecules) with a second probe pulse, delayed by time *t* (Fig. 1D). The probe pulse is transmitted through the top distributed Bragg reflector (DBR) of the cavity, and the reflection from the bottom DBR is measured. The differential reflectivity induced by the pump pulse is given by

$$\frac{\Delta R}{R}(t) = \frac{R_{ON}(t) - R_{OFF}}{R_{OFF}} \quad (1)$$

where R_{ON} (R_{OFF}) is the probe reflectivity with (without) the pump excitation. Note that control films (active layers without the microcavities) are measured under differential transmittivity $\Delta T/T$. The control films will allow us to identify the underlying photophysics of the molecules.

In our experimental setup (shown schematically in Fig. 1E), transient-absorption measurements were performed in a degenerate, almost collinear configuration. Pump and probe pulses were generated by a broadband noncollinear optical parametric amplifier (NOPA) (*31*) and spanned the wavelength range of 500 to 620 nm with a nearly transform-limited sub–20-fs duration (further details in Materials and Methods). An optical delay line was used to control the probe delay time, and a mechanical chopper was used to modulate the pump pulse, providing alternating probe-only and pump-probe pulses, allowing us to measure pump-induced absorption changes. Measurements at different molecular concentrations were performed, adjusting the pump fluence to maintain an approximately constant photon density (i.e., pump photons per LFO molecule) $r = kN_\gamma/N$, where N is the total number of molecules in the excitation volume, N_γ is the total number of pump laser photons, and k is the fraction of them that actually reaches the active layer of the microcavity. We estimate from the reflectivity data that only 6 to 8% of the initial pump excitation enters the cavity. We conducted our experiment in air at room temperature.

Results

We first show that ultrafast transient-absorption spectroscopy can monitor the population of excited molecules, even in a cavity, by comparing the control film and the microcavity spectra as shown in Fig. 2A. A representative control film $\Delta T/T$ spectrum is shown for a probe delay time of 1.0 ps, and the $\Delta R/R$ spectra of the microcavities are shown at a delay of 1.25 ps (further data are given in the Supplementary Materials). We found the control film spectra at all concentrations to show two positive bands around 530 and 577 nm, which both reflect excited-state populations. By comparison with the spectra in Fig. 1B, we attribute the 530-nm band to ground state bleaching, i.e., suppression of absorption due to molecules already being in their excited state. The 577-nm band instead corresponds to stimulated emission by excited molecules. For each of the microcavity spectra, we have a single prominent peak, which corresponds to the transient signal filtered by the cavity mode. This implies that the time-dependent transient reflectivity signal is proportional to the change in the number of excited molecules created by the pump (*32*), i.e., $\frac{\Delta R}{R}(t) \propto N_\uparrow(t)$. Since the energy stored in the molecules is also proportional to the number of excited molecules $E(t) \propto N_\uparrow(t)$, we can thus monitor the stored energy. While the experiment directly provides the time dependence, estimating the absolute scale of energy density requires multiplying $\Delta R/R$ by a time-independent constant. Estimating this constant from first principles is challenging, so we instead extract it through fitting to the theoretical model, which is discussed below. This fitting is discussed in section S3. We also note that two of the microcavity spectra show a negative $\Delta R/R$ band, which results from the change in the refractive index induced by the pump pulse (*33*).

Figure 2B shows the experimental values for the time-dependent stored energy density. In all microcavities studied, the energy density

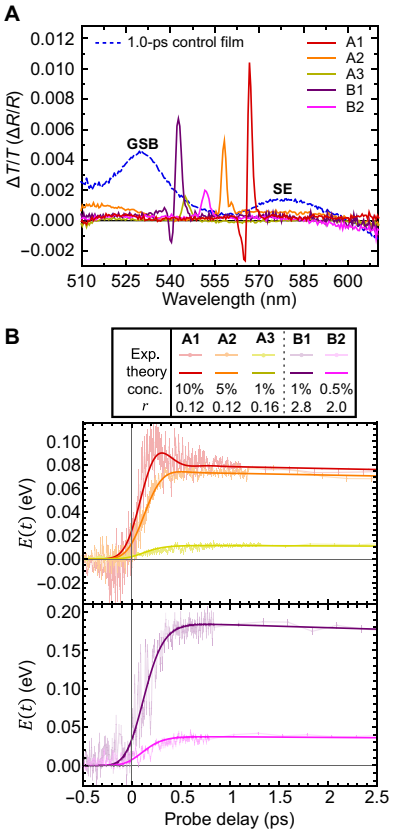

Fig. 2. Experimental demonstration of superextensive charging. (**A**) Differential transmittivity ($\Delta T/T$) spectra for the control film (at 1% LFO concentration) at a probe delay time of 1.0 ps and the differential reflectivity ($\Delta R/R$) spectra for the microcavities at 1.25-ps probe delay. (**B**) Temporally resolved energy density of the microcavities shows that rise time decreases as stored energy density increases, indicating superextensive charging. A1, A2, and A3 label results for microcavities containing LFO at concentrations of 10, 5, and 1%, as the ratio of pump photons to molecules is kept approximately constant at $r \simeq 0.14$. B1 and B2 label measurements for LFO at concentrations of 1 and 0.5%, with $r \simeq 2.4$. The use of two different r values was necessary to achieve a sufficiently high signal-to-noise ratio. Points mark the experimental data, while continuous solid lines are the results of the theoretical model, with parameters given by a chi-squared minimization of the experimental data. Experimental uncertainties are estimated from the point-to-point variance of the data. GSB, ground state bleaching; SE, stimulated emission.

undergoes a rapid rise followed by slow decay. The time scale of the rapid rise varies with concentration. We adjust the laser power to fix photon density r across comparable microcavities and compare behavior with different LFO concentrations. Details of how r is estimated are provided in the Supplementary Materials. We found that to achieve a sufficiently high signal-to-noise ratio, it was not possible to compare all microcavities at the same r value; instead, a constant r value was maintained for matched structures. Specifically, measurements were made on microcavities with LFO concentrations of 10, 5, and 1% with approximately constant $r \simeq 0.14$ (respectively labeled as A1, A2, and A3), and 1 and 0.5% with $r \simeq 2.4$ (labeled as B1 and B2).

Overlaying the experimental data are the corresponding theoretical predictions (see the "Theoretical model" section). To account

for both the instrument response time (~20 fs) and the cavity photon lifetime (which was estimated as discussed in the Supplementary Materials), the theoretical curves are convolved with a Gaussian response function with a full width at half maximum of ~120 fs. There is good agreement between the experimental data and the corresponding theoretical curves.

To obtain energetic dynamics, we take away the response function from the theoretical fit, as shown in fig. S15. Table 1 summarizes the rise time or the time to reach half maximum energy (τ), the peak stored energy density (E_{max}), and the charging rate or peak charging power density [P_{max} = max (dE/dt)]. These are extracted from the theoretical fit to the data presented in Fig. 2B. We see that τ decreases with N, while E_{max} and P_{max} increase with N. Recalling that E_{max} and P_{max} are the stored energy and charging power per molecule, this indicates superextensive behavior. The scaling with N is not the same across all experiments, and in table S2, we summarize the different scaling.

Our results demonstrate that as the number of molecules in the microcavity increases, its charging power density remarkably increases. This means that it takes less time to charge a single microcavity containing N molecules than it would to charge N single-molecule microcavities, even if the latter were charged simultaneously. Furthermore, one microcavity with N molecules would store more energy than N microcavities, where each contained a single molecule. These superextensive properties are the key experimental findings of our work and are supported by the theoretical modeling presented in the next section.

Theoretical model

The experimental dynamics can be reproduced by modeling, with the Lindblad master equation, the N TLSs in an optical cavity with light-matter coupling strength g, a driving laser with a Gaussian pulse envelope and peak amplitude η_0, and three decay channels corresponding to the cavity decay (κ), TLS dephasing (γ^z), and TLS relaxation (γ^-). To solve this many-body Lindblad master equation, we make use of the cumulant expansion (*34*–*36*), with model parameters given by a chi-squared minimization of the experimental data. Experimental uncertainties are estimated from the point-to-point variance of the data. Further details can be found in Materials and Methods and in the Supplementary Materials.

Table 1. Summary of the experimental results. In each experimental groupings A,B the number of molecules (N) increases while the ratio of photons to molecules remains constant ($r \approx 0.105$ and 2.4, respectively). The rise time τ is defined by the time to reach $E_{max}/2$, where E_{max} is the peak stored energy per molecule or energy density. The charging rate P_{max} = max(dE/dt) is the peak charging power per molecule or charging power density.

Exp.	N(×10^{10})	τ (ps)	E_{max} (eV)	P_{max} (eV/ps)
A1	16.0	0.094	0.108	0.791
A2	8.1	0.120	0.076	0.412
A3	1.6	0.118	0.011	0.060
B1	0.16	0.114	0.184	1.008
B2	0.21	0.105	0.037	0.221

From our cumulant expansion simulations, we show how τ, E_{max}, and P_{max} vary as a function of N in Fig. 3 (A and B). The interplay among the decay channels, driving laser, and cavity couplings gives rise to a rich set of behaviors. We identify three regimes: decay-dominated at small N and coupling-dominated at large N, along with a crossover regime between them. The system exhibits superextensive energy density scaling in the decay-dominated regime and subextensive charging time in the coupling-dominated regime. In the crossover regime, the system exhibits both superextensive energy density scaling and subextensive charging times. Charging power density is superextensive in all regimes.

Figure 3 (C and D) shows the typical time dependence in decay-dominated and coupling-dominated regimes, indicating how the model parameters affect the dynamics. In particular, the presence of the decay channels gives rise to ratchet states that are capable of absorbing but not emitting light (*37*), thereby allowing the energy to be stably stored. See Materials and Methods and the Supplementary Materials for further discussion on the operating regimes. Figure 3 is augmented with an animation of how the energetic dynamics changes with N (see movie S1).

Figure 3 (A and B) provides an explanation for the different scaling of the observables with N in Table 1. Specifically, A1 and A2 operate in the coupling-dominated regime, where τ scales slightly less than $N^{-1/2}$, E_{max} scales slightly more than N^0, and P_{max} scales

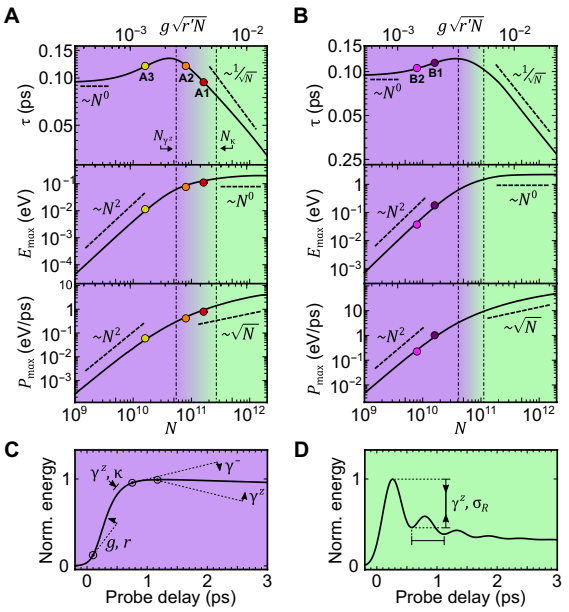

Fig. 3. Charging dynamics as a function of the number of molecules. (**A** and **B**) Theoretical model (solid line) for r = 0.14 and 2.4, respectively. We show three operating regimes: decay-dominated (purple), coupling-dominated (green), and a decay-coupling-crossover regime. The decay-dominated regime is bounded by $N_\kappa < \kappa^2/g^2r'$, and the coupling-dominated regime is bounded by $N_{\gamma z} > \gamma^{z2}/g^2r'$, where $r' = \max(1, r)$. The colored dots indicate where the experiments sit on these curves. The uncertainty in N is 10%, which is smaller than the dot size. (**C**) qualitatively depicts the effects of the model parameters in shaping the dynamics in the decay-dominated regime. (**D**) qualitatively depicts the effects of the additional model parameters in shaping the dynamics in the coupling-dominated regimes. σ_R is the temporal width of the instrument response function.

slightly more than $N^{1/2}$. For the region between A2 and A3, the average scaling of τ falls between N^0 and $N^{-1/2}$, E_{max} between N^2 and N^0, and P_{max} between N^2 and $N^{1/2}$. As A2 is further into the coupling-dominated regime than A3 is into the decay-dominated regime, the average scaling values between A2 and A3 are skewed toward the coupling-dominated scalings. B1 and B2 operate in the crossover regime, with an average scaling with N that is between the decay-dominated and coupling-dominated scalings, as reflected in Table 1.

Discussion

We have provided direct experimental evidence of superextensive energy storage capacity and charging in an organic microcavity by using ultrafast optical spectroscopy. Our realization of a prototype Dicke QB highlights the fact that purely closed unitary dynamics is insufficient for realizing a practical QB. The retention of energy requires finely tuned decoherence processes, allowing the battery to charge quickly and yet discharge much more slowly. This stabilization of stored energy is a key step to exploit superextensive charging. Our observation of dephasing shows that realistic noisy environments can aid the implementation and application of useful QBs. A challenge for future work is to explore further how concepts of ratchet states could keep a QB operating in the range of higher-lying energy states that are associated with maximum absorption enhancement, i.e., near the midpoint of the Dicke ladder (*37*).

We conclude by discussing the potential for future applications based on superextensive charging. One practical challenge noted above is that quenching limits the performance of the QB at high concentrations. Overcoming this limitation requires careful choice of materials to suppress intermolecular quenching. We note that there are classes of materials where quenching is particularly suppressed. For example, in proteins such as green fluorescent protein (*38*), the active chromophore is surrounded by a cage, which suppresses exciton-exciton quenching at high intensities. These materials might provide a route to allow the study of higher concentrations. Beyond energy storage, the key challenge for practical applications of this effect is its integration in devices where energy can be efficiently extracted and used. While our focus has been on the quantum advantage in charging, there do exist approaches to efficiently extract energy. For example, this may be achieved by including charge transport layers between the active layer and the cavity layers (*39*). The transport layers allow charge separation of the excitons as well as preventing recombination. This transforms the top cavity layer into a cathode and the bottom cavity into an anode, giving rise to an electric current. Hence, our work provides a direct path for the integration of the superextensive energy absorption process in an organic photovoltaic device. The fast dynamics of such a device may also be useful as an optical sensor in low-light conditions or potentially for energy harvesting applications (*40*–*43*). More generally, the idea of superextensive charging may have wide-reaching consequences for sensing and energy capture and storage technologies.

MATERIALS AND METHODS

Device fabrication

The microcavities constructed consist of a thin layer of LFO (Kremer Pigmente) dispersed in a PS (Sigma-Aldrich; average molecular weight of ~192,000) matrix. The bottom DBR consisted of 10 pairs of SiO_2/Nb_2O_5 and were fabricated using a mixture of thermal evaporation and ion-assisted electron beam deposition by Helia Photonics Ltd. Solutions of LFO dissolved in PS (25 mg/ml) in dichloromethane were prepared at 0.5, 1, 5, and 10% concentration by mass. Each LFO solution was then spin coated on top of the bottom DBR to produce a thin film with an approximate thickness of 185 nm. An eight-pair DBR was then deposited on top of the LFO layer using electron beam deposition. With this pair of mirrors, the reflectivity was >99% in the spectral region of interest (*44*).

The diluted molecules are expected to be isolated at a low concentration of 0.1 to 1%, but at higher dye concentrations, the 0-0 emission transition red-shifts by a few nanometers, and the second peak increases in intensity because of aggregation of the dye molecules. This is evident in fig. S2 (A and B), with additional broader features observed at longer wavelengths, which we assign to intermolecular states such as excimers.

The 0.5 and 1% cavities lie in the weak coupling regime, i.e., no polaritonic splitting could be seen in the cavity reflectivity spectrum, as shown in fig. S2. For the 5% cavity, we see a weak anticrossing feature in the reflectivity spectrum (a small kink near the crossing), indicating operation in the intermediate coupling regime. The 10% cavity operated in the strong coupling regime, showing a Rabi splitting of around 100 meV around the 0-0 transition (along with intermediate coupling between the cavity mode and the 0-1 transition). Figure S3 shows a transfer matrix simulation of the electric field distribution of the 1% cavity (the cavities exhibit similar distributions).

Pump-probe spectroscopy

Probe and pump pulses were generated by a NOPA. The NOPA was pumped by a fraction (450 μJ) of the laser beam generated by a regeneratively amplified Ti:Sapphire laser (Coherent Libra) producing 100-fs pulses at 800 nm at a repetition rate of 1 kHz. A pair of chirped mirrors were placed at the output of the NOPA to compensate for temporal dispersion, and by using seven "bounces," we were able to generate pulses with a temporal width below 20 fs. The laser beam was then split by a beam splitter, with the probe being delayed via a translation stage and the pump being modulated mechanically using a chopper at 500 Hz.

Lindblad master equation

As noted above, we find that the experimental behavior is well reproduced by the dynamics of the Dicke model, a model of a microcavity photon mode coupled to TLSs representing the molecules. As further discussed in the Supplementary Materials, such a model is generally an approximation for organic molecules but for some systems can become a very accurate approximation in the limit of low temperatures (*45*).

The open driven nature of the experimental system is modeled with the Lindblad master equation

$$\dot{\rho}(t) = -\frac{i}{\hbar}[H(t), \rho(t)] + \sum_{j=1}^{N} (\gamma^z \mathcal{L}[\sigma_j^z] + \gamma^- \mathcal{L}[\sigma_j^-]) + \kappa \mathcal{L}[a] \qquad (2)$$

where $\rho(t)$ is the density matrix, and $\mathcal{L}[O] \equiv O\rho O^\dagger - \frac{1}{2} O^\dagger O\rho - \frac{1}{2}\rho O^\dagger O$ is the Lindbladian superoperator. $a^\dagger$ and a are the cavity photon creation and annihilation operators, and $\sigma_j^{x,y,z}$ are the Pauli spin matrices for each molecule, with the raising and lowering spin operators defined as $\sigma_j^\pm = (\sigma_j^x \pm i\sigma_j^y)/2$. There are three decay channels corresponding to the cavity decay (κ), dephasing (γ^z), and relaxation rate (γ^-) of the individual TLSs. The Hamiltonian for the LFO molecules in cavity is modeled as a collection of noninteracting TLSs with characteristic frequency ω equal to that of the cavity

mode and resonantly coupled to the cavity with strength g. The molecules are driven by a laser described by a Gaussian pulse envelope $\eta(t) = \frac{\eta_0}{\sigma\sqrt{2\pi}} e^{-\frac{1}{2}\left(\frac{t-t_0}{\sigma}\right)^2}$ and a carrier frequency ω_L. We work in the frame of the laser carrier frequency, and so write

$$H(t) = \hbar\Delta a^\dagger a + \sum_{j=1}^{N}\left[\frac{\hbar\Delta}{2}\sigma_j^z + g(a^\dagger\sigma_j^- + a\sigma_j^+)\right] + i\hbar\eta(t)(a^\dagger - a) \quad (3)$$

where $\Delta = \omega - \omega_L$ is the detuning of the cavity frequency from the laser driving frequency. The LFO molecules are initially in the ground state, and the laser is on resonance ($\Delta = 0$).

Cumulant expansion

The energy density of the cavity containing identical molecules with transition energy ω is $E(t) = \frac{\hbar\omega}{2}[\langle\sigma^z(t)\rangle + 1]$. In general, the equation of motion $(\partial/\partial t)\langle\sigma^z\rangle = \mathrm{Tr}[\sigma^z\dot{\rho}]$ depends on both the first-order moments $\langle\sigma^{x,\,y,\,z}\rangle$ and $\langle a\rangle$ and higher-order moments, leading to a hierarchy of coupled equations. Within mean field theory, the second-order moments are factorized as $\langle AB\rangle = \langle A\rangle\langle B\rangle$, which closes the set of equations at first order. This approximation is valid at large N, as corrections scale as $1/N$. To capture the leading order effects of finite sizes, we make a second-order cumulant expansion (*34*–*36*), i.e., we keep second-order cumulants $\langle\langle AB\rangle\rangle = \langle AB\rangle - \langle A\rangle\langle B\rangle$ and assume that the third-order cumulants vanish, which allows us to rewrite third-order moments into products of first- and second-order moments (*46*). In our experiments, the number of molecules in the cavity is large ($>10^{10}$), and we find that higher-order correlations are negligible. We give the equations of motion up to second order in the Supplementary Materials.

Operating regimes

The decay-dominated (purple region in Fig. 3, A and B) regime occurs when the collective light-matter coupling is weaker than the decay channels, $g\sqrt{\mathrm{N}r'} < \{\kappa, \gamma^z, \gamma^-\}$, where $r' = \max(1, r)$. In this regime, the time scale of cavity dynamics is slow relative to the decay rate. Figure 3C shows a typical time dependence in this regime, indicating how the model parameters affect the dynamics. In this regime, the increase in the effective coupling relative to the decay strength sees an N^2 superextensive scaling of the energy and power density, while rise time remains constant. Experiment A3 operates near the boundary of this regime (Fig. 3A).

In the coupling-dominated (green region in Fig. 3, A and B) regime, the effective collective light-matter coupling $g\sqrt{\mathrm{N}r'} > \{\gamma^z, \gamma^-, \kappa\}$ dominates over the decay channels. In this regime, the time scale of cavity dynamics is fast relative to the decay rate, and we observe $\sqrt{N}$-superextensive power scaling and $1/\sqrt{N}$ dependence of rise time, while the maximum energy density remains constant. While power scaling is superextensive in both regimes, the origin of this differs: For the decay-dominated regime, this is the result of the superextensive energy scaling, while for the coupling-dominant regime, it is the result of a superextensive decrease in the rise time. Experiments A1 and A2 operate in this regime (Fig. 3A).

In the crossover between the regimes (purple-green), the collective coupling falls between the cavity decay rate and the TLS dephasing rate, $\{\kappa, \gamma^-\} < g\sqrt{\mathrm{N}r'} < \gamma^z$. In Fig. 3 (A and B), γ^- is small such that $g\sqrt{\mathrm{N}r'} \gg \gamma^-$ for all values of N, and so, there is no boundary labeled for this decay rate. In this case, capacity and rise time can simultaneously scale super- and subextensively, but at a rate slower than in the decay and coupling-dominated regimes, respectively. Experiments B1 and B2 operate in this regime (Fig. 3B).

Decay and coupling rates

The parameters needed in the theory calculations are the cavity leakage rate κ, the dephasing rate γ^z, the nonradiative decay rate γ^-, the interaction strength g, and the temporal width of the instrument response function σ_R. Note that the temporal width of the pump pulse is fixed at $\sigma = 20$ fs. For the dephasing rate, we note that as one enters the strong coupling regime, exciton delocalization suppresses the effect of dephasing (*47*). To approximately capture this effect, we assume that the dephasing rate scales with the number of molecules as $\gamma^z = \gamma_0^z(N_{5\%}/N)$, where γ_0^z is taken to be constant, and $N_{5\%}$ is the number of molecules in the 5% cavity. The experimental uncertainty in N is estimated to be 10%. The cavity lifetime T comes into the model in both $\sigma_R = T$ and the cavity leakage rate $\kappa = 1/T$. From transfer matrix modeling on the 1 and 0.5% cavities (where polariton effects are small), we estimate that $T \approx 306$ fs. However, on the basis of the measured finesse of the cavities, we estimate that $T = 120$ fs. Transfer matrix modeling assumes perfectly smooth mirrors, while measured finesse includes inhomogeneous broadening effects, neither of which we want to include in κ and σ_R. In the following optimization, we therefore assume that $T \in [120,306]$ fs, with lower values more likely due to transfer matrix calculations being prone to error.

For T values within this range, the remaining three parameters in the model (γ_0^z, γ^-, and g) were found through a global chi-squared optimization, simultaneously optimizing over all experiments. Uncertainties in these fitting parameters were then estimated by using the reduced $\tilde{\chi}^2$ distribution to find the 68% confidence interval of the model parameters. This corresponds to the range $\tilde{\chi}^2 \leq \tilde{\chi}^2_{\min} + \Delta$, where for a three-parameter optimization and k total data points, $\Delta \approx 3.51/(k-3)$ (*48*). In the Supplementary Materials, we present a figure showing the minimum reduced chi-squared value as a function of T, and for each point, we show the optimal set of parameters (γ_0^z, γ^-, and g) along with the 68% confidence intervals. From this, and by comparison of the experimentally measured and theoretically calculated reflectivity for each parameter set, we concluded that the lifetime most representative of the data was $T = 120$ fs, with $\gamma^- = (0.0141^{+0.0031}_{-0.0024})$ meV, $g = (10.6^{+2.2}_{-1.3})$ neV, and $\gamma_0^z = (1.68^{+0.25}_{-0.18})$ meV. See the Supplementary Materials for more details.

SUPPLEMENTARY MATERIALS

Supplementary material for this article is available at https://science.org/doi/10.1126/sciadv.abk3160

REFERENCES AND NOTES

1. M. Gross, S. Haroche, Superradiance: An essay on the theory of collective spontaneous emission. *Phys. Rep.* **93**, 301–396 (1982).
2. N. Skribanowitz, I. P. Herman, J. C. MacGillivray, M. S. Feld, Observation of Dicke superradiance in optically pumped HF Gas. *Phys. Rev. Lett.* **30**, 309–312 (1973).
3. H. M. Gibbs, Q. H. F. Vrehen, H. M. J. Hikspoors, Single-pulse superfluorescence in cesium. *Phys. Rev. Lett.* **39**, 547–550 (1977).
4. J. Feldmann, G. Peter, E. O. Gobel, P. Dawson, K. Moore, C. Foxon, R. J. Elliott, Linewidth dependence of radiative exciton lifetimes in quantum-wells. *Phys. Rev. Lett.* **59**, 2337–2340 (1987).
5. B. Deveaud, F. Clerot, N. Roy, K. Satzke, B. Sermage, D. S. Katzer, Enhanced radiative recombination of free excitons in GaAs quantum wells. *Phys. Rev. Lett.* **67**, 2355–2358 (1991).
6. T. Itoh, M. Furumiya, Size-dependent homogeneous broadening of confined excitons in cucl microcrystals. *JOL* **48-49**, 704–708 (1991).
7. S. Deboer, D. A. Wiersma, Dephasing-induced damping of superradiant emission in J-aggregates. *Chem. Phys. Lett.* **165**, 45–53 (1990).

8. S. Inouye, A. P. Chikkatur, D. M. Stamper-Kurn, J. Stenger, D. E. Pritchard, W. Ketterle, Superradiant Rayleigh scattering from a Bose-Einstein condensate. *Science* **285**, 571–574 (1999).
9. R. Reimann, W. Alt, T. Kampschulte, T. Macha, L. Ratschbacher, N. Thau, S. Yoon, D. Meschede, Cavity-modified collective Rayleigh scattering of two atoms. *Phys. Rev. Lett.* **114**, 023601 (2015).
10. A. Angerer, K. Streltsov, T. Astner, S. Putz, H. Sumiya, S. Onoda, J. Isoya, W. J. Munro, K. Nemoto, J. Schmiedmayer, J. Majer, Superradiant emission from colour centres in diamond. *Nat. Phys.* **14**, 1168–1172 (2018).
11. K. D. Higgins, S. C. Benjamin, T. M. Stace, G. J. Milburn, B. W. Lovett, E. M. Gauger, Superabsorption of light via quantum engineering. *Nat. Commun.* **5**, 4705 (2014).
12. D. Yang, S.-h. Oh, J. Han, G. Son, J. Kim, J. Kim, M. Lee, K. An, Realization of superabsorption by time reversal of superradiance. *Nat. Photonics* **15**, 272–276 (2021).
13. R. Alicki, M. Fannes, Entanglement boost for extractable work from ensembles of quantum batteries. *Phys. Rev. E Stat. Nonlin. Soft Matter Phys.* **87**, 042123 (2013).
14. K. V. Hovhannisyan, M. Perarnau-Llobet, M. Huber, A. Acin, Entanglement generation is not necessary for optimal work extraction. *Phys. Rev. Lett.* **111**, 240401 (2013).
15. F. C. Binder, S. Vinjanampathy, K. Modi, J. Goold, Quantacell: Powerful charging of quantum batteries. *New J. Phys.* **17**, 075015 (2015).
16. G. M. Andolina, D. Farina, A. Mari, V. Pellegrini, V. Giovannetti, M. Polini, Charger-mediated energy transfer in exactly solvable models for quantum batteries. *Phys. Rev. B* **98**, 205423 (2018).
17. G. M. Andolina, M. Keck, A. Mari, M. Campisi, V. Giovannetti, M. Polini, Extractable work, the role of correlations, and asymptotic freedom in quantum batteries. *Phys. Rev. Lett.* **122**, 047702 (2019).
18. R. Alicki, A quantum open system model of molecular battery charged by excitons. *J. Chem. Phys.* **150**, 214110 (2019).
19. Y. Y. Zhang, T. R. Yang, L. Fu, X. Wang, Powerful harmonic charging in a quantum battery. *Phys. Rev. E* **99**, 052106 (2019).
20. F. Campaioli, F. A. Pollock, F. C. Binder, L. Celeri, J. Goold, S. Vinjanampathy, K. Modi, Enhancing the charging power of quantum batteries. *Phys. Rev. Lett.* **118**, 150601 (2017).
21. J. Q. Quach, W. J. Munro, Using dark states to charge and stabilize open quantum batteries. *Phys. Rev. Appl.* **14**, 024092 (2020).
22. T. P. Le, J. Levinsen, K. Modi, M. M. Parish, F. A. Pollock, Spin-chain model of a many-body quantum battery. *Phys. Rev. A* **97**, 022106 (2018).
23. X. Zhang, M. Blaauboer, Enhanced energy transfer in a Dicke quantum battery. arXiv:1812.10139 (2018).
24. D. Ferraro, M. Campisi, G. M. Andolina, V. Pellegrini, M. Polini, High-power collective charging of a solid-state quantum battery. *Phys. Rev. Lett.* **120**, 117702 (2018).
25. S. Gherardini, F. Campaioli, F. Caruso, F. C. Binder, Stabilizing open quantum batteries by sequential measurements. *Phys. Rev. Res.* **2**, 013095 (2020).
26. A. C. Santos, A. Saguia, M. S. Sarandy, Stable and charge-switchable quantum batteries. *Phys. Rev. E* **101**, 062114 (2020).
27. W. M. Brown, E. M. Gauger, Light harvesting with guide-slide superabsorbing condensed-matter nanostructures. *J. Phys. Chem. Lett.* **10**, 4323–4329 (2019).
28. D. Sanvitto, S. Kéna-Cohen, The road towards polaritonic devices. *Nat. Mater.* **15**, 1061–1073 (2016).
29. V. Savona, L. C. Andreani, P. Schwendimann, A. Quattropani, Quantum well excitons in semiconductor microcavities: Unified treatment of weak and strong coupling regimes. *Solid State Commun.* **93**, 733–739 (1995).
30. G. Cerullo, C. Manzoni, L. Lüer, D. Polli, Time-resolved methods in biophysics. 4. Broadband pump–probe spectroscopy system with sub-20 fs temporal resolution for the study of energy transfer processes in photosynthesis. *Photochem. Photobiol. Sci.* **6**, 135–144 (2007).
31. C. Manzoni, G. Cerullo, Design criteria for ultrafast optical parametric amplifiers. *J. Opt.* **18**, 103501 (2016).
32. O. Svelto, D. C. Hanna, *Principles of Lasers* (Springer, 2010), vol. 1.
33. T. Virgili, D. G. Lidzey, D. D. C. Bradley, G. Cerullo, S. Stagira, S. De Silvestri, An ultrafast spectroscopy study of stimulated emission in poly(9,9-dioctylfluorene) films and microcavities. *Appl. Phys. Lett.* **74**, 2767–2769 (1999).
34. P. Kirton, J. Keeling, Suppressing and restoring the Dicke superradiance transition by dephasing and decay. *Phys. Rev. Lett.* **118**, 123602 (2017).
35. K. B. Arnardottir, A. J. Moilanen, A. Strashko, P. Törmä, J. Keeling, Multimode organic polariton lasing. arXiv:2004.06679 (2020).
36. M. Zens, D. O. Krimer, S. Rotter, Critical phenomena and nonlinear dynamics in a spin ensemble strongly coupled to a cavity. II. Semiclassical-to-quantum boundary. *Phys. Rev. A* **100**, 013856 (2019).
37. K. D. B. Higgins, B. W. Lovett, E. M. Gauger, Quantum-enhanced capture of photons using optical ratchet states. *J. Phys. Chem. C* **121**, 20714–20719 (2017).
38. C. P. Dietrich, A. Steude, L. Tropf, M. Schubert, N. M. Kronenberg, K. Ostermann, S. Hofling, M. C. Gather, An exciton-polariton laser based on biologically produced fluorescent protein. *Sci. Adv.* **2**, e1600666 (2016).
39. Y. Wang, P. Shen, J. Liu, Y. Xue, Y. Wang, M. Yao, L. Shen, Recent advances of organic solar cells with optical microcavities. *Solar RRL* **3**, 1900181 (2019).
40. B. Kippelen, J.-L. Brédas, Organic photovoltaics. *Energ. Environ. Sci.* **2**, 251–261 (2009).
41. K. A. Mazzio, C. K. Luscombe, The future of organic photovoltaics. *Chem. Soc. Rev.* **44**, 78–90 (2015).
42. G. J. Hedley, A. Ruseckas, I. D. W. Samuel, Light harvesting for organic photovoltaics. *Chem. Rev.* **117**, 796–837 (2017).
43. P. Cheng, G. Li, X. Zhan, Y. Yang, Next-generation organic photovoltaics based on non-fullerene acceptors. *Nat. Photonics* **12**, 131–142 (2018).
44. E. Hecht, *Optics* (Pearson Education Incorporated, 2017).
45. D. Wang, H. Kelkar, D. Martin-Cano, D. Rattenbacher, A. Shkarin, T. Utikal, S. Götzinger, V. Sandoghdar, Turning a molecule into a coherent two-level quantum system. *Nat. Phys.* **15**, 483–489 (2019).
46. C. Gardiner, *Stochastic Methods: A Handbook for the Natural and Social Sciences* (ed. 4, 2009).
47. J. del Pino, J. Feist, F. J. Garcia-Vidal, Quantum theory of collective strong coupling of molecular vibrations with a microcavity mode. *New J. Phys.* **17**, 053040 (2015).
48. J. V. Wall, C. R. Jenkins, *Practical Statistics for Astronomers* (Cambridge Univ. Press, 2003).
49. L. V. Wang, H.-i. Wu, *Biomedical Optics: Principles and Imaging* (John Wiley & Sons, 2012).
50. K. Yamashita, U. Huynh, J. Richter, L. Eyre, F. Deschler, A. Rao, K. Goto, T. Nishimura, T. Yamao, S. Hotta, H. Yanagi, M. Nakayama, R. H. Friend, Ultrafast dynamics of polariton cooling and renormalization in an organic single-crystal microcavity under nonresonant pumping. *ACS Photonics* **5**, 2182–2188 (2018).

Acknowledgments: We thank C. Clark and R. Preston at Helia Photonics Ltd. for fabricating the bottom DBRs. We also thank R. Grant for the measurement of concentration-dependent photoluminescence quantum yield of the LFO. **Funding:** We thank the U.K. EPSRC for partly funding this research via the Programme Grant "Hybrid Polaritonics" (EP/M025330/1). We also thank the Royal Society for an International Exchange Grant (IES\R3\170324) "Development of BODIPY dyes for strongly coupled microcavities." K.E.M. thanks the University of Sheffield for a PhD studentship via the EPSRC DTP account EP/R513313/1. D.M.R. acknowledges studentship funding from EPSRC under grant no. EP/L015110/1. T.V. and L.G. thank the Regione Lombardia Funding project IZEB. J.Q.Q. acknowledges the Ramsay fellowship and the Centre for Nanoscale BioPhotonics Family Friendly Fund for financial support of this work. **Author contributions:** J.Q.Q. conceived and managed the project. K.E.M. and D.G.L. contributed to the fabrication of the Dicke QBs. L.G., K.E.M., G.C., and T.V. contributed to the measurement of the Dicke QBs. D.M.R., J.Q.Q., B.W.L., E.M.G., and J.K. contributed to the theoretical analysis. All authors contributed to the discussion of the results and the writing of the manuscript. **Competing interests:** The authors declare that they have no competing interests. **Data and materials availability:** All data needed to evaluate the conclusions in the paper are present in the paper and/or the Supplementary Materials. The research data supporting this publication can be accessed at https://doi.org/10.17630/66875381-317e-4d6c-b884-d069547301ea.

Submitted 9 July 2021
Accepted 23 November 2021
Published 14 January 2022
10.1126/sciadv.abk3160

7.4 Author contributions

J.Q.Q. conceived and managed the project. K.E.M. designed and fabricated the Dicke QBs and carried out preliminary optical characterisation, with supervision from D.G.L.. L.G. and K.E.M. performed the time-resolved optical characterisation, with supervision from T.V. and G.C.. D.M.R., J.Q.Q., B.W.L., E.M.G., and J.K. performed the theoretical analysis. All authors contributed to the preparation of the manuscript.

7.5 References

[1] Niroula, P. Quantum batteries harvest energy from light (2022). URL https://physicsworld.com/a/quantum-batteries-harvest-energy-from-light/.

[2] Super fast quantum battery (2022). URL https://www.eurekalert.org/news-releases/940402.

[3] Choi, C. Q. These Superabsorbent Batteries Charge Faster the Larger They Get (2022). URL https://spectrum.ieee.org/quantum-battery.

[4] Irving, M. Proof of concept verifies physics that could enable quantum batteries (2022). URL https://newatlas.com/energy/quantum-battery-proof-concept-fast-charging/.

[5] Cuthbertson, A. Quantum Battery Breakthrough Paves Way for Revolution in Energy Storage (2022). URL https://www.independent.co.uk/life-style/gadgets-and-tech/quantum-battery-breakthrough-paves-way-for-revolution-in-energy-storage-b1995425.html.

[6] Aussie advance in quantum battery reality (2022). URL https://7news.com.au/technology/aussie-advance-in-quantum-battery-reality-c-5327018.

[7] Davidson, E. Quantum Batteries Could Become A Reality With Superabsorption (2022). URL https://www.rideapart.com/news/571642/quantum-batteries-reality-superabsorption/.

[8] Wordsworth, S. Quantum battery breakthrough could accelerate advance of electric vehicles (2022). URL https://www.ivtinternational.com/news/hybrid-electric-vehicles/quantum-battery-breakthrough-could-accelerate-advance-of-electric-vehicles.html.

8 Conclusions & future work

This thesis has looked at microcavities containing a variety of organic semiconductor dyes dispersed in polystyrene. Most of these cavities operated in the strong coupling regime, with the majority of the work focused on polariton condensation and lasing; however, some weakly-coupled cavities have also been studied.

In Chapter 4, a new structure for organic-based polariton microcavities was studied. By combining a thick layer of silver and a few DBR pairs, a hybrid metal-DBR mirror was formed. Compared to a conventional 10-pair DBR, these hybrid mirrors were shown to have broader reflectivity bandwidths and, when the hybrid mirror consisted of more than 4 DBR pairs, higher reflectivities. The hybrid mirrors were then incorporated into cavities, replacing the bottom 10-pair DBR in a double-DBR cavity containing the organic dye BODIPY-Br, which has previously been shown to exhibit polariton condensation [1, 2]. These hybrid-mirror cavities were found to have larger Rabi splittings than the corresponding DBR control and those with 4 or more DBR pairs also had higher Q-factors. The simplest structure, whose bottom mirror consisted only of one layer each of silver, silicon dioxide and niobium pentoxide, was shown to support polariton condensation with a threshold less than two times that of the DBR-DBR control. However, it was found that the condensate did not collapse fully to k=0. Studies involving scanning electron microscopy and atomic force microscopy indicated this was likely due to enhanced roughness in the hybrid mirror due to poor adhesion between the silver and silicon dioxide.

Despite this, the hybrid-mirror cavities are promising for use in polariton microcavities in both the linear and non-linear regimes. Indeed, future work should investigate the effect of the hybrid mirror on polariton condensation with other dyes and on lasing thresholds in weakly-coupled systems. Work should, however, be done to reduce the surface roughness of the hybrid mirror. This could include thermally annealing the silver prior to deposition of the silicon dioxide or including an adhesion promoter in order for the silicon dioxide to better adhere to the silver.

Chapter 5 focused on the investigation of a highly-photostable molecular dye for polariton condensation. DPAVB, a dye that has previously been used in weakly-coupled lasers and as a dopant in sky-blue LEDs, was incorporated at a high concentration (50% by mass in polystyrene) into a double-DBR cavity. Despite the dye's apparently-broad absorption linewidth, the cavity was found to operate in the strong coupling regime and polariton condensation was observed using sub-ns pulses. Most notably, photostability measurements were carried out that showed that the cavity remained in the condensation regime after more than 37,000 pulses, demonstrating remarkable photostability. This is in contrast to the BODIPY derivatives previously studied, which required complicated single-shot techniques and vacuum chambers in order to observe polariton condensation [1, 3, 4]. The enhanced photostability of DPAVB is highly beneficial for further studies on fundamental polariton physics; for example, on interacting condensates and polariton lattices. Future work should therefore look at such effects in DPAVB microcavities.

In Chapter 6, a new technique for confining organic polariton condensates was investigated. Microcavities containing two organic dyes separate by a spacer layer of polyvinyl alcohol were fabricated. The dyes were chosen such that one dye – BODIPY-Br – was strongly-coupled to the cavity mode and the second dye – BN-PFO, a modified polyfluorene derivative – was weakly-coupled to it. The thicknesses were chosen so that the LPB corresponded to the wavelength at which BODIPY-Br exhibits polariton condensation. Transient reflectivity measurements were then used to show that by selectively saturating the BN-PFO layer with 400 nm laser pulses, the LPB could be blueshifted with a magnitude dependent on the excitation fluence. This effect relied on a refractive index change that occurs in organic materials upon optical saturation of their oscillator strength. A maximum blueshift of 14 meV was reached in a time of 300 fs and decayed by 50% in 380 fs, suggesting this technique could be beneficial in organic devices that require fast switching times.

Having demonstrated a controllable blueshift in such cavities, the next step is to investigate whether it can be utilised to confine polariton condensates. This will be done by selectively exciting the BN-PFO in a ring shape to induce the blueshift and create an "energy barrier" surrounding a region of unchanged energy. The BODIPY-Br will then be excited to generate polariton condensation within the ring as discussed in Section 6.1. If this works, it will then be possible to study confined condensates and see how they behave when the conditions of the confinement are changed; for example, if the blueshift or the ring size are varied. This could be extended to multiple condensates, to investigate how they interact with one another when confined spatially close together, and eventually to polariton lattices. This could lead to many advances in polariton logic devices [5], quantum simulators [6], and topological insulators [7, 8]. The technique could also be utilised to induce a redshift of the LPB by using a dye with a redder absorption than BODIPY-Br for the weakly-coupled dye. However, any linewidth broadening produced by saturating this dye as was seen with BN-PFO (see Section 6.4.2) would be undesirable as, in the case of a redshift, the condensate would need to be generated in the same region. This is avoided in the blueshift cavities by generating the condensate in a region in which the BN-PFO is unsaturated. Cavities containing DPAVB instead of BODIPY-Br should also be investigated, as the low photostability of BODIPY-Br is limiting for practical applications.

In Chapter 7, a mix of strongly- and weakly-coupled cavities were investigated as prototype Dicke quantum batteries. Double-DBR cavities containing the organic dye lumogen-F orange at different concentrations were fabricated. Here, each dye molecule in a single cavity acted as a battery interacting with a common cavity mode. Using transient reflectivity, the superextensive properties of such a system were demonstrated through measurements of the rise ("charging") time and energy storage density. Here, it was shown that larger batteries (i.e. those with more molecules/a greater density of molecules) charged faster and could store a greater quantity of energy than smaller ones. Additionally, it was shown that dephasing plays a key role in slowing the discharge time of the system, such that it is significantly longer than the charging time, allowing energy to be stored.

This first demonstration of superabsorption in a large number of molecules shows promise for practical quantum batteries with far-reaching applications in energy storage, photovoltaics and other energy-harvesting technologies. Future work will look at different molecules with different absorptive and emissive properties in order to improve device performance. For example, low quenching at high concentrations is necessary to take advantage of superextensive effects. Additionally, it will be important to fully understand the effects of dephasing to maximise storage time while maintaining fast

charging. Another key challenge is the integration of such quantum batteries into practical devices; for example, organic photovoltaics that can harvest light more efficiently by utilising superabsorption.

It is therefore obvious that there is still much work to be done on organic-based microcavities. In particular, efforts should focus on the realisation of practical polariton simulators and logic devices, in which the interactions between polariton condensates can be controlled and utilised, and integrated quantum batteries that can harvest and store light with high efficiencies.

8.1 References

[1] Cookson, T. *et al.* A Yellow Polariton Condensate in a Dye Filled Microcavity. *Advanced Optical Materials* **5**, 1700203 (2017).

[2] Putintsev, A. *et al.* Nano-second exciton-polariton lasing in organic microcavities. *Applied Physics Letters* **117**, 123302 (2020).

[3] Sannikov, D. *et al.* Room Temperature Broadband Polariton Lasing from a Dye-Filled Microcavity. *Advanced Optical Materials* **7**, 1–5 (2019).

[4] McGhee, K. E. *et al.* Polariton condensation in an organic microcavity utilising a hybrid metal-DBR mirror. *Scientific Reports* **11**, 20879 (2021).

[5] Liew, T. C. *et al.* Exciton-polariton integrated circuits. *Physical Review B - Condensed Matter and Materials Physics* **82**, 1–4 (2010).

[6] Lagoudakis, P. G. & Berloff, N. G. A polariton graph simulator. *New Journal of Physics* **19** (2017).

[7] Suchomel, H. *et al.* Platform for Electrically Pumped Polariton Simulators and Topological Lasers. *Physical Review Letters* **121**, 257402 (2018).

[8] Kartashov, Y. V. & Skryabin, D. V. Two-Dimensional Topological Polariton Laser. *Physical Review Letters* **122**, 83902 (2019).

Appendices

1 Appendix A: Supplementary Information for Chapter 4

Supplementary Information: Polariton condensation in an organic microcavity utilising a hybrid metal-DBR mirror

Kirsty E. McGhee[1], Anton Putintsev[2], Rahul Jayaprakash[1], Kyriacos Georgiou[1,3], Mary E. O'Kane[1], Rachel C. Kilbride[1], Elena J. Cassella[1], Marco Cavazzini[4], Denis A. Sannikov[2], Pavlos G. Lagoudakis[2,5], and David G. Lidzey[1]*

1. Department of Physics and Astronomy, University of Sheffield, Hicks Building, Hounsfield Road, Sheffield S3 7RH, U.K.

2. Centre of Photonics and Quantum Materials, Skolkovo Institute of Science and Technology, Moscow, Russian Federation, 121205

3. Department of Physics, University of Cyprus, P.O. Box 20537, Nicosia 1678, Cyprus

4. Consiglio Nazionale delle Ricerche, Istituto di Scienze e Tecnologie Chimiche "Giulio Natta", Via C. Golgi 19, 20133 Milano, Italy

5. Department of Physics and Astronomy, University of Southampton, University Road, Southampton SO17 1BJ, U.K.

* Corresponding author: d.g.lidzey@sheffield.ac.uk

Contents:

1. Silver mirror reflectivity

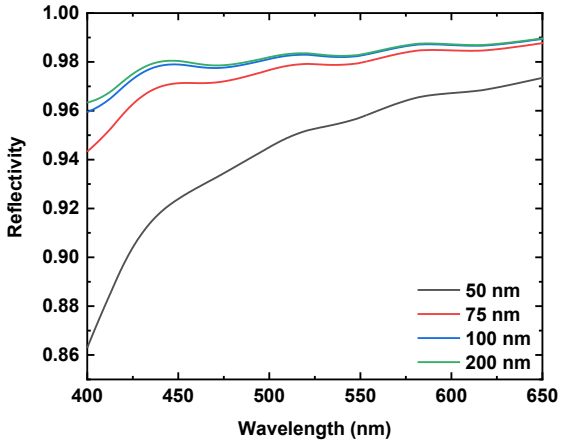

Figure S1. TMR model reflectivity of different thickness silver films. This indicates as expected that the reflectivity increases as thickness increases. Our model indicates that reflectivity does not increase once thickness exceeds ~ 200 nm and thus this is the thickness of silver used in our experiments.

2. Electric field simulations

In the main text, we show that the hybrid mirror cavities have enhanced Rabi splittings compared to the DBR-DBR cavity, which we attribute to the shorter effective length (L_{eff}) in cavities containing a layer of Ag. In the cavities studied here there are unintended thickness variations of the active layer, and thus the effective cavity lengths do not increase monotonically with increasing number of DBR pairs in the hybrid mirror. This is shown in Figure S2(a), where it can be seen that the 5-pair hybrid cavity has the longest effective length. In Figure S2(b), we plot L_{eff} assuming a constant active layer thickness of 200 nm. It can be seen from this that L_{eff} increases as the number of DBR pairs that are added to the hybrid mirror increases. Furthermore, we find as expected that the 10-pair hybrid and DBR-DBR cavities have the longest L_{eff}. The large L_{eff} of the 5-pair hybrid cavity shown in part (a) therefore principally results from an increased active layer thickness. This effect is also evident in Figure 3(c) (see main paper), where the reduced cavity mode linewidth observed in the 5-pair hybrid cavity results from its increased photonic character. Because of this complicating effect of thickness variation, we simply plot the penetration depth into the bottom mirror in Figure 3(b) (main paper), rather than L_{eff}.

We note that the Rabi splitting in planar cavities is dependent on the number of absorbers per unit length. Hence, in cavities in which the only difference is the active layer thickness (and hence the polariton detuning), the Rabi splitting is expected to remain roughly constant. In our experiments therefore, the small unintended variations in active layer thickness are not expected to substantially change the Rabi splitting energy. Rather we attribute the observed variation in Rabi splitting in the different cavities to the different penetration depths of the optical field into the bottom mirror. Additionally, in Figure S3 we plot the electric field distribution of the cavity mode and the refractive index in the active layer and bottom mirror for the 1-pair and 5-pair hybrid cavities and the DBR-DBR control.

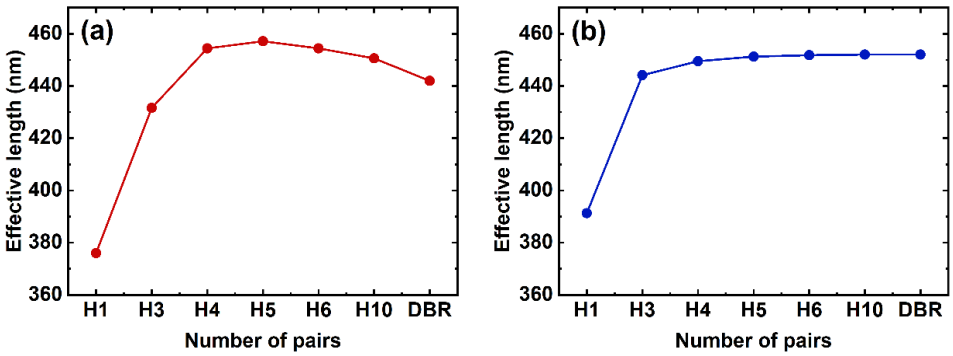

Figure S2. Effective lengths of the hybrid and DBR cavities. (a) shows the actual effective length, while (b) shows the effective length assuming a constant active layer thickness of 200 nm. From this it can be seen that the effective length increases as an increasing number of DBR pairs are added to the bottom mirror.

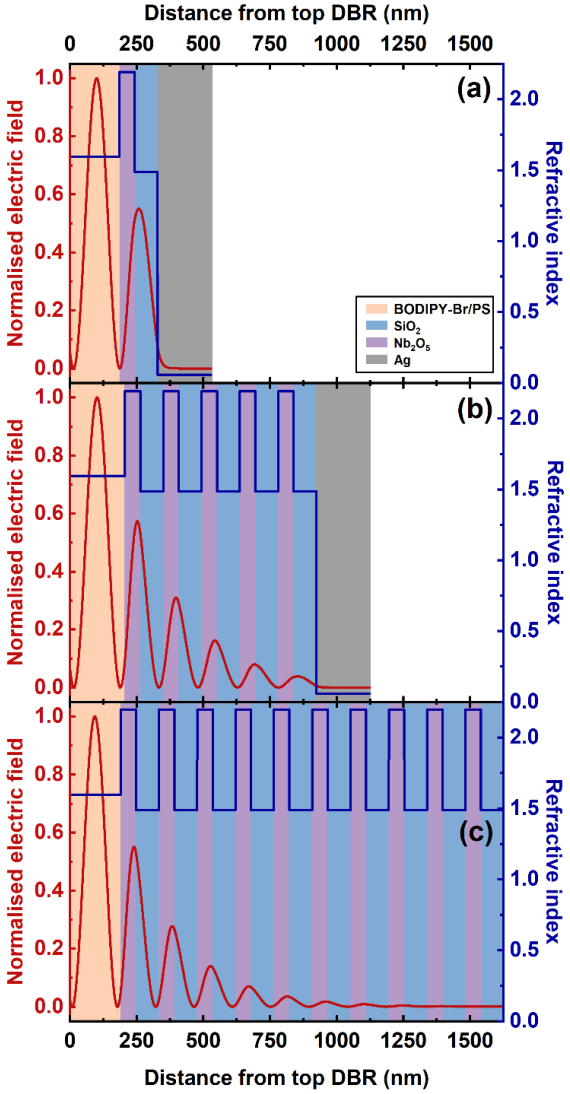

Figure S3. Electric field simulations of the cavity mode (red) and refractive index (blue) for (a) the 1-pair hybrid cavity, (b) the 5-pair hybrid cavity, and (c) the DBR-DBR control cavity. From this, it can be seen that the penetration length of the E-field changes in the different mirrors. Here, we omit the top DBR mirror as it is the same for all cavities, and thus the *x*-axis denotes the distance from the interface between the top DBR and the active layer. The different layers are shaded for clarity.

3. Polariton condensation

3.1 Blueshift

We find that the the blueshift that occurs in the hybrid cavity above threshold is twice that of the DBR cavity. We attempt to model this effect by predicting the blueshift of the LPB as we progressively reduce the oscillator strength of the BODIPY-Br active layer in the DBR-DBR and hybrid-DBR cavities (see Figure S4). It can be seen that in both cavities, we observe a linear shift of the bottom of the LPB as we start to saturate the excitonic layer, with this effect being greater in the hybrid cavity. This effect is likely explained by the increased Rabi splitting observed in the hybrid cavity. Indeed, we note that the energy difference between the bottom of the lower polariton branch and the minimum of the uncoupled photon mode ($k = 0$) is a direct function of the Rabi splitting energy. This suggests therefore that any given reduction in oscillator strength will generate a larger blueshift in cavities having a greater Rabi splitting energy, a result confirmed by our experiments. We note however that our TMR model suggests that the blueshift in the hybrid mirror cavity should be around 30% larger than the DBR-DBR cavity. Experimentally, however, we observe an energy shift in the hybrid mirror cavity which is a factor of two larger than in the DBR-DBR cavity. At present, we are not able to reconcile these observations. Further systematic experiments are planned to explore such effects in more detail.

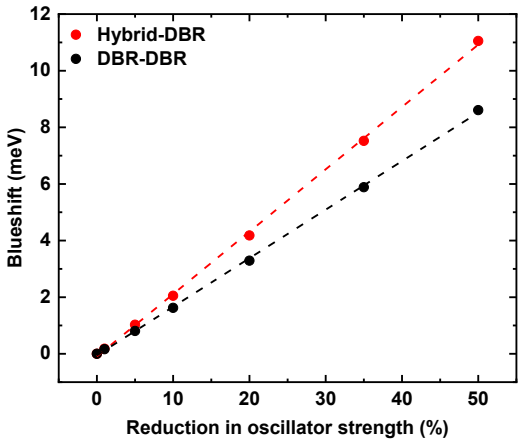

Figure S4. TMR simulations of the blueshift in the 1-pair hybrid (red) and DBR (black) cavities used in the condensation measurements as the oscillator strength of the BODIPY-Br/PS active layer is reduced.

3.2 Real-space condensate imaging

In Figure S5, we show the real-space images of the 1-pair hybrid and DBR cavities below and above threshold. It can clearly be seen that a very similar break-up of the condensate is seen in both the hybrid mirror cavity and the DBR cavity. This effect is ascribed to interactions between the condensate and the exciton reservoir.

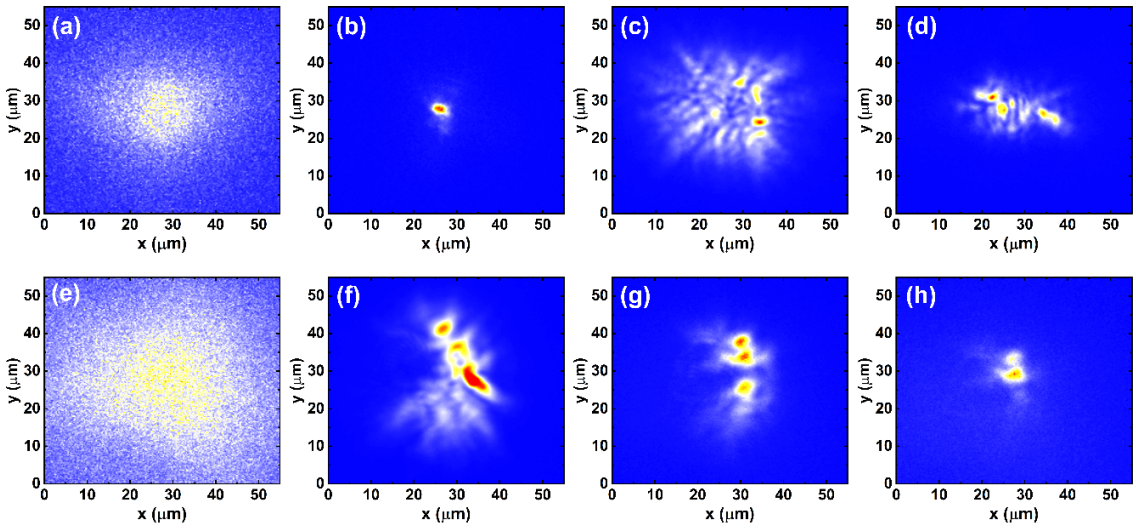

Figure S5. Part (a) shows a real space image of polariton luminescence emitted from the hybrid mirror cavity when pumped below threshold. Parts (b), (c) and (d) are images of polariton condensates generated at different regions in the hybrid mirror cavity when pumped above threshold. Part (e) shows a real space image of polariton luminescence emitted from the DBR-DBR control cavity when pumped below threshold. Parts (f), (g) and (h) are images of polariton condensates generated at different regions in the DBR-DBR control cavity when pumped above threshold. In all cases, the size of the image is (55 x 55) μm^2.

4. PL mapping below condensation threshold

In Figure S6(a), we show an additional sub-threshold PL map recorded for the DBR-DBR cavity, showing a similar trend in energy landscape to the map shown in Figure 6(a) of the main text. In part (b), we show the LPB spectra that correspond to the highest and lowest peak energies recorded in the map shown in Figure 6(a). In part (c) we show the 585 nm spectral line of a Ne/Ar lamp measured using the Andor spectrometer used in the PL mapping measurements. A Lorentz function was fitted to this spectrum and from this we determine a spectral resolution of 0.68 meV.

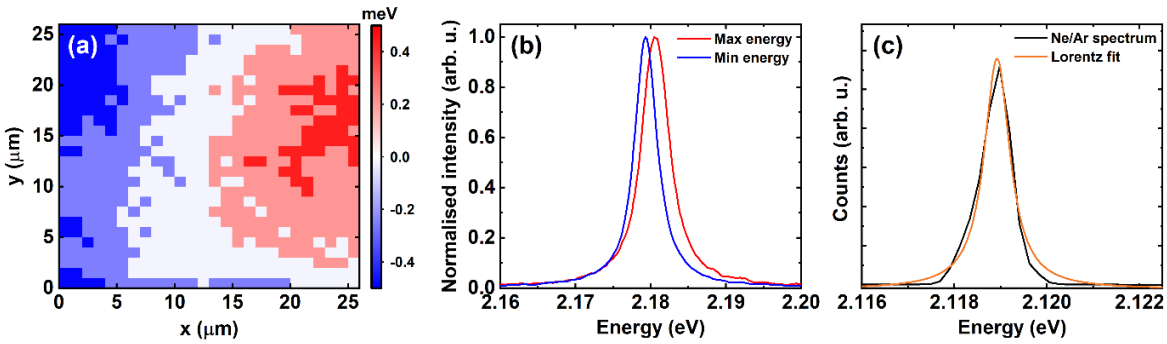

Figure S6. Additional photoluminescence map data. Part (a) shows an additional PL map for the DBR-DBR control cavity. Part (b) shows the LPB spectra corresponding to the maximum (red) and minimum (blue) peak energies from the map in Figure 6(a) of the main text. Part (c) shows the spectral line of a Ne/Ar lamp recorded using the PL mapping spectrometer (black) and a Lorentz fit to it (orange). From this, a spectral resolution of 0.68 meV is determined.

5. Atomic force microscopy (AFM)

To understand the origin of the enhanced energetic inhomogeneity in the hybrid mirror cavity, we have used AFM to determine whether the surface of the hybrid mirror is rougher than that of the DBR used in the DBR-DBR control cavity. AFM images were recorded on a series of surfaces as shown in Figure S7, including (a) the first Ag layer, (b) a SiO2 film on a glass surface, (c) a SiO2 film on a Ag film, and (d) a 1-pair hybrid mirror. This is compared with (e) a conventional 10-pair DBR mirror. The root mean square roughness from each surface is tabulated in Table 1 of the main manuscript. Each AFM scan is performed over an area of (10 x 10) μm^2. Our results indicate a general increase in surface roughness of the hybrid mirror compared to the DBR that SEM images indicate result from incomplete adhesion between the SiO_2 and the Ag film (see main text for details).

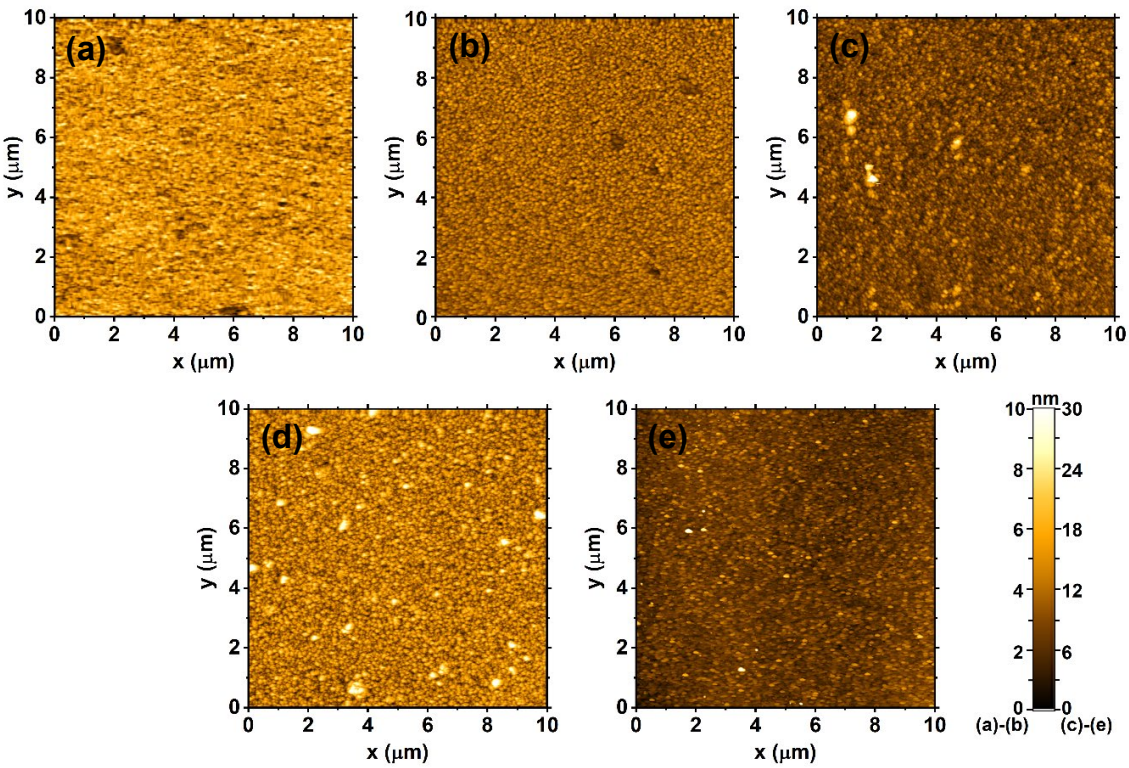

Figure S7. Atomic force microscopy maps of (a) Ag, (b) SiO_2, (c) Ag coated with SiO_2, (d) the 1-pair hybrid mirror ($Ag/SiO_2/Nb_2O_5$), and (e) the 10-pair DBR mirror. The colour scale in (a) and (b) corresponds to 10 nm, whereas for (c), (d) and (e) it corresponds to 30 nm. All structures were deposited on top of quartz-coated glass.

The effect of deposition rate of SiO_2 onto Ag was also investigated using AFM. It was found that the surface roughness was not significantly altered by changing the deposition rate of SiO_2 onto an Ag film, with RMS roughness values obtained of 2.91 nm, 2.91 nm and 2.98 nm for deposition rates of 0.5 Å/s, 1 Å/s and 2 Å/s, respectively

6. Surface profilometry imaging

In addition to the AFM mapping, the surface of the different structures were mapped over a larger area using a Bruker DektakXT profilometer. These images were taken over an area of (100 x 100) μm^2 and an example map for each structure is shown in Figure S8, with average roughness values given in Table S1. From the table, it can be seen that this data agrees with the AFM in that both the Ag and SiO_2 films are very smooth compared to the 1-pair hybrid mirror and the Ag/SiO_2 bilayer (although over such a large area, the actual roughness values are higher than for the AFM). This data also confirms that the 10-pair DBR is smoother than the 1-pair hybrid.

In the Ag/SiO_2 bilayer in Figure S8(c), it can be see that there is surface debris, and this results in a very high RMS roughness. We believe this may be caused by the Dektak tip penetrating the voids between the two layers (seen in the SEM images) as it moves across the sample surface. This then drags fragmented SiO_2 across the sample, creating such debris features. Figure S8(f) shows a microscope image (20x magnification), which shows the defects made in the film by the Dektak measurement. No such defects were found outside the measurement areas or in the other samples. We believe this is further evidence for the poor adhesion between SiO_2 and Ag.

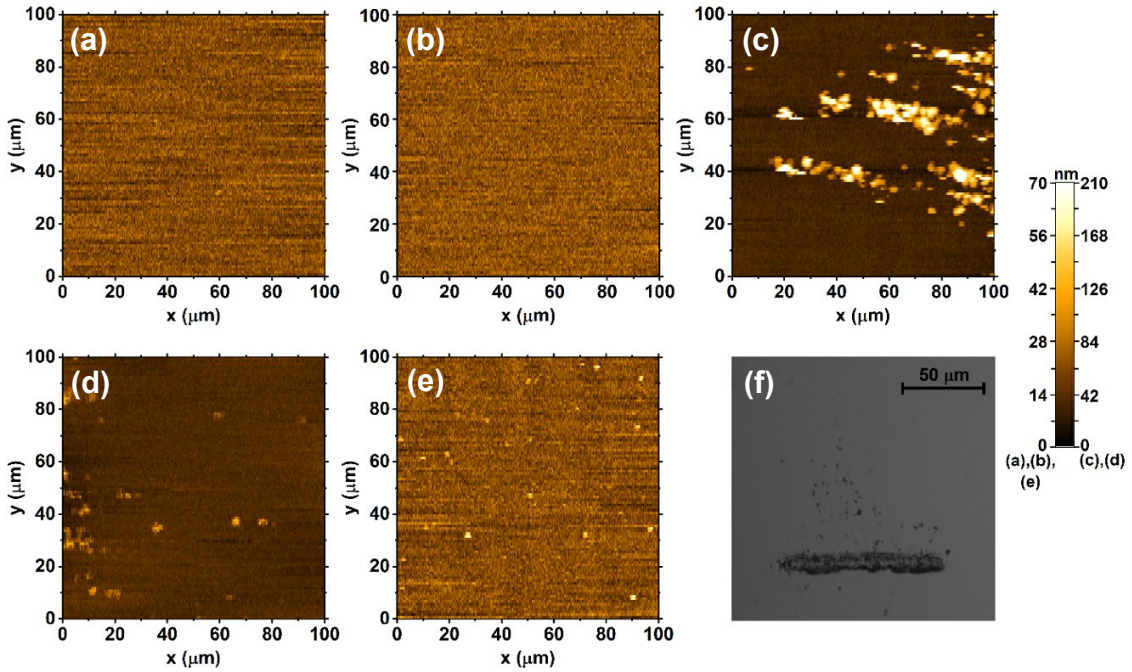

Figure S8. Surface profilometry (Dektak) maps of (a) Ag, (b) SiO_2, (c) Ag coated with SiO_2, (d) the 1-pair hybrid mirror (Ag/SiO_2/Nb_2O_5), and (e) the 10-pair DBR mirror. The colour scale in (a), (b) and (e) covers 70 nm, whereas for (c) and (d) it covers 210 nm. All structures were deposited on top of quartz-coated glass. Part (f) is a microscope image (20x magnification) of the Ag/SiO_2 film after performing Dektak measurements. The thick dark line is an artefact caused by the initial contact from the Dektak tip and indicates the start of the measurement area. This line is apparent on all samples; however, the dark specks above it are only seen in the Ag/SiO_2 image and only after the measurement. We believe they are fragments of SiO_2 dragged across the film by the tip due to its poor adhesion to the Ag.

Structure	**Ag**	**SiO_2**	**Ag + SiO_2**	**1-pair hybrid**	**10-pair DBR**
RMS roughness (nm)	4.6	5.3	33.5	14.4	5.6
Schematic	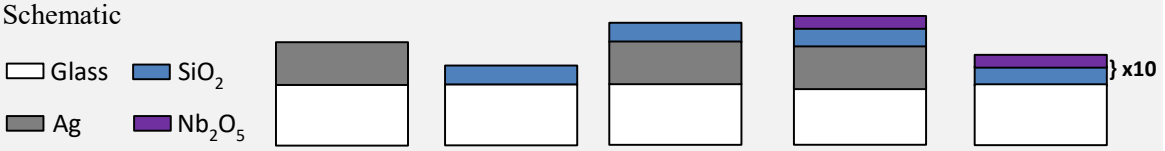				

Table S1. Root mean square (RMS) roughness of the different structures investigated, with a schematic of the structure shown beneath. These values were obtained by averaging multiple Dektak maps.

2 Appendix B: Supplementary Information for Chapter 5

Polariton condensation in a microcavity using a highly-stable molecular dye

Kirsty E. McGhee[1], Rahul Jayaprakash[1], Kyriacos Georgiou[1,2],

Stephanie L. Burg[1] and David G. Lidzey[1]*

1. Department of Physics and Astronomy, University of Sheffield, Hicks Building, Hounsfield Road, Sheffield, S3 7RH, United Kingdom
2. Department of Physics, University of Cyprus, P.O. Box 20537, Nicosia 1678, Cyprus

Contents:

1. Film properties

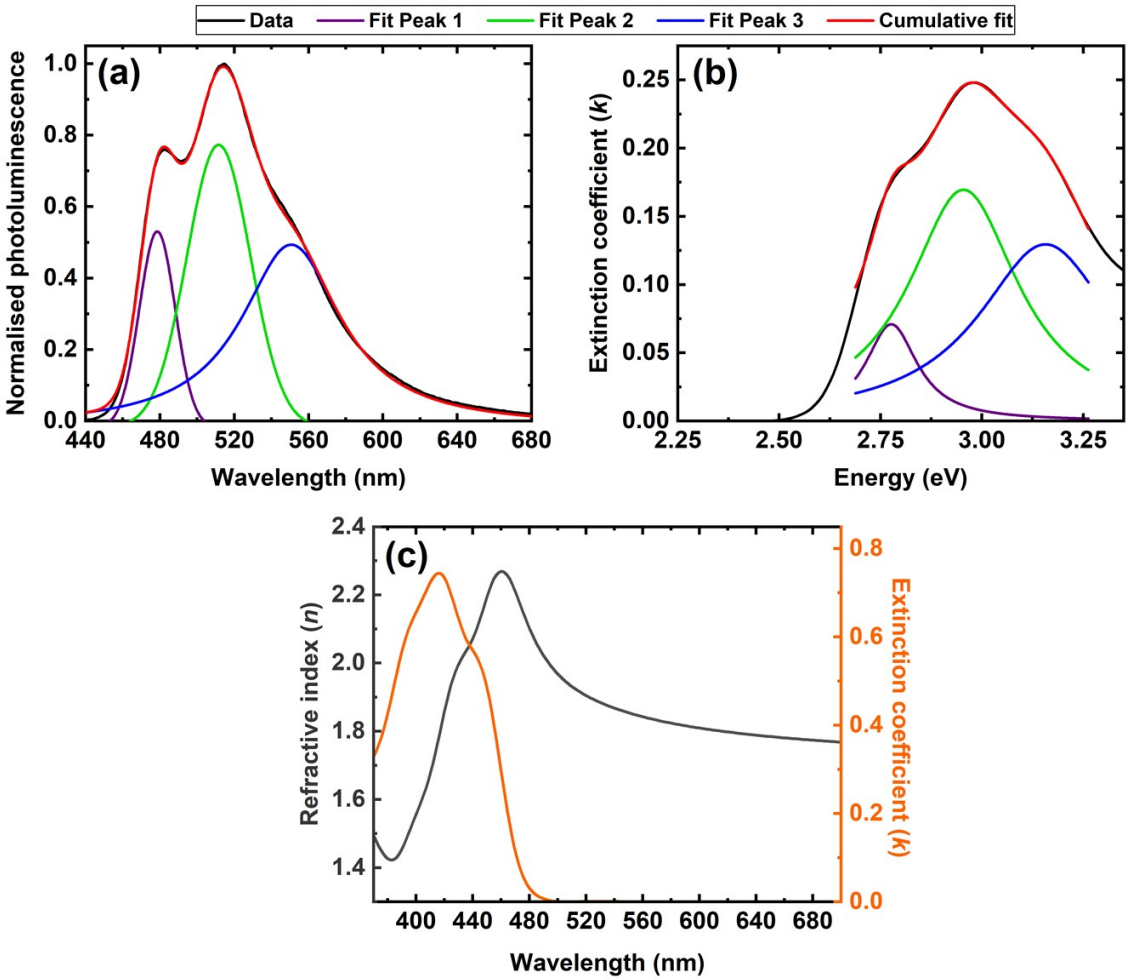

Figure S1. Multiple peak fits to DPAVB/PS film spectra and the ellipsometry data. Part (a) shows a triple-Voigt fit to the normalised photoluminescence, while part (b) shows a triple-Lorentzian fit to the calculated DPAVB/PS extinction coefficient. These Lorentzian functions are then used in the TMR model to describe the DPAVB transitions. Part (c) shows the refractive index and extinction coefficient obtained by ellipsometry for the pure DPAVB film.

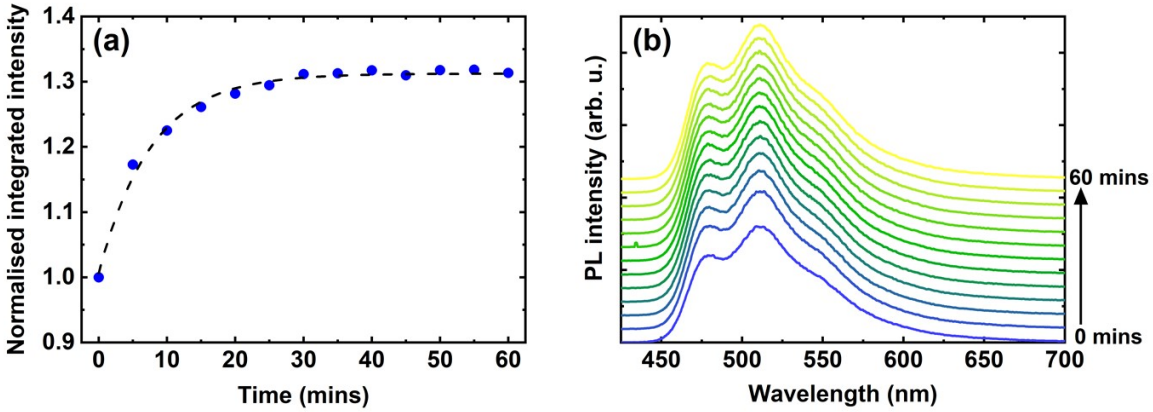

Figure S2. Photostability of DPAVB/PS film in the linear regime. Part (a) shows the time-dependence of the integrated PL intensity (blue circles) normalised to the value at time = 0 seconds. It can be seen that the PL intensity initially increases sharply and then saturates at ~130% of its initial value after about 30 minutes. The dashed line shows a single exponential fit to the data. Part (b) shows the PL spectra from 0 to 60 minutes at 5 minute intervals (with a constant *y*-offset), showing that while the intensity increases, its spectral shape remains the same.

2. Coupled oscillator fits

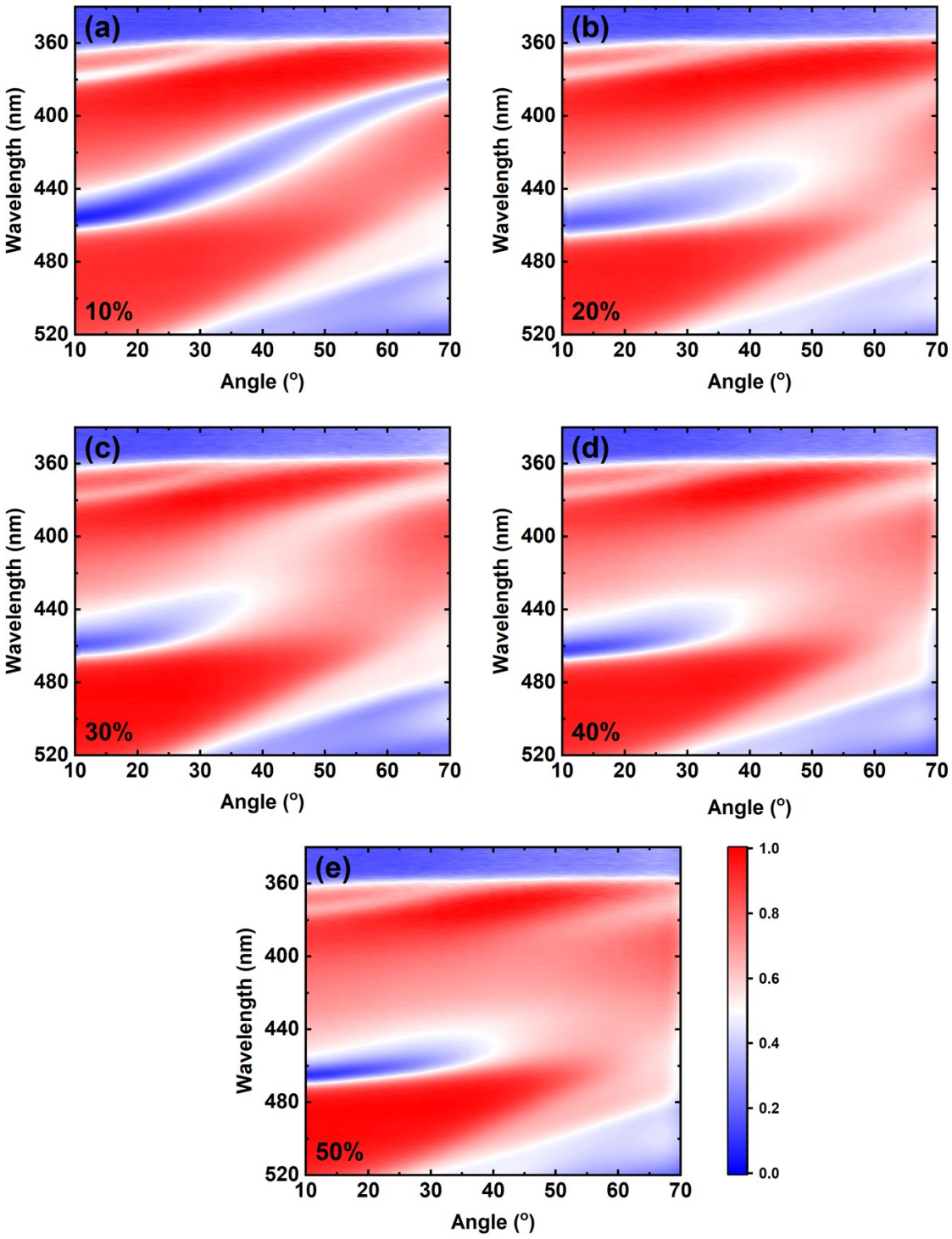

Figure S3. Angle-dependent white light reflectivity data for the DPAVB cavities with 6-pair DBRs. The DPAVB/PS concentration for each cavity was (a) 10%, (b) 20%, (c) 30%, (d) 40% and (e) 50%. It can be seen that at low concentrations the cavity is weakly-coupled, but that as the oscillator strength is increased, a splitting appears and the cavity enters the strong coupling regime.

Property	**T1**	**T2**	**T3**	**Cavity mode**
λ_{peak} **(nm)**	447	420	393	483

γ (meV)	78	164	203	3.4
Ω_{min} (meV)	110	232	287	/
$\Omega_{coupled}$ (meV)	168	260	227	/

Table S1. Parameters used to determine whether the various transitions within the 50% DPAVB/PS cavity with 6-pair DBRs are strongly-coupled. Here, λ_{peak} is the peak wavelength of each of the Lorentzian functions extracted from experimental data shown in Figure S1(b) and γ is their linewidth (half-width at half maximum). For the cavity mode, λ_{peak} and γ are the wavelength and half-width at half maximum at $k = 0$ extracted from the TMR model. Using the condition described by Equation 1 (main paper), we indicate the minimum Rabi splitting, Ω_{min}, at which the transitions should lie in the strong coupling regime. $\Omega_{coupled}$ are the Rabi splittings deduced using the coupled oscillator model. From this it can be seen that T1 and T2 meet the condition (green text), whereas T3 does not (red text).

We have also fitted the higher Q-factor cavity based on 10 and 12-pair DBRs using a coupled oscillator model. The analysis of the cavity is complicated by that fact that no upper polariton branch is visible in either reflectivity measurements or in photoluminescence emission. We believe this is caused by a combination of large negative cavity detuning and the high reflectivity of the DBRs.

To fit the dispersion of the lower branch, we first determined whether the coupling constant (g) changed when the DPAVB is placed in a 10/12 pair cavity compared to what is determined in a 6/6 pair cavity. Here we base our estimates on a similar system (BODIPY-Br in polystyrene) having a similar oscillator strength and an active layer of similar thickness. Using this, our TMR model indicates that the Rabi splitting is only expected to decrease by 2% when the number of DBR pairs is increased from 6/6 pairs to 10/12 pairs. Given the likely error associated with this estimate, we assume the Rabi splitting in the 10/12 cavity is the same as it is in the 6/6 cavity We then use this as input to the coupled oscillator model (values of $\Omega_1 = 168$ meV, $\Omega_2 = 260$ meV and $\Omega_3 = 227$ meV used in simulations) and fit to the measured reflectivity model as is shown below. Here, it can be seen that the fit to the LPB is very good; however, without a visible UPB, we treat this conclusion with a significant degree of caution.

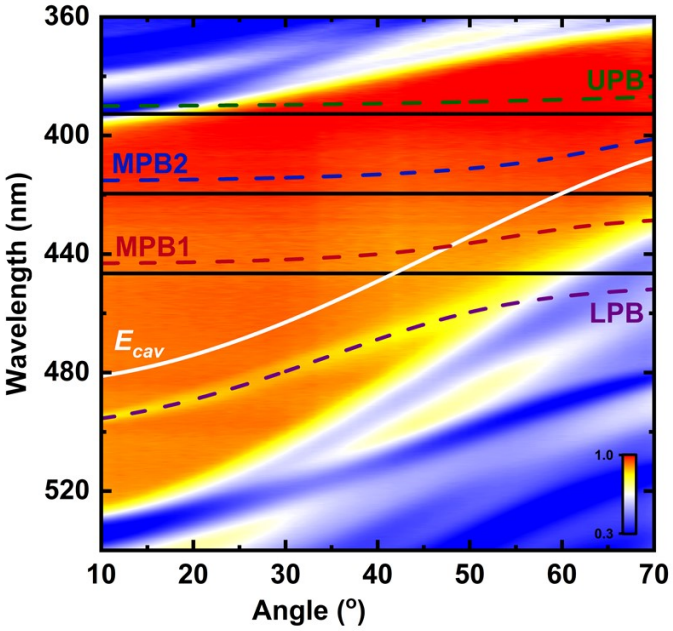

Figure S4. Coupled oscillator fit to 50% DPAVB cavity reflectivity with 10- and 12-pair DBRs. The fits to the LPB (purple), MPB1 (red), MPB2 (blue), and UPB (green) are shown by the dashed lines, while the cavity mode (white) and the DPAVB transitions (black) are shown by the solid lines. The labels for the transitions, T_1, T_2 and T_3, are not shown here for clarity, but they are the same as in Figures 2(c) and (d) of the main text.

3. Threshold calculation parameters

We detail our estimation of the threshold fluence for amplified spontaneous emission (ASE) and polariton condensation below.

To calculate the ASE threshold, we first determined the relative absorption of a DPAVB/PS film at the excitation-laser wavelength. This was done by measuring the power of a 355 nm laser beam before (2.0 μW) and after (1.34 μW) transmission through a 200 nm thick DPAVB/PS film. We also measured the intensity of the reflected beam (0.17 μW). This indicates that 25% of incident laser power was absorbed by the film. This was then used with the laser repetition rate (100 Hz) and the excitation spot size (see Table S2), to convert the threshold power into an absorbed threshold fluence.

For the microcavity, we found that the intensity of incident laser is reduced by 40% as it passes through the bottom DBR (through which excitation is made). This suggests that the intensity of a 2.0 μW laser beam (at 355 nm) would be reduced to 1.06 μW as it passes into the active region. From the absorption coefficient of a 50% DPAVB/PS film (23,500 cm^{-1}) we estimate that a minimum of 28% of the incident laser is absorbed by the active layer (thickness = 317 nm). This simple calculation clearly neglects optical interference effects of the excitation laser-light within the cavity. This was again used with the laser repetition rate (100 Hz) and the excitation spot size (see Table S2), to convert the threshold power into an absorbed threshold fluence.

Parameters	ASE	Condensation
Power threshold (μW)	8.6	0.59
Spot size (μm x μm)	6080 x 210	31.1 x 31.4
Spot area (cm^2)	$1.28x10^{-2}$	$7.68x10^{-6}$
% absorption at 355 nm	24.5	27.8
Fluence threshold ($\mu J/cm^2$)	1.7	215

Table S2. Parameters used for the calculation of the ASE and condensation thresholds.

4. Origins of blueshift

To determine the origin of the blueshift, we performed two analyses and found the blueshift can be attributed to two mechanisms: a reversible photobleaching and an irreversible degradation of the DPAVB molecules in the cavity.

To demonstrate reversible photobleaching, we measured the emission from the LPB at a low power below threshold. We then measured the emission above threshold, and then below threshold again. Here emission was recorded using the same *k*-space setup used to obtain the data in Figures 3 and 4 of the main text. The spectra at $k = 0$ are shown in Figure S5(a), where it can be seen that the emission blueshifts by 1.6 meV above threshold and then returns to its original position when excited below threshold. This clearly indicates that provided the cavity is not exposed for a prolonged period to a large laser flux, a substantial blueshift occurs that is fully reversible, and that this blueshift results from bleaching of the excitonic ground-state.

It is clear however that laser excitation does result in some degree of irreversible photodegradation – this is evidenced by the drop-off in intensity of polariton lasing as demonstrated in Figure 4(a) (Main paper). To assess the significance of this effect, we plotted the peak wavelength of the LPB emission above threshold (i.e. time-series data from Figure 4) as a function of number of pump pulses. This data is shown in Figure S5(b), where it can be seen that there is indeed a blueshift that occurs with increasing exposure. Here, we find that the LPB maximum undergoes a blueshift of 0.44 nm (2.2 meV) during the course of exposure to 37,750 laser pulses.

We have attempted to use the data in Fig S5(b) to explore the extent to which the power sweep data shown in Fig 3(b) (main paper) is determined by irreversible photodegradation. During the course of the power sweep measurements the sample received approximately 8,500 pulses (17 measurements, 5 s exposure, 100 Hz). However, the majority (82%) of the laser pulses during this measurement had a power lower than that used in the photostability measurement ($2P_{th}$) At present, we do not understand how the photodegradation rate scales with excitation intensity, but suspect that any blueshift due to photodegradation will be significantly less than that suggested by Figure 5(b) (0.55-1.1 meV at 8,500 pulses). We therefore conclude that the observed blueshift in Figure 3(b) can likely be attributed to a

combination of reversible photobleaching together with some irreversible photodegradation, however the relative magnitude of these effects is at present unclear.

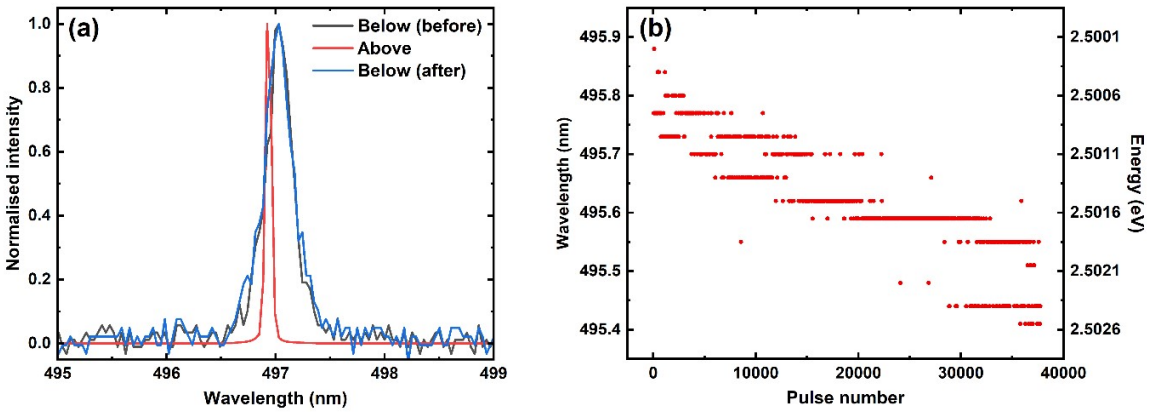

Figure S5. Origin of blueshift. Part (a) shows the normalised LPB spectra when the sample is first excited below threshold (before, grey), 1.7 times above threshold (red) and then again below threshold (after, blue). It can clearly be seen that the blueshift of the LPB above threshold is reversible. Part (b) shows the shift in emission wavelength of the condensate against pulse number at $2P_{th}$.

5. Raman spectroscopy

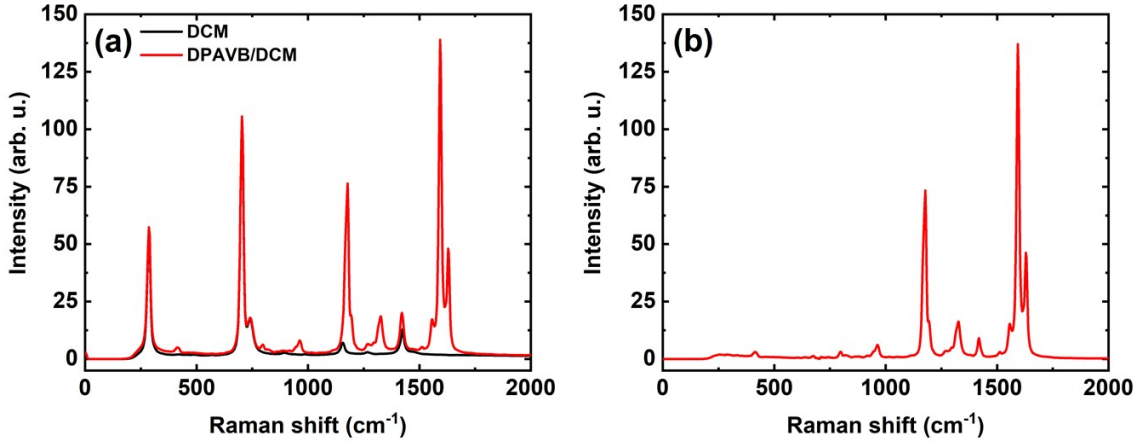

Figure S6. Raman spectra for DPAVB in dichloromethane (DCM). Part (a) shows the spectra for a pure DCM solution (black) and for a 10 mg/mL DPAVB/DCM solution (red). Part (b) shows the spectrum for pure DPAVB calculated by subtracting the two signals shown in part (a).

3 Appendix C: Supplementary data for Chapter 6

3.1 BN-PFO complex refractive index

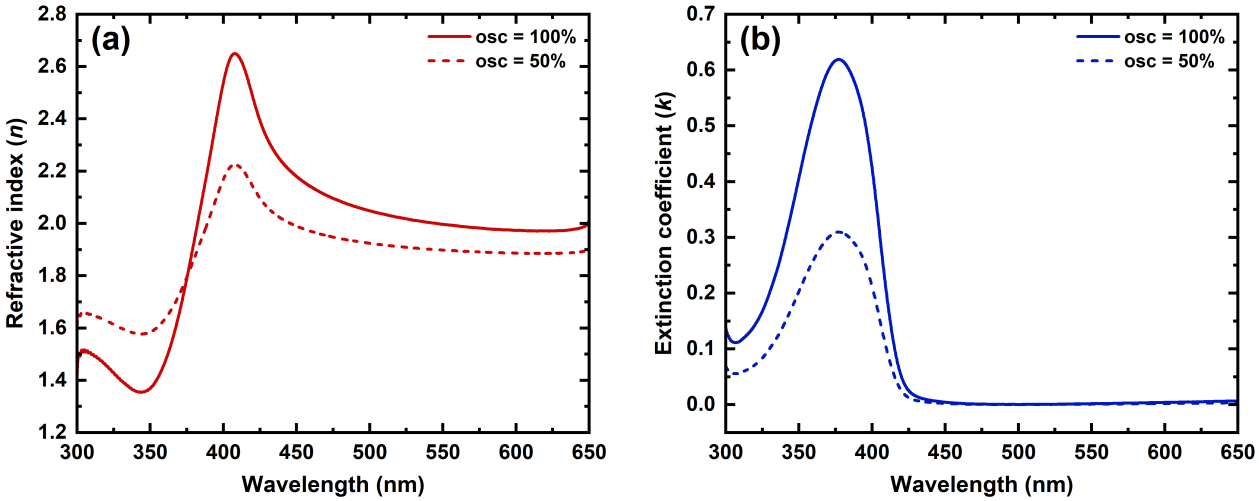

Figure 8.1. Effect on BN-PFO complex refractive index upon saturating its oscillator strength. Parts (a) and (b) show the effect on (a) the real part (n) and (b) the imaginary part (extinction coefficient, k) of the refractive index (n) when the oscillator strength is unsaturated (osc = 100%, solid) and saturated to 50% (dashed).

3.2 Transient absorption and reflectivity probe spectrum

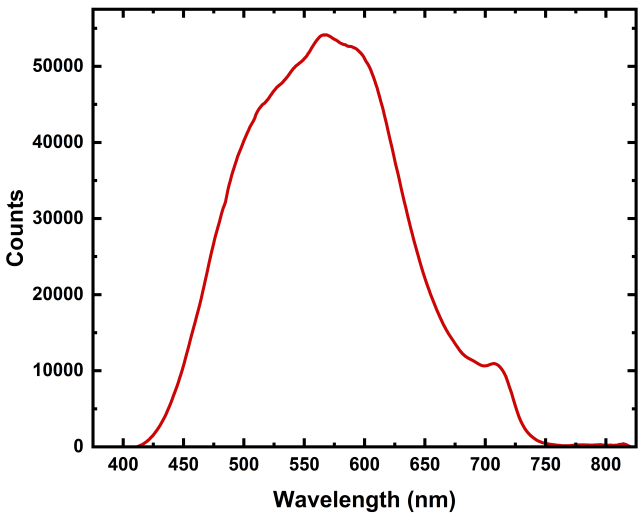

Figure 8.2. Example probe spectrum used in the measurements on the films and cavities.

3.3 Transient reflectivity data on control films

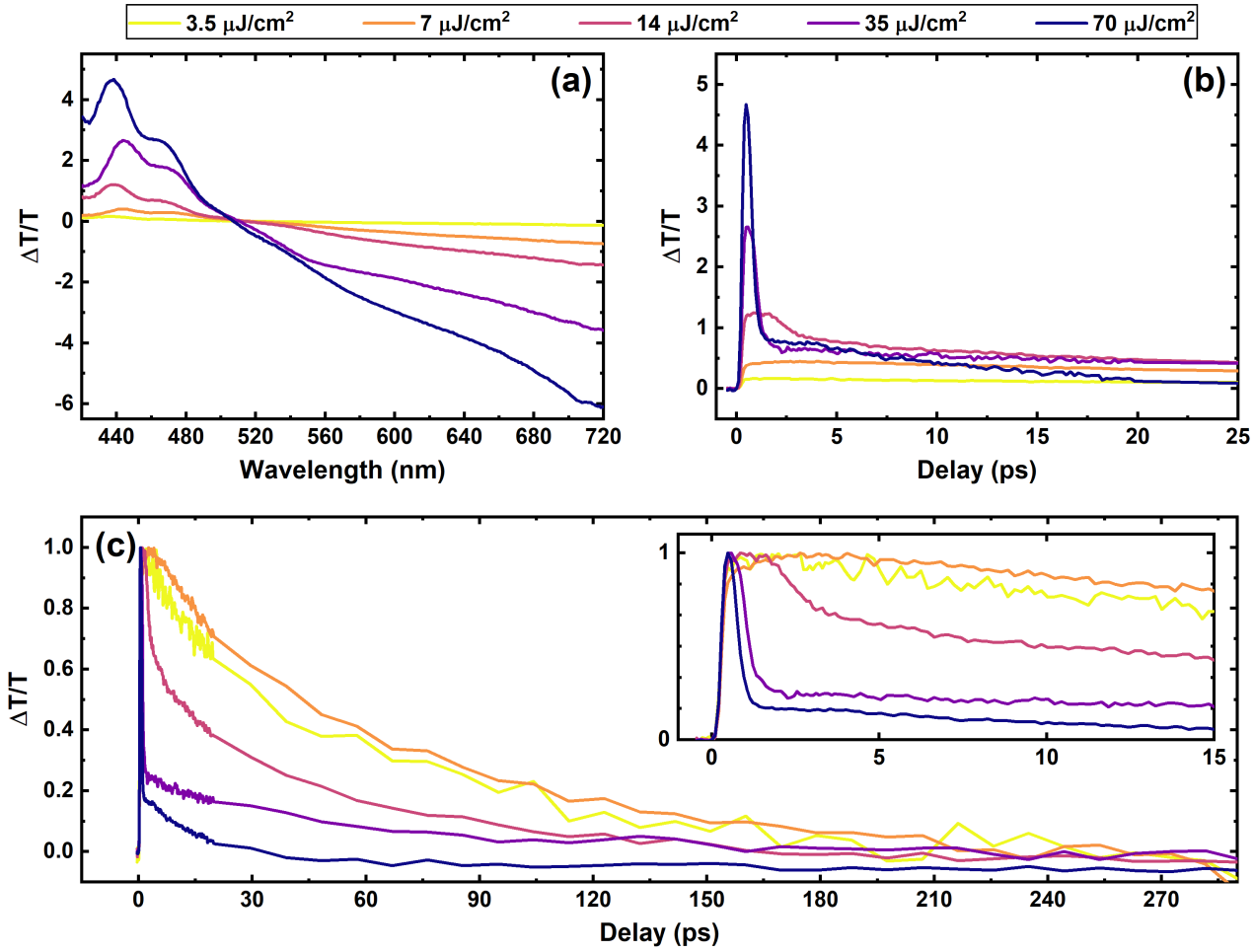

Figure 8.3. Fluence dependent transient absorption measurements on the multilayer film. Part (a) shows the fractional change in the transmission spectrum at a range of fluences. Part (b) shows the time dynamics of the $^{\Delta T}/_{T}$ signal up to a delay time of 25 ps at the peak of the BN-PFO PL emission (445 nm). Part (c) shows the normalised dynamics for the same spectra up to a delay time of 290 ps, with a close-up of the first 15 ps shown in the inset.

3.4 Transient reflectivity and blueshift data on the multilayer cavity measured at 20° and 30°

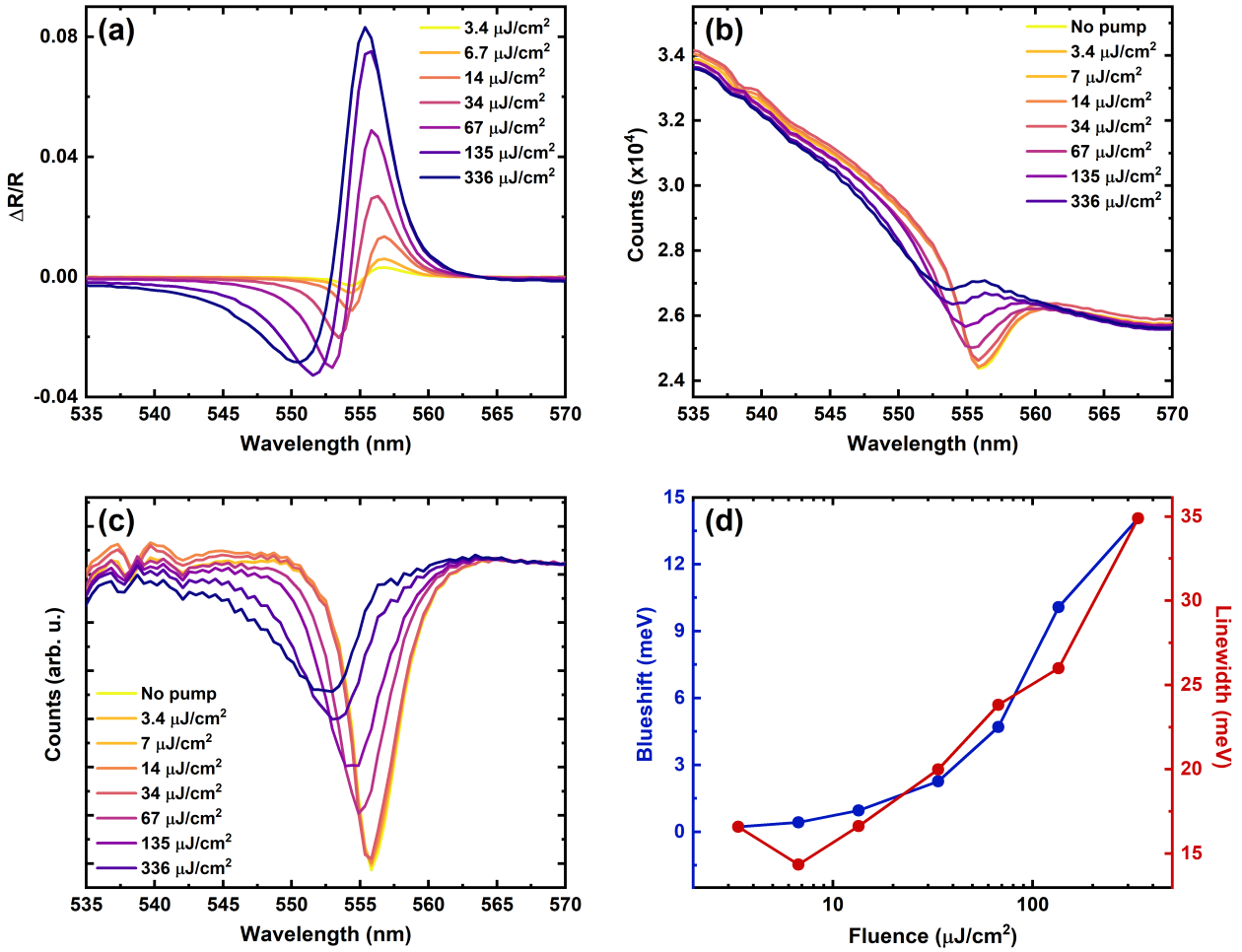

Figure 8.4. Transient reflectivity measurements on BODIPY-Br/BN-PFO cavity recorded at an angle of 20° to the cavity normal. Part (a) shows the fractional change in the cavity reflectivity, $^{\Delta R}/_{R}$, at different fluences. The derivative shape is characteristic of a blueshift of the mode – in this case, the LPB. Part (b) shows the reflected probe at different fluences, showing that there is indeed a blueshift of the LPB as the fluence is increased. Part (c) shows the same data after a baseline subtraction. Part (d) shows the blueshift (blue) and linewidth (red) (in meV) as a function of fluence with a double y-axis, with the scales chosen in such a way that the first and last data points overlap. From this it can be seen that they follow a similar trend with increasing fluence. There is a maximum blueshift of 3.5 nm or 14.1 meV at a fluence of 336 μJ/cm^2. The blueshift and linewidth were extracted from a Lorentzian fit to the LPB in part (c).

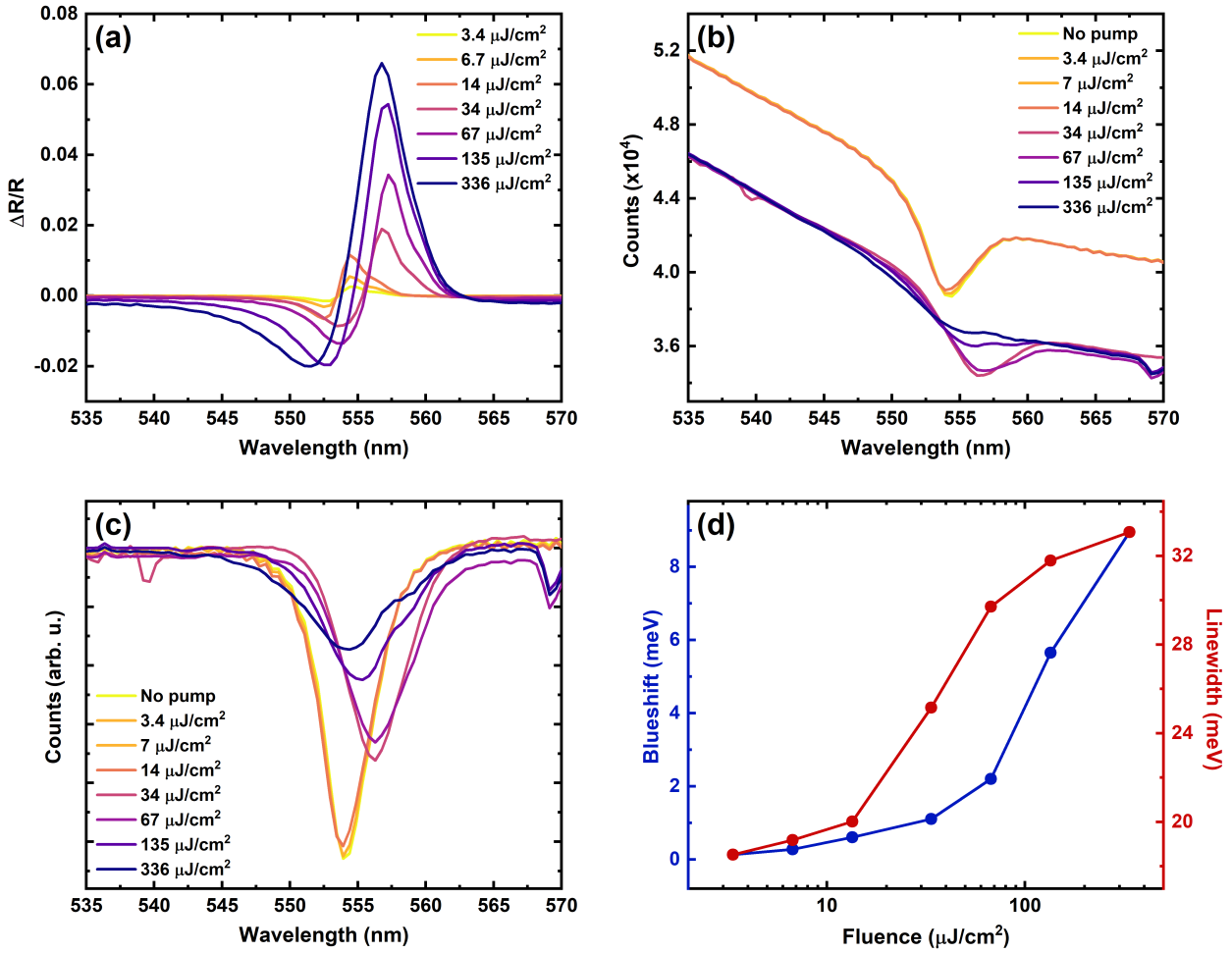

Figure 8.5. Transient reflectivity measurements on BODIPY-Br/BN-PFO cavity at an angle of 30° to the cavity normal. Part (a) shows the fractional change in the cavity reflectivity, $^{\Delta R}/_{R}$, at different fluences. The derivative shape is characteristic of a blueshift of the mode – in this case, the LPB. Part (b) shows the reflected probe at different fluences, showing that there is indeed a blueshift of the LPB as the fluence is increased. It can be seen that there is a big difference between the probe spectra recorded above 14 μJ/cm^2 compared to below. This is likely due to a realignment of the setup in the middle of the measurements, which resulted in an altered probe. However, as the blueshifts and linewidths are calculated from the probe with the pump off at the start of each measurement, the altered probe should not affect the results. Part (c) shows the same data after a baseline subtraction. Part (d) shows the blueshift (blue) and linewidth (red) (in meV) as a function of fluence with a double y-axis, with the scales chosen in such a way that the first and last data points overlap. From this it can be seen that they follow a similar trend with increasing fluence. There is a maximum blueshift of 2.2 nm or 9.0 meV at a fluence of 336 μJ/cm^2. The blueshift and linewidth were extracted from a Lorentzian fit to the LPB in part (c).

3.5 Transient reflectivity dynamics in cavity at 10°

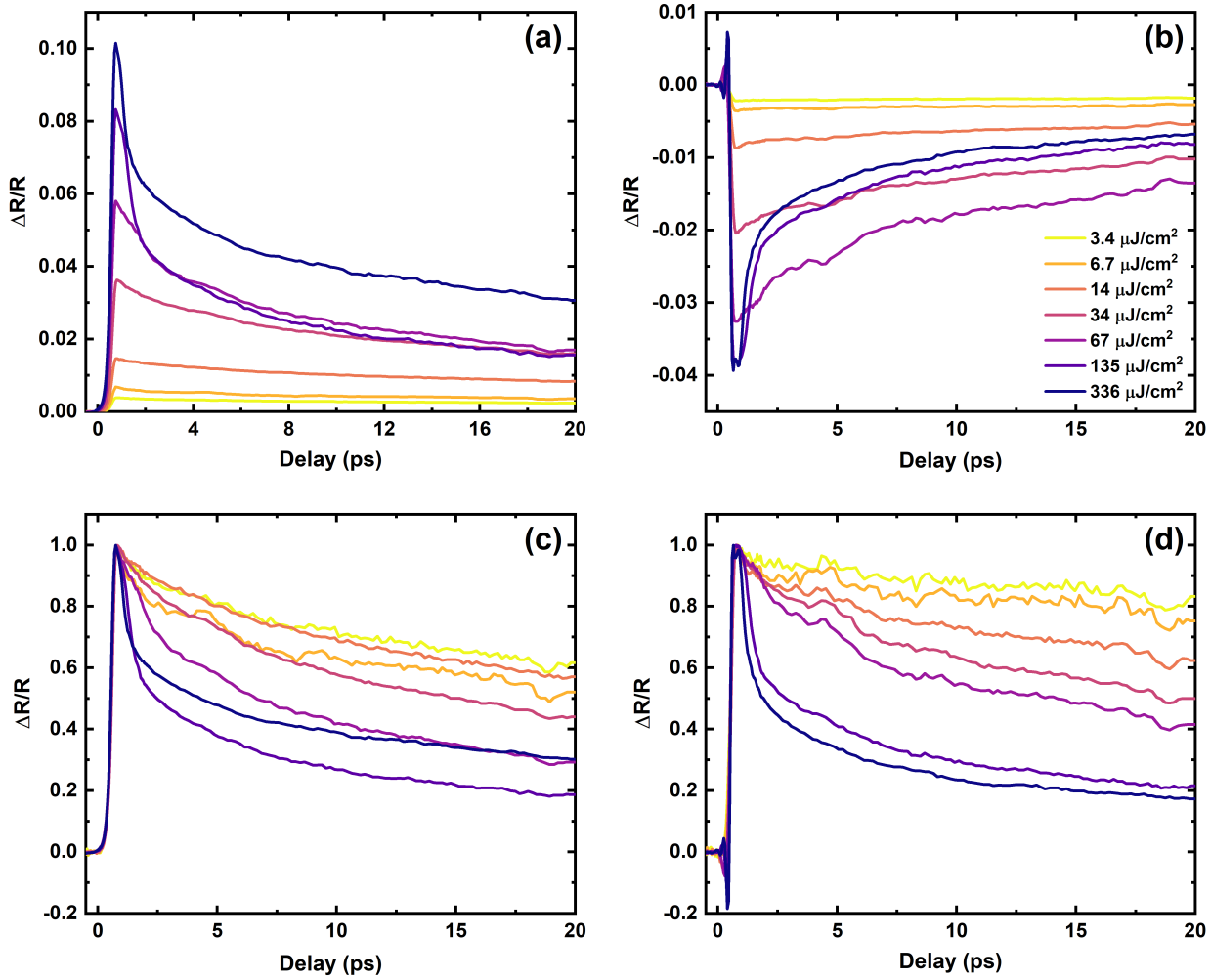

Figure 8.6. Transient reflectivity dynamics for BODIPY-Br/BN-PFO cavity at an angle of 10° to the cavity normal. Parts (a) and (b) show $^{\Delta R}/_{R}$ as a function of delay for the positive (original LPB) and negative (shifted LPB) peaks in Figure 6.7(a), respectively. Parts (c) and (d) show the normalised data for (a) and (b), respectively. It can be seen from this that as the fluence is increased, the signal decays more quickly. The legend in (b) applies to all four panels.

4 Appendix D: Supplementary Materials for Chapter 7

Science Advances
AAAS

Supplementary Materials for

Superabsorption in an organic microcavity: Toward a quantum battery

James Q. Quach*, Kirsty E. McGhee, Lucia Ganzer, Dominic M. Rouse, Brendon W. Lovett, Erik M. Gauger, Jonathan Keeling, Giulio Cerullo, David G. Lidzey, Tersilla Virgili*

*Corresponding author. Email: quach.james@gmail.com (J.Q.Q.); tersilla.virgili@polimi.it (T.V.)

Published 14 January 2022, *Sci. Adv.* **8**, eabk3160 (2022)
DOI: 10.1126/sciadv.abk3160

The PDF file includes:

Other Supplementary Material for this manuscript includes the following:

S1. CHARACTERISATION OF SAMPLES AND CALIBRATION MEASUREMENTS

This section presents further details of the properties of the fabricated microcavities, and measurements used to calibrate the results in the main text.

a. Quenching at large concentrations Figure S1 shows the photoluminescence quantum yield (PLQY) as a function of dye concentration. At large concentration the yield drops to zero; this provides an upper limit on the concentration that can be studied in experiment. The photoluminescence measurements were taken using a Coherent Mira 900 laser operating at 400 nm with a repetition rate of 80 MHz. The laser beam was focused onto the surface of a sample placed at the centre of an integrating sphere. The laser light and the emission from the sample were scattered by the diffuse interior of the sphere and collected by an optic fibre, which was coupled to an Andor Shamrock SR-303i-A CCD spectrometer. Spectra were taken for different concentration LFO films, as well as a blank glass substrate in order to calculate the proportion of laser light absorbed by the LFO samples.

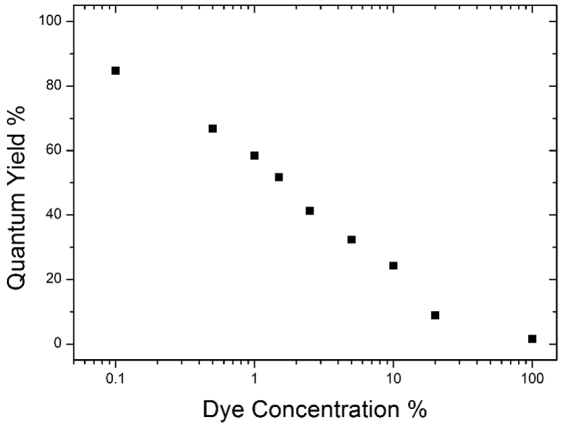

FIG. S1. Photoluminescence quantum yield as a function of LFO concentration.

b. Film and microcavity spectra Figure S2 shows the molecular absorption and emission spectra, and examples of the microcavity reflectivity spectra. Panels (a,b) show the properties of the bare molecular film. These show the small Stokes shift between absorption and photoluminescence, and also show how high film concentrations modify the photoluminescence spectrum, consistent with the reduced PLQY shown above. The microcavity reflectivity spectra (c,d) show the crossover from weak- to strong-coupling as the concentration is increased.

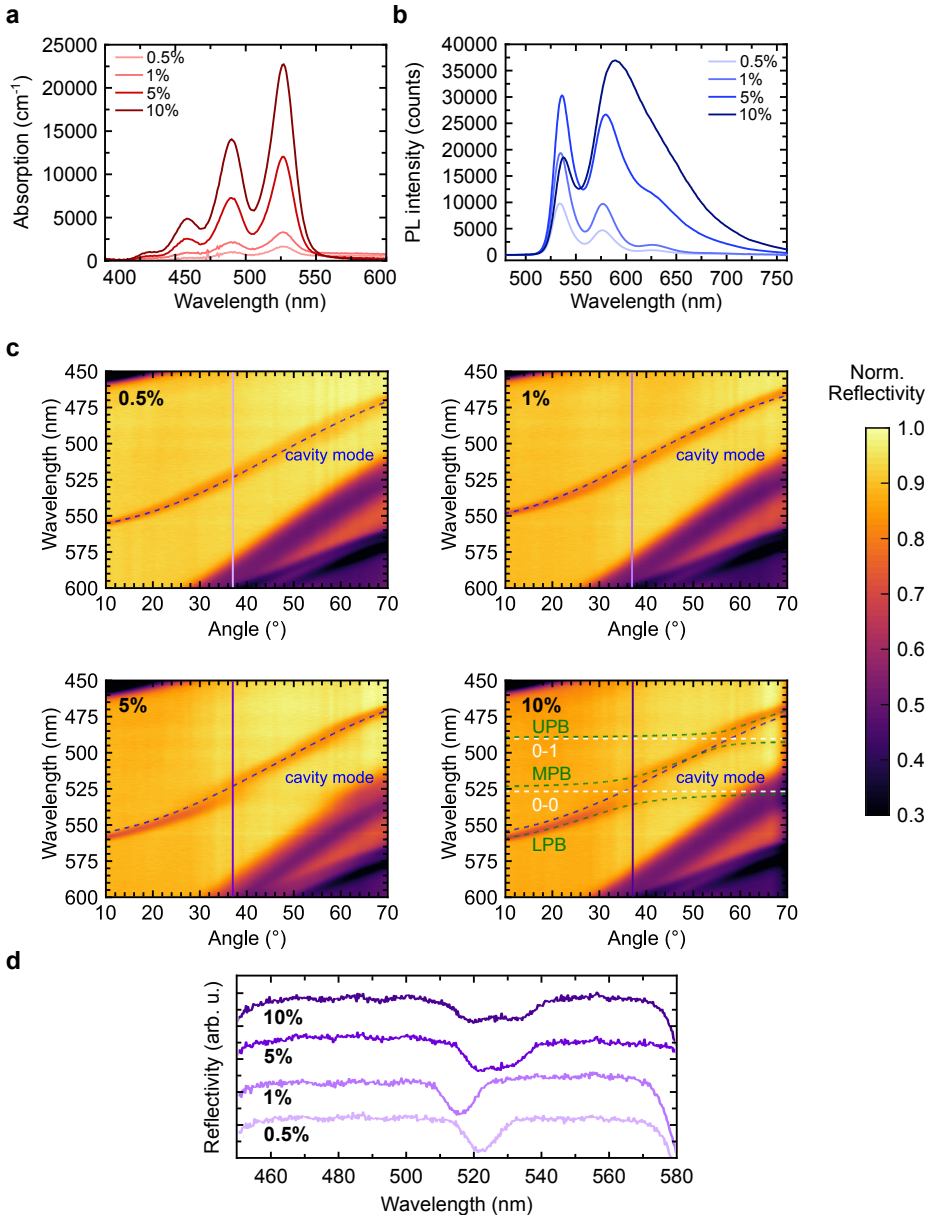

FIG. S2. **Absorption, photoluminescence of the LFO films and reflectivity spectra of the microcavities.** (a) Absorption and (b) photoluminescence spectra for the 0.5%, 1%, 5%, and 10% LFO-concentration films. (c) Reflectivity spectra for 0.5%, 1%, 5%, and 10% LFO-concentration microcavities. UPB, MPB, and LPB label the upper, middle, and lower polariton branches, respectively. Also indicated are the 0-0 and 0-1 transition wavelengths. (d) is a slice of the reflectivity spectra at 37°. The single dip in the 0.5% and 1% concentration spectra indicate the weak-coupling regime. The double dip seen in the 10% concentration spectra, represent the polaritonic states, indicating the strong-coupling regime. The 5% concentration spectrum represents a situation intermediate between a single and double dip, indicating an intermediate-coupling regime.

c. Transfer matrix calculations To provide bounds on the cavity lifetime, separate from the measured cavity linewidth—which contains effects of inhomogeneous broadening—we make use of transfer matrix calculations of the cavity structure. These calculations, shown in Fig. S3, also enable one to visualise the electric field intensity in the microcavity structure. These calculations give a designed cavity lifetime of 306fs, which serves as an upper bound of the actual cavity lifetime.

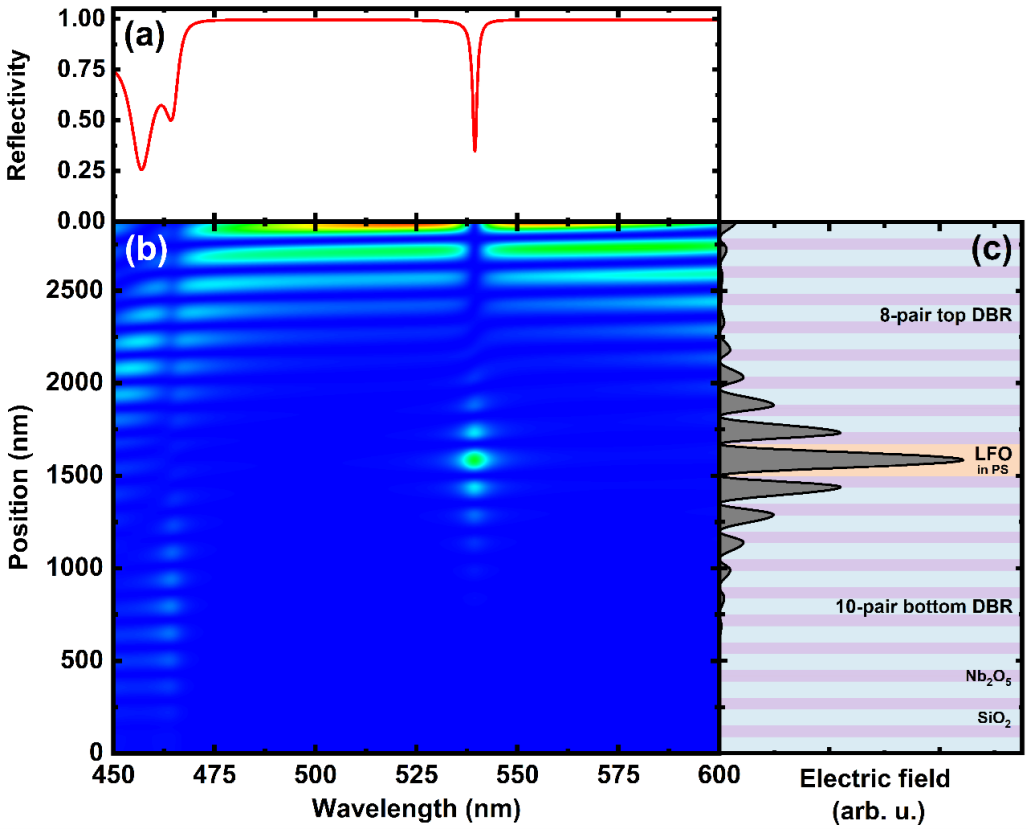

FIG. S3. **Transfer matrix simulation of the electric field distribution for the 1% cavity.** (a) shows the cavity reflectivity, (b) the spectrally-resolved electric field amplitude, and (c) the electric field amplitude at the cavity mode wavelength. The shaded sections of (c) indicate the different materials which make up the cavity, with Nb2O5 in purple (refractive index, n = 2.25), SiO2 in blue (n = 1.52), and LFO in PS in orange (n = 1.60). All simulations were made using transfer matrix modelling at an angle of 20° to the cavity normal to maintain consistency with the transient reflectivity measurements.

d. Pump-probe dynamics of bare films For comparison to the pump-probe dynamics of the cavity shown in the main text, Figs. S4,S5 show the transient transmission spectra of the bare films. (Note that, as discussed in the main text, a transmission geometry is required for transient spectroscopy of the bare films).

Figure S4 compares the dynamics at 525 nm (ground state bleaching) and 571 nm (stimulated emission region) for the 1% concentration film. Unfortunately a coherent artefact, due to the degenerate pump-probe configuration, masks the time dynamics in the first 100 fs. However, the same rise and decay times are seen at both probe wavelengths, indicating that we are probing the same exciton population.

We also explored pump-fluence dependence of the bare films. No dependence on the excitation fluence was detected in any control film. This indicates the absence of bimolecular effects or multi-photon excitation. Figure S5 shows such data for all concentrations, at two different pump fluences. As in Fig. S4, a coherent artefact is present at zero delay due to the degenerate pump and probe spectra.

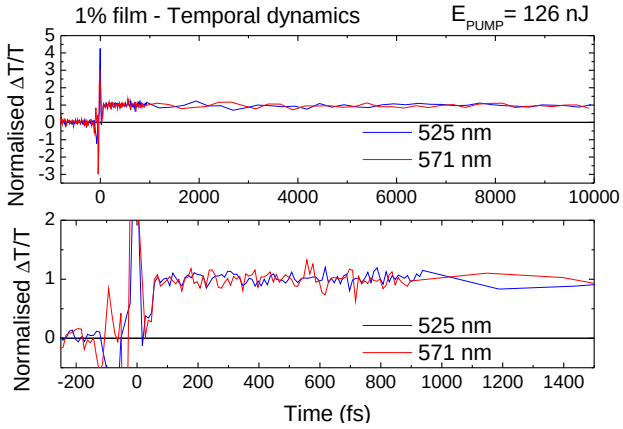

FIG. S4. **Dynamics of the control 1% control film at different wavelengths.** The two panels show two different time windows (top panel until 10 ps, bottom panel until 1.4 ps. The same behavior is observed for other film concentrations.

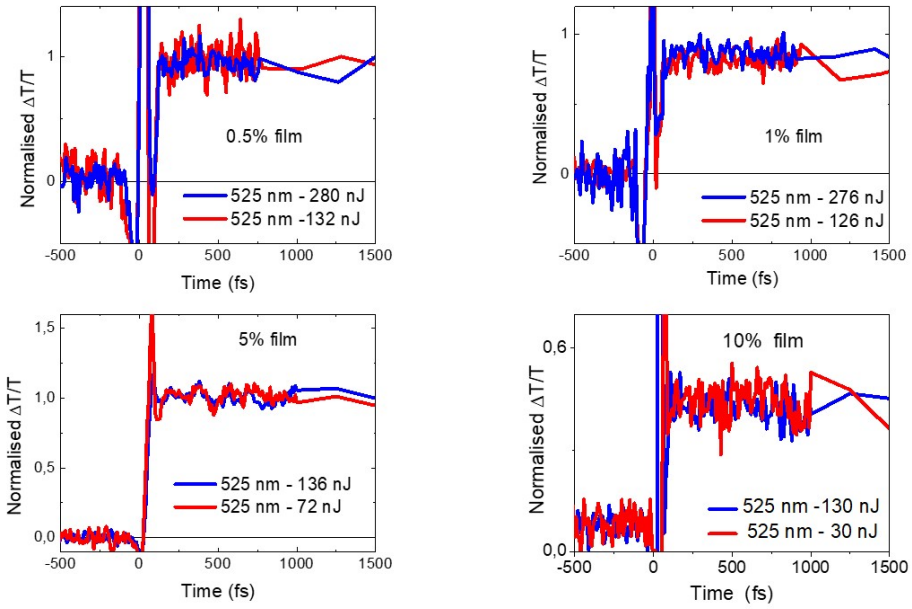

FIG. S5. **Dynamics of the control films, at different concentrations.** Each panel shows the dynamics for a different concentration, as indicated.

e. Estimating number of molecules in film. To determine the number of LFO molecules in the microcavities we study, we first determined the absorption cross-section of a single LFO molecule, σ_{LFO}. The transmission spectrum of a 0.1% solution of LFO in 25 mg/mL PS/dichloromethane in a 1 mm thick cuvette was measured using a Horiba Fluoromax 4 fluorometer with a xenon lamp. The absorption coefficient ($\alpha = n\sigma_{LFO}$) of the 0–0 transition was then calculated using the relation $T/T_0 = e^{-\alpha d}$, where T/T_0 is the fractional transmission of the xenon lamp at the 0–0 transition, d is the cuvette thickness, n is the number density of absorbing molecules in solution per unit volume, and σ_{LFO} is the absorption cross-section of a single LFO molecule [49]. Using the known value of n for this solution, σ_{LFO} was calculated as 3.3×10^{-16} cm^2. The transmission of the 10% LFO concentration in film was then measured to obtain α and hence n (number density of molecules in the cavity active layer), using the measured value of σ_{LFO}, with d (film thickness) measured using a Bruker DektakXT profilometer. This value was then multiplied by the area of the laser beam and d to obtain N. Here we assume a uniform distribution in the active layer. N for other concentrations were scaled accordingly.

f. Estimating number of photons in cavity. To estimate the number of photons entering the cavity in each different cavity, we consider the overlap between the pump spectrum and the cavity transmission. The number of photons in the cavity is given by multiplying the number of pump photons by $1 - R$, where R is the reflectivity of the cavity: $n = N_\gamma(1 - R)$. An example of this is shown in Fig. S6, for the 1% cavity. Starting from the pump spectrum (yellow curve), by considering the reflectivity spectrum of the cavity (black line), we calculate the fraction of photons entering into the cavity (purple line). Table S1 shows the resulting estimates of photon numbers for each experiment.

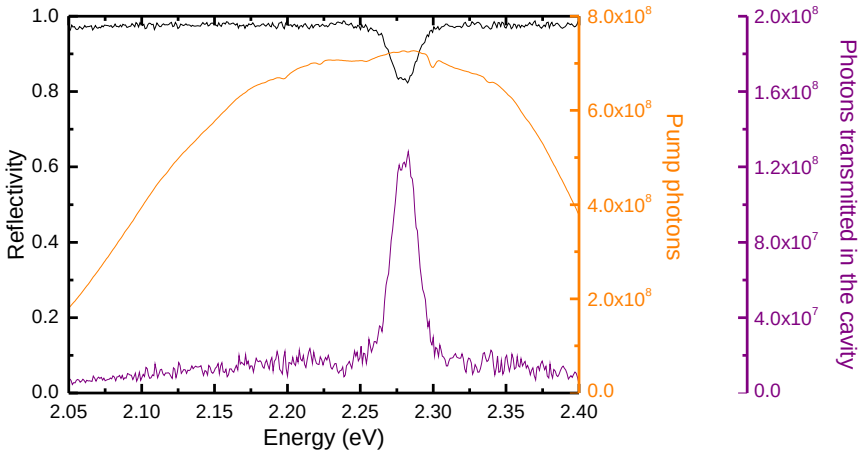

FIG. S6. **Calculating photon number**. Yellow curve (right axis): pump spectrum. Black curve (left axis) reflectivity spectrum of 1% cavity. Purple curve (right axis): photons transmitted into the cavity.

Experiment	$N_{\text{dye}}(\times 10^{10})$	$N_{\text{photon}}(\times 10^{10})$
A1	16.20	1.90
A2	8.08	0.98
A3	1.62	0.26
B1	1.62	4.53
B2	0.81	0.16

TABLE S1. Estimated photon number and molecule number for each experiment.

g. Derivative features in the differential transmitivity As seen in Fig. 2 of the main text, the transient signal shows both positive and negative features in the differential transmitivity. This can be understood from the existence of a derivative feature in the spectrum. Such a feature occurs if the pump causes an absorption

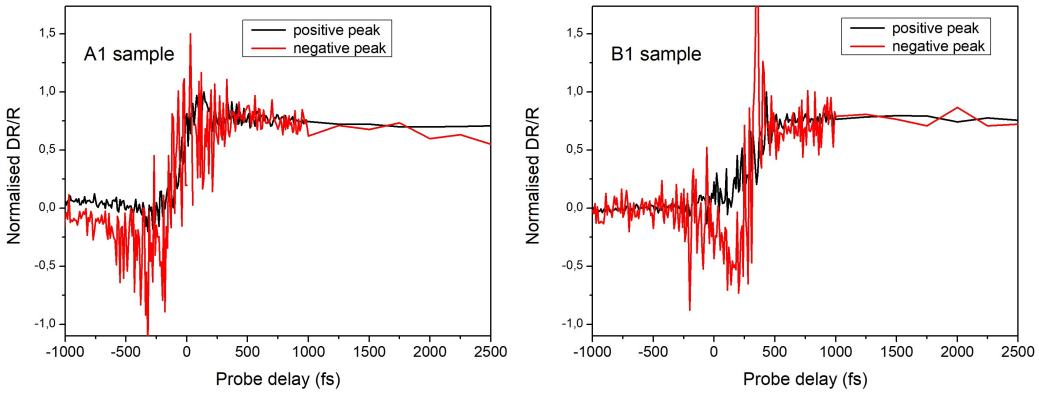

FIG. S7. Time evolution of positive and negative features in the differential transmitivity.

peak to move in energy. In that case the change of absorption will see a decrease in absorption where the feature used to be, and an increase where the feature now is [33,50]. This leads to a feature that takes the form of the derivative of the original absorption peak with respect to energy, and which thus contains both negative and positive contributions. This structure is exactly what we observe, indicating that the feature corresponds to a resonance which moves with excited state population. This feature though coexists with other positive features in the transient reflectivity, arising from mechanisms such as ground state bleaching or stimulated emission. Whether a negative feature is seen depends on how these contributions compete and whether the feature is above the detection threshold.

The presence of this derivative feature does not influence our determination of the energy stored in the molecules and the charging time. As shown in the Fig. S7, the time dependence of the negative and positive peaks is the same. (The negative feature does show more noise, as this signal is weaker compared to background noise.) Since both features show the same time evolution, they would both recover the same theoretical fits.

S2. THEORETICAL MODELLING

In this section we describe our approach to modelling the system. We first provide a more detailed discussion of the model we use, and the physical origin of the terms involved. We then derive the equations of motion for the expectation values using a second-order cumulant approach.

A. Details of theoretical model

As discussed in the main text, we model the experiments through a Dicke model—which describes N two-level systems coupled to a photon mode. Describing organic molecules as two-level systems is an approximation, as it neglects both the role of rotational and vibrational molecular modes, as well as the existence of higher excited states of the molecules. It is known that this approximation can become valid in some limiting situations, such as at low temperatures [45]. While our experiments are performed at room temperature, we nonetheless expect the model to provide a reasonable approximation. This is because, as noted in the main text, the molecules we consider show a small Stokes shift, indicating vibrational dressing of optical transitions is weak. Moreover, as seen in the main text and discussed further below, our model matches the experimental results well without such additional features.

The Hamiltonian describing our system, including the external pump laser, takes the form (setting $\hbar = 1$):

$$H = \Delta_c a^\dagger a + \sum_{j=1}^{N} \left[\frac{\Delta_a}{2} \sigma_j^z + g(a^\dagger \sigma_j^- + a\sigma_j^+) \right] + i\eta(t)(a^\dagger - a)\,, \tag{1}$$

where a ($a^\dagger$) is the photon annihilation (creation) operator, σ_i^α for $\alpha = x, y, z$ are the Pauli matrices. We write the Hamiltonian in the rotating frame of the pump laser, so Δ_a (Δ_c) is the energy detuning of the laser from the cavity (molecules), g is the coupling strength of each molecule to the photon mode, $\eta(t)$ is the Gaussian profile of the pump laser. In the following we assume that the molecules and cavity are resonant ($\Delta_a = \Delta_c \equiv \Delta$) and that $\Delta = 0$ unless specifically noted.

To account for dissipative processes, we consider the time evolution of the density matrix, including Lindblad terms for various dissipative processes:

$$\dot{\rho} = -i[H, \rho] + \kappa \mathcal{L}[a] + \sum_{j=1}^{N} \left(\gamma^z \mathcal{L}[\sigma_j^z] + \gamma^- \mathcal{L}[\sigma_j^-] \right)\,, \tag{2}$$

where $\mathcal{L}[X] = X\rho X^\dagger - (1/2)\{X^\dagger X, \rho\}$. The first term, with rate κ, describes loss of photons, due to the finite reflectivity of the cavity mirrors. The second term, with rate γ^z, describes dephasing of the molecular excitations. This term describes the effect of coupling between the molecular electronic state and vibrational degrees of freedom—vibrations both of the molecule and of the polystyrene matrix in which it is contained. The final term, γ^-, describes the decay of electronic excitation, due to emission into non-cavity modes, such that $1/\gamma^-$ would be the excited state lifetime in the absence of the cavity.

As noted in the main text, dephasing γ^z plays a crucial role in the dynamics, with quite distinct behaviour occurring with and without dephasing. In particular, dephasing introduces transitions between the "bright" and "dark" molecular excited states. To understand these states, let us first consider states with a single excitation. The form of Eq. (1) shows that the cavity photon couples only to the totally symmetric molecular excited state, i.e. a state with equal weight and phase of excitation on all molecules. However, for N molecules, N excited states exist. The remaining $N - 1$ states are orthogonal to the coupling to light, and are known as "dark states". While we have introduced this for the space with a single excitation, a generalization to higher excited states exists. In this case, the language of superradiant and subradiant states is often used [1], with superradiant states referring to those that can be reached using the collective raising and lowering operators, $\sum_j \sigma_j^\pm$. Because the dephasing term acts on individual molecules, it describes a process that allows loss of phase coherence between different molecules. As such, this causes a transition from the optically bright state created by the laser, to an incoherent mixture of bright and dark states. Since the dark states do not couple to the cavity, this process is responsible for the asymmetry between collectively enhanced absorption, and the lack of collective enhancement of emission.

For N identical molecules of energy ω_a (in the lab frame), the energy density stored on the molecules is given by

$$E(t) = \frac{\omega_a}{2}\left(\langle\sigma^z(t)\rangle + 1\right) . \tag{3}$$

As such, in the following, our aim is to predict the time evolution of this quantity.

B. Cumulant equations

To determine the time evolution of $\langle\sigma^z(t)\rangle = \mathrm{Tr}\left[\sigma^z\rho(t)\right]$ we begin by writing down the first order expectation values of the system. We adopt the notation $C_a(t) \equiv \langle a(t)\rangle$ for photon operators, and $C_{\alpha=x,y,z}(t) \equiv \langle\sigma^\alpha(t)\rangle$ for spin operators, along with a similar notation for higher order expectations, e.g., $C_{ax}(t) \equiv \langle a\sigma^x(t)\rangle$. The equations of motion for the first order expectation values are

$$\partial_t C_a = -\left(i\Delta_c + \tfrac{1}{2}\kappa\right)C_a - \tfrac{1}{2}gN\left(iC_x + C_y\right) + \eta(t)\,, \tag{4}$$
$$\partial_t C_x = -\Delta_a C_y - 2g\mathrm{Im}\left[C_{az}\right] - \gamma^{\mathrm{tot}}C_x\,, \tag{5}$$
$$\partial_t C_y = \Delta_a C_x - 2g\mathrm{Re}\left[C_{az}\right] - \gamma^{\mathrm{tot}}C_y\,, \tag{6}$$
$$\partial_t C_z = 2g\left(\mathrm{Re}\left[C_{ay}\right] + \mathrm{Im}\left[C_{ax}\right]\right) - \gamma^-\left(C_z + 1\right) , \tag{7}$$

where ∂_t is short for $\frac{\partial}{\partial \mathrm{t}}$, $\gamma^{\mathrm{tot}} = 2\gamma^z + \frac{1}{2}\gamma^-$, and for notational ease we have dropped the explicit time dependence of observables. As described in the main text, in mean field theory we would now set the second order cumulants to zero. These are defined as

$$\langle\langle AB\rangle\rangle = \langle AB\rangle - \langle A\rangle\langle B\rangle\,. \tag{8}$$

This would result in the usual decomposition of second order expectation values into products of first order ones, $C_{AB} = C_A C_B$, which is the assumption that molecule-molecule, molecule-photon, photon-photon and all higher order correlations are negligible. However, we instead derive equations of motion for the second order expectation values, capturing the leading order $1/N$ corrections to mean field theory. The second order photon correlations obey:

$$\partial_t C_{a^\dagger a} = -\kappa C_{a^\dagger a} - gN\left(i\mathrm{Im}\left[C_{ax}\right] + \mathrm{Re}\left[C_{ay}\right]\right) + 2\eta(t)\mathrm{Re}\left[C_a\right] , \tag{9}$$
$$\partial_t C_{aa} = -\left(2i\Delta_c + \kappa\right)C_{aa} - gN\left(iC_{ax} + C_{ay}\right) + 2\eta(t)C_a\,, \tag{10}$$

while molecule-photon correlations follow:

$$\begin{aligned}\partial_t C_{ax} = &-\left(i\Delta_c + \tfrac{1}{2}\kappa + \gamma^{\mathrm{tot}}\right)C_{ax} - \Delta_a C_{ay} - i\frac{g}{2}\left[1 + (N-1)\right]C_{xx} \\ &- \frac{g}{2}\left[iC_z + (N-1)\,C_{xy}\right] + ig\left(C_{aaz} - C_{a^\dagger az}\right) + \eta(t)C_x\,,\end{aligned} \tag{11}$$

$$\begin{aligned}\partial_t C_{ay} = &-\left(i\Delta_c + \tfrac{1}{2}\kappa + \gamma^{\mathrm{tot}}\right)C_{ay} + \Delta_a C_{ax} - i\frac{g}{2}\left[-iC_z + (N-1)\,C_{xy}\right] \\ &- \frac{g}{2}\left[1 + (N-1)\,C_{yy}\right] - g\left(C_{aaz} + C_{a^\dagger az}\right) + \eta(t)C_y\,,\end{aligned} \tag{12}$$

$$\begin{aligned}\partial_t C_{az} = &-\left(i\Delta_c + \tfrac{1}{2}\kappa\right)C_{az} - \gamma^-\left(C_{az} + C_a\right) - \frac{g}{2}\left[-iC_x + (N-1)\,C_{yz}\right] \\ &- i\frac{g}{2}\left[iC_y + (N-1)\,C_{xz}\right] + g\left(C_{aay} + C_{a^\dagger ay}\right) - ig\left(C_{aax} - C_{a^\dagger ax}\right) + \eta(t)C_z\,.\end{aligned} \tag{13}$$

These now depend on third order expectation values, some of which contain multiple Pauli operators. We must note that these terms indicate Pauli operators representing different molecules and so commute — we have already taken into account the cases where the Pauli operators correspond to the same molecule by using the Pauli algebra $\sigma^\alpha\sigma^\beta = \mathbb{1}\delta^{\alpha\beta} + i\sigma^\gamma\epsilon^{\alpha\beta\gamma}$. The molecule-molecule expectation values for the same Pauli operator acting on different molecules are

$$\partial_t C_{xx} = -2\Delta_a C_{xy} - 4g\mathrm{Im}\left[C_{axz}\right] - 2\gamma^{\mathrm{tot}}C_{xx}\,, \tag{14}$$
$$\partial_t C_{yy} = 2\Delta_a C_{xy} - 4g\mathrm{Re}\left[C_{ayz}\right] - 2\gamma^{\mathrm{tot}}C_{yy}\,, \tag{15}$$
$$\partial_t C_{zz} = 4g\left(\mathrm{Im}\left[C_{axz}\right] + \mathrm{Re}\left[C_{ayz}\right]\right) - 2\gamma^-\left(C_{zz} + C_z\right) . \tag{16}$$

Finally, the molecule-molecule expectation values for different Pauli operators acting on different molecules are

$$\partial_t C_{xy} = \Delta_a \left(C_{xx} - C_{yy}\right) - 2g \left(\mathrm{Re}\left[C_{axz}\right] + \mathrm{Im}\left[C_{ayz}\right]\right) - 2\gamma^{\mathrm{tot}} C_{xy} \,, \tag{17}$$

$$\partial_t C_{xz} = -\Delta_a C_{yz} + 2g \left(\mathrm{Re}\left[C_{axy}\right] + \mathrm{Im}\left[C_{axx}\right] - \mathrm{Im}\left[C_{azz}\right]\right) - \gamma^{\mathrm{tot}} C_{xz} - \gamma^{-} \left(C_{xz} + C_x\right) \,, \tag{18}$$

$$\partial_t C_{yz} = \Delta_a C_{xz} + 2g \left(\mathrm{Re}\left[C_{ayy}\right] - \mathrm{Re}\left[C_{azz}\right] + \mathrm{Im}\left[C_{axy}\right]\right) - \gamma^{\mathrm{tot}} C_{yz} - \gamma^{-} \left(C_{yz} + C_y\right) \,. \tag{19}$$

In principle one can continue to write equations of motion for increasingly higher orders of expectation values, however, at large N, most essential physics is obtained at second order. We therefore truncate the cumulant expansion by setting third order cumulants to zero. These are defined as

$$\langle\langle ABC \rangle\rangle = \langle ABC\rangle - \langle AB\rangle\langle C\rangle - \langle A\rangle\langle BC\rangle - \langle AC\rangle\langle B\rangle + 2\langle A\rangle\langle B\rangle\langle C\rangle \,, \tag{20}$$

and so setting $\langle\langle ABC\rangle\rangle = 0$ closes the system of differential equations, allowing us to write $\langle ABC\rangle$ in terms of first and second order correlations.

C. Behaviour in the thermodynamic limit

In Fig. S8 we present the theoretical N-dependence of the charging time τ, maximum energy density E_{max}, and maximum power density P_{max} over a wider range of N than shown in Fig. 3 of the main text. This shows that in addition to the decay-dominated (purple) and coupling-dominated (green) behavior described in the main text, a third region occurs at even larger N, which we discuss below.

In the main text we discussed the energetic dynamics around the decay-to-coupling dominated crossover regime, as this was the experimental operating region. Moving deeper into coupling-dominated regime does not necessarily improve the energy storage properties. This is illustrated in Fig. S8(b) which shows the simulated four points, corresponding to the circles in Fig. S8(a). Within the coupling-dominated regime, energy stored within the microcavity rapidly oscillates which is not a desirable feature. This occurs because the light and matter degrees of freedom hybridise to form polaritons with upper and lower branches split by Rabi frequency $\pm g\sqrt{N}$, leading to beating between these modes. These oscillations are not present in the experimentally studied crossover region. In this region, dephasing is strong enough to prevent oscillation in energy, yet weak enough to warrant superextensive charging. Therefore, this is the optimal region to produce a QB. Going deeper into the coupling-dominated regime would only be advantageous if energy was extracted on a shorter timescale than the period of oscillations, or additional mechanisms were in place to stabilise the oscillations.

At even larger N (red region) the stored energy falls with increasing N. This can be understood as arising from a condition where the polariton energy splitting exceeds the bandwidth of the pump (set by its finite pulse duration), suppressing energy absorption. Numerically, we find this occurs when $N > N_\sigma$ where $g\sqrt{N_\sigma} = (2/5)^{\frac{1}{4}}\,(1/\sigma)$, which signifies the onset of this non-resonant regime. The prefactor $(2/5)^{\frac{1}{4}}$ will be explained in Section S2 D. To build an efficient QB in this regime, one should tune the frequency of the laser to match the polariton energies. Additionally, the time dynamics of energy absorption here change significantly, with the second half of the laser pulse causing stimulated emission, reducing the stored energy — such dynamics arises naturally from a toy model of strongly coupled modes with a splitting larger than the pulse bandwidth, and can be seen in the form of the red line in Fig. S8(b).

In Figure S9, we show the theoretical N-dependence of τ, E_{max} and P_{max} when the frequency of the driving laser is tuned resonant to the lower polariton, i.e. $\Delta_a = \Delta_c = g\sqrt{N}$ in the cumulant equations given in Section S2 B. We emphasise that this is not the condition under which the experiments were performed, but of theoretical interest. By comparison of Figures S9 and S8 one can see that the behaviour of the measures with the different driving frequencies are the same until $N > N_\sigma$. In Figure S9 when $N > N_\sigma$, the laser frequency continues to drive at the frequency of the lower polariton, instead of at the molecular energy as in Figure S8. In this case, the total energy and power in the cavity continue to grow linearly with N, and so the energy and power densities are constant.

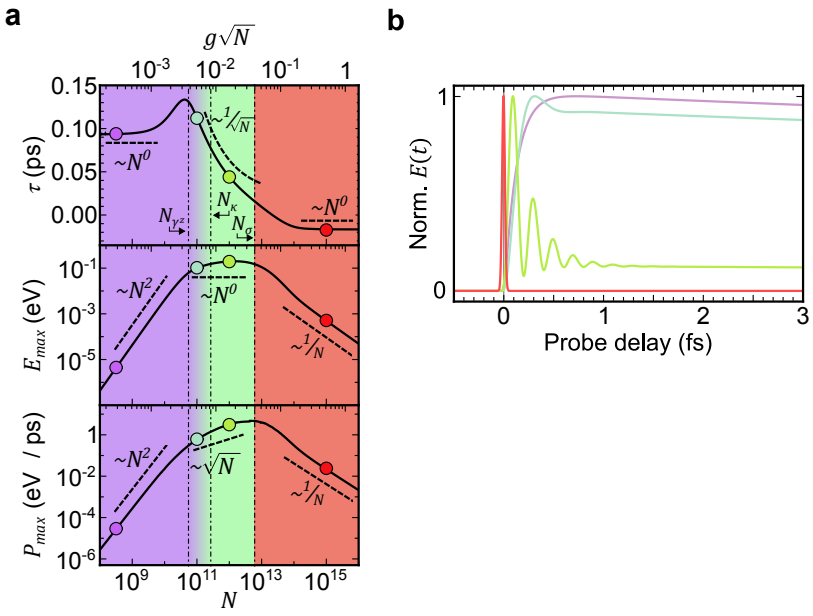

FIG. S8. **Charging dynamics vs number of molecules N.** (a) Charging time, peak stored energy, and maximum power as a function of N. This figure is identical to Fig. 3(a) in the main text, but extended to larger range of N. At large N the stored energy can reach half maximum before the laser pulse finishes, in which case the charging time τ becomes negative. (b) Examples of dynamics in each regime. The values of N used in these dynamics corresponds to the circles of the same colour in (a).

D. The boundary between decay and coupling dominant regimes

There are two timescales in this system: the vacuum Rabi splitting (i.e. polariton detuning) $g\sqrt{N}$ and the Rabi splitting $g\sqrt{rN}$ where rN is the number of photons in the cavity. In Fig. 3(a), we show that the microcavity charges super-extensively once $g\sqrt{N}$ is greater than all decay channels. However, this is only true if $r \leq 1$, as is true in experiments A1, A2 and A3. In Fig. 3(b), the boundaries N_κ and N_{γ^z} are instead determined by $g\sqrt{rN}$ being equal to the decay rates. This is because $r \geq 1$ in experiments B1 and B2. More generally, the important timescale is the larger of the polariton detuning and the Rabi splitting, and so the coupling dominant regime occurs when $g\sqrt{\text{Max}(1,r)N}$ is larger than all decay channels.

In Figure S10 we plot the charging time τ as a function of N and r. Here, we set $\kappa = \gamma^- = \gamma^z \equiv \Gamma = 2$ meV (note that γ^z is independent of N) so that there is only one boundary between the decay dominant and coupling dominant regimes. The green, red and dashed-black lines show the boundaries between the decay dominant and coupling dominant regimes ($N = N_\Gamma$) if $g\sqrt{N}$, $g\sqrt{rN}$ or $g\sqrt{\text{Max}(1,r)N}$ are used as the relevant coupling scale respectively. Clearly, the boundary is determined by $g\sqrt{\text{Max}(1,r)N}$ for all values of r. We also show the boundary between the coupling dominant and non-resonant regimes ($N = N_\sigma$) as the cyan line. When $r > 1$, we find that N_σ becomes linearly dependent on r. The prefactor $(2/5)^{\frac{1}{4}}$ is necessary for N_σ to align with the contours of increased charging time for $r > 1$.

E. Dependence on laser intensity

Figure S11 shows how capacity, charging time and power vary as a function of laser intensity r at fixed number of molecules N. For small r, we find that the maximum energy and power densities vary linearly with r, while charging time is constant. This simply reflects the total energy in the cavity. The charging time is constant because decay channels still dominate over coherent dynamics. As r is increased beyond $r = 1$, the important timescale $g\sqrt{\text{max}(1,r)N}$ begins to scale with r, and so the boundaries separating

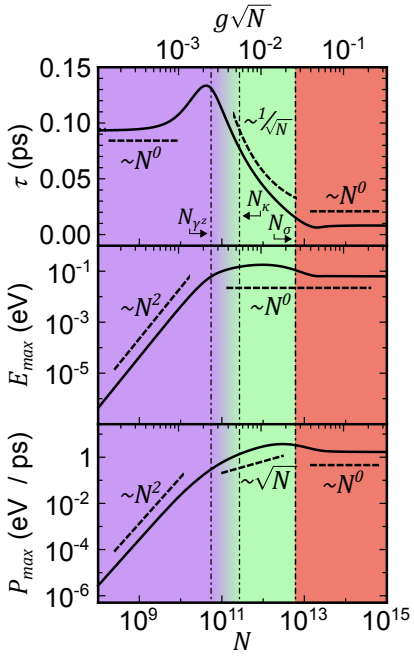

FIG. S9. **Charging dynamics when pumping at lower polariton.** Charging time, peak stored energy, and maximum power as a function of N. This figure is identical to Fig. S8 except that the frequency of the laser is tuned to the lower polariton energy, $\Delta_a = \Delta_c = g\sqrt{N}$, rather than the molecular energy.

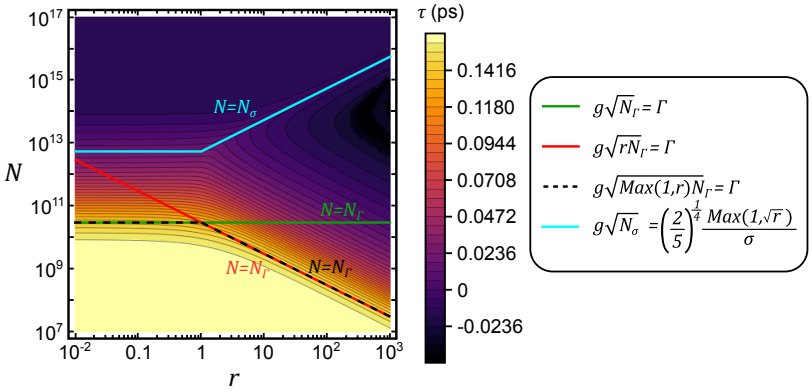

FIG. S10. **Charging time as a function of number of molecules N and laser intensity r.** All parameters are equivalent to the Q1% cavity (see main text) with the exception that the dephasing and non-radiative decay rates are equal to the cavity leakage rate (set to $\gamma^z = \kappa = \Gamma = 2$ meV) and note that the dephasing rate is independent of N.

the coupling dominant and decay dominant regions N_κ and N_{γ^z} are pushed to smaller N. When these boundaries become smaller than the number of molecules in the cavity, the charging time begins to scale as $1/\sqrt{r}$. Additionally, the energy density begins to saturate because there are already many more photons than there are molecules within the cavity. In Figure S11(b) we also plot the experimentally measured energy densities, and we see there is good agreement to the theoretical curve. The coloured points in Figure S11(a) indicate the charging time, maximum capacity and maximum power of the temporal dynamics of the same colour in Figure S11(b).

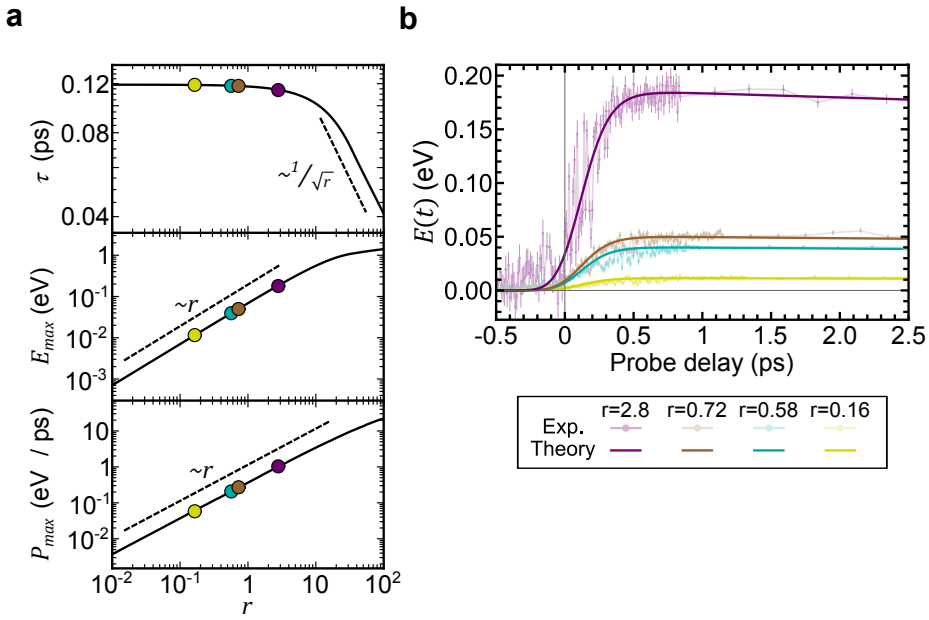

FIG. S11. **Charging dynamics vs pump intensity** r**.** (a) Capacity, charging time and maximum power vs r for a fixed number of molecules $N = 1.62 \times 10^{10}$ (the 1% cavity). All other parameters align with those used to model the 1% cavity. (b) Comparison of theoretical and experimental charging dynamics for four values of r. These are indicated by circles in the charging time panel of (a), showing the experimentally measured values.

S3. FITTING OF MODEL PARAMETERS

As outlined in the main text, we used a reduced chi-squared optimisation procedure to determine the light matter coupling g, dephasing constant γ_0^z and non-radiative decay rate γ^-, as well as to estimate uncertainties on these parameters. As these quantities represent molecular properties, we would expect them to be the same in all the different experiments. For this reason, we performed a global fit rather than performing the procedure individually for each experiment. In this section we give further details on this calculation. As also discussed in the main text, our fitting process is key in estimating the charging time, stored energy and peak charging power. Extracting these quantities requires a smooth curve of charge vs time. Any smoothing process implicitly introduces an effective fitting function (such as e.g. fitting the data to piecewise cubic splines). Since our best guess for such a fitting function is in fact the theoretical model described above, we use this continuous function, fit to the experimental data, to extract charging times, energies, and powers.

In performing our fitting, it is necessary to use the values of the molecule numbers, estimated as discussed above. Because of this, errors in the estimates of N affect the fitting parameters, and thus the resulting charging timescales and powers. These correlated errors make it challenging to estimate errors in the power-law scaling of charging time vs N.

The cavity lifetime (or equivalently the cavity linewidth κ) can also be considered as a fitting parameter, however the value of this parameter is more strongly constrained by other measurements. As noted above, transfer matrix simulations on the designed cavity give an upper bound of 306fs. An alternate estimate is provided by comparing the theoretical and measured reflectivity spectra of the cavities. As discussed below, this implies a cavity lifetime of 120fs. In the following, we first present fitting results for a cavity lifetime of 120fs, and then in Sec. S3 B we discuss how the results change with alternate cavity lifetimes in the range 120fs to 306fs.

A. Fitting procedure

The steps for our fitting procedure are as follows:

1. Calculate the theoretical $E(t)$ curves for a grid of parameter values g, γ^z, γ^-, along with the values of N relevant for all five experiments, A1, A2, A3, B1 and B2. Based on previous observations, we chose the search region of the parameter space as $g \in [0.1, 5000]$ neV; $\gamma_0^z \in [0.1, 5000]$ meV and $\gamma^- = [0.001, 1]$ meV. Subsequent refinements of this search region were made to give higher resolution near the optimal point.

2. We estimate uncertainties, σ_i on each experimental data point (transient reflectivity vs time), by considering the point-to-point variation. Because the uncertainty is higher near $t = 0$, when the pump arrives, we use different error estimates in different time windows. Specifically, we divide experiments A1 and A2 into five windows $t < -300\text{fs}; -300\text{fs} < t < 300\text{fs}; 300\text{fs} < t < 700\text{fs}; 700\text{fs} < t < 1000\text{fs}; t > 1000\text{fs}$. For experiments A3, B1 and B2 we found that four windows $t < -300\text{fs}; -300\text{fs} < t < 300\text{fs}; 300\text{fs} < t < 1000\text{fs}; t > 1000\text{fs}$ was sufficient. In each window, the uncertainty estimate for each experiment is taken from the variance over a narrow range of points (typically 150fs) where there is no strong time dependence.

3. For each set of parameters, we performed an "internal" chi-squared minimisation to find the optimal scaling factor S between the stored energy $E(t)$ and the measured differential reflectivity $\Delta R/R$, and a time shift between the theory and experiment T_0. That is, we minimise

$$\chi^2 = \sum_i \left[\frac{S \times (\Delta R/R)_i - E(t_i + T_0)}{\sigma_i} \right]^2, \tag{21}$$

   with respect to S and T_0. We treat the result of this minimisation as the chi-squared value which we use in the following steps to estimate the meaningful parameters g, γ^z, γ^- and their uncertainties.

   Estimating the scaling factor S from first principles is difficult because of reflections by the cavity mirror, hence this factor is found by the best fit value. The time shift reflects uncertainty of delays in the optics, so that it is not a-prior clear when the peak of the pump pulse arrives. After this shift, we define $t = 0$ as the moment the pump arrives. This is important when calculating the charging time τ, which we defined as the time from the arrival of the pump until reaching half maximum energy.

4. We then use the chi-squared value described above, and divide by the total number of degrees of freedom $k_{\text{eff}} = k - 3$ (where k is the total number of data points), to arrive at the final reduced chi-squared $\tilde{\chi}^2$ map. A slice of this three dimensional reduced chi-squared map for the 120 fs lifetime is shown in Figure S12 for $\gamma^- = 0.0263$ meV, which is the optimal non-radiative decay rate given in the main text. The optimal parameter set used in the main text that optimises $\tilde{\chi}^2$ is shown as the red point in Figure S12. We find $\tilde{\chi}^2_{min} = 3.048$, suggesting our estimated measurement uncertainties on $\tilde{\chi}$ are reasonable, but likely underestimates.

5. Finally, the 68% confidence interval for each parameter was estimated by considering the contour for which $\tilde{\chi}^2 = \tilde{\chi}^2_{min} + \frac{1}{k_{\text{eff}}}\Delta^*$ where $\Delta^* = 3.51$ is extracted from the reduced chi-squared distribution for 3 parameters and error tolerance (68%), see [48]. In the right panel of Fig. S12 we show the contour as a white line, and the actual parameter values which lie within this 68% contour as black points.

B. Fitting cavity lifetime

Figure S13 shows the optimal reduced chi-squared as a function of cavity lifetime, along with the corresponding best-fit values of the parameters g, γ_0^z and γ^-, following the fitting procedure described above. The minimal reduced chi-squared is 2.803 occurring for a lifetime of 185 fs.

As noted earlier, the cavity lifetime is also constrained by the measured reflectivity spectrum, shown in Figure S2(d). To check this consistency, Fig. S14 shows the calculated absorption spectra for the 0.5%, 1%, 5% and 10% cavities using the optimal parameter sets given by the 185 fs and 120 fs lifetimes. These are

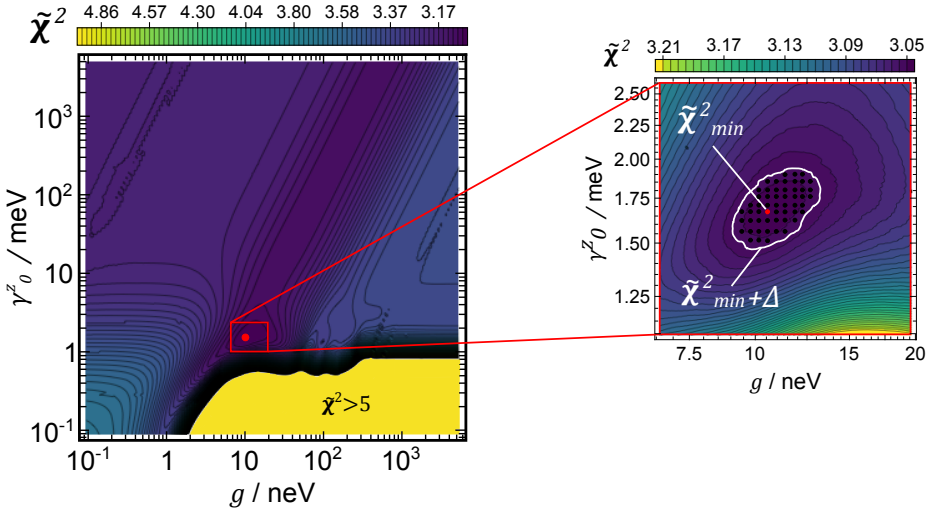

FIG. S12. **Reduced-chi square map to find the optimal parameters for the theoretical model and their 68% confidence intervals.** The chi-squared contour plots shown in this figure are slices of the full three-dimensional map at the optimum non-radiative decay rate $\gamma^- = 0.0141$ meV used in the main text for a cavity lifetime of 120 fs. In the yellow region of the bottom right corner $\tilde{\chi}^2 > 5$, which we do not show to emphasise smaller variations in $\tilde{\chi}^2$. In the right panel, the highlighted contour shows the 68% confidence interval, found using $\Delta = \Delta^*/k_{\text{eff}}$.

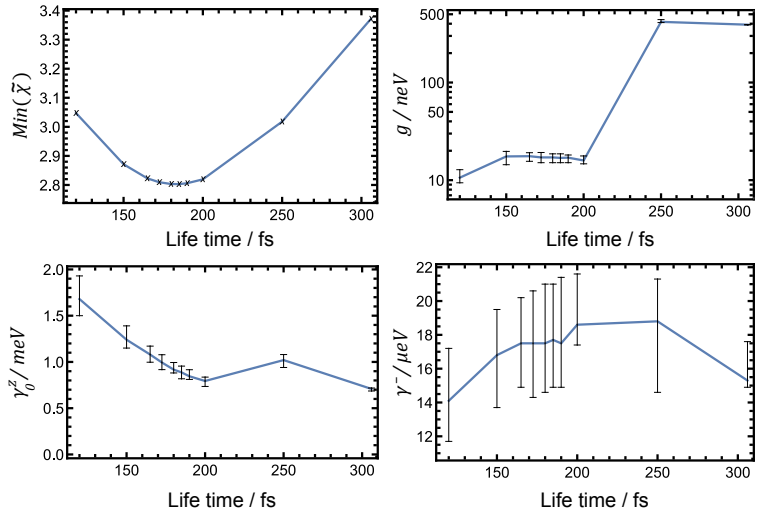

FIG. S13. **Optimal reduced chi-squared, and associated best-fit parameters as a function of cavity lifetime.** Error bars indicate 68% confidence intervals, calculated through the procedure described in Section S3 A.

calculated as $\text{Abs}(\Delta\nu) = \text{Re}\int_0^\infty \exp[i(\Delta\nu+\omega)t]\langle a(t)a^\dagger(0)\rangle$ where $\Delta\nu$ is the energy detuning from the cavity and molecules. When evaluated from our model using the quantum regression theorem, we find

$$\text{Abs}(\Delta\nu) = -\text{Re}\left[\frac{i\Delta\nu - \gamma^{\text{tot}}}{\left(i\left[\Delta\nu + \Omega_{\text{eff}}\right] - \frac{2\gamma^{\text{tot}}+\kappa}{4}\right)\left(i\left[\Delta\nu - \Omega_{\text{eff}}\right] - \frac{2\gamma^{\text{tot}}+\kappa}{4}\right)}\right], \tag{22}$$

where $\Omega_{\text{eff}} = \sqrt{g^2N - (\kappa - 2\gamma^{\text{tot}})^2/4}$ is the effective Rabi splitting. From the measured spectra in Figure S2(d), we expect the 0.5% and 1% cavities to show no polariton splitting, the 5% cavity to have a small

splitting, and the 10% cavity to clearly show strong coupling.

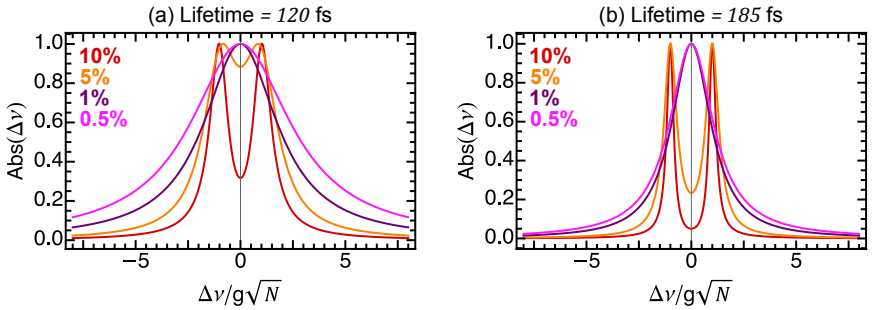

FIG. S14. **Absorption spectra for the** 0.5%**,** 1%**,** 5% **and** 10% **cavities**. The spectrum is calculated using Eq. (22) for the best-fit parameters (see Figure S13) for both 120 fs and 185 fs cavity lifetimes. In the 5% and 10% cavities, there are clear polariton peaks forming at $\Delta\nu = \pm g\sqrt{N}$.

It is clear from Figure S14 that although the 185 fs cavity lifetime gives a smaller reduced chi-squared, these parameters predict significantly stronger coupling than is seen in experimental reflectivity spectra. In contrast, the 120 fs cavity lifetime parameters reproduce the polariton splittings across all cavities more accurately, while showing a reduced chi-squared that is not significantly larger. We therefore conclude that 120 fs cavity lifetime, with g, γ_0^z and γ^- given in the main text provides the best fit to the experimental data. In Table S2, we summarise the scaling factors S and time shifts T_0 that relate the measured differential reflectivity $\Delta R/R$ to the theoretically calculated stored energy $E(t)$, as used to calculate the fits plotted in Figure 2(b) of the main text. For a formal defintion of S, T_0, see Eq. (21).

Experiment	Scaling factor, S	Time shift, T_0/ fs
A1	2.32	47.4
A2	2.01	-47.4
A3	2.93	-140.0
B1	3.75	-159.8
B2	6.24	-210.5

TABLE S2. **The optimal scaling factors and time shifts used to calculate the theoretical curves in Figure 2(b) in the main text.**

C. Results of fitting procedure

The theoretical time evolution arising from using the above fitting procedure is shown in Figure 3 of the main text. In plotting that figure, the results of the theoretical fit are convolved with an instrument response function, as required to match the experimental data. Figure S15 shows the same data but without convolution by the instrument response, thus providing a more direct picture of the intrinsic dynamics of the system. From the theoretical curves, one can extract the rise time of stored energy τ, the peak stored energy $E_{\max}$, and maximum charging power $P_{\max}$. These values are summarised in Table 1 in the main text.

As well as the scaling to the observables with N shown in Figure 3 in the main text, we could also estimate an effective power-law scaling of the observables $q_i \in \{\tau, E_{\max}, P_{\max}\}$ directly from pairs of experiments i, j by the relation $q_i/q_j = (N_i/N_j)^{f_q}$. As all our observables are intensive (i.e. densities), $f_q > 0$ indicates superextensive behaviour, $f_q = 0$ indicates extensive, and $f_q < 0$ subextensive behaviours. Table S3 gives the observed values of f_q.

D. Residuals of the best fit

To check whether systematic errors arise from our fitting procedure, Fig. S16 shows the residual errors—i.e. difference between the theoretical curves and the experimental data—for the five experiments shown in

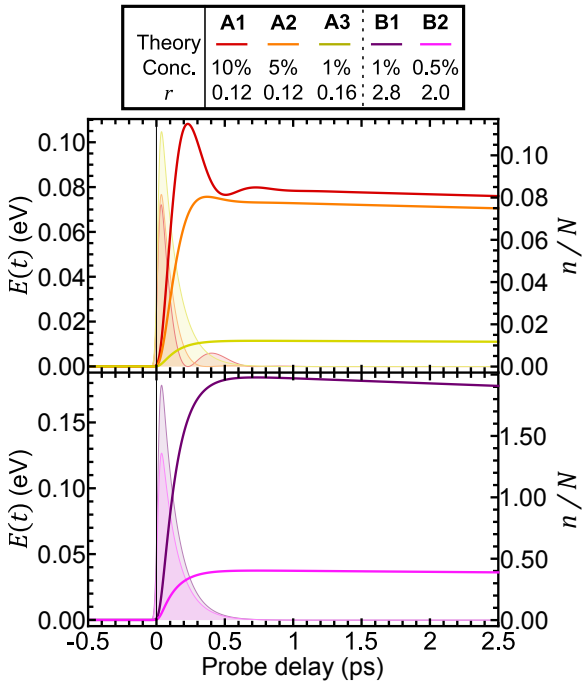

FIG. S15. **Further details of the dynamics of the quantum batteries**. These plots show the time dependence of energy without convolution by the instrument response function (lines without fill) and the ratio of the number of photons, n to molecules, N in the cavity (lines with fill).

Experiments	f_τ	$f_{E_{\max}}$	$f_{P_{\max}}$
A1/A2	-0.35	0.52	0.94
A2/A3	0.01	1.18	1.20
B1/B2	0.12	2.30	2.19

TABLE S3. **Observed subextensive and superextensive scaling behaviours in rise-time, stored energy, and charging power.** Power-law exponent f_q for observable $q \in \{\tau, E_{\max}, P_{\max}\}$, where $f_q > 0$, $f_q = 0$, $f_q < 0$ indicates superextensivity, extensivity, and subextensivity, respectively. Table values indicate that charging time τ is subextensive, whilst stored energy $E_{\max}$ and charging power $P_{\max}$ are superextensive. The first column indicates the corresponding experiments.

Figure 2 of the main text. As is clear, there are no discernible features in the residuals that are consistently present across the different experiments. This indicates that the theoretical curves account for the essential characteristics of the data.

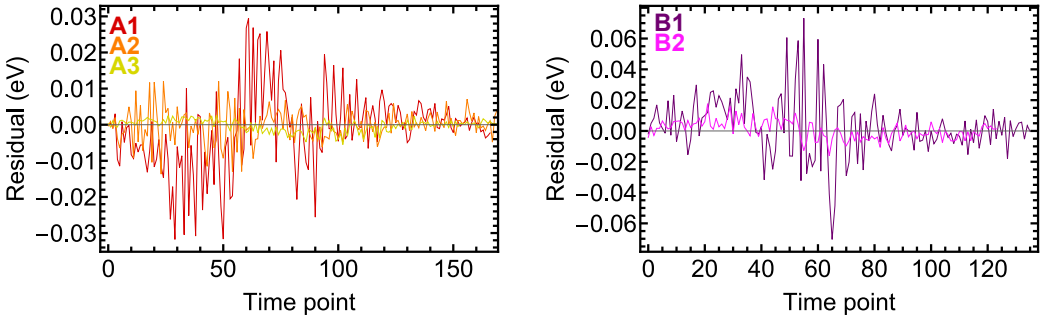

FIG. S16. The residuals of the theoretical curves and the experimental data over the duration of the experiments.

E. Theoretical fits for 185 fs lifetime

In Figure S17, we show the theoretical fits to the experimental data for experiments A1, A2, A3, B1 and B2 for a lifetime of 185 fs. This lifetime gave the optimal reduce chi-square in Figure S13. From the reduced chi-square fitting procedure, we found that the optimal parameters for this lifetime were $g = 16.9^{+1.7}_{-1.8}$ neV, $\gamma_0^z = 0.887^{+0.068}_{-0.060}$ meV and $\gamma^- = 0.0177^{+0.0033}_{-0.0029}$ meV.

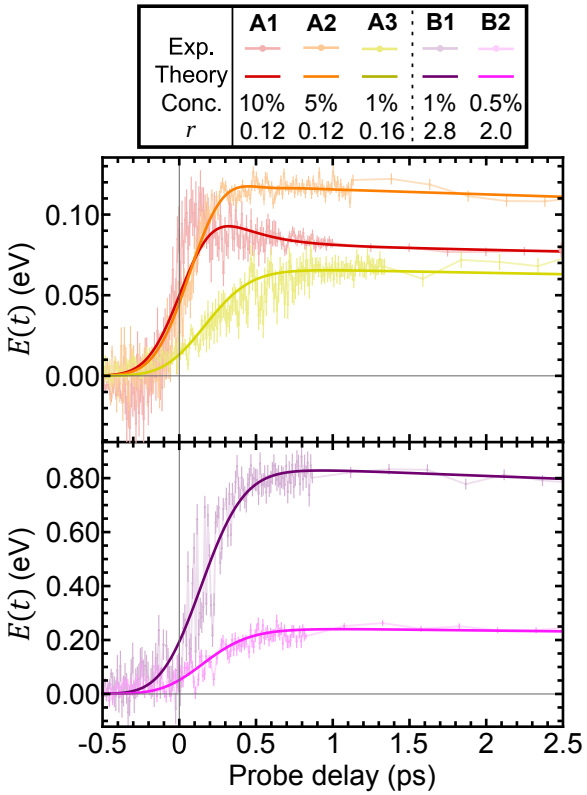

FIG. S17. The fits to the experimental data using a lifetime of 185 fs.

S4. MOVIE

Movie S1: Animation showing the molecular energy evolution for a range of N values.
Caption: The plots on the left-hand-side show the time evolution of the molecular energy over two different time scales. As the animation progresses, the value of N is increased, with the value indicated by the solid vertical line in the right-hand plot. Parameters are the same as those used in Figure S9.
File: Animation_LT120_Caption.mp4

REFERENCES AND NOTES

1. M. Gross, S. Haroche, Superradiance: An essay on the theory of collective spontaneous emission. *Phys. Rep.* **93**, 301–396 (1982).

2. N. Skribanowitz, I. P. Herman, J. C. MacGillivray, M. S. Feld, Observation of Dicke superradiance in optically pumped HF Gas. *Phys. Rev. Lett.* **30**, 309–312 (1973).

3. H. M. Gibbs, Q. H. F. Vrehen, H. M. J. Hikspoors, Single-pulse superfluorescence in cesium. *Phys. Rev. Lett.* **39**, 547–550 (1977).

4. J. Feldmann, G. Peter, E. O. Gobel, P. Dawson, K. Moore, C. Foxon, R. J. Elliott, Linewidth dependence of radiative exciton lifetimes in quantum-wells. *Phys. Rev. Lett.* **59**, 2337–2340 (1987).

5. B. Deveaud, F. Clerot, N. Roy, K. Satzke, B. Sermage, D. S. Katzer, Enhanced radiative recombination of free excitons in GaAs quantum wells. *Phys. Rev. Lett.* **67**, 2355–2358 (1991).

6. T. Itoh, M. Furumiya, Size-dependent homogeneous broadening of confined excitons in cucl microcrystals. *JOL* **48-49**, 704–708 (1991).

7. S. Deboer, D. A. Wiersma, Dephasing-induced damping of superradiant emission in J-aggregates. *Chem. Phys. Lett.* **165**, 45–53 (1990).

8. S. Inouye, A. P. Chikkatur, D. M. Stamper-Kurn, J. Stenger, D. E. Pritchard, W. Ketterle, Superradiant Rayleigh scattering from a Bose-Einstein condensate. *Science* **285**, 571–574 (1999).

9. R. Reimann, W. Alt, T. Kampschulte, T. Macha, L. Ratschbacher, N. Thau, S. Yoon, D. Meschede, Cavity-modified collective Rayleigh scattering of two atoms. *Phys. Rev. Lett.* **114**, 023601 (2015).

10. A. Angerer, K. Streltsov, T. Astner, S. Putz, H. Sumiya, S. Onoda, J. Isoya, W. J. Munro, K. Nemoto, J. Schmiedmayer, J. Majer, Superradiant emission from colour centres in diamond. *Nat. Phys.* **14**, 1168–1172 (2018).

11. K. D. Higgins, S. C. Benjamin, T. M. Stace, G. J. Milburn, B. W. Lovett, E. M. Gauger, Superabsorption of light via quantum engineering. *Nat. Commun.* **5**, 4705 (2014).

12. D. Yang, S.-h. Oh, J. Han, G. Son, J. Kim, J. Kim, M. Lee, K. An, Realization of superabsorption by time reversal of superradiance. *Nat. Photonics* **15**, 272–276 (2021).

13. R. Alicki, M. Fannes, Entanglement boost for extractable work from ensembles of quantum batteries. *Phys. Rev. E Stat. Nonlin. Soft Matter Phys.* **87**, 042123 (2013).

14. K. V. Hovhannisyan, M. Perarnau-Llobet, M. Huber, A. Acin, Entanglement generation is not necessary for optimal work extraction. *Phys. Rev. Lett.* **111**, 240401 (2013).

15. F. C. Binder, S. Vinjanampathy, K. Modi, J. Goold, Quantacell: Powerful charging of quantum batteries. *New J. Phys.* **17**, 075015 (2015).

16. G. M. Andolina, D. Farina, A. Mari, V. Pellegrini, V. Giovannetti, M. Polini, Charger-mediated energy transfer in exactly solvable models for quantum batteries. *Phys. Rev. B* **98**, 205423 (2018).

17. G. M. Andolina, M. Keck, A. Mari, M. Campisi, V. Giovannetti, M. Polini, Extractable work, the role of correlations, and asymptotic freedom in quantum batteries. *Phys. Rev. Lett.* **122**, 047702 (2019).

18. R. Alicki, A quantum open system model of molecular battery charged by excitons. *J. Chem. Phys.* **150**, 214110 (2019).

19. Y. Y. Zhang, T. R. Yang, L. Fu, X. Wang, Powerful harmonic charging in a quantum battery. *Phys. Rev. E* **99**, 052106 (2019).

20. F. Campaioli, F. A. Pollock, F. C. Binder, L. Celeri, J. Goold, S. Vinjanampathy, K. Modi, Enhancing the charging power of quantum batteries. *Phys. Rev. Lett.* **118**, 150601 (2017).

21. J. Q. Quach, W. J. Munro, Using dark states to charge and stabilize open quantum batteries. *Phys. Rev. Appl.* **14**, 024092 (2020).

22. T. P. Le, J. Levinsen, K. Modi, M. M. Parish, F. A. Pollock, Spin-chain model of a many-body quantum battery. *Phys. Rev. A* **97**, 022106 (2018).

23. X. Zhang, M. Blaauboer, Enhanced energy transfer in a Dicke quantum battery. arXiv:1812.10139 (2018).

24. D. Ferraro, M. Campisi, G. M. Andolina, V. Pellegrini, M. Polini, High-power collective charging of a solid-state quantum battery. *Phys. Rev. Lett.* **120**, 117702 (2018).

25. S. Gherardini, F. Campaioli, F. Caruso, F. C. Binder, Stabilizing open quantum batteries by sequential measurements. *Phys. Rev. Res.* **2**, 013095 (2020).

26. A. C. Santos, A. Saguia, M. S. Sarandy, Stable and charge-switchable quantum batteries. *Phys. Rev. E* **101**, 062114 (2020).

27. W. M. Brown, E. M. Gauger, Light harvesting with guide-slide superabsorbing condensed-matter nanostructures. *J. Phys. Chem. Lett.* **10**, 4323–4329 (2019).

28. D. Sanvitto, S. Kéna-Cohen, The road towards polaritonic devices. *Nat. Mater.* **15**, 1061–1073 (2016).

29. V. Savona, L. C. Andreani, P. Schwendimann, A. Quattropani, Quantum well excitons in semiconductor microcavities: Unified treatment of weak and strong coupling regimes. *Solid State Commun.* **93**, 733–739 (1995).

30. G. Cerullo, C. Manzoni, L. Lüer, D. Polli, Time-resolved methods in biophysics. 4. Broadband pump–probe spectroscopy system with sub-20 fs temporal resolution for the study of energy transfer processes in photosynthesis. *Photochem. Photobiol. Sci.* **6**, 135–144 (2007).

31. C. Manzoni, G. Cerullo, Design criteria for ultrafast optical parametric amplifiers. *J. Opt.* **18**, 103501 (2016).

32. O. Svelto, D. C. Hanna, *Principles of Lasers* (Springer, 2010), vol. 1.

33. T. Virgili, D. G. Lidzey, D. D. C. Bradley, G. Cerullo, S. Stagira, S. De Silvestri, An ultrafast spectroscopy study of stimulated emission in poly(9,9-dioctylfluorene) films and microcavities. *Appl. Phys. Lett.* **74**, 2767–2769 (1999).

34. P. Kirton, J. Keeling, Suppressing and restoring the Dicke superradiance transition by dephasing and decay. *Phys. Rev. Lett.* **118**, 123602 (2017).

35. K. B. Arnardottir, A. J. Moilanen, A. Strashko, P. Törmä, J. Keeling, Multimode organic polariton lasing. arXiv:2004.06679 (2020).

36. M. Zens, D. O. Krimer, S. Rotter, Critical phenomena and nonlinear dynamics in a spin ensemble strongly coupled to a cavity. II. Semiclassical-to-quantum boundary. *Phys. Rev. A* **100**, 013856 (2019).

37. K. D. B. Higgins, B. W. Lovett, E. M. Gauger, Quantum-enhanced capture of photons using optical ratchet states. *J. Phys. Chem. C* **121**, 20714–20719 (2017).

38. C. P. Dietrich, A. Steude, L. Tropf, M. Schubert, N. M. Kronenberg, K. Ostermann, S. Hofling, M. C. Gather, An exciton-polariton laser based on biologically produced fluorescent protein. *Sci. Adv.* **2**, e1600666 (2016).

39. Y. Wang, P. Shen, J. Liu, Y. Xue, Y. Wang, M. Yao, L. Shen, Recent advances of organic solar cells with optical microcavities. *Solar RRL* **3**, 1900181 (2019).

40. B. Kippelen, J.-L. Brédas, Organic photovoltaics. *Energ. Environ. Sci.* **2**, 251–261 (2009).

41. K. A. Mazzio, C. K. Luscombe, The future of organic photovoltaics. *Chem. Soc. Rev.* **44**, 78–90 (2015).

42. G. J. Hedley, A. Ruseckas, I. D. W. Samuel, Light harvesting for organic photovoltaics. *Chem. Rev.* **117**, 796–837 (2017).

43. P. Cheng, G. Li, X. Zhan, Y. Yang, Next-generation organic photovoltaics based on non-fullerene acceptors. *Nat. Photonics* **12**, 131–142 (2018).

44. E. Hecht, *Optics* (Pearson Education Incorporated, 2017).

45. D. Wang, H. Kelkar, D. Martin-Cano, D. Rattenbacher, A. Shkarin, T. Utikal, S. Götzinger, V. Sandoghdar, Turning a molecule into a coherent two-level quantum system. *Nat. Phys.* **15**, 483–489 (2019).

46. C. Gardiner, *Handbook of Stochastic Methods for Physics, Chemistry, and the Natural Sciences Springer* (ed. 4, 2009).

47. J. del Pino, J. Feist, F. J. Garcia-Vidal, Quantum theory of collective strong coupling of molecular vibrations with a microcavity mode. *New J. Phys.* **17**, 053040 (2015).

48. J. V. Wall, C. R. Jenkins, *Practical Statistics for Astronomers* (Cambridge Univ. Press, 2003).

49. L. V. Wang, H.-i. Wu, *Biomedical Optics: Principles and Imaging* (John Wiley & Sons, 2012).

50. K. Yamashita, U. Huynh, J. Richter, L. Eyre, F. Deschler, A. Rao, K. Goto, T. Nishimura, T. Yamao, S. Hotta, H. Yanagi, M. Nakayama, R. H. Friend, Ultrafast dynamics of polariton cooling and renormalization in an organic single-crystal microcavity under nonresonant pumping. *ACS Photonics* **5**, 2182–2188 (2018).